WARSAW UNIVERSITY OF TECHNOLOGY

DISCIPLINE OF SCIENCE - MECHANICAL ENGINEERING
FIELD OF SCIENCE - ENGINEERING AND TECHNOLOGY

Ph.D. Thesis

Przemysław Paszkiewicz, M.Sc.

Experimental characterization of a sub-Newton electrothermal thruster using 98% hydrogen peroxide

Supervisor
Prof. Jan Kindracki, D.Sc., D.Eng.

WARSAW 2023

Acknowledgements

I would like to express my gratitude to my supervisor, Prof. Jan Kindracki
for the guidance and support that I received
throughout the years of cooperation

Streszczenie

Na przestrzeni ostatnich lat wyraźnie nakreślony został trend zmierzający do ograniczenia użycia szkodliwych dla człowieka i środowiska związków chemicznych, wykorzystywanych jako materiały pędne w technikach rakietowych. Wspominany kierunek zmian nie jest spowodowany wyłącznie względami bezpieczeństwa. Wynika on także ze zmieniających się realiów rynkowych, dotyczących aktywności w kosmosie, w których udział prywatnych, stosunkowo niewielkich firm, staje się znaczny. Wymusza to konieczność poszukiwania korzystnych cenowo rozwiązań, gwarantujących dostępność i tym samym konkurencyjność. Jedną z substancji w znacznym stopniu spełniającą wymagania rynku jest wysoko stężony nadtlenek wodoru. Mając na uwadze potencjał aplikacyjny wspomnianego związku, podjęte zostały przez autora prace eksperymentalne mające na celu poszerzenie wiedzy na temat egzotermicznego zjawiska rozkładu tejże substancji.

Podjęto prace badawcze mające na celu potwierdzenie możliwości praktycznego zastosowania koncepcji silnika, w którym egzotermiczny rozkład 98% nadtlenku wodoru realizowany jest w reaktorze bez dedykowanego wypełnienia materiałem o własnościach silnie katalitycznych, a poprzez zastosowanie rezystancyjnego elementu grzejnego. W zakresie prac mieścił się projekt i budowa dedykowanego stanowiska, spełniającego założone wymagania badawcze. Oceny procesów wewnątrzkomorowych dokonano w oparciu o analizy stabilności ciśnienia w komorze, czasu narastania oraz opadania ciśnienia a także wartości prędkości charakterystycznej. Wspomniane miary przedstawiono w funkcji temperatury produktów rozkładu oraz temperatury zewnętrznej ścianki komory. Kampania testowa podzielona została na trzy etapy, w których głównymi zmiennymi były moc rezystancyjnego elementu grzejnego oraz długotrwałość próby. Przeprowadzono szereg testów, w wyniku których potwierdzono możliwość inicjacji oraz podtrzymania stabilnego rozkładu nadtlenku, także w przypadku gdy ciepło nie było dostarczane do reaktora za pośrednictwem elementu grzejnego – proces samopodtrzymujący. Temperatura umożliwiająca inicjację spontanicznego rozkładu w warunkach w jakich prowadzone były badania to ~150°C, co odpowiada normalnemu punktowi wrzenia 98% H_2O_2.

Słowa kluczowe: nadtlenek wodoru, silniki rakietowe, ekologiczne materiały pędne

Abstract

In recent years, a trend has been outlined to limit the application of chemical compounds used as rocket propellants that are harmful to humans and the environment. The tendency mentioned above, in fact, is not only due to safety-related issues; another cause is the changing space industry environment in which space activities are no longer a domain of only large national and international space agencies as privately founded, relatively small companies operate in parallel. Consequently, readily available, low-cost solutions are required to guarantee competitiveness. One of the promising candidates as a propellant in space propulsion systems that meets market requirements is highly concentrated hydrogen peroxide. Knowing the potential of the discussed chemical, the author undertook an experimental investigation to broaden the knowledge about the exothermic decomposition of hydrogen peroxide. The research was oriented towards a direct application of peroxide in a monopropellant propulsion system.

An experimental campaign was undertaken to confirm the possibility of practical application of the concept of a monopropellant thruster in which exothermal decomposition of 98% hydrogen peroxide was obtained in a reactor that was not filled with a dedicated catalytic material; instead, a resistively heated element was implemented in the chamber. The scope of the work included the design and preparation of a dedicated test rig necessary to meet all research objectives. The internal chamber processes were assessed based on pressure roughness, pressure rise and fall time and characteristic velocity. The metrics used were presented as a function of temperatures measured directly in the decomposition chamber and the temperature of the external wall of the reactor. The test campaign was divided into three parts, in which the most significant variables were heater power and experiment duration. Performed tests confirmed that initiating and sustaining stable decomposition was possible even when the power supply to the resistively heated element in the chamber was turned off - the process was self-sustaining. The threshold wall temperature allowing initiation of spontaneous decomposition in the reactor under test conditions was 150°C, corresponding to the normal boiling point of 98% hydrogen peroxide.

Keywords: hydrogen peroxide, rocket propulsion, green propellants

Contents

List of Figures

List of Tables

Nomenclature

Acronyms

ADN	Ammonium Dinitramide
AMU	Astronaut Maneuvering Unit
ATO	Assisted Take-off Unit
ESA	European Space Agency
FCV	Flow Control Valve
GTO	Geosynchronous Transfer Orbit
HAN	Hydroxylammonium Nitrate
HF	Hydrogen Fluoride
HTP	High Test Peroxide
ID	Inside Diameter
IRFNA	Inhibited Red Fuming Nitric Acid
LH_2	Liquid Hydrogen
LMP-103S	AND-based liquid monopropellant
LOX	Liquid Oxygen
MMH	Monomethylhydrazine
MON	Mixed Oxides of Nitrogen
NTO	Dinitrogen Tetroxide
OD	Outer Diameter
OFR	Oxidizer to Fuel Ratio
RP-1	Rocket Petroleum
RCS	Reaction Control System
REACH	Registration, Evaluation, Authorization and Restriction of Chemicals
UDMH	Unsymmetrical Dimethylhydrazine

Symbols

A	Frequency factor

A_e	Nozzle exit area
A_t	Throat cross-section area
c^*	Characteristic velocity
c_i	Concentration of the i^{th} reaction component
D	Diameter
E_a	Activation energy
F	Thrust
I_{sp}	Specific impulse
I_{tot}	Total Impulse
k	Rate coefficient
m	Mass
$\dot{m}$	Mass flow rate
n	Number of elements
P	Pressure
R	Gas constant
Rou	Pressure roughness
T	Temperature
t	Time
q	Heat
V	Velocity
x_i	The value of i^{th} data point
$\bar{x}$	The mean value of the data set

Greek Symbols

α	Order of reaction
Δ	Difference, increase
ϵ	Nozzle area ratio (A_e/A_t)
η_{c^*}	Characteristic velocity efficiency
κ	Specific heat ratio
ν	Stoichiometric coefficient of the i^{th} reaction component
ρ	Density
σ	Standard deviation
υ	Rate of reaction

Chapter 1

Introduction

In recent years, a growing interest can be observed in the exploration and commercialization of outer space. The space industry is no longer a domain of national and international space agencies; privately funded companies operate in parallel. This evolution of space activities was termed ‘New Space’ [1].

A growing need for low-thrust space propulsion systems can be noted. Two primary examples may be given to explain that need. The first case is typical large satellites, which require extreme accuracy regarding attitude and position. Low-thrust propulsion systems are required to mitigate perturbations, but on the other hand, the requirements on the size, mass and power of the propulsive unit are not very strict. The second scenario is when a small satellite is to be equipped with a propulsion system. Due to the size of the satellite, low thrust and low impulse bits are necessary, along with a small envelope, low mass, and reduced power requirements of the subsystem [2].

One of the trends associated with the ‘New Space’ era is to lower the entry-level and make space activities more affordable and cost-effective. As for the propulsion systems in use, hydrazine has a great heritage and is widely applied in advanced units, but despite good performance in terms of propulsive characteristics, it suffers a severe disadvantage – toxicity. This calls for sophisticated safety requirements, and any activities involving hydrazine are inevitably very costly. In 2011, hydrazine was added to the Registration, Evaluation, Authorization and Restriction of Chemicals (REACH) of the European Parliament and the Council. REACH is the European Union’s regulation which aims to aggregate compounds of a hazardous nature [3,4]. Based on the information provided, it can be easily noticed that non-toxic propellants would fit the market needs ideally. One of the promising candidates is highly concentrated hydrogen peroxide (H_2O_2), which belongs to the so-called ‘green propellants’ group, for which risks and costs related to handling (human exposure), storage and transport can be significantly reduced. The following subsections will present general information concerning hydrogen peroxide and satellite propulsion systems.

1.1 Historical propulsive applications of hydrogen peroxide

Between 1933 and 1936, in Germany, a preparation technique was developed which allowed manufacturing of hydrogen peroxide at concentrations ranging from 80 to 82% [5]. In 1935, Hellmuth Walter established a company, Walterwerke, and by 1936, developed a turbine for submarine applications, generating 400 horsepower and a 10 kN assisted take-off unit (ATO). Both devices used hydrogen peroxide (80-82% weight concentration) decomposed by injection of liquid permanganate salt. During World War II, decomposition products of hydrogen peroxide were used to run the turbopumps of V-2 rockets. The pump delivered liquid oxygen and ethanol to the engine's combustion chamber. The catapult used to accelerate the V-1 flying bomb was also powered by the decomposition products of H_2O_2 [5,6]. Hydrogen peroxide was implemented in the propulsion system of the German rocket plane Messerschmitt Me 163 Komet. The engine was a bipropellant unit, using hydrogen peroxide and fuel - a blend of hydrazine hydrate, methanol and copper compound salt (this blend was denoted as C-Stoff). The H_2O_2/C-Stoff propellant combination is hypergolic - spontaneous ignition occurs when compounds are in contact [7].

Post-war activities in the British rocket industry employed hydrogen peroxide extensively, to some extent, because of the post-war transfer of experienced German staff familiar with the considered compound, including Hellmuth Walter. Different types of engines were developed; this includes monopropellant units, like the Sprite engine, considered for implementation in the De Havilland Comet jet airliner to facilitate take off at high altitude airports during hot weather. The first British bipropellant engines using hydrogen peroxide and C-Stoff were denoted as Alpha. The following series was Beta. Beta 1 was the first British engine to use a turbopump propellant feed system in which part of the propellant was decomposed by a silver-plated gauze and used to run the turbopump. The engine incorporated regenerative cooling (using H_2O_2) [8]. The most advanced British engines belonged to the Gamma series and were used to power the Black Arrow rocket, the first and only British space rocket that in 1971 successfully delivered a satellite into orbit [9]. A hydrogen peroxide propulsion system was implemented in the first commercial geostationary satellite – Intelsat 1 Early Bird, launched in 1965. The unit comprised four thrusters, four tanks and a total initial propellant mass of five kilograms (the concentration used was 95%). Intelsat II was as well equipped with a hydrogen peroxide-based propulsion system containing 9,6 kg of propellant

(90% concentration) [10]. H_2O_2 was present in the first manned spaceflight program – the Mercury Project. The capsule's reaction control system (RCS) employed hydrogen peroxide as a monopropellant [11]. Some additional applications included an astronaut manoeuvring unit (AMU) developed for the Gemini project. The AMU was a 76 kg backpack containing a hydrogen peroxide-based propulsion system. AMU was intended for application by astronauts during extravehicular activities, making them independent of the spacecraft [12]. Small monopropellant thrusters were implemented in the X-15 hypersonic aircraft to facilitate control during high-altitude flights (exceeding 100 km) when the aerodynamic surfaces became ineffective [13]. The early design of the Centaur vehicle employed hydrogen peroxide thrusters for propellant settling and attitude control during coast periods [14].

Decomposition products of hydrogen products are convenient turbine drive gases, as the final temperature can be controlled by changing the concentration of the compound; even for anhydrous H_2O_2, the hot gas temperature of ~1000°C is acceptable for uncooled turbines [5].

The biggest drawback of the early propulsive units using H_2O_2 was excessive, uncontrolled decomposition of the propellant in the tanks during long-term storage. In 1964, as a joint venture, Shell Chemical Company and NASA JPL successfully developed a highly active, iridium-based catalyst, allowing efficient decomposition of hydrazine [15]. Only three years later, in November 1967, the NASA ATS-III spacecraft was flown, equipped with a propulsion system using catalytic decomposition of hydrazine, built by Hamilton Standard company [16]. The higher stability of hydrazine led to the elimination of pressure relief valves in the tanks and allowed great extension in the mission duration. Hydrazine offered a significantly lower self-decomposition rate than hydrogen peroxide and higher propulsive performance (~20% increase in specific impulse) [17]. Consequently, the development of hydrogen peroxide propulsion systems was virtually stopped for many years.

Recently, renewed interest in hydrogen peroxide as a rocket propellant can be observed. Apart from environmental matters, the reasons are modern propellant manufacturing techniques, allowing the production of a high-purity compound and a better understanding of the decomposition process and compatibility issues [18]. The abovementioned factors positively affected storability characteristics, allowing more demanding applications. Fundamental research concerning the properties and behaviour of hydrogen peroxide is still necessary; therefore, many projects utilizing hydrogen peroxide have been initiated lately, with some propulsion systems already in orbit [19].

1.2 Physical properties of hydrogen peroxide

Hydrogen peroxide, H_2O_2, is a colourless liquid, commercially available in a wide range of concentrations and commonly used as an oxidizer in the chemical industry and for paper bleaching or water treatment [20]. The density of anhydrous hydrogen peroxide at a temperature of 20°C is 1448 kg m^{-3} [21]. The density of anhydrous and aqueous solutions (90, 95 and 98 weight %) within a temperature range from 0 to 40°C can be seen in Figure 1.1 (a).

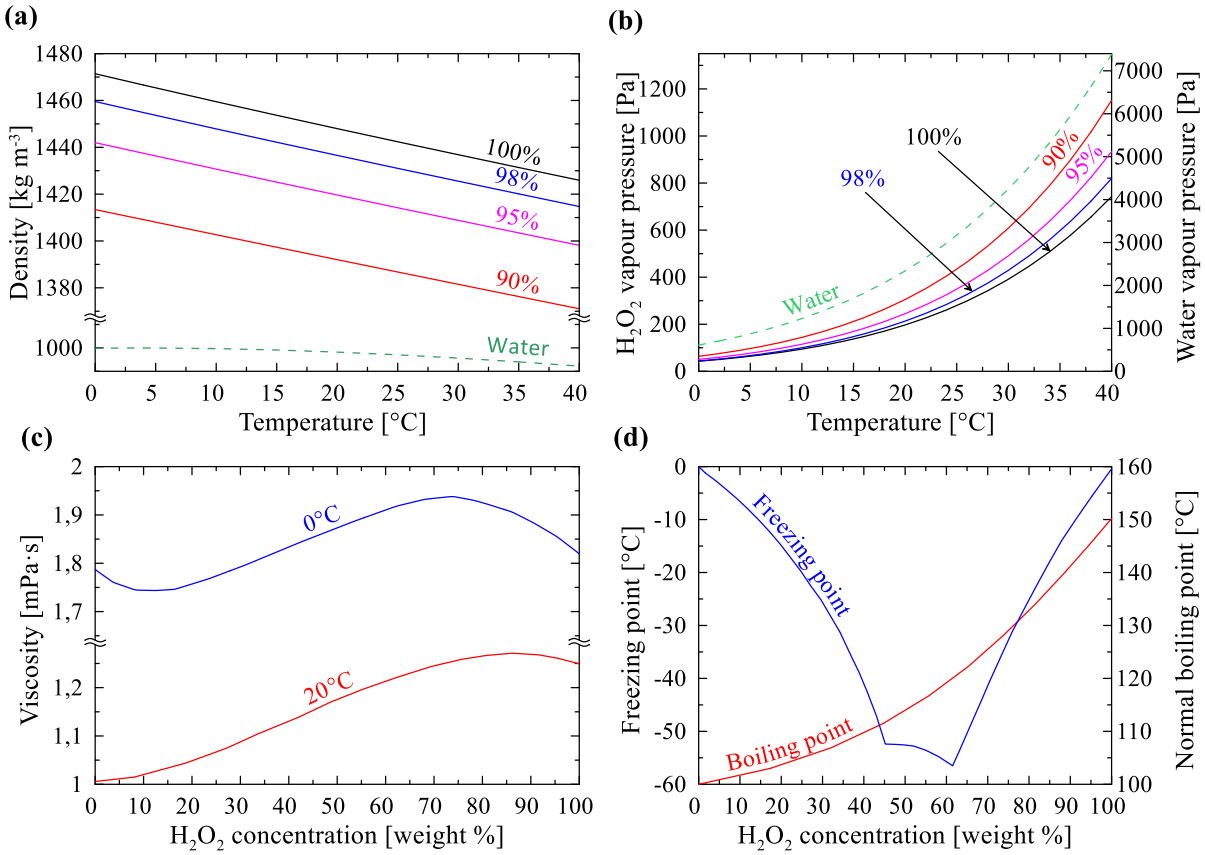

Figure 1.1 Physical properties of hydrogen peroxide: **(a)** – density of anhydrous and aqueous solutions (90, 95 and 98 weight %), prepared based on [21]. **(b)** – vapour pressures of anhydrous and aqueous solutions of 90, 95 and 98 weight % H_2O_2, prepared based on [22] water added for comparison purposes, as in (a). **(c)** – viscosity of water solutions of hydrogen peroxide at 0 and 20°C. Reproduced from [21]. **(d)** – freezing and normal boiling point of H_2O_2 as a function of concentration. Reproduced from [21].

The volatility of hydrogen peroxide, when compared to water, is low. The vapour pressure of an anhydrous compound at 20°C equals ~197 Pa [22] and is nearly twelve times lower than for water at the same temperature. The normal boiling point of aqueous peroxide solutions strongly depends on the concentration and equals 150,2°C for 100% concentration. The freezing point is as low as -56,5°C for a weight concentration of 61,5% and is -0,43°C for an anhydrous substance. Viscosity is nearly as for water and equals 1,819 and 1,249 mP s at a temperature of 0 and 20°C (for water: 1,792 and 1,005 mPa s) [21,22]. Graphical relations between vapour

pressure and temperature, viscosity, freezing and normal boiling point as a function of concentration can be viewed in Figure 1.1 (b)-(d). Hydrogen peroxide at a concentration suitable for propulsive applications is often termed high test peroxide (HTP). In this thesis, whenever reference is made to the concentration of hydrogen peroxide, this would apply to an aqueous, weight solution of the compound.

1.3 Fundamentals of space propulsion

Once the satellite is launched into space, propulsive manoeuvres may be necessary to accomplish the desired mission. Additionally, when in orbit, the satellite is exposed to a range of perturbations, such as (I) Gravitational influence of other bodies (e.g. Sun or Moon), (II) Solar radiation and solar wind. Solar radiation is a range of electromagnetic waves, from X-rays to radio waves, while solar wind comprises charged particles [23]. (III) Oblateness and nonhomogeneity of the Earth. The Earth is not a perfect sphere; the radius is not constant, and the density is a variable. Consequently, the gravitational field varies around the Earth, resulting in varying forces acting on a satellite [24]. (IV) Residual atmosphere. (V) Other disturbances, including the misalignment of thrusters, the interaction of magnetic fields of celestial bodies, or propellant sloshing in the tanks. The severity of selected factors presented depends on the type of orbit.

Typical applications of propulsion systems include:

- Apogee injection and orbit change. For a geostationary satellite, the launcher delivers the satellite to the so-called geostationary transfer orbit (GTO). Additional velocity increase is necessary at the apogee of the elliptical orbit to obtain the final circular form (Hohmann transfer). The apogee engine is used, delivering a thrust of approximately 400N and being a part of a satellite’s propulsion system.

- Orbit corrections (station keeping). Due to orbital perturbations presented before, the orbit will drift, and counteractive measures are necessary to maintain the required orbital elements.

- Attitude control. This applies to the satellite's orientation – the propulsion system is used to allow accurate pointing towards a specified object, removal of disturbances associated with orbit correction/change, and unloading of reaction wheels [17].

- Deorbiting or ‘graveyard’ orbit injection. At the mission's end, the orbit's altitude can be lowered, facilitating deorbiting, or a satellite can be moved to the so-called graveyard orbit – eliminating the risk of collision with operational satellites [17,25].

- Other applications include course corrections, breaking maneuverers during interplanetary missions, or maintaining proper relative separation for satellites operating in a formation [25].

1.3.1 Classification of propulsion systems

Many types of propulsion systems are available; the selection depends on the specific mission requirements and the type and size of the spacecraft [17]. A brief description of selected types will be provided below. The types discussed are somehow linked to the thruster under investigation. Figure 1.2 from (a) to (d) were prepared to graphically illustrate the most significant components of some of the thrusters discussed.

Cold gas propulsion is the simplest solution available, in which the thrust is generated by an expansion of a gas through a convergent-divergent nozzle. The gas is delivered from a high-pressure storage tank, usually through a pressure-reducing regulator. The thrust range is from tens of millinewtons to tens of Newtons. The specific impulse (ratio of thrust and mass flow rate) depends on the type of propellant used and ranges from a few hundred to a few thousand meters per second [26] and is usually low when compared to alternative solutions; on the other hand, due to simplicity, cold gas propulsion offers high reliability, repeatability and is a low-cost solution [27].

In the case of monopropellant propulsion systems, a single propellant is usually decomposed catalytically or thermally into a hot stream of gas and is next accelerated in a nozzle. Relative simplicity is an advantage, as only a single propellant is used. Hydrazine (N_2H_4) is the most popular propellant used. While hydrazine offers relatively high performance and good stability, toxicity is an issue [28]. Hydrogen peroxide is a propellant of interest as a low-toxicity option. In terms of specific impulse, the performance is lower, but H_2O_2 enjoys greater density, which somewhat mimics this disadvantage. Some alternative, highly energetic compounds were recently applied as rocket monopropellants and are based on hydroxylammonium nitrates (HAN) and ammonium dinitramide (ADN) ionic liquids. LMP-103S, for example, a propellant being a mixture of ADN, water, methanol and ammonia,

delivers a theoretical specific impulse which is ~ 6% higher than what is achieved using hydrazine; additionally, the density specific impulse is ~ 30% higher [29]. One serious disadvantage of HAN and ADN-based propellants is high chamber temperature, which for LMP-103S is ~1630°C – a value significantly exceeding that of hydrazine or 98% hydrogen peroxide (up to 1000°C) – this calls for the application of high-temperature materials and a very robust catalyst [30]. Another advantage of hydrogen peroxide is its relatively low cost. LMP-103s may be classified as an option for high-performance applications; on the other hand, in the current environment, with decreasing orbital launch costs, low-cost, robust propulsion systems may be favoured over high-performance, complicated units [31].

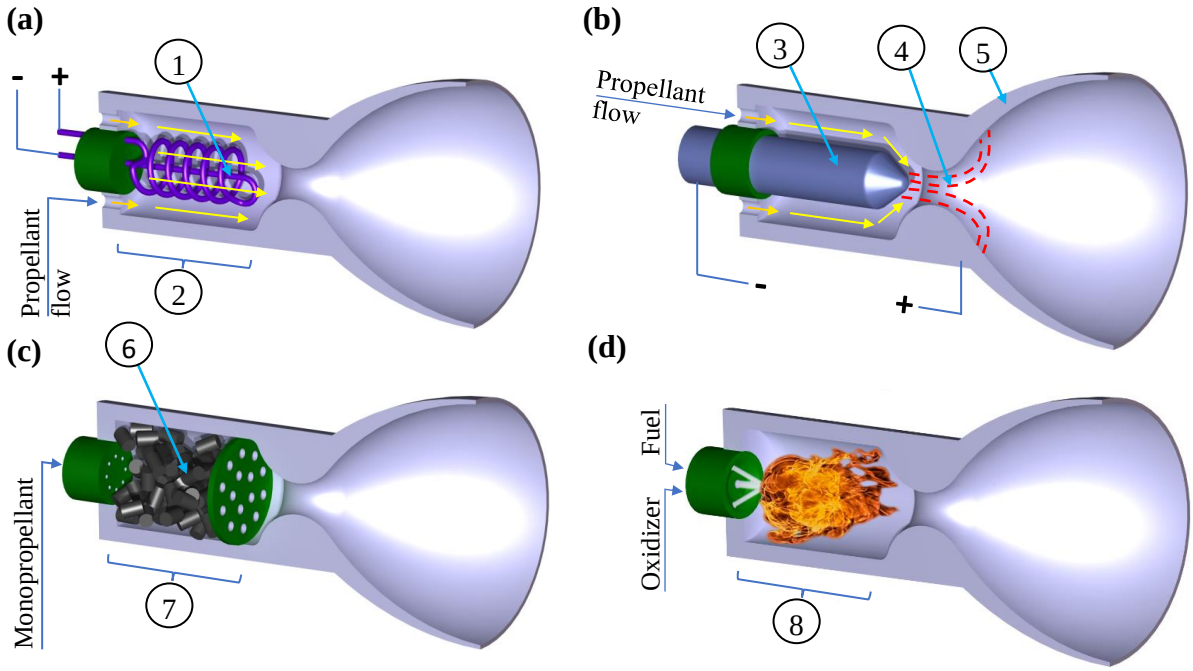

Figure 1.2 Schematic representation of selected types of thrusters. **(a)** – Resistojet; **(b)** – Arcjet; **(c)** – Monopropellant thruster; **(d)** – Bipropellant thruster; 1 – Resistively heated element; 2 – Heat exchanger; 3 – cathode; 4 – Arc between cathode and anode; 5 – Anode; 6 – Catalyst pack; 7 – Decomposition chamber; 8 – Combustion chamber. Prepared by the author.

Bipropellant propulsion systems offer the highest performance in the chemical propulsion group. On the other hand, complexity is much more significant when compared to monopropellant systems, as two compounds – fuel and oxidizer must be delivered to the chamber at a proper mass flow ratio. Combustion is a high-temperature process, and advanced materials are necessary in combination with additional cooling techniques, such as film cooling and, consequently, sophisticated injection systems [32]. The most common oxidizers are dinitrogen tetroxide (N_2O_4), denoted as NTO and mixtures of N_2O_4 and nitric oxide (NO_2), termed MON (mixed oxides of nitrogen). As a fuel, monomethyl hydrazine (MMH) and unsymmetrical dimethylhydrazine (UDMH) are used [25]. These propellants suffer from a

severe drawback – toxicity. Alternative, more eco-friendly propellant combinations are investigated, among which hydrogen peroxide is one of the candidates as an oxidizer [33,34]. As an example of a bipropellant unit, Figure 1.3 (b) shows an igniter developed by the author for use in a 400 N bipropellant thruster employing kerosine and gaseous oxygen as propellants. The igniter comprises a catalytic chamber filled with a catalyst, decomposing 98% hydrogen peroxide. Next, gaseous hydrogen is injected radially into the hot stream of oxygen-rich decomposition products, allowing ignition of the mixture in the combustion chamber. Combustion products are next delivered to the main combustion chamber, allowing ignition. Figure 1.3 (a) presents the test of the ignition system, while Figure 1.3 (c) depicts the 400 N engine operating at nominal conditions.

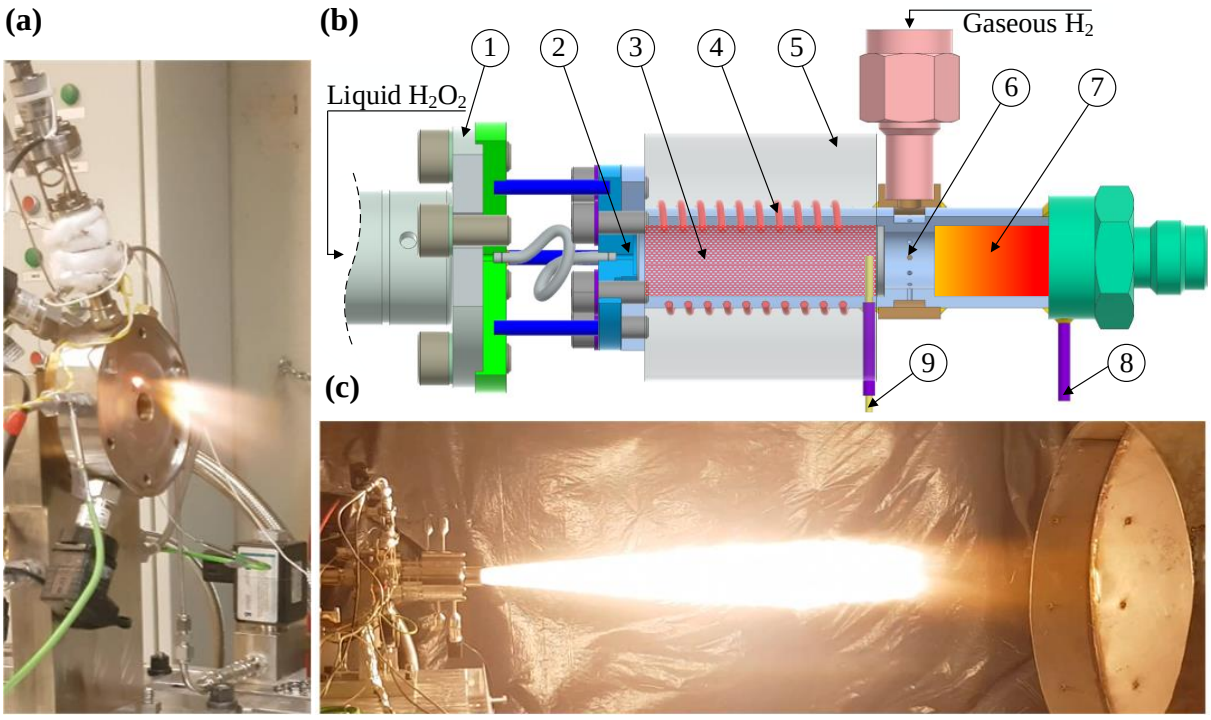

Figure 1.3 **(a)** – Ignition system, utilizing 98% hydrogen peroxide and gaseous hydrogen, during the test campaign; **(b)** – Cross-section view of the igniter: 1 – FCV, 2 – HTP injector, 3 – Catalyst pack, 4 – heater, 5 – insulation, 6 – H_2 injector, 7 – Combustion chamber, 8 – Pressure tap, 9 – K-type thermocouple; (prepared by the author); **(c)** – static test of a 400N bipropellant thruster using kerosine and gaseous oxygen.

A group of so-called electric propulsion systems exists, comprising three main subcategories: electrothermal, electrostatic, and electromagnetic propulsive devices [35]. Two leading solutions can be extracted for electrothermal thrusters: (I) resistojets, in which a heat exchanger comprising a resistively heated element is present. The working fluid's temperature is increased due to direct contact with heated surfaces [36]. (II) In arcjet, on the other hand, an electric arc is used to heat the propellant [37]. Electric and magnetic fields accelerate charged particles in electrostatic and electromagnetic thrusters [38].

1.3.2 Rocket propulsion fundamentals

The characteristic feature of a rocket engine is that no fluid from its surroundings is necessary during operation. Consequently, this propulsion type can be used in any environment – underwater, in space (vacuum) or the atmosphere of any planet. The thrust, F, of a rocket engine can be calculated according to Equation 1.1:

$$F = \dot{m}V_2 + (P_2 - P_3)A_2 \tag{1.1}$$

In Equation 1.1, $\dot{m}$ and V_2 are, respectively, the mass flow rate of the working fluid and exhaust velocity, P_2 and P_3 are static pressures, respectively, at the nozzle exit and external (ambient) pressure, A_2 is the exit cross-sectional area of the nozzle. For convenience, characteristic sections were highlighted in Figure 1.4 (b)

Assuming that the flow in the throat is sonic, the nozzle exit velocity, V_2, can be calculated as:

$$V_2 = \sqrt{\frac{2\kappa}{\kappa - 1}RT_1\left[1 - \left(\frac{P_2}{P_1}\right)^{\frac{\kappa-1}{\kappa}}\right] + V_1^2} \tag{1.2}$$

Where κ is specific heat ratio, R is gas constant, T_1, P_1 and V_1 are respectively nozzle inlet temperature, pressure and velocity.

The throat velocity is sonic if the ratio of static throat pressure, P_t, and chamber total pressure at nozzle inlet, P_{01}, is as presented in Equation 1.3 (so-called critical pressure ratio).

$$\frac{P_t}{P_{01}} = \left(\frac{2}{\kappa + 1}\right)^{\frac{\kappa}{\kappa-1}} \tag{1.3}$$

Specific impulse, I_{sp}, is a handy and common measure, defined as the thrust delivered by the engine per unit mass flow rate of the propellant [39], and is used to compare the performance of different propellant combinations and specific engine design concepts [40]. I_{sp}, is defined as per Equation 1.4. Figure 1.4 (a) shows theoretical values of vacuum specific impulse for different propellant combinations.

$$I_{sp} = \frac{F}{\dot{m}} \tag{1.4}$$

As can be noted based on Equation 1.1, if the nozzle exit pressure (P_2) equals ambient pressure (P_3), I_{sp} equals exhaust velocity (V_2), such conditions are called optimal.

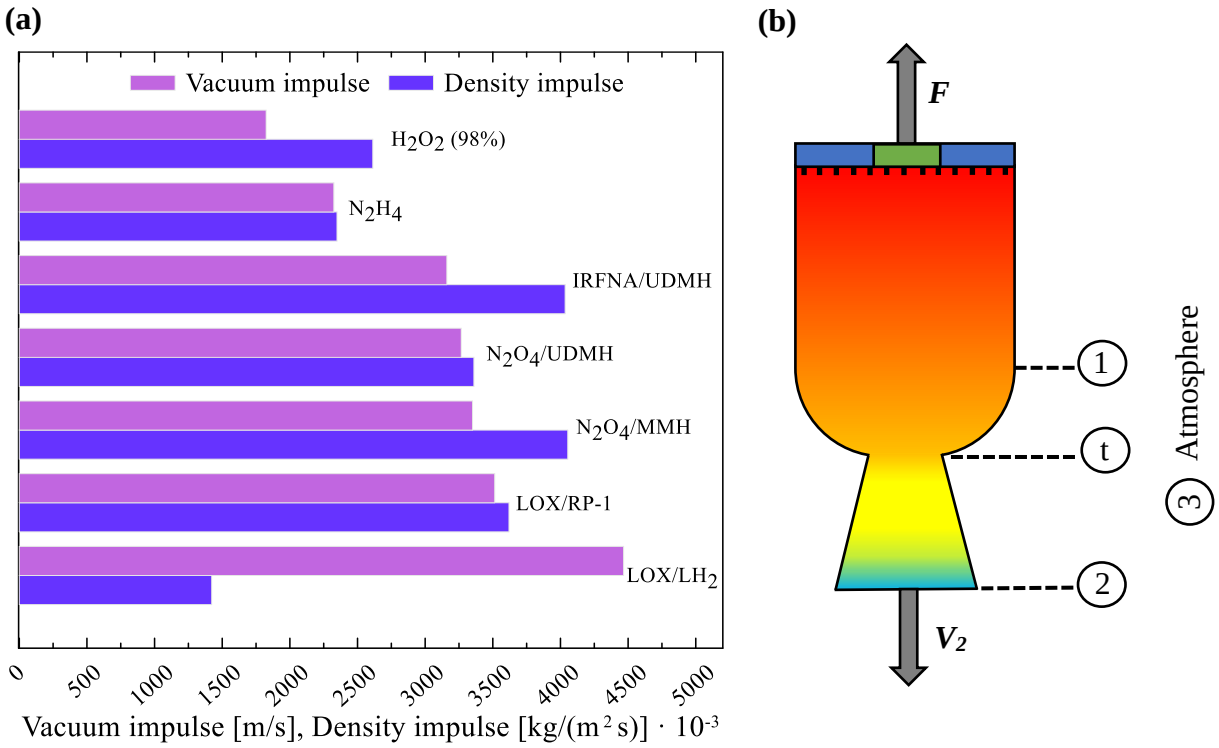

Figure 1.4 **(a)** Theoretical performance of different propellants/propellant combinations. LOX (liquid oxygen) + LH_2 (liquid hydrogen); LOX + RP-1 (kerosene); N_2O_4 + MMH (monomethylhydrazine); IRFNA (II-A, inhibited red fuming nitric acid, composition: 83,4% HNO_3; 14% NO_2; 2% H_2O; 0,6% HF) + UDMH (unsymmetrical dimethylhydrazine). Data taken from [41], P_1 = 69bar, nozzle area ratio $\epsilon = A_2/A_t = 40$, shifting equilibrium. N_2O_4 + UDMH and N_2H_4 – data taken from [40], shifting equilibrium, ϵ = 30. 98% H_2O_2 – data taken from [42], P_1 = 10bar, ϵ = 50. **(b)** schematic view of the combustion chamber and the nozzle, with significant sections marked. Both figures were prepared by the author.

Total impulse, I_{tot}, on the other hand, is a change in the momentum, being a result of force applied over time [43] and is defined as the integral of thrust over time, as presented in Equation 1.5 [39]:

$$I_{tot} = \int_0^{t_b} F dt \tag{1.5}$$

In Equation 1.5, t_b is the total burn duration. For manoeuvres in the space environment, it is often a requirement towards the thruster to be able to deliver as small impulse bits as possible. According to [44], the minimum impulse bit is defined as the "smallest impulse delivered by a thruster at a given level of reproducibility, as a result of given command". The pulsing performance of a thruster depends on the characteristics of the flow control valve (FCV) used, as well as dribble volumes (e.g. length and diameter of the tubing between FCV and the chamber) or chamber design (e.g. catalyst used) [40].

Volumetric specific impulse, I_V, can be expressed as a product of specific impulse and propellant density (Equation 1.6). The greater the density of the propellant, the smaller the volume necessary; that is why not only high specific impulse should be considered but also the density of the compounds [45]. Figure 1.4 (a) gives values of I_V for some common propellants.

$$I_V = \varrho_{avg}\, I_{sp} \tag{1.6}$$

In the case of bipropellant rocket systems, the mean density ϱ_{avg}, for specified oxidizer-to-fuel ratio (*OFR*), is a combination of the density of oxidizer (ϱ_o) and fuel (ϱ_f), and can be calculated according to Equation 1.7:

$$\varrho_{avg} = \frac{OFR + 1}{\frac{OFR}{\varrho_o} + \frac{1}{\varrho_f}} \tag{1.7}$$

Another quantity of great importance is characteristic velocity, c^*, which reflects the quality of the design of the injection system and combustion (decomposition) chamber in a rocket engine. It also provides information on the performance of propellants from an energetic point of view. Characteristic velocity, for an engine with a specified size (throat diameter) and sonic velocity in the throat, indicates the mass flow rate of selected propellants (propellant) necessary to maintain required chamber total pressure at nozzle inlet, according to Equation 1.8 [41]:

$$c^* = \frac{p_{01}}{A_t \dot{m}} \tag{1.8}$$

Where A_t is the throat cross-section area. In Equation 1.8, each quantity necessary to calculate c^*can be relatively easily measured; therefore, comparison with theoretical value, defined in Equation 1.9, gives information about the efficiency of the internal chamber processes.

$$c^* = \frac{\sqrt{\kappa R T_{01}}}{\kappa\sqrt{\left[\frac{2}{\kappa + 1}\right]^{\frac{\kappa+1}{\kappa-1}}}} \tag{1.9}$$

In Equation 1.9, T_{01} is chamber total temperature. Measured characteristic velocity, c^*_{exp}, can be confronted with theoretical value (c^*_{theo}), as presented in Equation 1.10:

$$\eta_{c*} = \frac{c^*_{exp}}{c^*_{theo}} \tag{1.10}$$

η_{c*} is called c^* efficiency and is widely used when comparing different engine design configurations from an efficiency point of view.

The total and ideal velocity change, ΔV, of a spacecraft depends on the characteristics of the propulsion system used (specific impulse, I_{sp}) and the amount of propellant available. According to the Tsiolkovsky equation, ΔV can be calculated as:

$$\Delta V = I_{sp} ln\left(\frac{m_0}{m_f}\right) \tag{1.11}$$

In Equation 1.11, m_0 is the initial mass of a spacecraft, while m_f is the mass after the propulsive manoeuvre [25].

1.4 Decomposition of hydrogen peroxide

1.4.1 General information

Hydrogen peroxide is a quasi-stable compound that can be exothermically decomposed according to the net reaction as follows:

$$2H_2O_2 \longrightarrow 2H_2O + O_2 + q \tag{1.12}$$

The heat, q, released during the decomposition of 1kg of anhydrous compound is 2,887 kJ [46]. As for the decomposition products, the contribution of molecular oxygen is 47 weight percent if anhydrous hydrogen peroxide is decomposed.

As described in [47], three regions can be distinguished on the concentration scale of H_2O_2: (I) first one, where the concentration is so low that the heat delivered as a consequence of the decomposition only causes a temperature rise of the water, but below the saturation temperature. The decomposition products are liquid water and gaseous oxygen; (II) In the second region, the heat released is high enough to boil the water; therefore, the decomposition products are boiling water, saturated steam and oxygen. The percentage of evaporated water is a function of the concentration of H_2O_2. In this region, the final temperature resulting from heat delivery equals water boiling temperature at specified pressure (water saturation temperature); (III) The third region is where the concentration of decomposing hydrogen peroxide is high enough to evaporate all the water. The decomposition products are superheated steam and oxygen; the final temperature is higher than the water saturation temperature. The mentioned concentration limits were calculated in [47] and are respectively 11,6 and 64,7 weight % - the

values given apply to the pressure of 1 bar. These limits change as a function of reaction pressure. Relations between the final temperature and the percentage of evaporated water for different reaction pressures and the entire spectrum of concentrations can be viewed in Figure 1.5 (a) and (b). In the case of propulsive applications of HTP, it is advantageous to use as high a concentration as possible. Figure 1.5 (c) depicts the relation between theoretical vacuum impulse and decomposition temperature at the 80 to 100% concentration range.

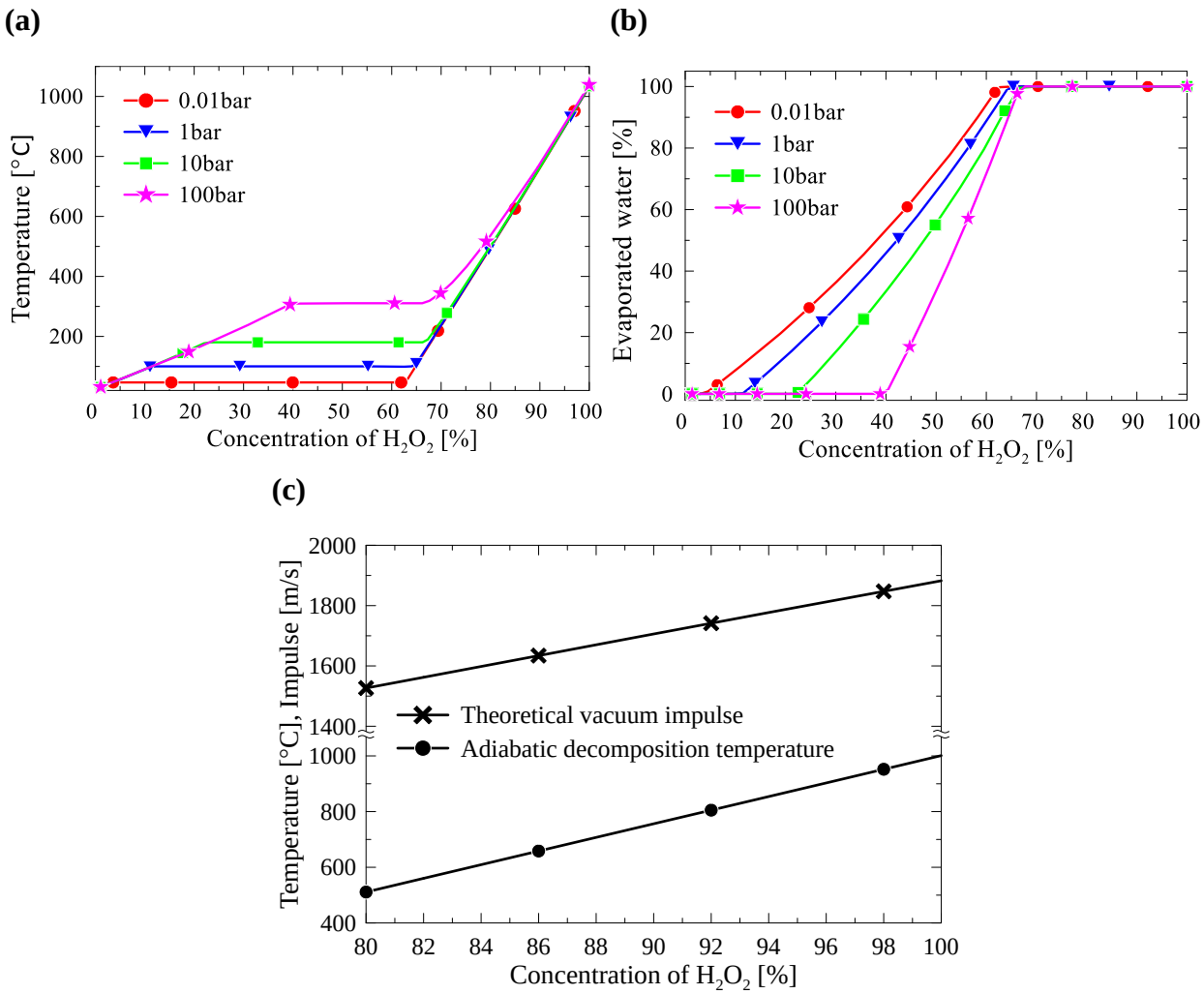

Figure 1.5 Propulsive and thermodynamic properties of hydrogen peroxide as a function of initial propellant concentration (aqueous solutions); **(a)** Final temperature after H_2O_2 decomposition; **(b)** Percentage of evaporated water**; (c)** Theoretical vacuum impulse and adiabatic decomposition temperature – prepared using NASA CEA software, Ae/At = 60, chamber pressure: 10bar, equilibrium composition, propellant initial temperature: 25°C; Figures (a) and (b) prepared using data from [47].

Hydrogen peroxide can be decomposed both in liquid and gaseous phases in homogeneous and heterogeneous reactions. Due to its degree of instability, apart from controlled decomposition, e.g. in decomposition chambers of gas-generator units, it tends to decompose slowly during storage. This phenomenon is highly undesirable and shall be minimised as much as possible.

In [22], five reactions were identified for a case in which both liquid and vapour phase is present: (I) liquid phase homogeneous decomposition as a result of catalytic and oxidizable components dissolved in the compound; (II) heterogeneous reaction between liquid H_2O_2 and the vessel's surface (wall-catalyzed surface heterogeneous reaction) or solid particles in the liquid compound. In order to minimize the influence of this factor, the propellant should be free from contaminants, and materials to be in contact with hydrogen peroxide shall be carefully selected; this applies not only to the tank but to each component of the fluidic subsystem, including sealings, lubricants, etc. Apart from materials, proper surface treatment shall be selected, e.g. passivation or polishing, to minimize effective surface area. During the design process, the surface-to-volume ratio for the compartments to be filled with H_2O_2 shall be maintained as low as possible [48]. (III) heterogeneous decomposition of vapour when in contact with a surface covered with a film of condensed hydrogen peroxide; (IV) heterogeneous decomposition of the vapour phase when in contact with dry surfaces; (V) vapour phase homogeneous decomposition. Figure 1.6 was prepared to illustrate selected decomposition modes graphically.

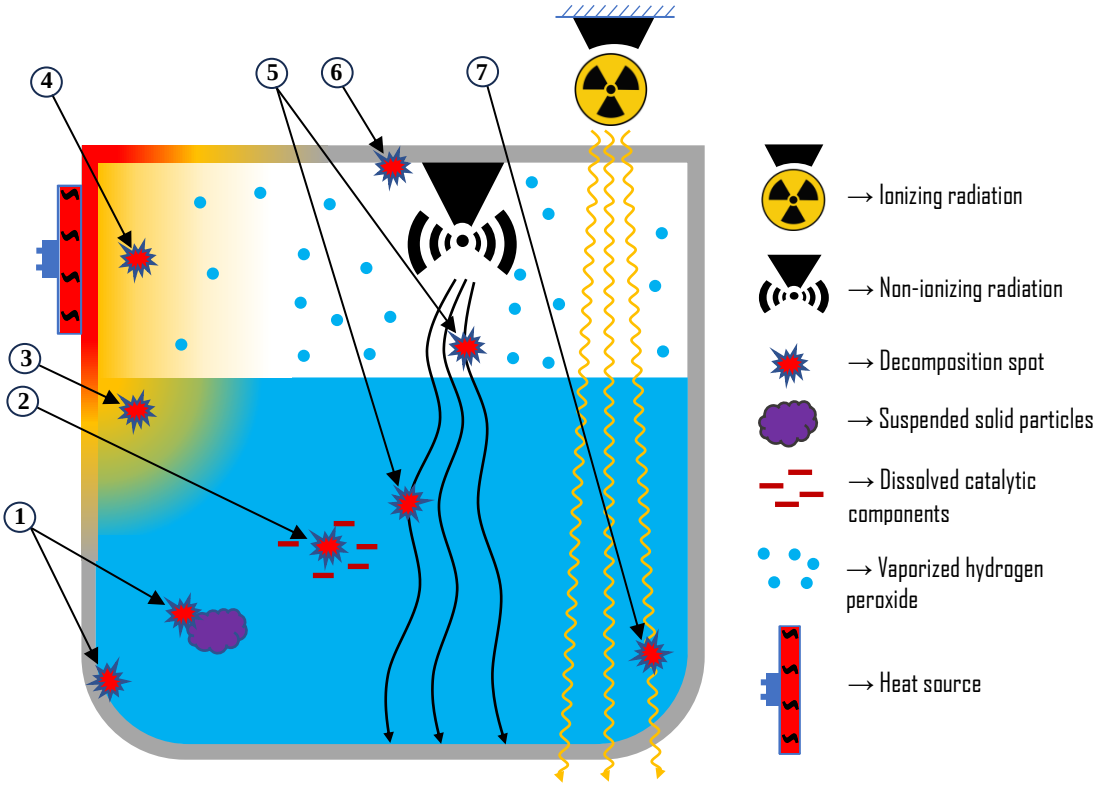

Figure 1.6 Graphical illustration of selected decomposition modes of H_2O_2;1–heterogeneous liquid decomposition; 2–homogeneous liquid decomposition, 3-thermal, homogeneous liquid decomposition; 4 – thermal vapour phase decomposition, 5–photolysis, 6–heterogeneous vapour decomposition, 7–radiolysis. Prepared by the author

One of the factors influencing the significance of reaction type is temperature; in [22], a reference was made to a study of the decomposition of 90% H_2O_2 in which, at ambient

temperature, reaction types IV and V were ignored. On the other hand, considering the propulsive applications of hydrogen peroxide, the decomposition of vapour through homogeneous and heterogeneous reactions plays an important role and will be discussed separately; the same will be done with liquid peroxide's homogeneous thermal decomposition, not mentioned previously.

It should be added that hydrogen peroxide can be decomposed by radiation. A distinction is made between decomposition initiated by nonionizing radiation, primarily ultraviolet (termed a photochemical process or photolysis) and ionizing radiation (the processes induced are called radiolysis) [22]. Radiolysis is of particular concern for chemicals being placed in outer space, as highly penetrating cosmic radiation may influence the composition of stored compounds [49,50].

Apart from the abovementioned factors, it should be noted that hydrogen peroxide can be decomposed electrolytically [51]. Additionally, in [52], research was presented aiming to determine the influence of vibration and stirring on concentration loss. During vibration testing, frequencies of 50 and 100 Hz and amplitudes of 1,5 to 15 g did not affect concentration, while stirring at a speed of up to 6000 rpm caused concentration loss of 0,25 to 0,5% per hour.

The following subsections aim to briefly present the most significant information concerning the selected decomposition modes, being of importance with regard to this thesis's main subject.
First, the fundamental aspects of chemical kinetics will be introduced shortly.

1.4.2 Fundamentals of chemical kinetics

Chemical kinetics is a branch of chemistry that aims to study the reaction rates and mechanisms with which the reactions occur. Reactions can be classified as follows:

- Homogeneous – reaction occurs in one phase
- Heterogeneous – the components of the reaction occur in different phases

The probability of simultaneous collision involving many molecules (three or more) is very low; intermediate, one-step reactions are usually present, eventually leading to final products. The one-step reactions are called elementary reactions. This set of elementary reactions is called a mechanism. The number of reactant particles involved in an elementary act

is molecularity. The overall reaction rate is limited by the slowest step (elementary reaction) in the process; this slowest reaction is called a rate-determining step [53–55].

For a constant volume, the rate of reaction, v, can be written as follows [56]:

$$v = \frac{1}{\nu_i}\frac{dc_i}{dt} \tag{1.13}$$

In Equation 1.13, ν_i and c_i are respectively stoichiometric coefficient and concentration of the i-th component of the reaction.

1.4.2.1 Factors influencing reaction rate

Several factors influence the rate of reaction; the most important are: (I) Concentration of components of the reaction, (II) Temperature, (III) Catalysts, (IV) Intensity of absorbed radiation [57]. The subsequent subsections will discuss the first three constituents in more detail.

Concentration

In some cases, the rate of reaction can be expressed as presented in Equation 1.14

$$v = k[A]^{\alpha_1}[B]^{\alpha_2} \tag{1.14}$$

Where k is the rate constant; $[A], [B]$ – concentrations of, respectively, species A and B; α_1, α_2 – order of reaction with respect to species A and B. The sum of $\alpha_1 + \alpha_2 + \cdots$ is the overall (total) order of reaction [56].

As can be seen in equation 1.14, the unit of rate constant, k, depends on the total order of reaction, and for first-order reactions, is s^{-1}. An experimental investigation is necessary to determine reaction orders.

Temperature

A common relation used to determine the influence of temperature on the rate constant is the Arrhenius equation, as presented in Equation 1.15.

$$k = Ae^{\frac{-Ea}{RT}} \tag{1.15}$$

Where R is gas constant, T is temperature, Ea is activation energy, and A is defined as frequency factor or pre-exponential factor [56].

The logarithmic version of the Arrhenius equation is as follows:

$$\ln k = \ln A - \frac{Ea}{R}\frac{1}{T} \tag{1.16}$$

As can be seen in Equation 1.16, the relationship between $\ln k$ and $^1/_T$ is linear with a slope of $-Ea/R$. The described relation, if graphically illustrated, is termed an Arrhenius plot and is used to evaluate activation energy [54].

Catalysis

A catalyst is a substance that speeds up reactions. When in contact with reactants, the catalyst changes the reaction mechanism so that energy requirements for the reaction are lowered - the activation energy necessary is significantly lower when compared to an uncatalyzed reaction. The catalytic reaction begins with the bonding of reactant molecules to the catalyst. After this step, a reaction involving a catalyst occurs, leading to the final product. Next, the product separates from the catalyst, leaving it unchanged. It must be stated that the catalyst only influences the kinetics of the reaction; the free energy for the catalyzed and uncatalyzed reactions remains the same [58].

A distinction can be made between:

- Homogeneous catalysis: catalyst is in the same phase as the reactants, mostly liquid.
- Heterogeneous catalysis: the catalyst belongs to a different phase than reactants and is usually solid [59]. The speed of the reaction following heterogeneous catalysis depends mainly on the (I) concentration of the reactants and reaction products (partial pressures for gaseous compounds), (II) Temperature, (III) the nature of the catalyst, e.g. contact area.

A good catalyst is often defined as one that gives high rates and selectivity towards desired final products [53].

In some cases, the catalyst may become inactive due to so-called poisoning. The poison acts as a blocker of the active centres, disallowing the bonding of the reactants. Some poisons change the structure of the atomic surface, reducing the catalytic activity [60].

1.4.3 Liquid phase thermal decomposition of hydrogen peroxide

The thermal decomposition of HP in the liquid phase remains largely unstudied. Little data exists concerning this phenomenon. In [61], the decomposition rate of the aqueous solution was measured at elevated temperatures. The measured activation energy was 71 kJ/mol. It was noted that the results obtained at the reactor temperature of less than 100°C resulted in a significant error caused by slow reaction and greater influence of reactor surfaces (catalytic decomposition).

In [62], second-hand, unpublished data from Food Machining and Chemical Corporation was cited, indicating activation energy and pre-Arrhenius constant of 79,3 kJ/mol and 7020 1/s for liquid phase, but no information was provided on the measurement methodology or conditions.

In [63], tests were presented that aimed to investigate the possibility of using 98% hydrogen peroxide for regenerative cooling in micro-thrusters. A stainless steel tube was used, 95μm inside diameter and 4mm long. At a tube temperature of 150°C (the tube was electrically heated), explosions occurred, and the temperature limit was independent of the internal liquid pressure. The mechanism of the explosions was not explained, but one of the conclusions was that local explosive gasification could be the cause.

In [64], authors suspected that explosions following the heating of pure unconfined hydrogen peroxide to temperatures near the boiling point occurred in the vapour phase. The authors describe an experiment in which 90-98% hydrogen peroxide drops were placed on a heating plate. No explosions were observed until the plate's temperature was as high as 150°C (normal boiling point of aqueous hydrogen peroxide).

1.4.4 Thermal decomposition of hydrogen peroxide vapour

McLane [65] implemented a flow system in which a filtrated stream of nitrogen or oxygen was saturated by passing two times through 90% hydrogen peroxide; as a result, the partial pressure of hydrogen peroxide in the gas was ~200 Pa (1,5 mmHg). Next, the saturated gas was flown through a reaction vessel placed in a furnace; the temperatures investigated were in the range of 470 to 530°C. The concentration of hydrogen peroxide was measured upstream and downstream from the reaction vessel, and two types of vessels were used, denoted as lower and higher surface vessels. The activation energy measured using a higher surface vessel was

167,5 kJ/mol (40 kcal/mole) for both carrier gases used; the reaction was found to be of first order. As for the low-surface area vessel, using a nitrogen atmosphere, the activation energy was 209 kJ/mole (50 kcal/mole). Based on the results obtained, it was stated that the reaction is not taking place exclusively on the vessel's surface, but also a volume reaction occurs, with higher activation energy, and a transition to volume reaction occurs at higher temperatures.

Giguére and Liu [66] investigated the thermal decomposition of hydrogen peroxide vapour at static conditions and at low pressures (~0.27 to 26.7 mbar). Figure 1.7 presents the schematic view of the apparatus used. The rig comprised a reaction vessel, usually a 2-litre flask made from Pyrex or Vycor, an electric furnace (the flask was placed in), a pressure transducer and all the necessary armature. Liquid hydrogen peroxide (concentration of 99.9%) was kept in the bulb at a temperature of 70-80°C; the vapours were delivered to the reaction vessel. Tests were performed at a furnace temperature of 300-600°C, while to prevent condensation, the components outside the furnace were preheated to 90°C.

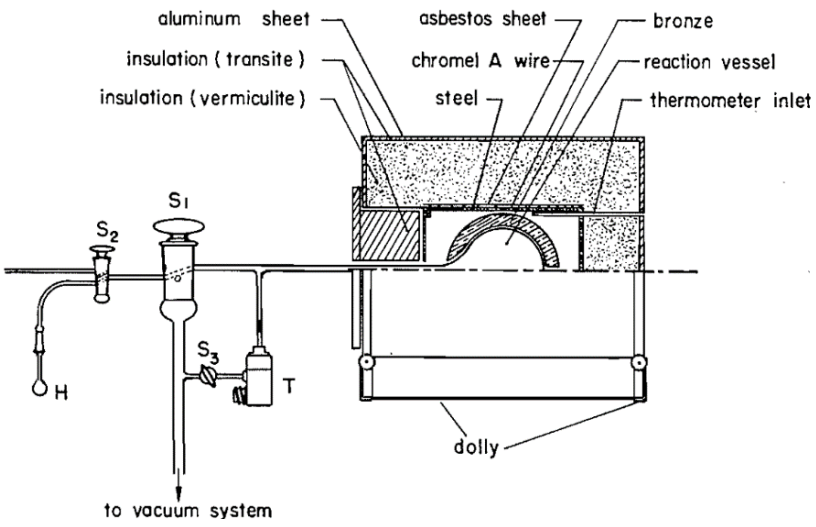

Figure 1.7 Test apparatus used by Giguére and Liu during the investigation concerning the thermal decomposition of hydrogen peroxide vapour. T - Pressure transducer, S1 - three-way stopcock, H – sample of liquid hydrogen peroxide [66].

In the presented research, authors mainly investigated the homogeneous decomposition; it was stated that the reaction was of first order, the estimated activation energy for the homogeneous process was 48±3 kcal (200,8±12,55 kJ), and the obtained frequency factor was 10^{13}. What is more, it was noted that at a temperature slightly exceeding 400°C, the character of the reaction changed from heterogeneous to homogeneous. According to the tests performed, the decomposition reaction was 60% homogeneous at a temperature of 400°C and 90% homogeneous at 450°C.

For some tests, the contact area inside the reaction vessel was increased by placing Pyrex tubes inside. The initial surface-to-volume ratio was 0,4 cm^{-1} and was increased to 0,7 and 1,1 cm^{-1}. A relatively significant reaction rate increase was observed for temperatures lower than ~400°C (heterogeneous decomposition), but the influence on the homogeneous rate (temperature above 400-425°C) was much less significant. During some experiments, a range of gases was added to the reaction vessel (air, O_2, Ar, He), but the reaction rate was not affected insignificantly.

The following mechanism was proposed for the uncatalyzed decomposition:

$$H_2O_2 \rightarrow 2\,OH \tag{1.17}$$

$$OH + H_2O_2 \rightarrow H_2O + HO_2 \tag{1.18}$$

$$HO_2 + HO_2 \rightarrow H_2O_2 + O_2 \tag{1.19}$$

$$HO_2 + OH \rightarrow H_2O + O_2 \tag{1.20}$$

Another research concerning the homogeneous decomposition of hydrogen peroxide vapour was presented in [67]. Aqueous hydrogen peroxide solution was boiled, and the vapours were transferred through a Pyrex tube placed in a bath that was maintained at a constant temperature. Vapour samples were collected at the inlet and outlet of the tube, quickly condensed, and the concentration was analysed. It was noted that:

- It was not possible to detect homogeneous decomposition of the vapour at temperatures of less than 250°C.
- The transition from heterogeneous to homogeneous reaction was observed in the temperature range of 400-450°C.
- Three tubes were used, and different decomposition rates were measured, but only in the heterogeneous temperature range. As for the higher temperatures, the results were similar. The influence of the temperature on the decomposition rate can be viewed in the reproduced Figure 1.8.

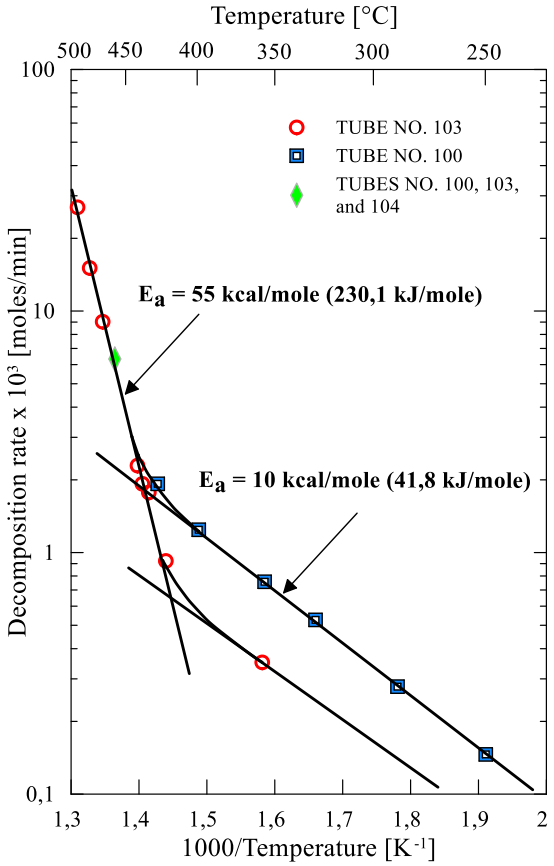

Figure 1.8 Influence of temperature on the decomposition rate of hydrogen peroxide vapour (p_{H2O2} = 0,02 atm). Reproduced from [66]

The activation energies for the homogeneous and heterogeneous reactions were estimated as 230,1 kJ/mol (55 kcal/mol) and 41,8 kJ/mol (10 kcal/mole), respectively, while the reported order of homogeneous reaction was $^{3}/_{2}$.

Conway [68] expressed doubt concerning the analysis presented in [67] and concluded that the reaction mechanism proposed by the authors was mainly based on a simple calculation concerning only one of the reactions involved.

Thermal decomposition of hydrogen peroxide was also investigated by Hoare et al. [69]. The authors implemented a flow technique where the carrier gases were flown through bubblers containing hydrogen peroxide; N_2, CO_2, He and O_2 were used. In the first series of tests, carrier gas at 1 atm pressure was used, and the temperatures tested were from 241 to 478°C. The carrier gas pressure was reduced in the second part of the campaign, and the temperatures implemented were from 569 to 659°C. The first part of the campaign, performed at a pressure of 1 atm, indicated that the time necessary for the concentration of hydrogen peroxide to be halved at temperatures below 420°C was independent of the initial concentration, indicating that the reaction was of first order. Additionally, the reaction rate was increased by an increase in the surface-to-volume ratio, indicating the reaction was heterogeneous. The homogeneous reaction overtook at a temperature of 420°C; the activation energy for the homogeneous decomposition, including correction for the heterogeneous process, was 201 ± 17 kJ/mole (48 ± 4 kcal/mole). It was additionally noted that the type of carrier gas used had an influence on the rate in the following order $CO_2 > N_2 > O_2 >$ He. When the carrier gas pressure was reduced, it was observed that hydrogen peroxide pressure had little effect on the rate constant, but increasing the carrier gas pressure increased the rate constant.

Analysis of thermal decomposition using a static method was documented in [70]. A Two-liter spherical Pyrex vessel was used during research, and hydrogen peroxide vapour was generated by evaporation of 99%+ liquid compound at 75°C. It was estimated that the decomposition reaction was 65% homogeneous at 431,5°C and a pressure of 1333 Pa (10 mmHg), which was less than 80%, at the same conditions suggested in [67].

1.4.5 Ignition limits of hydrogen peroxide vapour

Back in 1949, Hart [71] observed that at a pressure of ~2,7 kPa (~2 cm of mercury) or higher, using a Pyrex tube with a diameter of 3 cm, heated to 100°C, it was possible to initiate

‘decomposition flames’ and explosions. The reaction, in a vapour phase, was initiated using a hot wire, which, according to the author, at atmospheric pressure, must be heated to at least about 600°C. Hart additionally stated that at atmospheric pressure, explosions became very violent. Hart claimed it was possible to stabilize the flame on a jet at a pressure of ~5,3 kPa (4 cm of mercury).

Satterfield et al. [72] performed experiments to determine the composition of vapours and pressure that would lead to explosive decomposition. At atmospheric pressure, gaseous mixtures comprised mainly vapour of hydrogen peroxide, vapour of water and oxygen and were ignited by a hot wire. Table 1 shows the results presented by the authors.

Table 1.1. Vapour compositions studied in [72] and the results concerning explosion attempts. Pressure unit converted from mmHg to bar.

Partial pressure [bar]			**Observations**	
H_2O_2	**H_2O**	**O_2**	**Attempts**	**Explosions**
0,204	0,689	0,132	10	0
0,237	0,733	0,029	10	0
0,264	0,745	0,007	9	1
0,264	0,743	0,008	10	3
0,272	0,649	0,092	10	10
0,296	0,699	0,025	10	10
0,301	0,697	0,020	10	10
0,308	0,691	0,008	10	10

In [64], the authors extended the research presented in [72] to investigate the explosive characteristics of hydrogen peroxide vapour. Hydrogen peroxide was vaporized in a boiler and delivered to an explosion bulb and, next, to the condenser. A heated platinum wire or a spark gap was inserted into the explosion bulb. The authors noted that when the vapour concentration was only close to the explosion limit, no noise was heard, and whether or not the explosion occurred was determined by examining the disappearance of the fog in the condenser. If the vapour concentration was significantly above the explosive limit, an audible ‘pop’ was heard, and for some cases, if the concentration of the vapour was very significant, the explosion resulted in the destruction of the apparatus. Tests showed, that at 1 atmosphere, the ignition limit was 26 mole % hydrogen peroxide, and varying oxygen to water vapour ratio did not have an influence on the limit. Authors stated, that at a pressure of 1 atmosphere, if the vapours are within the explosive range, explosion may be initiated by a contact with relatively inert materials at a relatively low temperature or even at room temperature if the material in contact possesses slightly catalytic properties. Additionally, it was noted that the heating wire

temperature had little effect on the ignition limit. Wire temperatures tested ranged from 1350 to 1750 K. Changing the igniting device from a heated wire to an aluminium spark gap did not influence the abovementioned limit. The influence of gas composition at a total pressure of 1 atmosphere and total pressure on the ignition limit can be viewed in Figure 1.9 (a) and (b), respectively. Interestingly, some qualitative tests were performed, during which wires made from silver, copper, platinum, nickel and stainless steel, at room temperature, were suddenly placed in a stream of concentrated hydrogen peroxide vapour. In each case, the introduction of the wire resulted in an explosion.

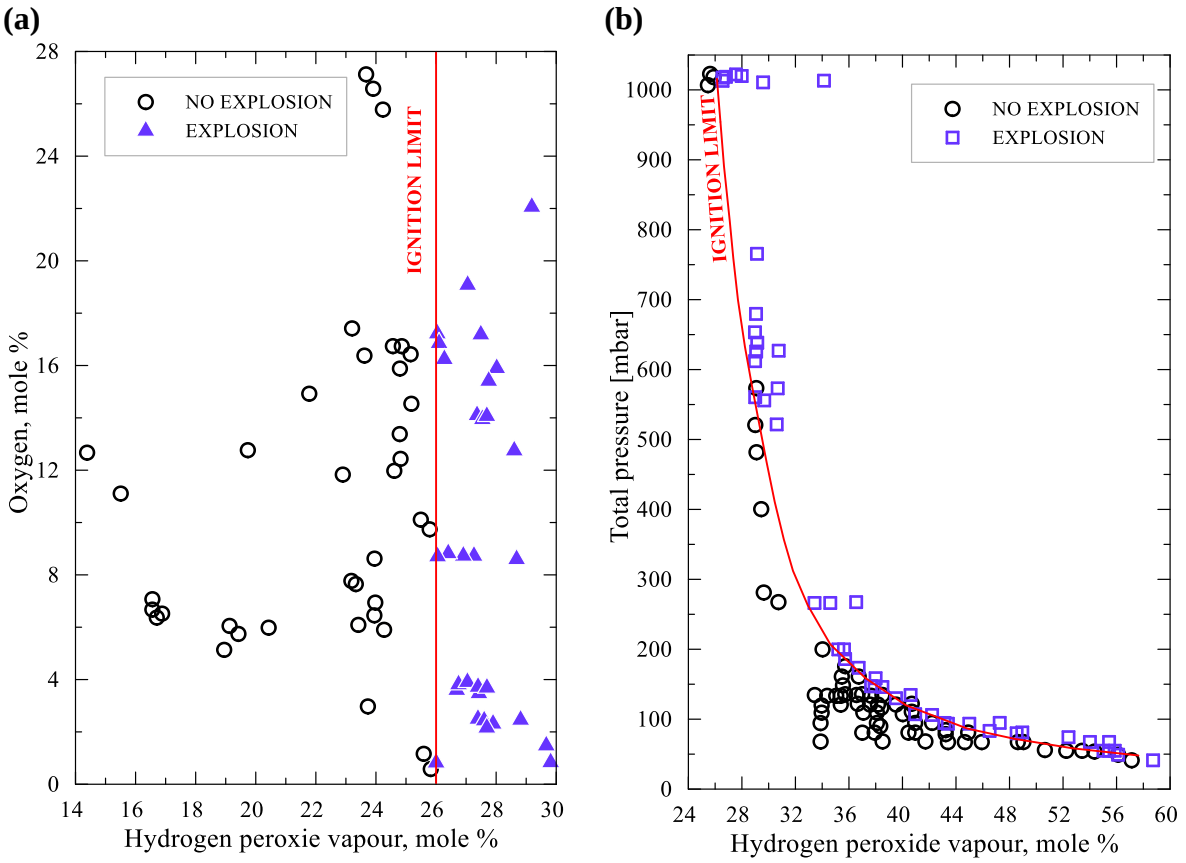

Figure 1.9 Ignition limits of hydrogen peroxide vapour: **(a)** Influence of gas composition (additional oxygen was delivered to the explosion bulb), total pressure of one atmosphere, mixture initiated using a platinum wire heated to 1350K; **(b)** Influence of total pressure on the ignition limit, ignition initiated using aluminium spark-gap. Figures reproduced from [64]; pressure unit was changed from mmHg to mbar.

In [73], authors investigated the influence of oxygen, helium, nitrogen, and carbon dioxide on the ignition limit of hydrogen peroxide vapour at a total pressure of ~267 mbar (200 mmHg). At that total pressure, the ignition limit, like in the previous research, was 32.5-mole percent and was unaffected by a change in oxygen concentration between 0 and 39%. The same results were obtained for helium and nitrogen as diluent gases. On the other hand, carbon dioxide had a damping effect when at a concentration higher than a few percent. Additionally, the limit was determined with an explosion bulb filled with borosilicate glass Rashig rings for

pressures ranging from ~267 down to ~67 mbar. By this packing, the ignition limit was switched to only slightly higher HTP vapour concentrations.

In [74] investigation was presented that aimed to determine the ignition limit of hydrogen peroxide vapours at pressures from ~1 bar to ~6,6 bar abs (14,7 to 95 psia). The ignition limit at a pressure of 2 to 6 atm. was at a constant level of 20.7-mole percent.

Apart from the research performed by Satterfield et al. [64,72–74], explosive limits of hydrogen peroxide vapours were also investigated by Monger et al. [75]. Few test rigs were used. The first one, for high-pressure tests, was made from 304 stainless steel. The rig employed a continuous flow pressure feed system. A backpressure regulator maintained gas pressure in the test section at a desired level. The stream of hydrogen peroxide passed through a heated coil and was delivered to a vapour-liquid separator. The vapour section of the separator was equipped with a spark gap energized periodically. The temperature of the stream was raised at constant pressure until the explosion occurred. Interestingly, the authors noted that at higher pressures, several spontaneous explosions occurred in the preheater, which resulted in the rupture of the stainless steel tubing.

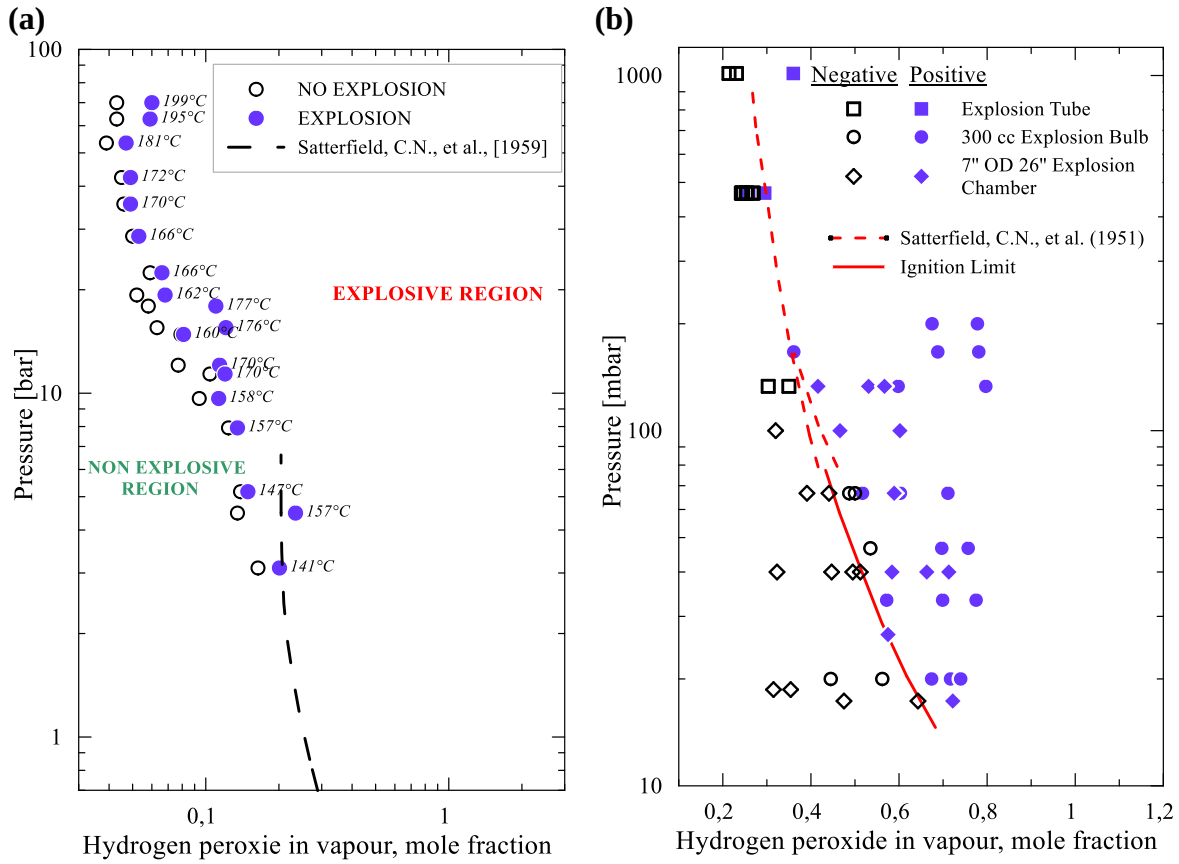

Figure 1.10 **(a)** High-pressure explosion limit of vaporized H_2O_2, spark gap was used to initiate the explosion, all stainless steel test rig used for research. **(b)** Subatmospheric explosion limits, data obtained using all glass test rigs. Figures reproduced based on data taken from [75]. Pressure units changed from mmHg to bar/mbar.

Figure 1.10 (a) and (b) present results obtained by Monger et al. [75]; additionally, in Figure 1.10 (a), stream temperatures were added for each explosion point, and data obtained by Satterfield et al. [74] was also included. The aforementioned results published by Satterfield et al. do not agree well with the experimental data and semiempirical model presented in [75]. According to Monger, one of the sources of discrepancy could be the criteria for a positive test. Figure 1.10 (b) presents experimental results of low-pressure (up to 1013,5 mbar) vapour explosion limits obtained by Monger et al. Tests were carried out using different glass apparatus, which will not be described here in detail. The results seem to agree with the data published by Satterfield et al. [64].

Quenching distances and minimum spark ignition energies were determined by Marshall [76] for various pressures and vapour concentrations of hydrogen peroxide. Vapour concentrations and pressures tested ranged from 35 to 50-mole percent H_2O_2 and 3,33 to 26,66 kPa (50 to 200 mm Hg). Vapour temperature was maintained 9°C above the condensation temperature. Flanged electrodes were employed in the spark gap assembly; with one electrode being movable, it was possible to accurately change the distance between the flanges and obtain both quenching distance and minimum spark ignition energy. The measured quenching distances were between 5,1 and 16,3 mm, and minimum ignition energy ranged from 0,53 to 25,5 mJ.

In [77,78], research was presented that aimed to determine the velocity of the decomposition front using a Bunsen burner and shadow photography.

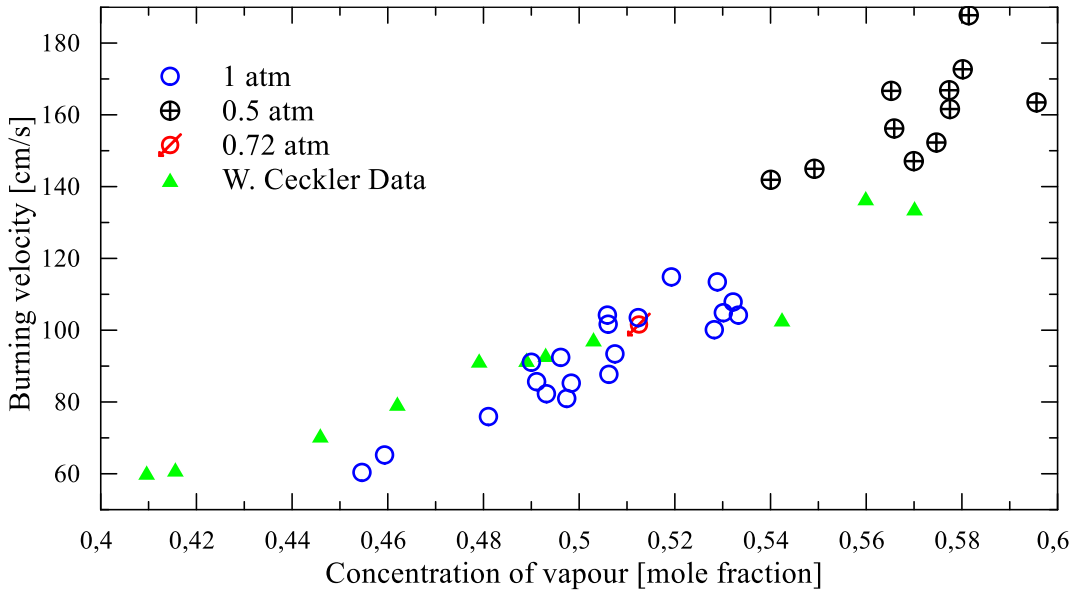

Figure 1.11 Burning (decomposition) velocity of hydrogen peroxide vapour as a function of concentration and pressure. Reproduced from [77].

Tests were performed at three pressures, 0,5; 0,72 and 1 atm. The decomposition velocities (referred to by authors as burning velocities) can be viewed in Figure 1.11 as a function of vapour concentration and pressure. In each case, the vapour temperature was maintained at 2 to 3°C higher than the boiling temperature. Based on the experimental data, it was found that the decomposition follows first-order kinetics, with an activation energy of 35 kcal/mole (146,44 kJ/mole).

Hart [71] first observed that initiating vapour decomposition over a boiling, concentrated hydrogen peroxide was possible. Hart stated that the decomposition front rests on the liquid surface, increasing the boiling rate, and the liquid propellant goes straight to the decomposition products. This observation was further investigated by Satterfield and co-authors [79], and a test campaign was carried out, which aimed to determine the conditions under which the decomposition front can be initiated above the liquid surface and characterize the process. Hydrogen peroxide was placed in a heated tube; the diameter of the tube was 15 mm, the length was 300 mm, and the liquid level drop was observed. As the decomposition of the vaporized compound over the liquid was initiated, it was found by measurement of the decomposition temperature above the liquid surface that the highest temperature occurred less than 1 mm above the surface. The decomposition front was not luminous, and the condensed decomposition products showed that the amount of undecomposed hydrogen peroxide passing through the decomposition front was negligible for most cases.

1.4.6 Detonative properties of hydrogen peroxide

1.4.6.1 Gas phase detonation of H_2O_2 vapours

Monger et al. [80] conducted tests to determine the detonative properties of hydrogen peroxide vapour. Tests were performed in a pipe with an internal diameter of ~49,25 mm and a total internal length of 2432 mm. The pipe was made of aluminium 6063-T6 and was heated to a temperature slightly higher than the vapour temperature. Point source initiators were used. Three initial pressures were tested: 0,2; 0,47 bar (2,9 and 6,77 psi), and atmospheric pressure. Detonations occurred only at atmospheric pressure, and the velocity was up to 2033 m/s for a hydrogen peroxide mole fraction of 0,35. Tests employing higher vapour concentrations were attempted but resulted in spontaneous decomposition or premature ignition.

Campbell et al. conducted an extensive test campaign concerning the detonation of the vapour of hydrogen peroxide [81]. The authors investigated limiting pressures, compositions

and the influence of tube diameter and packing. A few detonation tube configurations were tested; each was made of glass and had a length of 5,2 m; internal diameters were: 9, 15, 25 and 35 mm. The tube was preheated to over 110°C. Two initiation mechanisms were used. The first one employed spark electrodes – this technique was used to investigate the deflagration-to-detonation transition (DDT). As for the detonation limits of hydrogen peroxide vapour, an acetylene/oxygen mixture was used to generate initiating shock wave. For tube diameters of 9, 15, and 25 mm, it was possible to obtain DDT for a range of vapour concentrations and pressures. A tube which was 25 mm in diameter was used for shock-initiated detonation testing of hydrogen peroxide vapour at different concentrations and pressures. As a result, limiting conditions were obtained. Detonation velocity was determined as a function of vapour concentration and ranged from ~1450 to 1860 m/s.

1.4.6.2 Liquid phase detonation

Not as readily as vaporized hydrogen peroxide, but liquid HTP can also be detonated. Sensitivity to shock initiation of 86 and 90,7% aqueous hydrogen peroxide solution was tested and documented in [82]. Aluminium (61ST6 alloy) tubes were used during experiments; the tubes were 406,4 mm long, with internal diameters of 12,7; 20,8; 26,7; 31,75, and 40,9 mm. The shock was initiated with 51 g of tetryl. As for 86% H_2O_2, diameters of 26,7, 31,75 and 40,9 mm were tested at temperatures from 25 to 70°C, and detonations with velocities of about 5600 m/s were observed only for the largest diameter, at a temperature of 50°C and more. All tubes were tested with 90,7% hydrogen peroxide, and it was possible to observe detonations for each diameter; the temperatures necessary to detonate the propellant were: 70°C (ID12,7 mm); 55°C (ID20,8 mm); 35°C (ID 26,7 mm); 25°C (ID = 31,75 and 40,9 mm). Detonation velocities were from 5500 to 6000 m/s. Based on averaged values, the critical diameter for 90,7% HTP decreased from ~40,6 to 20,3 mm as the temperature was increased from 25 to 70°C.

In [83], authors described a test (detailed source was not provided) in which 15 g of dynamite was initiated in the centre of a metal drum containing 113kg of 90 and 99,5% hydrogen peroxide at room temperature and at a temperature of ~71°C. Only minor damage to the aluminium drum was observed. Another interesting experiment, propagation test, mentioned in [83], aimed to initiate detonation in a 38,1 mm stainless steel tube connected to a pure aluminium shipping drum containing ~113 kg of 98% hydrogen peroxide. The detonation was successfully initiated by means of an explosive, but the effect was not carried out to the drum. As previously, no detailed data concerning the experiment was provided.

In [84], authors documented shock initiation studies performed using 98% aqueous hydrogen peroxide solutions using a gas-driven, two-stage gun. For some experiments, initiation was observed. It was stated that the initial shock pressurizes and heats the propellant. After a specified period (induction time), an evolving reactive wave is generated, gets stronger and finally overdrives the initial wave, initiating detonation.

1.4.6.3 Detonability during space propulsion priming activities

The space propulsion system is initially inactive when the mission commences. It is a common practice that the propellant tanks are separated from the combustion/decomposition chambers through three barriers (valves). In most cases, the propellant lines are vented to the space environment before activating the propulsion system. One of the steps during the propulsion system's activation is the opening of insulation valves (so-called priming). This activity allows propellant to flow into the evacuated lines. Following the insulation valve opening, the propellant enters the evacuated tubing and undergoes flash evaporation; additionally, the gas dissolved in the propellant will desorb and mix with the vapour and any residual gas in the line [85]. As a result, a gas cushion is generated at the liquid front - a piston analogy may be used, in which the liquid front hits the closed ends (e.g. thruster valves), generating a substantial pressure surge known as a waterhammer [86]. The priming process can cause severe pressure peaks, which may eventually lead to the malfunctioning of the subsystem. Apart from a mechanical load, gas compression at the liquid front may result in a significant temperature rise (adiabatic process).

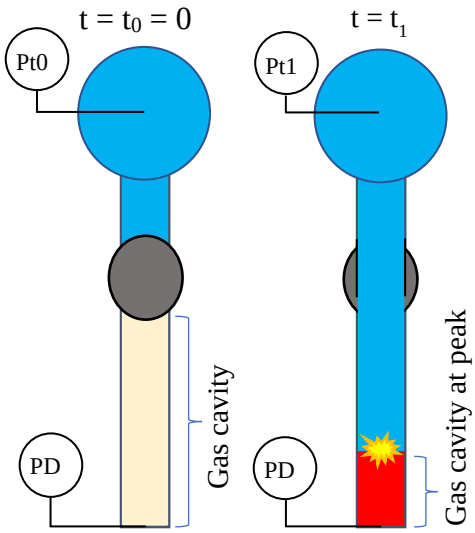

Figure 1.12 Graphical illustration of the waterhammer phenomenon, schematic overview of the system comprising tank (filled with liquid, and pressurized to Pt0), separated from a gas cavity by means of a valve; prior to valve opening (t=0) and at the moment peak pressure is achieved ($t=t_1$). Prepared by the author.

In the case of monopropellant compounds, the priming phenomenon is of particular concern as the temperature rise of the gas in the line may initiate thermal decomposition or even detonation of the propellant. Adiabatic detonation is a possible outcome following priming, so it must be remembered that monopropellant compounds are susceptible to detonation under certain conditions [87]. These conditions are, e.g. compression ratio (peak pressure and initial line pressure), tubing geometry or material and initial temperature [88]. Figure 1.12 shows a graphical illustration of the waterhammer phenomenon. It is a common practice to perform acceptance testing of the propulsion system configuration. A laboratory version of the fluidic subsystem is prepared, usually a flat version of the flight unit and using as many flight-like components as possible; this includes valves, tubing materials and geometry, filters, etc. [89] Thruster valves are replaced with pressure sensors and waterhammer testing is performed at specified conditions (tank pressure, propellant saturation level, etc.). In reference [90], a test rig can be viewed, designed and built by the author at the Łukasiewicz Institute of Aviation, intended for use during testing of the POLON – Polish microsatellite propulsion system using 98% hydrogen peroxide.

1.5 Electrically heated noncatalytic hydrazine thrusters

As the availability of data concerning the thermal decomposition of hydrogen peroxide in thruster-like conditions is limited, an overview and study of literature concerning hydrazine applications in such conditions was carried out. A distinction has to be made between nonaugmented and augmented units. A nonaugmented thruster does not contain a dedicated catalytic chamber filled with a catalyst. Instead, a thermal bed comprising heated surfaces is implemented. The heated surface temperature while initiating the operation is below the temperature of the normal decomposition temperature of the propellant but high enough to initiate the reaction. In the augmented concept, the temperature of the decomposition products is increased above normal decomposition temperature, mainly by means of high-temperature resistive heaters or electric arc, allowing further increase in the propulsive performance (specific impulse) [91]. Interestingly, nonaugmented hydrazine thrusters deliver higher specific impulse than their catalytic counterparts. This is primarily due to lower ammonia dissociation compared to conventional monopropellant thrusters utilizing catalytic chambers. The decomposition of hydrazine can be expressed as:

$$3N_2H_4 \longrightarrow 4(1-X)NH_3 + (1+2X)N_2 + 6XH_2 \tag{1.21}$$

X in Equation 1.21 is the fraction of dissociated ammonia and depends on a range of factors, such as temperature, dwell time in the reactor and catalyst activity [91,92]. In the case of thermal beds (no catalytic bed present), the ammonia dissociation can be lowered; therefore, the temperature of the decomposition products is higher. Figure 1.13 depicts the relation between vacuum specific impulse, adiabatic decomposition temperature, average molecular mass and composition of reaction products with regard to the fraction of dissociated ammonia.

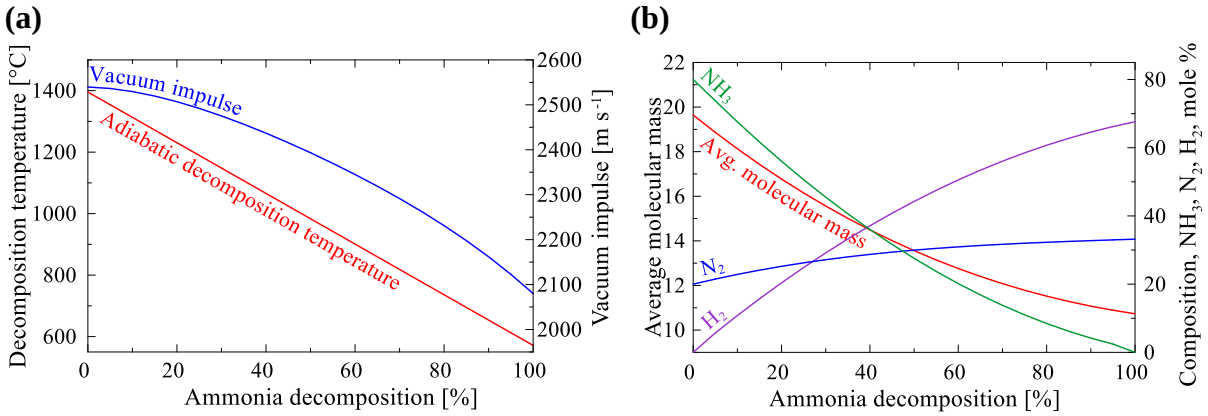

Figure 1.13 Propulsive performance and properties of hydrazine decomposition products. **(a)** variation of theoretical vacuum impulse and adiabatic decomposition temperature with a percentage of decomposed ammonia, **(b)** composition of decomposition products as a function of the amount of decomposed ammonia. Reproduced from [91].

It has to be mentioned that the lack of a catalyst does not mean that the decomposition process in a thermal reactor is entirely thermal. Even relatively inert materials (e.g., used to manufacture the chamber) at elevated temperatures will possess at least slightly catalytic properties. It must be noted that in some cases to be discussed below, metallic platinum was implemented in the decomposition chamber as a packing or platinum heater was used. This material possesses catalytic properties but is unable to initiate spontaneous decomposition of hydrazine at room temperature.

The following remarks and characteristics concerning electrothermal, monopropellant thrusters should be mentioned:

- The lack of a dedicated catalytic bed means that issues associated with loss of catalytic activity and mechanical attrition are no longer a substantial problem, as the thruster can be designed so that only high-temperature, metallic, electrically heated surfaces will be present in the reaction chamber. On the other hand, the catalytic monopropellant thrusters are also equipped with a heater to minimize thermal shocks during start-up and to improve the response time, as the activity of the catalyst depends on the temperature.

A so-called cold start (a run performed without a previous preheating of the bed) in the case of a catalytic thruster is, in most cases, possible, but usually, a limited number of times, as extensive thermal cycling will result in premature damage of the catalyst. Additionally, if the catalytic bed is not preheated, the catalytic activity is lowered, and the response of the thruster is extended; this will result in propellant accumulation in the chamber, causing significant overpressure after the reaction is accelerated, leading to mechanical damage of the catalyst.

- As the size of the thruster is reduced, the surface-to-area ratio increases, resulting in significant heat loss. This means that the problem of inhibition of the decomposition process may occur [93] and is of particular interest if the engine is to operate in low duty cycle pulsed mode; in such a case, a large portion of released heat will be transferred to the catalyst and the structure of the thruster. Preheating the unit is a solution, but if the preheating temperature is high enough, the catalytic bed can be eliminated, and the thruster can operate in a thermal mode [94,95].
- Robustness due to simple design. Low cost.
- The electrothermal thruster has the potential to operate reliably using alternative propellant combinations and be immune to a range of additives which could be implemented, e.g. to improve the storability characteristics of HTP. During the development of thermal thrusters using hydrazine, an attempt was made to allow the application of monomethylhydrazine (MMH) unsymmetrical dimethylhydrazine and other alternative propellants. The reason for that was a much lower melting point, which could be very advantageous in the case of deep space missions. Application of MMH and UDMH in current hydrazine thrusters is not possible, as both propellants contain carbon, which causes premature degradation of iridium-based catalysts.

For comparison purposes, the most significant physical properties of hydrazine, MMH, UDMH and anhydrous hydrogen peroxide were collected in Table 1.2.

The following disadvantages of electrothermal thrusters must be noted:

- If the heater in the electrothermal thruster fails or a power supply to the thruster will not be possible, the thruster becomes inoperative. Redundancy is a partial solution to the problem.
- The thruster must be preheated prior to operation; therefore, instant availability would not be possible without keeping the chamber preheated.

Table 1.2 Selected physical properties of hydrazine, monomethylhydrazine, unsymmetrical dimethylhydrazine and anhydrous hydrogen peroxide [91]

Property	**Unit**	**Hydrazine**	**Monomethyl--hydrazine (MMH)**	**Unsymmetrical dimethylhydrazine (UDMH)**	**Hydrogen peroxide, 100%**
Molecular formula		N_2H_4	$CH_3(NH)NH_2$	$H_2NN(CH_3)_2$	H_2O_2
Melting point	°C	2,01	-52,37	-57,21	-0,43
Boiling point	°C	114,2	87,65	62,32	150,2
Vapour pressure	kPa	1,89	6,6	22,3	0,279
Density, liquid	kg m^{-3}	1003,7	870,2	786,1	1442,4
Viscosity, liquid	mPa s	0,913	0,775	0,492	1,25*

*Viscosity at 20°C

In [16], the authors presented preliminary test results gathered while testing different thermal hydrazine thrusters' configurations. Initial trials were performed using thrusters comprising tubular heaters; the throat diameter was 0,25 mm, and heater power was 8.5 W. Significant in magnitude, periodic pressure peaks were observed, and flooding was also an issue. Data concerning measured thrust was provided for other tubular heater thrusters, employing nozzles with a throat diameter of 0,25 and 0,64 mm; a specific impulse of ~2800 m/s was achieved in vacuum conditions for the latter throat size at a thrust range of ~0,02 N and heater power of 55 W (augmentation was implemented), but, as reported, the thrusters were difficult to control. It was not possible to sustain decomposition if the heater was turned off. Next, transparent quartz thrusters (~6,1 mm ID) were fabricated with a coil heater inside. Pulsations were observed at low flow rates (~1,8 to ~$4{,}5\cdot10^{-3}$ g/s), but after the mass flow rate was increased, pulsation stopped, and it was possible to turn the power supply off and sustain decomposition. Based on the previous experience, wire coil thrusters were tested; a range of test configurations were manufactured and examined, employing various injection systems (orifice plate, porous material, alumina tube), chamber geometries, heater powers, nozzle sizes and, for some cases, chamber packing was implemented. The flow rate was from ~$2{,}27\cdot10^{-3}$ g/s to ~0,068 g/s. A range of successful runs was performed, and for comparison purposes, a catalytic thruster was developed and tested, and the results were compared to the thermal counterpart. Monopropellant thruster using Shell 405 catalyst delivered specific impulse of ~1960 m/s at a thrust of ~0,46 N and respectively 1423 and ~1325 m/s for a thrust of 0,046 and ~0,022 N while for one of the thermal thrusters tested, specific impulse delivered was 1825 m/s at a thrust of ~0,016 N (no electrical power supplied to the heater).

A range of thruster configurations was discussed in [96]. NASA's contract resulted in a substantial test campaign and analytical investigations concerning operating principles of

hybrid resistojets using hydrazine. A simple tubular configuration was investigated during the preliminary testing, with only the heating wire placed in the chamber (configuration A). Next, a ceramic rod was placed in the chamber as a 'flame holder' (configuration B). Configuration denoted as C employed a porous ceramic tube as an injector. Figure 1.14 (a)-(c) shows each configuration mentioned. As for thruster-like conditions, a pre-prototype model was developed based on previously obtained data and thoroughly tested. This model can be viewed in Figure 1.14 (d). It was stated that configuration C was superior to configurations A and B regarding decomposition efficiency and stability. As for the pre-prototype thruster, a steady-state specific impulse of ~2350 m/s was measured without a power supply to the heater for a mass flow rate corresponding to a thrust of ~0,26 N.

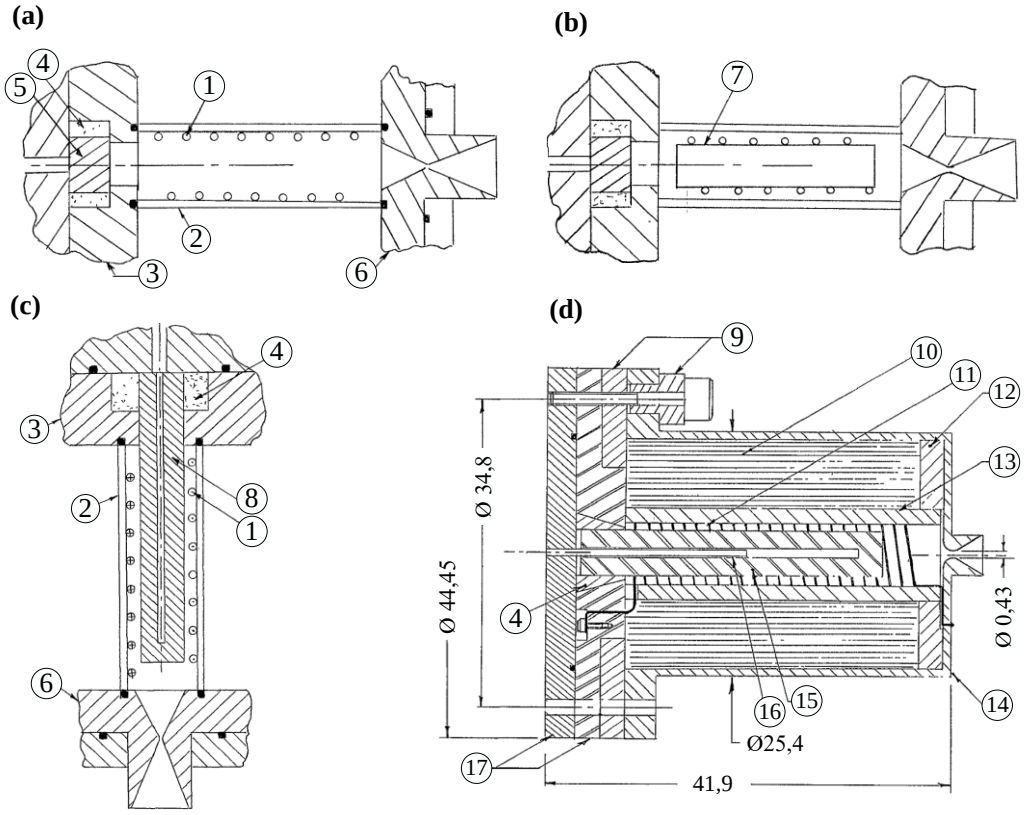

Figure 1.14 Thruster configurations investigated in [96]. **(a)** configuration A, **(b)** configuration B, **(c)** configuration C, **(d)** pre-prototype thruster. 1 – heater coil, 2 – quartz tube, 3 – base plate, 4 – Teflon seal, 5 – porous injector, 6 – nozzle, 7 – porous ceramic rod, 8 – porous ceramic, 9 – Teflon insulator, 10 – Fiberfrax insulation, 11 – molybdenum coil wire, Ø 0,25mm, 12 - Lava insulator, 13 – alumina insulator, 14 – outer housing, material: TZM, 15 – zirconia tube, 16 – tube, material: stainless steel, 17 – base plate, material: stainless steel [96]. Units converted to millimetres.

Following the activities documented in [96], attempts were made to deliver models resembling flight units. In [97], two thermal engine concepts were tested – the first with axial and the second with a radial propellant injection. The thrust level in each case was ~0,045 to ~0,22 N. Declared specific impulse was ~1865 m/s for pulsed mode and ~2250 m/s during steady-state operation. Engines were started with a heater power of 5 W or less. The axial engine

comprised a heater section, where the propellant's vaporisation occurred. Beryllia ceramic was combined with heating wire for electrical insulation, high thermal conductivity and large surface area. The decomposition was to occur in the quartz-packed reaction zone, as seen in Figure 1.15 (a). As for the radial injection engine, the decomposition chamber was equipped with a central heater coil and the propellant was delivered radially.

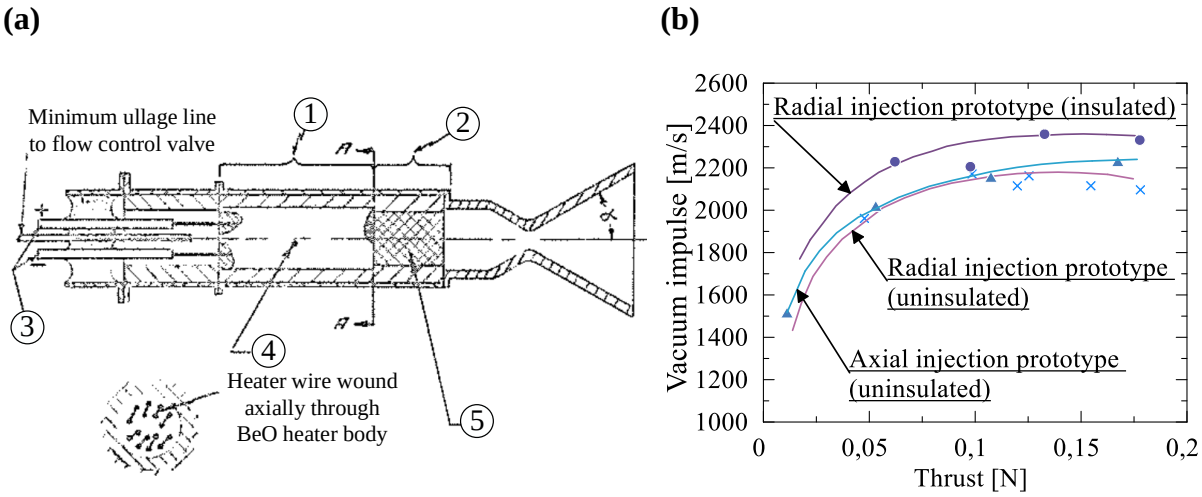

Figure 1.15 **(a)** Axial injection engine, throat diameter was 0,43mm, α=30° 1 – heater section, 2 – reaction zone, 3 – electrical connections, 4 – BeO heater assembly, 5 – packed quartz **(b)** Performance, in terms of specific impulse, as a function of thrust for axial and radial engines. Reproduced from [97].

In the axial injection concept, the assumption was to separate the vaporization and decomposition section, while in the radial one, the liquid propellant was injected into the chamber and mixed with the decomposition products, allowing vaporization and decomposition. Figure 1.15 (b) presents the relationship between specific impulse and thrust for axial and radial injection concepts.

In the previous papers concerning electrothermal hydrazine thrusters, small size, tenth Newton units were only investigated. In [98], a thruster with a thrust of ~10 N was tested. As in the previous cases, a resistance heater was used to preheat the chamber and initiate the decomposition. No details regarding the engine's design were given, but valuable experimental data was provided. Authors claim that in a pulsed mode (interval duration of 12 s and pulse width of 5.25 s), the average specific impulse was ~2150 m/s. By applying forty 0,42 s pulses in 3 s intervals, the specific impulse increased from ~1960 to ~2490 m/s at the end of the pulse train, the mean thrust was 6,8 N, and the initial reactor temperature rose from 715 to 950°C by the final pulse.

A set of interesting data can be found in [99]. A five-pound (~22 N) thruster was vacuum-tested; the engine was equipped with two heaters, the first one in the chamber and the

second one placed on the outer side. The heater power was from 10 to 15 W, depending on the operation mode. Detailed design features were not provided. The three most significant observations were: (I) It was possible to operate the thruster at a tank pressure from ~27,6 down to ~1,38 (blowdown ratio of 20); (II) Specific impulse was relatively constant for a thrust range from ~2,2 to ~25,6 N and had a value of ~2370 m/s; (III) It was noted that a relationship between wall temperature and specific impulse exists. The 'transition temperature' was between ~815 and ~870°C. If the temperature was above that limit, the specific impulse was relatively constant, and the influence of pulse width and duty cycle was insignificant – as shown in Figure 1.16.

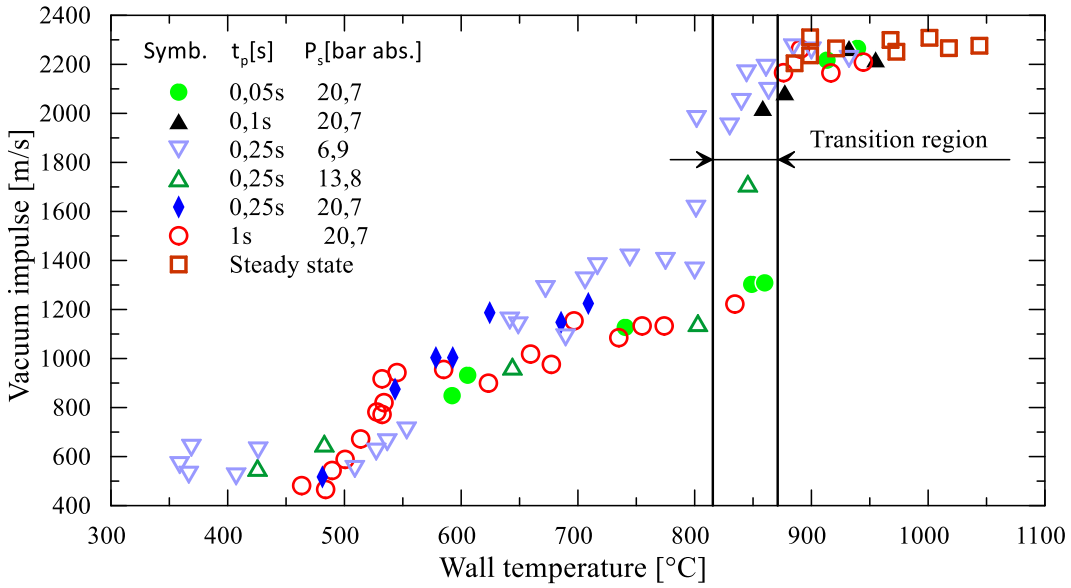

Figure 1.16 Variation of specific impulse for electrothermal hydrazine thruster presented in [99] as a function of chamber wall temperature for a range of pulse widths (t_p) and supply pressures (P_s). Reproduced from [99], units were converted, transition region lines were added.

A series of papers and reports were published by engineers working at TRW Systems Group. In [100], tests were presented of a low-thrust electrothermal hydrazine thruster operating at a thrust range of ~0,22 to ~0,31 N. The thrust chamber had an inside diameter of ~5,1 mm and a length of ~12,7 mm. A platinum and Haynes 25 screen occupied part of the chamber, and the 5W heater was wound on the outer wall. The reported pressure rise time, measured from when the valve was commanded to open to when 90% of steady-state pressure was measured, was lower than 20 ms, and pressure decay time (down to 10% of steady-state value) was also on the order of 20 ms. A cycle life test was performed, and tests were intentionally stopped after 1 017 000 cycles. The pulse-to-pulse impulse bit variation was lower than 15% at constant inlet pressure. During steady state operation, the vacuum impulse exceeded 2250 m/s. Tests presented in [100] were in more detail described in the preliminary design task summary report [101]. The thruster under investigation can be viewed in Figure 1.17 (a) and (b).

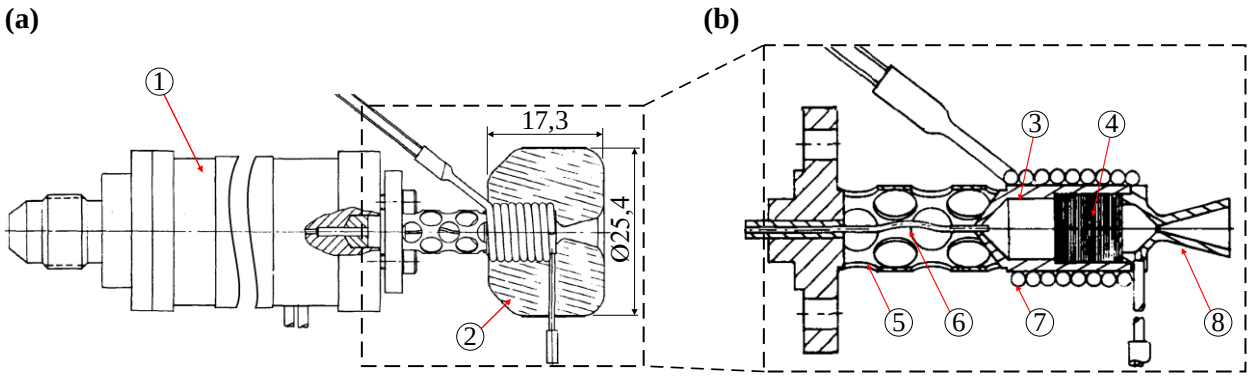

Figure 1.17 **(a)** Complete thruster assembly, tested in [100,101]; **(b)** Internal configuration of the unit; 1 – valve; 2 – insulation; 3 – thruster body; 4 – screen-pack; 5 – barrier tube; 6 – injector tube; 7 – heater; 8 – nozzle; Reproduced from [94].

Another TRW report [102] presents an engineering model's fabrication details, an evolution of the thruster mentioned above. Extensive test data was presented as well. The modifications were not significant and included a screen pack with increased density (compressed stack of platinum screen discs). The biggest challenges encountered were related to the injector tube. Three materials were tested: Inconel 600, Haynes 25 and platinum-10% iridium alloy. In the case of Inconel and Haynes, nitriding of the injector was a significant problem, while platinum alloy caused vaporization in the injector. The test campaign performed on the thruster resulted in 300 000 pulsed cycles and 30 hours of steady-state operation.

In [103], an investigation was documented, which aimed to determine the possibility of using alternative propellants in an electrothermal thruster with a thrust of up to ~0,45 N. The test-thruster was optimized for each propellant (e.g. injector configuration, materials of construction, etc.). Hydrazine tests were performed for each configuration before testing the alternative propellant combination. Table 1.3 shows the propellants tested, along with the corresponding freezing point and two ranking factors – steady state, being a ratio of a steady state specific impulse to that of hydrazine and pulsed mode, which is the ratio of pulsed to steady state specific impulse. Thruster disassembly following tests (>30 min duration) incorporating Aerozine 50 revealed some carbon deposited in stagnant regions. MMH delivered a specific impulse of ~2010 to 2110 m/s; carbon deposition was observed following disassembly, but according to the authors, the amount was insufficient to affect the thruster's performance.

Apart from a small-size thruster, the authors in [103] developed an engine delivering a thrust of ~22 N. Following the optimization of components, which included testing 21 configurations, it was possible to demonstrate reliable, steady-state and pulsed mode operation.

Table 1.3. Monopropellant thruster performance comparison. Reproduced from [103]. Steady-state ranking factor – a ratio of the steady-state specific impulse to that of hydrazine at the same inlet pressure. Pulsed mode ranking factor – a ratio of pulsed mode (0,075 s ON, 0,925 s OFF) and steady-state specific impulse.

Propellant	Freezing point [°C]	Steady-State Ranking Factor	Pulsed Mode Ranking Factor
N_2H_4	1,2	1	0,87
77% N_2H_4 + 23% hydrazine azide	-17,8	1,01	0,85
Aerozine 50 (50% UDMH + 50% N_2H_4)	-5,9	0,96	0,77
MMH	-52,6	0,95	0,81
50% MMH + 50% N_2H_4	-17,8	0,95	0,79
35% N_2H_4 + 50% MMH + 15% NH_3	-54,2	0,94	0,81
85% N_2H_4 + 15% Water	-17,8	0,88	0,79
80% N_2H_4 + 20% NH_3	-17,8	0,88	0,77

Twardy [94] presented a very interesting set of experimental data. Tests were performed for a thrust range of 100 to 500 mN, the reaction chamber size was Ø15 x 80 mm, and the heater was placed inside. The first configuration tested employed only the heater coil in the reactor, and it was noticed, as in [99], that the influence of wall temperature is significant, and both pressure roughness and reaction delay time depend on that parameter – as presented in Figure 1.18 (a) and (b), respectively for heater coil and pack heater configuration.

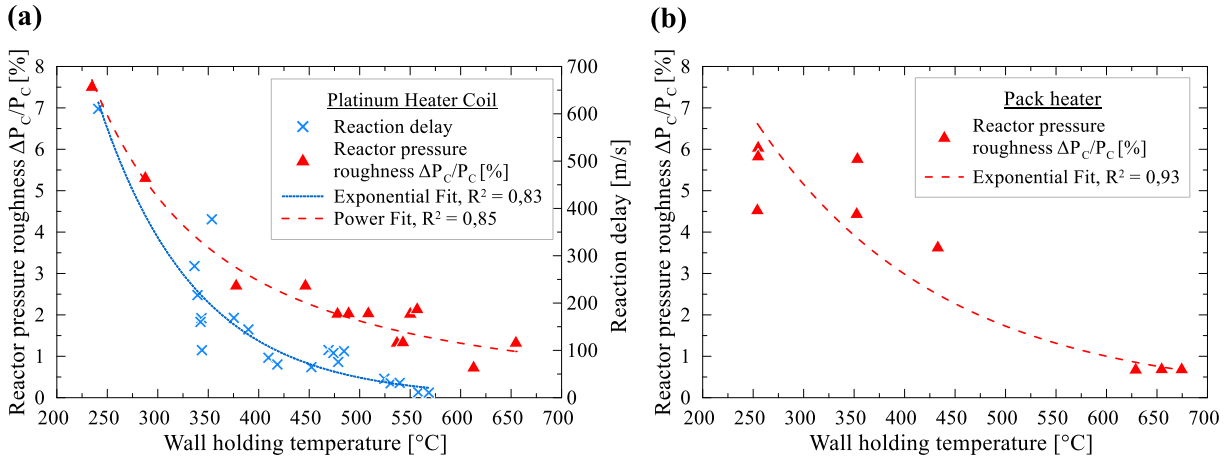

Figure 1.18 Characteristics of 100-500 mN electrothermal hydrazine thruster configurations **(a)** Chamber pressure roughness and reaction delay time varying with wall temperature **(b)** Pressure roughness for a reactor equipped with a pack heater as a function of wall temperature. Reproduced from [94], temperature units were converted to °C, and fit curves were added, replacing the original ones.

In order to confirm the significant influence of wall temperature on the operating characteristics of the engines tested, some runs were performed with a cooling of the external wall (temperature was maintained at 20°C); it was concluded that even though the heater coil temperature was ~650°C, 'the decomposition process was very rough'. In each case for the heater coil configuration, it was possible to maintain the decomposition after turning the power supply off. Alternative configurations tested included (I) wire gauze heater – but the performance was

lower than for heater coil; (II) pack heater, being an intertwined platinum wire, packed in the tube and supported by a screen on both sides, with heater coil on the outside of the tube, the entire pack was placed in the chamber; promising results were obtained for one of the injector configurations, allowing self-sustainable operation and wide flow range; (III) Metal foam pack heater – after proper insulation and injection technique selection, it was possible to initiate reliable decomposition with a heater power as low as 4 W.

In 1971, AVCO company managed to flight-test one of its units on a Sol Rad 10 satellite. As reported, several firings took place, which were reported as successful, but eventually, system failure occurred, and due to limited data available, it was not possible to define the cause of the malfunctioning.

1.5.1 Augmented hydrazine thrusters

The so-called augmentation process aims to deliver external energy to the decomposition products. As can be seen in Figure 1.19, the monopropellant compound is first decomposed catalytically or thermally, and in the next step, heat is transferred to the stream of decomposition products. Augmentation can be achieved by employing a resistively heated element (resistojet) or electric arc (arcjet).

In the case of arcjet thrusters using hydrazine as a propellant, the specific impulse that can be achieved exceed 5000 m/s [104].

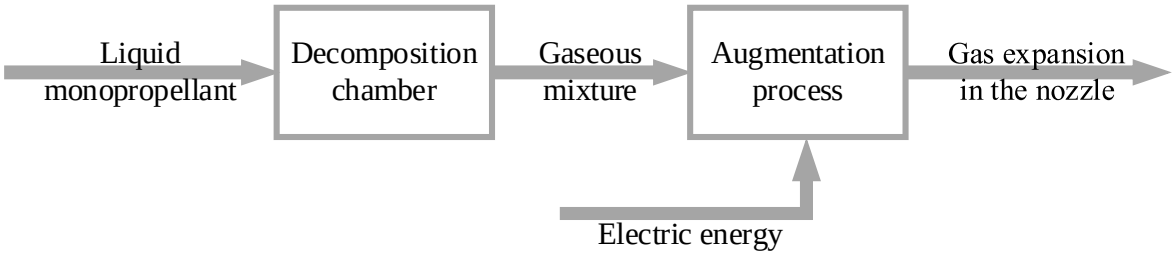

Figure 1.19 Schematic diagram illustrating the operating principle of an augmented monopropellant thruster [105]

As for resistojets, the energy can be added to the gas internally (immersion type heater) through direct contact of the decomposition products with the heating element or externally (nonimmersion radiative heater) by heating walls of the augmentation chamber [105,106].

Figure 1.20 (a) shows a High-Performance Electrothermal Hydrazine Thruster (HiPEHT) developed by the TRW company. As can be viewed, the thruster decomposes hydrazine thermally using a thermal bed similar to the one shown in Figure 1.17 (b).

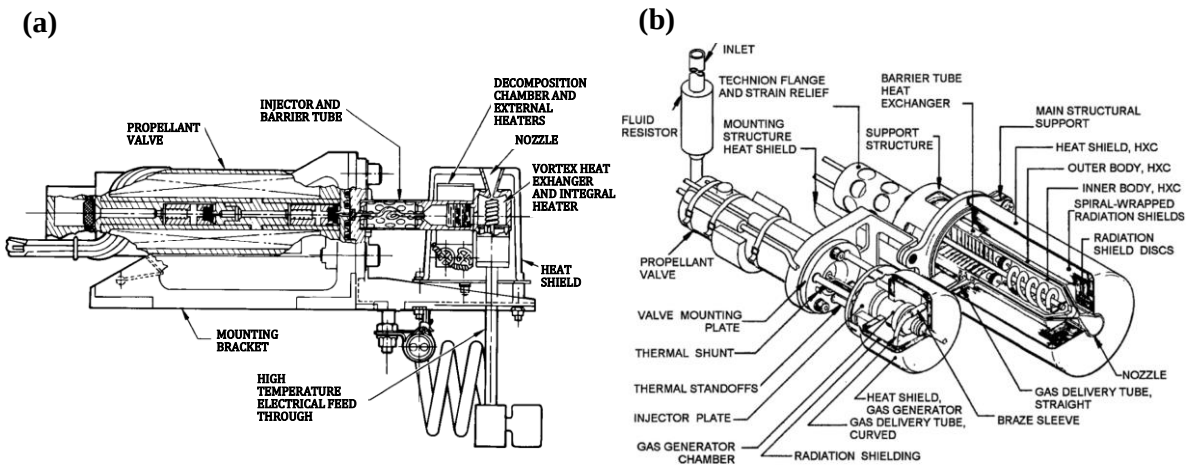

Figure 1.20 Augmented electrothermal hydrazine thrusters: **(a)** developed by TRW [107], **(b)** developed by Primex Aerospace Company [108].

The thruster delivered a specific impulse of up to ~3140 m/s, and the necessary heater power was ~6 W for each 4,5 mN (1 millipound) thrust. A vortex heat exchanger was used for augmentation and was directly exposed to decomposition products (internal heat addition) [108]. The temperature of the gas was up to ~1930°C. The heater of the heat exchanger was turned on fifteen to thirty seconds after the propellant valve was opened and was turned off five to fifteen seconds before the end of the firing. In case of failure of the vortex heat exchanger, e.g., a burned heater, the thruster could operate in nonaugmented mode, delivering a specific impulse of ~2260 m/s. The thrust level was ~0,5 to ~0,22 N, and the thrusters were flown on Intelsat V satellites (the first satellite was launched in 1980) [107].

Figure 1.20 (b) illustrates the augmented catalytic thruster (ACT). In this case, hydrazine is decomposed catalytically, and decomposition products are delivered to the heat exchanger, different from the one described previously. The heat exchanger comprises two cylindrical sections with a flow passage between them. The high-temperature heater is placed in the central location, and the heat from the heater is delivered radiatively to the exchanger tube. Next, the heat is transferred to the flow through radiation, convection and conduction. The augmentation heater does not come in contact with the hydrazine decomposition products [108]. The heater is vented to the space and can not be operated in conditions different from a vacuum. The thruster can not be operated in pulsed mode. The current version of the thruster, MR-502A, offered by Aerojet Rocketdyne, delivers a specific impulse of up to ~2970 m/s and a thrust of 0,8 to 0,36 N, and augmentation heater power is 885 to 610 W [109].

1.6 Thermal decomposition of HTP in thruster-like conditions

Limited data is available concerning propulsive applications of resistively heated, noncatalytic thrusters using highly concentrated hydrogen peroxide. The most significant investigations will be briefly discussed in this section.

Research performed at Rocketdyne was mentioned in [22]. Based on two cited sources (the first was unpublished, and the second one was a summary report dating back to 1960, which was unobtainable to the author of this thesis), it was stated that the usefulness of thermal decomposition of 90 and 98% hydrogen peroxide was limited. The decomposition could be sustained only with small loadings (mass flow rate per cross-sectional area); more significant loadings usually lead to quenching of the decomposition process. The conclusion was that due to a low rate of thermal decomposition, gas generators not possessing a dedicated catalytic pack can not compete with their catalytic counterparts.

Figure 1.21 illustrates the patent concerning an adjustable flow gas generator, submitted by Watkins (Pratt&Whitney) in 2001 [110]. The generator comprises a catalyst section, where hydrogen peroxide is decomposed catalytically and a mixer section, where the additional propellant is injected into the stream of hot decomposition products, resulting in the thermal decomposition of this secondary flow.

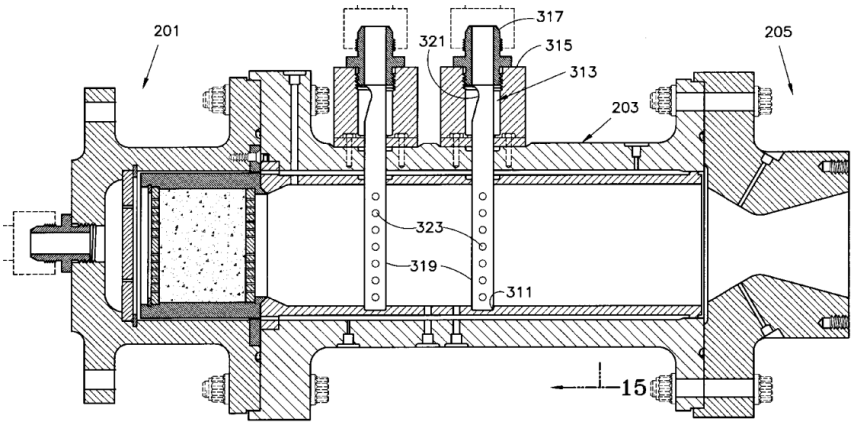

Figure 1.21 Pratt&Whitney adjustable flow gas generator patent [110]. Most significant elements: 201 – catalyst section; 203 – mixer section; 205 – nozzle; 313 – spray bar assembly; 315 – spray body assembly; 317 – coupling threaded to the body; the secondary flow of hydrogen peroxide goes through: 319 – tubes and 323 – ports; 321 – tube end located in the body.

In [62], authors presented experimental results obtained during cross-flow injection of liquid 90 and 98% hydrogen peroxide into the stream of decomposition products of 90% HTP.

Chamber pressure ranged from 20 to 55 bar; two cross-flow injector orifice sizes were tested. Chamber length was a variable as well as the mass flow rate of the primary (catalytically decomposed) and secondary (radially injected) flow. Figure 1.22 (a) and (b) present the chamber assembly and injector for the secondary flow, respectively.

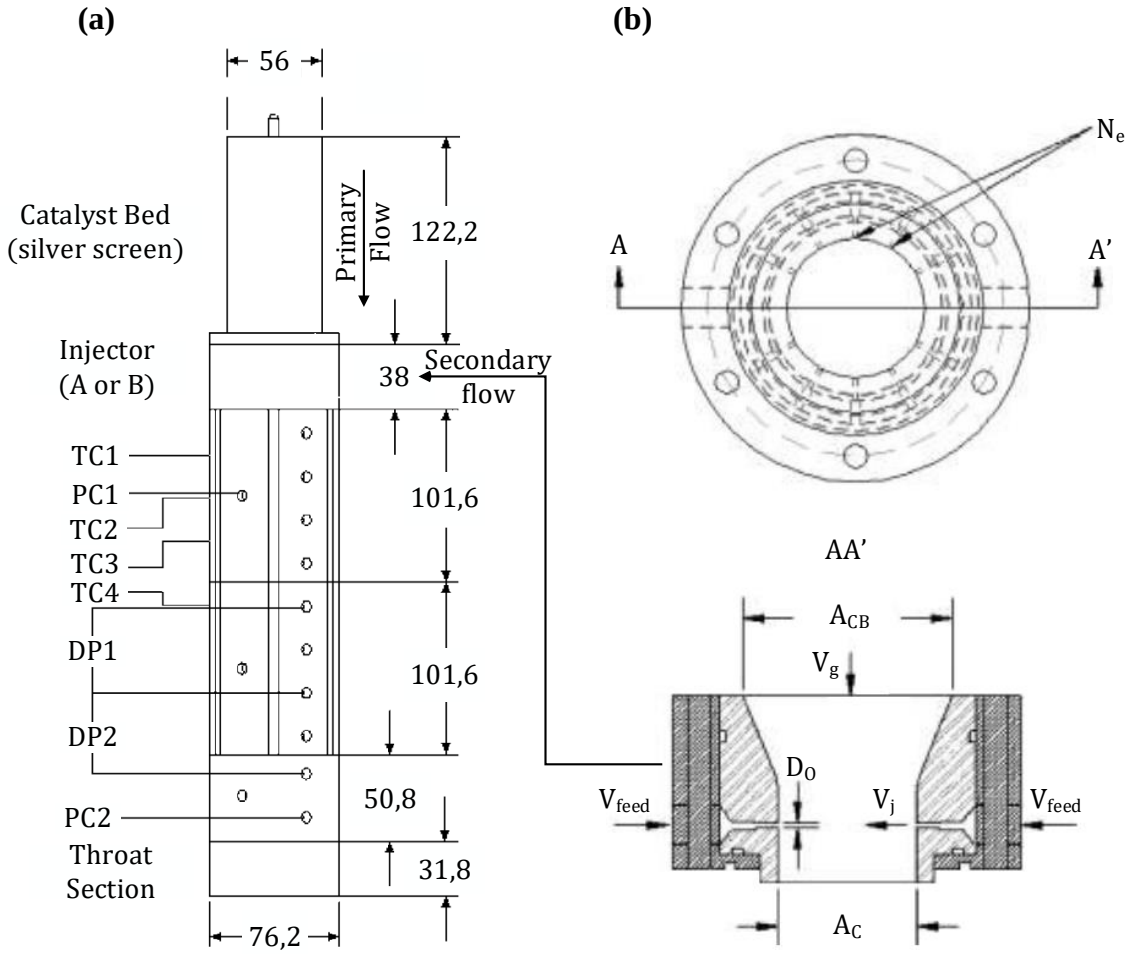

Figure 1.22 Test article used in [62]. **(a)** Assembly of the chamber showing the most significant sections, dimensions and locations of measurement ports. Two chamber sections, each 101,6 mm long, are present in the drawing (a). Different chamber stacking was implemented during the test campaign, resulting in cylindrical section lengths ranging from 102 to 254 mm. All dimensions were recalculated and are in millimetres. **(b)** Ring injector assembly. The injector was located 20 mm downstream from the catalyst bed; number of injector orifices, N_e=10; orifice diameter, D_O, respectively 0,91 and 0,61 mm for injectors denoted as A and B. Chamber diameter at the radial injector plane was 30,5 mm. Prepared based on [62].

The general observations were that the decomposition efficiency for the secondary flow increases with increased residence time in the chamber and decreases with increasing liquid fraction in the secondary flow. Additionally, it was noted that if the concentration of HTP used for secondary flow was 98% instead of 90%, the decomposition efficiency increased and, for some experiments, was 20-30% higher. The explanation for the latter was higher vaporization and decomposition rates caused by higher decomposition temperature resulting from increased concentration of the propellant.

Additionally, it was stated that local cooling takes place due to vaporisation before exothermal decomposition. When an injector with a lower orifice diameter was used (injector B), it was observed that the high-velocity jets did not break up into drops and collided in the centerline of the chamber; as a consequence, a high local liquid mass fraction was obtained, resulting in lowered heat transfer, lower temperature and lower performance when compared to injector A, in which the orifice diameter was greater.

In [111], the authors presented a one-dimensional model developed to investigate the thermal decomposition of hydrogen peroxide occurring in a secondary flow of the previously described thruster. Results obtained in [62] were used to validate the model. The results showed that for secondary flow accounting for only 5% of the primary mass flow rate, the chamber length required to decompose the secondary stream of 90% HTP was on the order of 460 mm (chamber diameter and pressure: 25,4 mm, and ~34,5 bar). By increasing the concentration of the peroxide in the secondary flow, the required length was shorter, but as stated, still too long distances were required for practical aerospace applications.

A preliminary test campaign was presented in [112], during which a resistively heated thruster using 90% hydrogen peroxide was investigated. The catalyst was replaced with 1/8'' alumina pellet or 1/4'' SUS304 stainless steel balls that were used in the second configuration. A spray injector was implemented; the heater chamber was 16 mm long, and the diameter was 40 mm. The mass flow rate tested was between 4 and 10 g/s. Alumina was first tested as a heater pack; the initial temperature prior to hydrogen peroxide injection was 520°C. The test was only five seconds long, and it was not possible to stabilize the process; pressure fluctuations were significant, but the downstream heater temperature rose to 843°C. Tests performed with stainless steel balls showed insignificant values of temperature and pressure in the upstream and downstream sections of the heater bed.

In [113] and [114], authors presented research performed in thruster-like conditions, where the catalyst bed was replaced with a heater, and hydrogen peroxide at a concentration of 98% was sprayed on the heater placed directly in the decomposition chamber. A commercially available oil-burner nozzle was implemented in the injection system. The mass flow rate was ~0,4 and 0,9 g/s for a chamber pressure of 10 and 5 bar, respectively. It was noticed that for the nozzle with a smaller throat diameter and with reduced mass flow rate and increased chamber pressure, the decomposition efficiency was improved when compared to the case with low chamber pressure and higher mass flow rate. This was probably accomplished by extending the residence time and is in good agreement with [62].

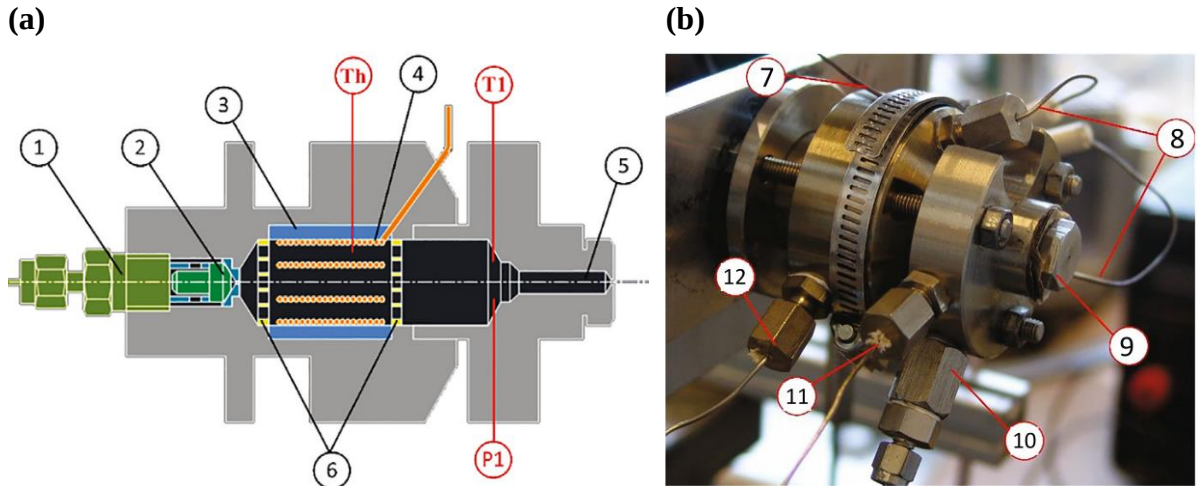

Figure 1.23 Thruster used in [113] and [114]. **(a)** Cross-sectional view: 1 – feed-line connector, 2 – injector, 3 – ceramic insulator, 4 – heater, 5 – nozzle, 6 – restrictors, not used in the final version. **(b)** Thruster, prior to the experiment: 7 – thermocouple (external wall temperature), 8 – heater connectors, 9 – nozzle, 10 – chamber pressure port (P_1), 11 – chamber temperature port (T_1), 12 – heater temperature port (T_h).

For a higher mass flow rate, pressure oscillations were close to 20% of the mean chamber pressure, while after the pressure was increased (by changing the nozzle), this value was reduced to 2%. Interestingly, the authors performed tests in which the chamber was preheated and the heater was turned off before FCV opening - initiation of the decomposition was possible. Authors noted that for some experiments, downward peaks occurred, which were possibly caused by the supply system. The duration of experiments was relatively short, 7s in [113] and 15 s in [114]; this calls for additional tests involving a modified rig and extended duration of experiments; such an attempt was made and will be presented in the following sections of this dissertation, being a continuation of the work presented in [113] and [114].

Chapter 2

Objectives and methodology

2.1 Objectives

The primary motivation of this dissertation is to experimentally characterize the operating parameters of a laboratory version of a monopropellant thruster for space applications in which no dedicated catalytic material was used to decompose the propellant used – 98% hydrogen peroxide. The thesis of this dissertation is as follows:

It is possible to obtain a self-sustaining, stable decomposition of 98% hydrogen peroxide in a sub-Newton, electrothermal, monopropellant thruster not equipped with a dedicated catalyst bed.

As limited data is available concerning the possibility of initiating and sustaining reliable decomposition in resistively heated, sub-Newton units, the primary goals are to:

- Design a laboratory thruster with a reduced mass and find engineering solutions allowing thorough examination.
- Investigate if conditions exist for explosive decomposition; therefore, determine if the proposed concept can be safely tested and operated without posing a critical or catastrophic failure threat.
- Capture factors that influence the characteristics of the investigated engine. Based on the available literature data, it can be found that decomposition can be initiated, but the conditions during the aforementioned research did not allow a thorough examination of the process, as the mass of the unit tested in the cited documents was significant, and duration of experiments was short, therefore data concerning factors that affect the operating parameters is missing. The goal is to broaden the knowledge by providing information concerning:
  - Temperature characteristics – estimate the temperature limits necessary to operate the test article effectively.
  - Propulsive characteristics and investigate their temperature dependence.
- Investigate if the decomposition process can be self-sustained in a thruster with reduced mass and test experiment durations on the order of minutes.

2.2 Methodology

Figure 2.1 presents the philosophy applied during the research and shows how the test campaign was organized. First, the test rig was designed and built based on requirements that were defined considering the research objectives. The central part of the test facility is the thruster, being a laboratory concept; therefore, factors such as dribble volume in the propellant injection system (the volume between the flow control valve and the injector) or mechanical design are by no means optimal. This is justified by the fact that priority was given to the ease of assembling and data collection. As for the dribble volume, this parameter primarily influences the pressure rise and decay time and is crucial for a flight unit as it directly affects the minimum impulse bit that the engine can provide. Nevertheless, from the perspective of the presented research, priority was given to the ability to compare the rise and fall times for different test conditions, and this requirement was met with the proposed design.

The campaign was divided into two main parts. First, to initially investigate the process's behaviour, so-called high-power mode testing was carried out. In this part of the research, the heater placed inside the chamber was supplied with a high voltage; as a result, the power delivered was in the range of up to 300 W. Such high values were selected to assess the possibility of obtaining reliable decomposition and capture relations between measured temperatures and metrics of interest. During tests, the heater was turned on for a specified time (6 to 34 s) before opening the FCV; the duration of this period, called preheating, was changed between experiments and results were compared. Apart from the preheating time, the heater power was also variable. The heater was powered by a laboratory power supply, which allowed flexibility in terms of voltage adjustment.

During the second part of the campaign, called low-power campaign, the heater power was significantly reduced, and the preheating phase was extended. These experiments aimed to test the performance of the thruster at conditions (heater power) that were much closer to the values utilized by the catalytic monopropellant thrusters generating similar thrust (~1 N). Heater power was also variable; each low-power experiment's preheating time was the same, resulting in different decomposition chamber temperatures before valve opening. During tests with the reduced heater power, two different experiment durations were under investigation – 70 and 120 seconds, excluding short, 5 s tests, prior to each long experiment after the voltage setting was changed, to accept or reject the decomposition quality and minimise risks associated with the unpredictable behaviour of the test article.

Experiment duration was defined as the time during which the flow control valve was in an open position, allowing the propellant to be delivered to the chamber.

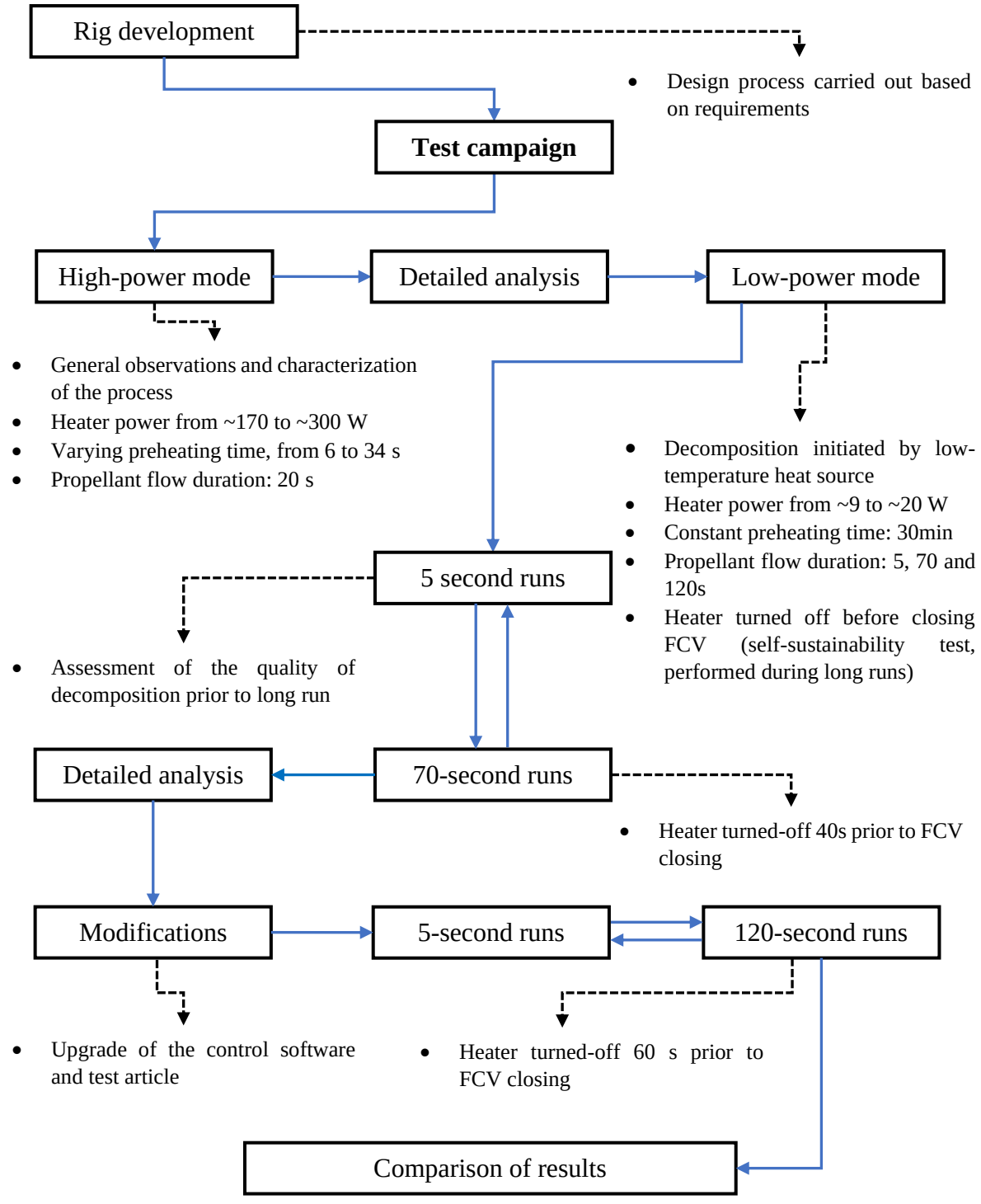

Figure 2.1 Methodology applied during the experimental campaign

Altogether, more than 1500 experiments were performed, mostly failed, to fine-tune the rig, optimize procedures (including safety-related activities) and deal with technical issues that emerged; this relates to some of the components that were procured, material compatibility or

leak tightness. A detailed description of all the actions and modifications undertaken will not be provided; only the final design and tests using that configuration will be discussed.

The following sections are organized as follows. First, a thorough description of the test facility was provided. In that chapter, the most significant components were presented, as well as design solutions and implemented procedures. Next, a detailed analysis of the results was given. First, the so-called high power mode was discussed. The test methodology was thoroughly explained, together with observations made during experiments and final conclusions. Next, the reduced heater power was analyzed. This section was divided into two parts; the first dedicated to 70 s runs, while the second briefly outlines 120-second experiments. Next, a comparison of the data obtained was given, showing the relations obtained, and final conclusions were presented.

Chapter 3

Experimental facility

3.1 General overview of the test rig

Figure 3.1 presents a schematic overview of a dedicated test rig developed specifically for the presented research. The rig employs a laboratory pressure feed system; HTP was pressurized with nitrogen delivered from a high-pressure cylinder through a pressure-reducing regulator and a buffer tank; a buffer tank was implemented to minimize pressure fluctuations during tests.

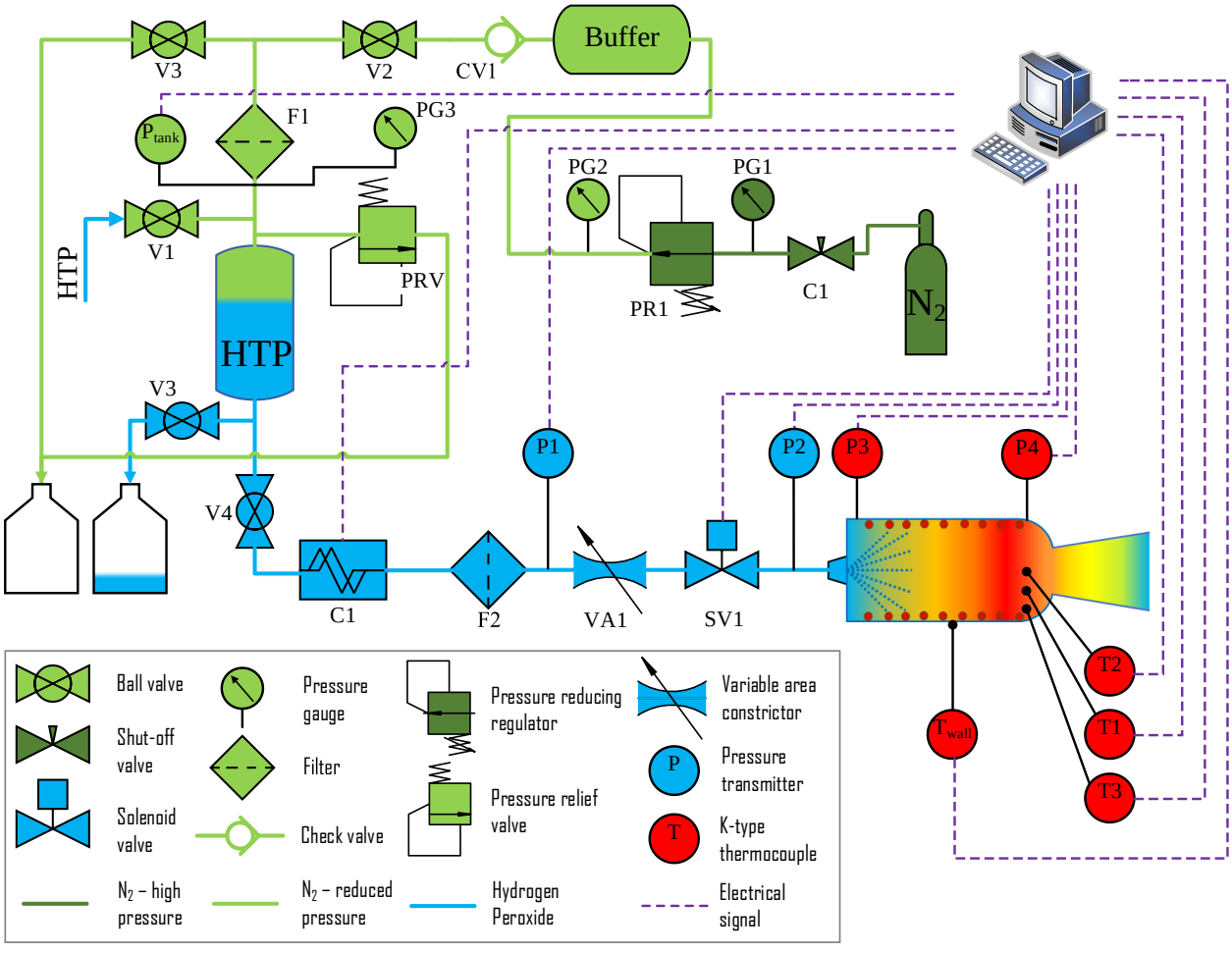

Figure 3.1 Schematic representation of the test rig used during the research

Manual ball valves were used, but the rig will be automated in the future. In order to improve the safety level, the amount of propellant delivered to the tank was up to 70ml, and to allow for accurate mass flow rate adjustment at a specified tank pressure, a variable area restrictor was designed and integrated with the flow control valve (FCV). The entire facility was designed to work in a wide range of pressures – up to the maximum allowable FCV pressure of 86 bar. Figure 3.2 depicts the facility used during the test campaign.

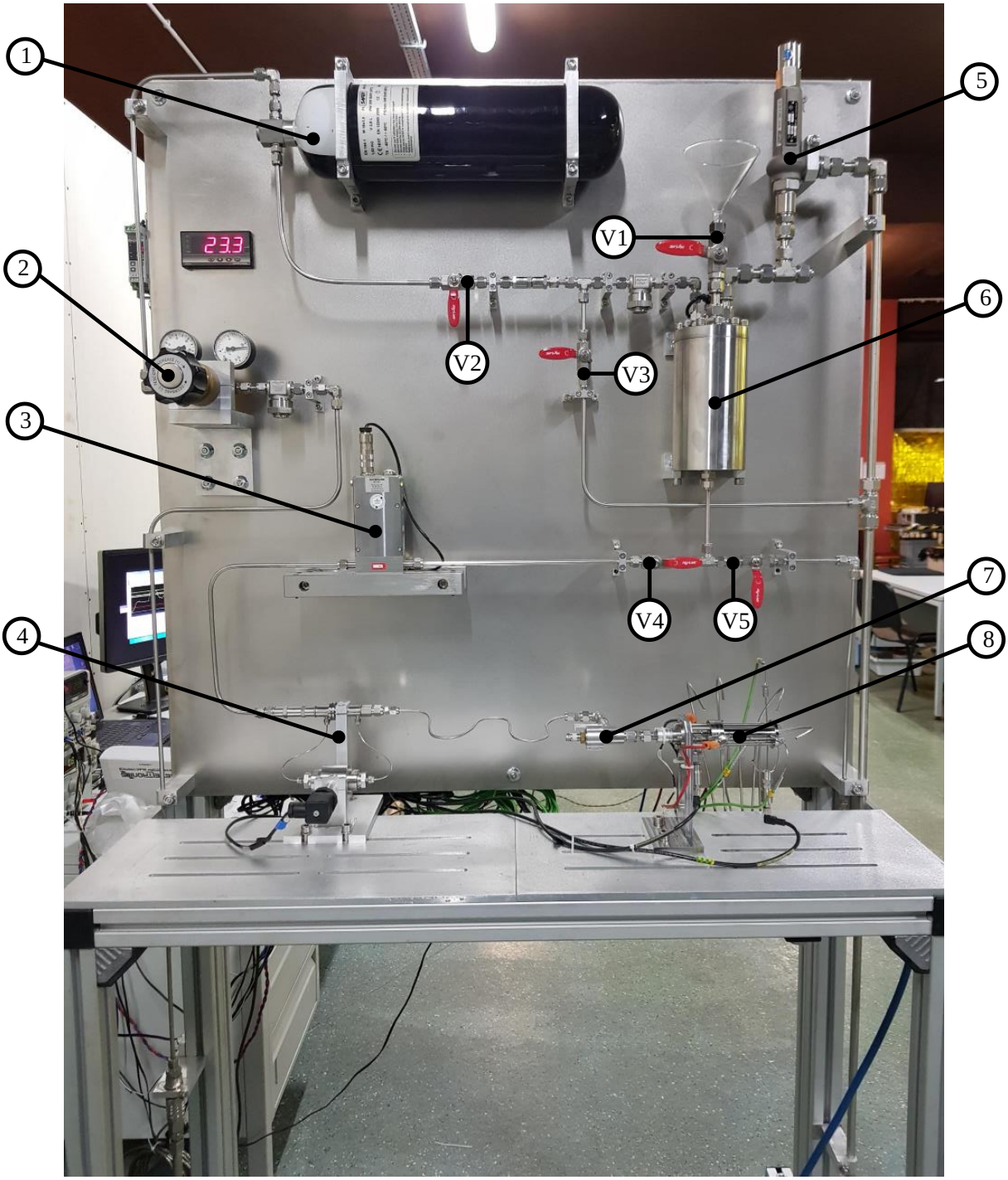

Figure 3.2 Test rig used during the research, undergoing final testing in the assembly room. 1 – buffer tank, 2 – pressure reducing regulator, 3 – Coriolis mass flow meter, 4 – orifice plate flow meter, 5 – safety valve, 6 – propellant tank, 7 – variable area restrictor, 8 – thruster.

Five pressure measurement ports were introduced, namely: in the HTP tank (P_{tank}), upstream of the flow restrictor (*P1*), upstream of the injector (*P2*) and two measurement ports in the chamber – one in the injector plane (*P3*) and the second one at the nozzle entry section (*P4*).

A dedicated orifice plate flow meter was developed for measurements during pulsed mode operation. In the presented research, only steady-state runs were of concern; therefore, the slow response during mass flow measurement was not a significant issue, and because of greater accuracy, the Coriolis mass flow meter was selected as a primary measurement unit.

3.2 Test procedure

Figure 3.3 presents the test procedure that was implemented during the test campaign; this includes the manual valve opening sequences and additional activities that were carried out. As the maximum volume of the propellant in the tank was limited to 70 ml, the tank was usually filled with an additional amount of HTP before each test. The temperature of the thruster prior to each experiment was, for most cases, the same and was close to room temperature; as the chamber was thermally insulated (details will be given in the following subsections), the temperature decay after tests was unacceptably slow, and to accelerate the post-test temperature decay, a cooling system was implemented. The system comprised eight 1/8'', fixed, stainless steel tubes, each pointing at different part of the thruster. The tubes were connected to the pressurized air reservoir by means of a manifold and a solenoid valve. The airflow was activated ~ 2 minutes after the test, and the cooling process usually lasted about fifteen minutes until the centrally located thermocouple in the thruster chamber (thruster description will be provided later) indicated a temperature of 25°C. The thermal insulation was not removed between tests in order not to change the test conditions. The procedure presented in the flowchart does not include experiments carried out without the cooling of the chamber after the preceding test; as the number of such experiments was low, it was omitted in order not to complicate Figure 3.3. As was presented in Figure 3.3, at the end of each test day, the lines were washed with water and purged with nitrogen. The next day, when the research was continued, the first test that was carried out aimed to fill and wash the lines with HTP, therefore remove remaining water and gas to minimize their negative influence on the results. The aforementioned experiment was usually 5s long, and the results were not analyzed. The lines were depressurized shortly after experiments and pressurised before tests. Experiments were executed remotely from a dedicated room.

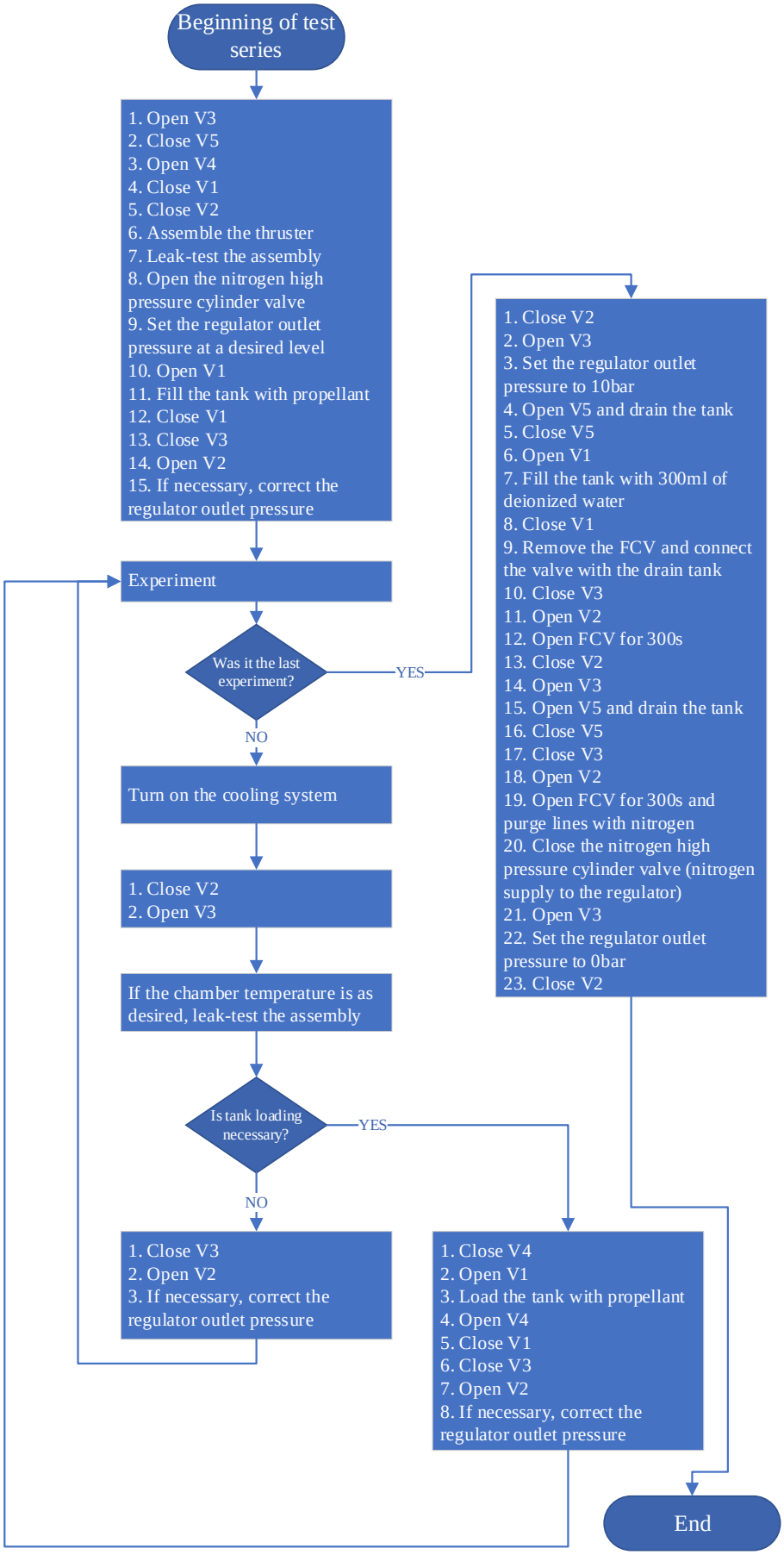

Figure 3.3 Simplified test procedure applied during each test day

3.3 Thruster design

Figure 3.4 depicts cross-sectional views of the assembled thruster used during research. The decomposition chamber was 40 mm long, and the internal diameter and wall thickness were 15 and 2 mm, respectively. In order to integrate the heater with the chamber, the decomposition chamber was divided into two parts; the first incorporated the flange used for integration with the injection system, and the second one contained a nozzle. In order to make the connection between two sections of the decomposition chamber leak-tight, a 0.3 mm-thick mica seal was used. This seal type proved to be reliable and allowed multiple runs without any degradation, even though the seal was directly exposed to the chamber environment. There was no divergent section in the nozzle, as it was assumed that in this campaign, the thrust would not be measured; therefore, the only function of the nozzle was to maintain chamber pressure at a desired level. The temperature of decomposition products was measured at three points in the nozzle entry plane. The first thermocouple was placed centrally – measuring junction was located in the axis of the chamber (*T2*), the second one between the internal chamber wall and the axis (7.5 mm from chamber axis – *T1*) and the third one 1 mm from the internal chamber wall (*T3*). 1/16” (1,59 mm outside diameter, wall thickness of ~0.3 mm) stainless steel tubes were used to connect the pressure transmitters and thermocouples with the chamber; the diameter of tubes was minimized to limit the influence of measurement ports on the results.

The chamber integration process was carried out according to the following procedure:

1. The heater was first integrated with the injector-side chamber section; the heating cable was swaged using dedicated fittings.
2. Next, the excess heating cable was cut, and the heater's cold ends were prepared. The connections between cold junctions and the heating cable conductor were insulated using high-temperature ceramic adhesive.
3. The pressure transmitter and thermocouples were integrated with the nozzle part of the chamber in the following step; lengths of chamber-extending parts of thermocouples were adjusted carefully.
4. Finally, both sections of the decomposition chamber were assembled; the mica seal was placed between sections of the reactor, and both components were torqued in place.
5. Next, leak tightness of the assembly was tested, an external thermocouple was attached to the wall, and the chamber was insulated. In the final step, the leak tightness of the assembly was tested once again.

In order to limit heat loss, the chamber was insulated with ~15 mm layer of ceramic fibre-based insulating material (max. working temperature of 1260°C).

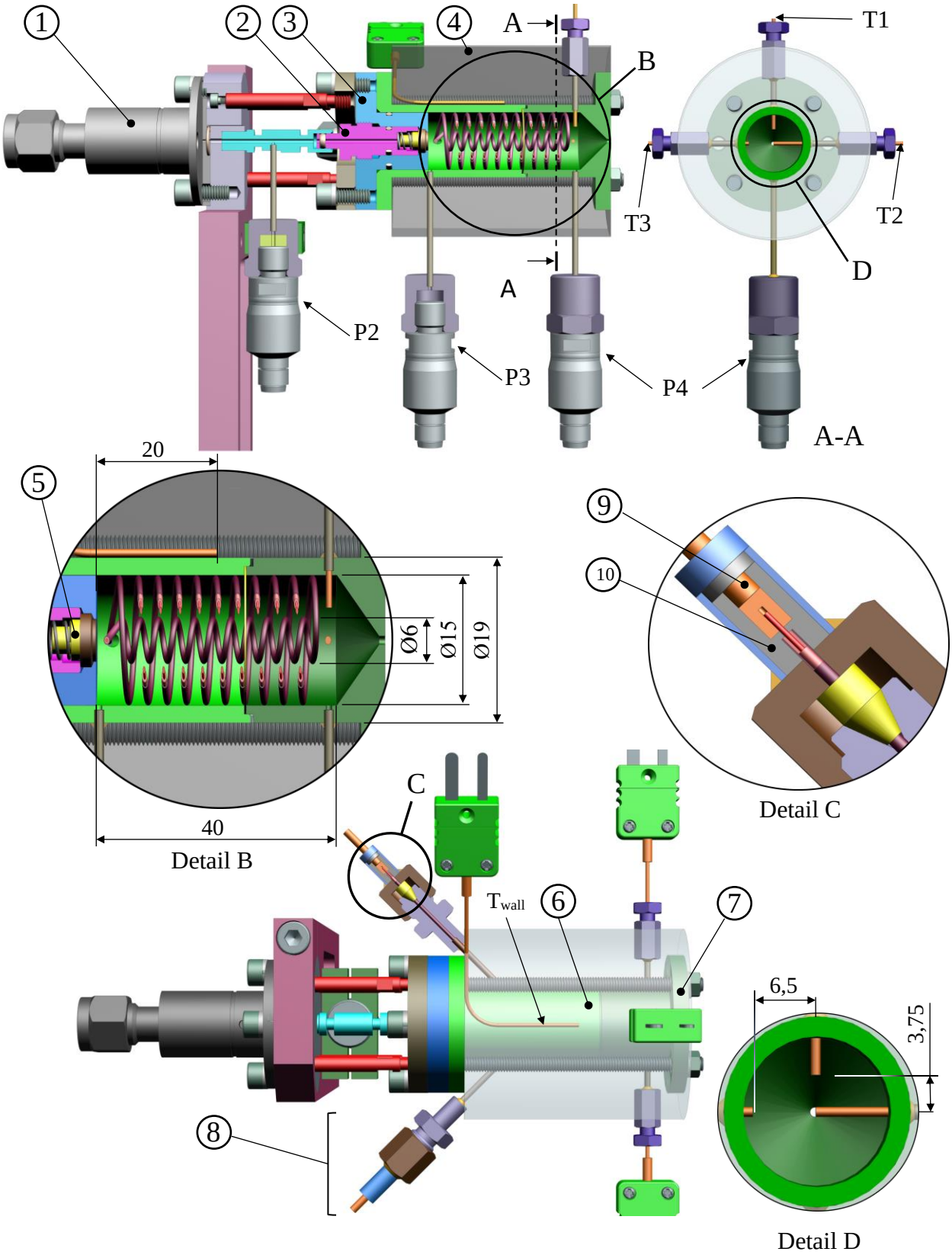

Figure 3.4 Cross-sectional view of the thruster assembly. 1 – Flow control valve (FCV), 2 – Injector pressing screw, 3 – Injector housing, 4 – Insulating material, 5 – Injector, 6 – Decomposition chamber, 7 – Decomposition chamber with nozzle section, 8 – Modified swaged fitting; 9 – Cold junction (copper); 10 – Electric insulation and mechanical support of the junction (ceramic adhesive); T1, T2, T3, T_{wall} – thermocouples, P1, P2, P3, P4 – pressure transmitters.

After the insulation was placed on the chamber, to minimize the insulating material's degradation due to the impact of the air from the chamber cooling system, the insulating material was covered with a 0,3 mm thick, formed aluminium sheet.
The hot part of the thruster was separated from the valve by applying four stainless steel pins, each with a diameter of 4 mm and a total length of 35 mm. The pins were internally threaded on the valve side, and an external M4 thread was applied on the hot part. Such a design allowed accurate adjustment of the distance between the valve and the chamber, which was particularly useful to correctly set the distance between the pressing screw and the drilled pin delivering propellant to the chamber, as this connection compensated thermal expansion. The philosophy during the design was to allow easy and fast reconfiguration, if necessary.

A High-speed, high-pressure, commercially available, electromagnetic valve was used as the FCV. The declared response time of the valve was less than 2 ms, the operating pressure was up to 86.2 bar, and the orifice diameter used was 0.79 mm.

3.4 Injection system

A commercially available Delavan precision oil burner nozzle was selected for application. The complete nozzle delivered by the manufacturer was disassembled, and only selected parts were used, denoted here as a swirler and orifice, and presented in Figure 3.5

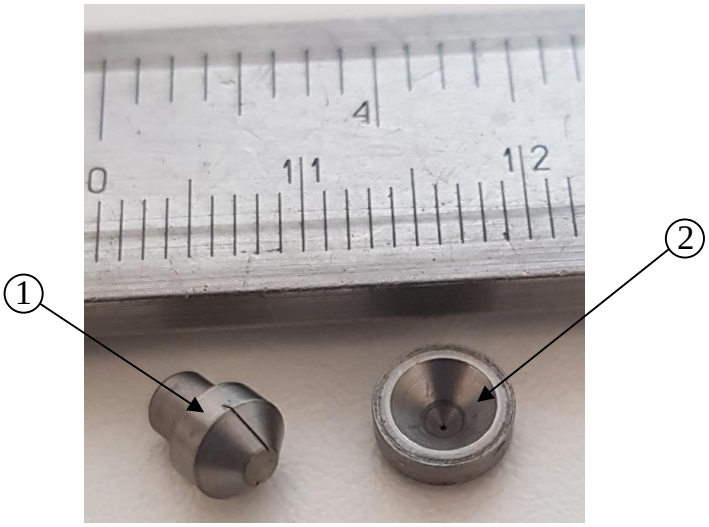

Figure 3.5 Swirler (1) and orifice (2) implemented in the injection system

Different, commercially available nozzles were considered and tested, each delivering a full 60° cone spray. The tests performed prior to nozzle manufacturer selection mostly included HTP compatibility experiments.

Dedicated housing for the nozzle and swirler was designed to allow for application in the test thruster. Two different injector housing concepts were considered. Both can be seen in Figure 3.6.

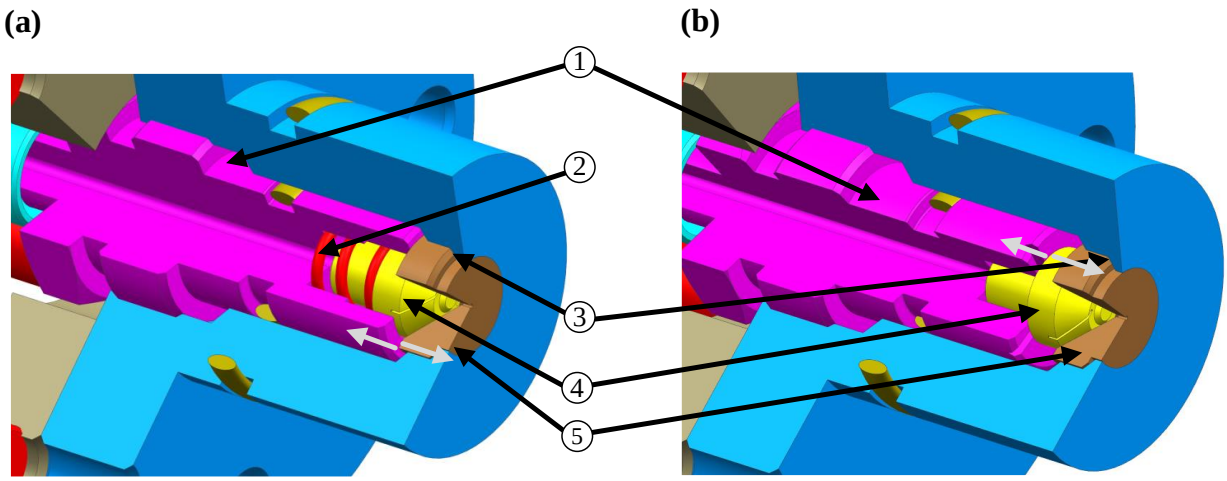

Figure 3.6 Two injection system configurations considered **(a)** spring-loaded version, denoted as SL, **(b)** screw loaded concept, PL. 1 – pressing screw, 2 – spring, 3 – metal-metal connection, 4 – swirler, 5 – orifice. White arrows indicate the surfaces that transfer the force.

In the spring-loaded configuration of the injection system, the pressing screw delivered a force high enough to make the conical, metal-metal connection between the orifice and the injector body leak-tight. As shown in Figure 3.6 (a), the swirler was pressed to the orifice by a spring – such a solution guaranteed constant pressing force after each injector assembling process. The second concept considered, the so-called screw-loaded version, did not employ a spring; instead, the swirler was directly pressed by the pressing screw. In that case, the possible influence of the chamber pressure on the contact between the swirled and the orifice was eliminated, but on the other hand, the dribble volume was higher – and as a result, the response time would be extended. Additionally, the torque applied to the pressing screw could not be controlled accurately; therefore, there was a risk that the pressing force applied to the swirler (and orifice) could have a more significant influence on the spray quality than in the previously presented design.

During injector selection, a range of nozzle sizes were cold-flow tested using HTP. Figure 3.7 presents the results that were obtained. Only pressure drop was measured, so a decision was made to select the nozzle with a size of 0.5. The prefix SL and PL in Figure 3.7 corresponds to spring-loaded (SL) and screw-loaded (PL). As can be seen, the pressure drop test indicated that the injector configuration had no influence on the pressure drop obtained. The spring-loaded configuration was selected as a baseline solution during the campaign.

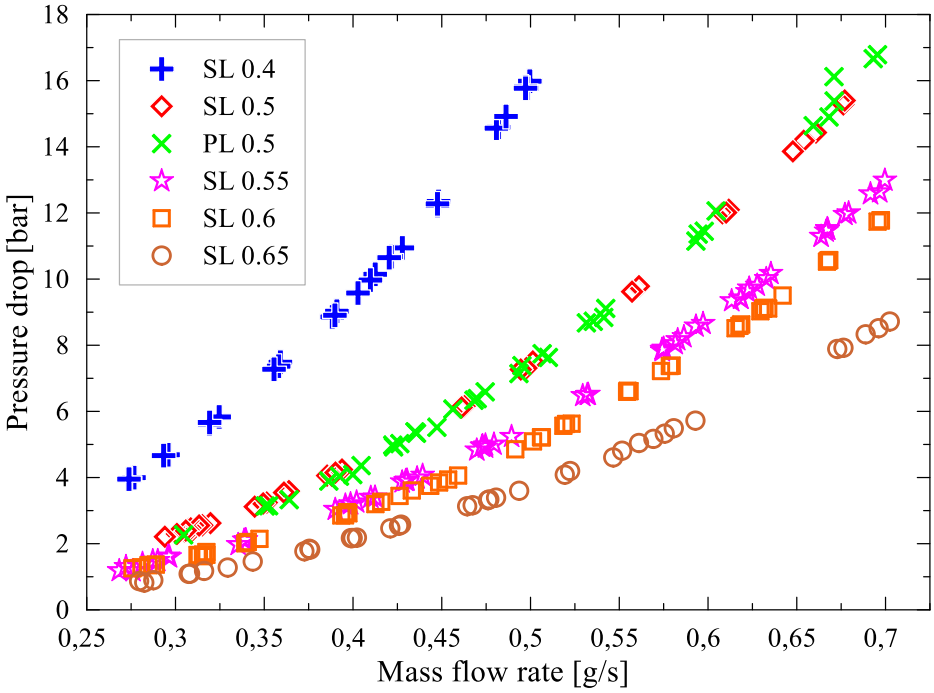

Figure 3.7 Pressure drop as a function of mass flow rate for a range of injector sizes. Tests were performed using 98% HTP.

The water test of the injection system can be viewed in Figure 3.8. The tightness of the connection between the orifice and the injector housing was visually inspected before and after the test campaign – during a high mass flow rate water test.

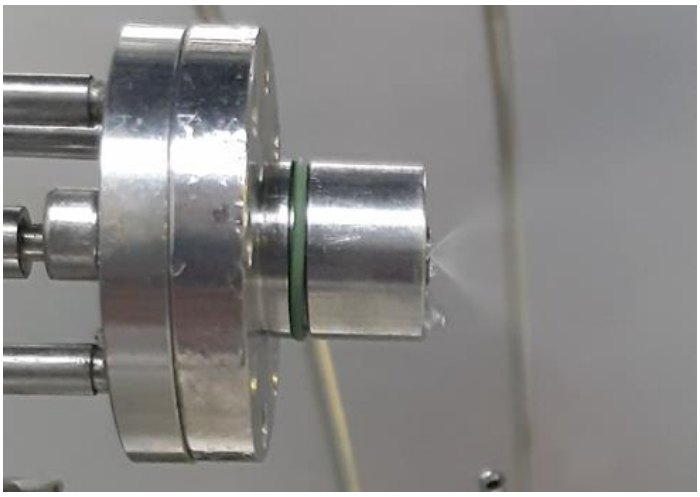

Figure 3.8 Water test of the injection system

3.5 Heater design

The heater was placed directly inside the decomposition chamber, therefore, the propellant was allowed to contact the heater. The evident disadvantages of such a solution are:

- Direct exposure of the heater to the highly oxidizing environment.

- Difficulty with the final integration (placing the heater in the chamber) and sealing the connection between wires and the chamber. This process required many attempts, and dedicated support equipment had to be made to facilitate the process and allow for repeatability.

The heater was made from an insulated heating cable with an external diameter of 1 mm. The cable consisted of a heating conductor (NiCr, 80/20, diameter of 0,39 mm), MgO powder as an insulator and Inconel 600 sheath (with a wall thickness of 0,1 mm). The resistance of the heating conductor, as provided by the supplier (S-Products), was 9 Ω/m at 20°C. The heating cable manufacturer did not deliver any data concerning temperature characteristics; therefore, the OMEGA™ company's data obtained for a straight, horizontal heating wire was used. The values were interpolated for a range of temperatures and for the conductor diameter as used in the research. The resulting current-temperature characteristics can be viewed in Figure 3.9 (a).

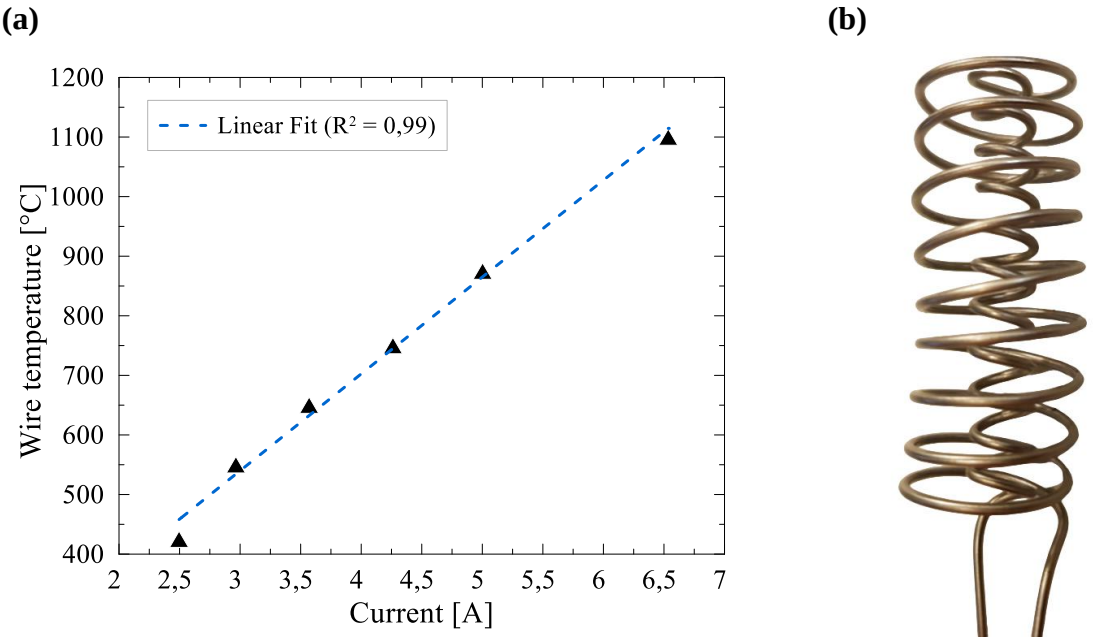

Figure 3.9 **(a)** Current–temperature characteristics of the heating wire used during the test campaign; **(b)** view of the heater after the forming process.

This rough estimation was used to define the operating parameters of the power supply during high-power testing.

The overall heating cable length implemented in the thruster was ~0.8 m, which yielded a total initial estimated room temperature resistance of ~7 Ω. The implemented heater comprised two coils – external, tightly fitting the chamber and internal, with an outside diameter of 6mm. The heater was made from a single cable.

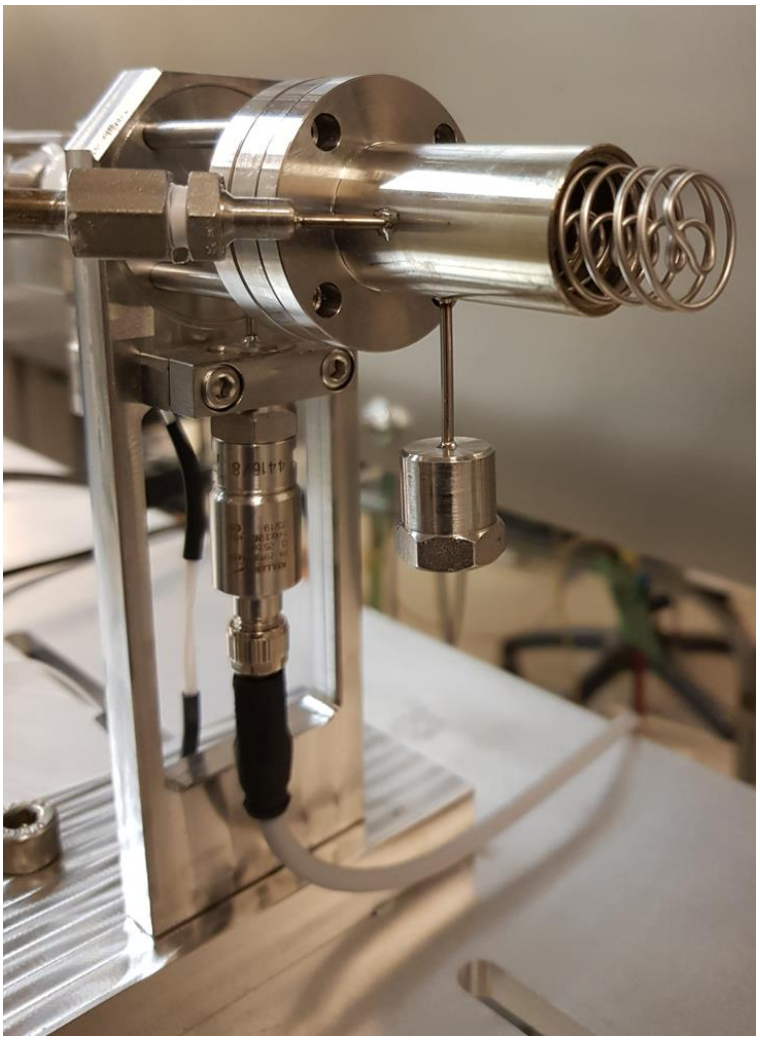

Figure 3.10 The decomposition chamber integrated with the heater before the final assembly process.

Figure 3.10 presents the heater assembled with the chamber prior to the nozzle section installation.

3.6 Additional support equipment

3.6.1 Heater preparation tooling

Each heater used was prepared in-house. Many integration tests were performed before the final assembling and heating wire sealing technique was established. In order to obtain acceptable repeatability, a dedicated tooling used for heater preparation was designed and manufactured. The CAD model of the tooling and the winded heater can be viewed in Figure 3.11 (a) and (b). As can be seen in Figure 3.11 (a) and (b), the tooling was equipped with dedicated grooves to hold the wire at a desired distance. The final configuration of the heater prepared using the discussed tooling can be viewed in Figure 3.9 (b) and Figure 3.10.

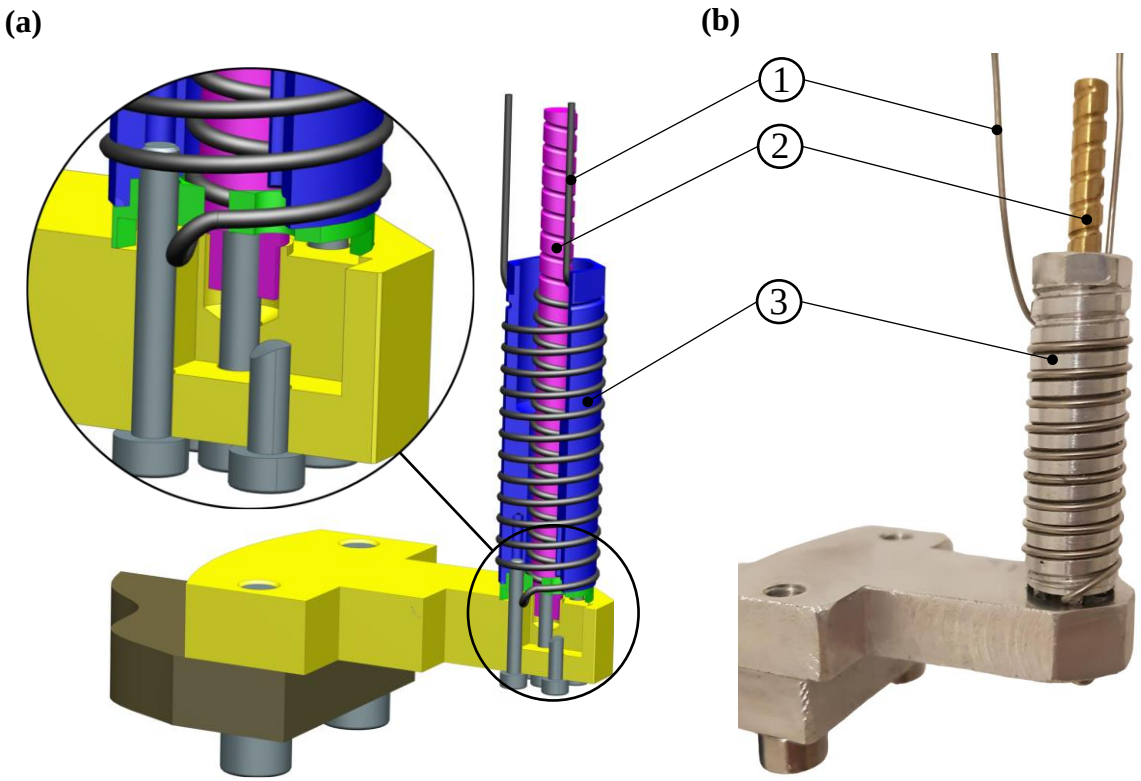

Figure 3.11 Support equipment used to prepare heaters used in the test campaign: **(a)** CAD model, **(b)** winded heater before removing from the tooling. Marked elements: (1) – Heating cable; (2) – Internal coil forming pin; (3) – External coil forming pin

3.6.2 Leak-testing equipment

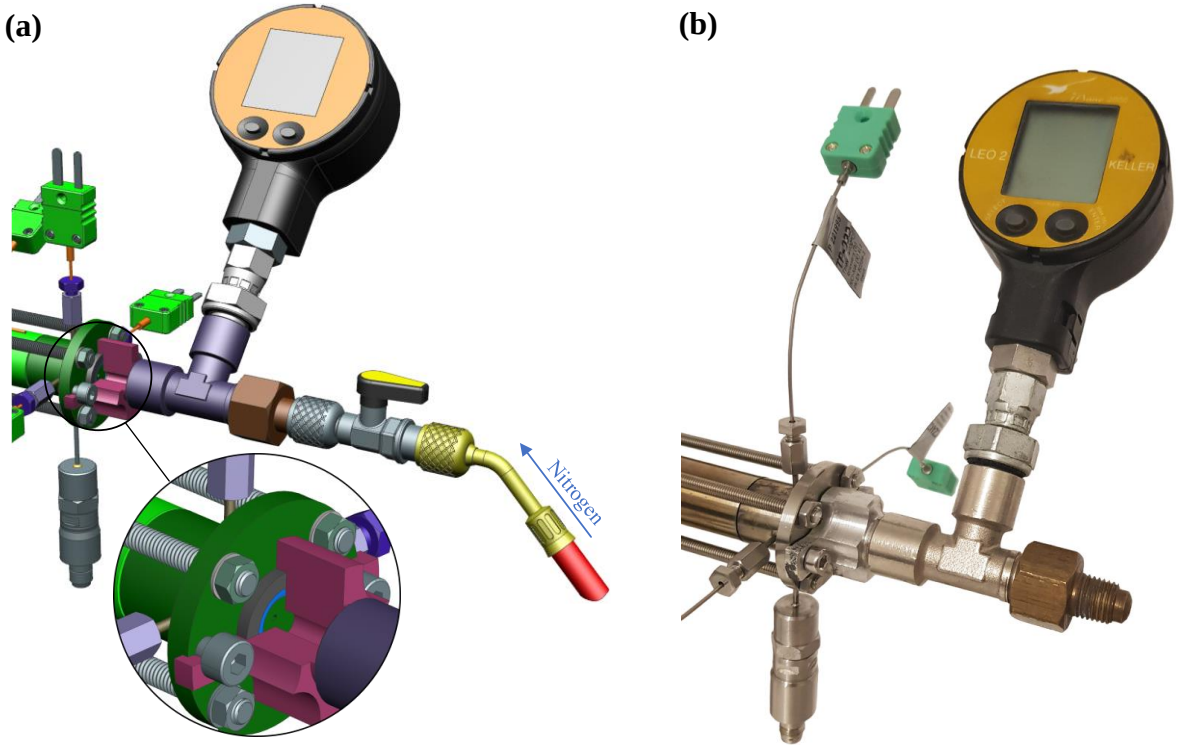

Figure 3.12 **(a)** - CAD model of the leak testing tool, **(b)** the tool assembled with the thruster

Before each test, a specially designed device was attached to the nozzle section, and the chamber was pressurized with nitrogen through the nozzle to investigate if the connections were tight enough and if there would be no pressure loss during the experiment. The aforementioned device was equipped with a digital manometer. The chamber was pressurized to 7 bar; next, the valve delivering nitrogen to the chamber was closed, and a pressure drop was observed. The chamber was considered leak-tight if the pressure drop indicated by the manometer during a 30-second test was within the measurement error of the manometer. The device used for leak testing can be seen in Figure 3.12 (a) and (b).

As was mentioned, a leak test was performed prior to each experiment, as the relatively low wall thickness of the chamber and numerous sealing points were of concern. Experience showed that correctly assembled and carefully sealed thruster did not tend to lose its preliminary tightness.

3.6.3 Data acquisition system

As was partially mentioned in previous sections, the quantities measured were: pressure, temperature, mass flow rate, current and voltage.

Commercially available miniature pressure transmitters, Keller 21PY, were used for pressure measurement. Three different measuring ranges were used: 0-100 bar (P_{tank}), 0-40 bar (*P1*) and 0-25 bar (*P2*, *P3*, and *P4*), with reference pressure at 1 bar. The total measurement error of transmitters was ±0.7% of full scale (FS) for the temperature range of -10 to 80°C. The maximum operating temperature for the selected transmitter type was 100°C.

Regarding *P3* and *P4* (pressure measurement in the chamber), the temperature of the sensors was not measured; however, the relatively significant distance between the external wall of the thruster and the sensor (~33 mm) together with a small outside diameter (1,59 mm) and a wall thickness of ~0,3 mm of the connecting tube lead to the assumption, that the temperature of 80°C was not exceeded. Therefore, for these sensors, a total error was assumed to be 0.7% FS. Each pressure sensor was made from AISI 316L stainless steel, and the sensor design included a Viton seal. The difference between *P3* and *P4* readings was always within the measurement error; therefore, only *P4* was used for analysis.

The rig was equipped with a digital tank pressure indicator to set the regulator outlet pressure accurately before initiating the experiment.

As for the temperature measurement, K-type, ø1 mm, shielded, ungrounded thermocouples were used. As mentioned previously, the thermocouples were placed in the chamber through 1/16” stainless steel tubing. A PTFE insert was used to seal the connection between the connector (which was welded at the end of the tube) and the thermocouple. The insert was compressed until the required tightness was obtained. A quad-channel thermocouple amplifier with built-in cold junction compensation was used to convert the K-type thermocouple signal into a 0-5 V linear output. The total measurement error for each thermocouple was 1,5°C for the temperature range of up to 375°C and 0,4% of the measured value for the temperature in the range of 376 to 1000°C.

In order to estimate the power of the heater, current measurement was carried out using a Hall effect-based linear current sensor. Voltage measurement was carried out using a voltage divider and Toshiba TLP7920 amplifier.

Bronkhorst M14, Coriolis type mass flow meter was used during the test campaign. The biggest drawback of this unit is the response time. During most of the tests that were carried out, that negative feature was not a significant problem, as relatively long runs were of concern, but short pulse operation would not be an option using this device. Regarding advantages, the meter features relatively high accuracy, which depends on the measured value, and the total measurement error can be as low as 0.2% of reading for liquid compounds. As for the conditions during research, the error was up to ~0.8% of the measured value, as the mass flow rate was close to the minimum flow rate acceptable. Additionally, the meter can be used for gases and liquids at a pressure of up to 200 bar, and the only material in contact with the compound is AISI 316L stainless steel.

National Instruments USB-6259, PC-based, multifunctional input/output device, was used for measurement. The device allowed up to sixteen analogue input channels and was used to generate analogue 5 V control signals supplied to the solid state relays responsible for switching the flow control valve and the heater.

The sampling rate for each channel was 2 kHz. This value was lowered to 100 Hz during the long-lasting (30 min) preheating phase, where a high sampling rate was not necessary as large source files would have been generated.

A dedicated software prepared in the Institute of Heat Engineering was used to operate the test facility and acquire the data.

Table 3.1 lists all of the significant instrumentation used during the test campaign.

Table 3.1 List of most significant measurement equipment used during research

Element	Manufacturer/model	Measuring range	Measurement accuracy
Pressure transmitter	Keller Series 21PY	0-100bar (P_{tank}) 0-40bar (*P1*) 0-25bar (*P2*, *P3*, *P4*)	±0.7%FS
Coriolis MFM	Bronkhorst mini CORI-FLOW M14	Up to 8.33g/s	0.6g/s: ± 0.48%* 0.5g/s: ± 0.53%* 0.4g/s: ± 0.62%* 0.3g/s: ± 0.76%* * of measured value
K-type thermocouple	Czaki TP-202K-1b-100-1	Max. 1000°C	1,5°C (T = -40 to 375°C) 0,4% of reading (T = 376 to 1000°C)

Chapter 4

Results and discussion

4.1 High-power campaign

4.1.1 Methodology and evaluation criteria

In order to present the philosophy that was implemented during the high-power campaign, a simplified schematic overview of the test run was prepared and can be viewed in Figure 4.1. The schematic illustrates the traces of chamber pressure, temperature, and control signals corresponding to FCV and heater.

The decomposition chamber was preheated before opening the flow control valve. During each experiment, the heating was initiated 0,1 s after the data acquisition system was activated. The duration of the preheating phase was a variable that was changed between experiments and ranged from 6 to 34 seconds.

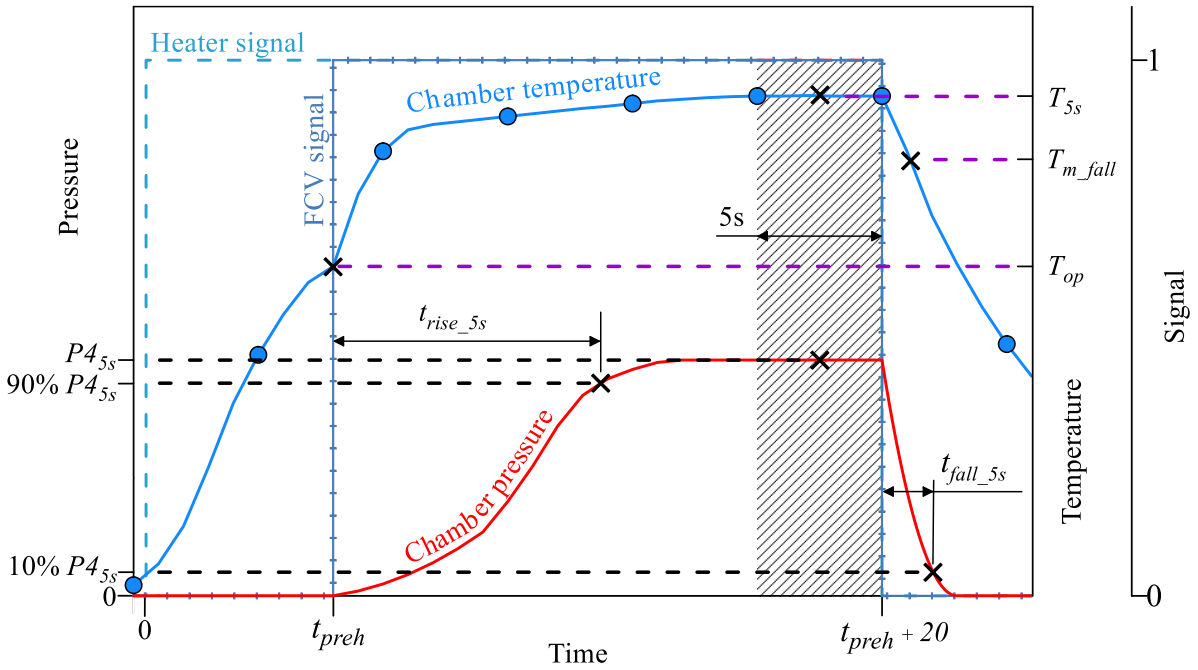

Figure 4.1 Schematic representation of a high-power experiment. t_{preh} – preheating duration; t_{rise_5s} – pressure rise time; t_{fall_5s} – pressure fall time; T_{m_fall} – mean temperature in the t_{fall_5s} period; T_{op} – temperature captured directly before opening the FCV; hatched area – reference interval, used to calculate pressure roughness, mean temperatures (T_{5s}) and chamber pressure ($P4_{5s}$).

The preheating sequence was denoted in Figure 4.1 as t_{preh}. After the preheating phase, the flow control valve was commended to open, and the flow of the propellant was started. The valve remained open for 20 seconds during each experiment executed in this sub-campaign. Apart from the test denoted as Z1210, the heater was deactivated, and the valve was closed at the exact moment; therefore, during experiments (except test Z1210), the heater was active for t_{preh} + 20 s. The data was additionally registered from 8 to 10 seconds after closing FCV.

The preheating sequences were carried out at different heater powers; this quantity was changed between experiments by switching the voltage delivered by the laboratory power supply connected to the heater. Three different voltages were tested: 40, 45 and 50 V and this parameter was used as an identifier for comparison purposes. At least two experiments were performed for each voltage and preheating time.

As stated, the heater was active during propellant flow, moreover, voltage settings remained unchanged during the preheating phase and the propellant injection sequence. Tests were initiated at room temperature (with two exceptions to be discussed later).

Two minutes after the experiment was conducted, a dedicated cooling system was activated; this cooling sequence aimed to reduce the time necessary for the test article to lower its temperature to room conditions, as described in subsection 3.2. Between experiments, only the leak-tightness of the laboratory thruster was checked (using the equipment described in subsection 3.6.2). The internal and external configuration of the thruster remained intact between experiments to minimize the influence of any modifications on the test results; therefore, the entire test campaign concerning high-power experiments and 70s-long low-power tests was conducted using the same, unmodified apparatus. Some minor modifications concerning 120s low-power tests were implemented, which included upgraded insulation and modified software; however, details will be presented in a dedicated section.

Table 4.1 summarizes basic information concerning all tests performed within the framework of the experimental campaign discussed in this section. Altogether, fifty-six high-power tests were carried out. Table 4.1 gathers data such as experiment identifiers (*ID*), supply voltage (U_{supp}), preheating time (t_{preh}), two heater power values, which cover the preheating phase and the period when propellant was delivered to the chamber (P_{preh} and P_{run}, respectively) and selected mean values measured during the last five seconds prior to FCV closing: mass flow rate ($\dot{m}_{5s}$), chamber pressure ($P4_{5s}$), wall temperature (T_{wall_5s}) and temperature in the axis of the decomposition chamber (nozzle entrance section, $T2_{5s}$).

Table 4.1 Set of experiments conducted during the high-power test campaign.

No.	ID	U_{sup} [V]	t_{preh} [s]	P_{preh} [W]	P_{run} [W]	$\dot{m}_{5s}$ [g/s]	$P4_{5s}$ [bar]	T_{wall_5s} [◦C]	$T2_{5s}$ [°C]
1	Z1149	40	6	205,6	196,0	0,427	4,21	166	864
2	Z1150	40	6	204,3	196,6	0,405	4,72	180	900
3	Z1151	40	6	204,3	196,1	0,400	4,68	186	921
4	Z1152	40	8	201,6	193,6	0,370	5,62	188	922
5	Z1153	40	8	205,1	194,4	0,361	5,23	184	927
6	Z1154	40	8	203,7	193,4	0,361	5,18	195	922
7	Z1155	40	10	205,5	193,8	0,355	3,80	200	954
8	Z1156	40	10	203,8	192,1	0,352	4,97	197	950
9	Z1157	40	10	199,7	190,6	0,332	4,54	212	943
10	Z1158	40	12	203,6	191,1	0,352	3,92	216	953
11	Z1159	40	12	203,3	191,7	0,353	4,47	215	946
12	Z1160	40	12	202,9	190,2	0,366	4,67	216	947
13	Z1161	40	14	202,8	189,8	0,370	4,61	223	946
14	Z1162	40	14	202,4	173,5	0,357	4,23	226	939
15	Z1163	40	14	201,2	188,3	0,341	4,36	219	949
16	Z1164	40	16	200,9	188,1	0,365	4,22	229	947
17	Z1165	40	16	195,6	185,7	0,354	3,90	275	934
18	Z1166	40	16	200,3	187,3	0,365	4,18	283	945
19	Z1167	40	18	194,5	185,6	0,361	3,84	285	941
20	Z1194	40	18	195,6	180,3	0,354	3,61	299	931
21	Z1195	40	18	198,7	185,0	0,339	3,82	300	930
22	Z1168	40	20	194,5	185,1	0,365	3,92	293	945
23	Z1169	40	20	194,9	184,8	0,350	3,84	291	942
32*	Z1170*	40	20	188,2	181,1	0,348	3,61	450	958
24	Z1196	40	22	193,8	178,8	0,351	3,68	331	920
25	Z1197	40	22	195,7	174,2	0,351	3,63	330	919
26	Z1198	40	26	194,9	183,3	0,356	3,71	355	925
27	Z1199	40	26	192,4	183,0	0,344	3,50	356	923
28	Z1200	40	30	191,6	182,7	0,341	3,61	380	915
29	Z1201	40	30	192,4	182,6	0,339	3,60	380	912
30	Z1202	40	34	191,9	182,8	0,339	3,61	400	923
31	Z1203	40	34	191,1	182,4	0,333	3,55	399	920
33	Z1177	45	6	254,5	240,8	0,327	5,91	187	916
34	Z1178	45	6	257,2	240,2	0,318	4,40	192	931
35	Z1179	45	10	256,2	238,0	0,328	3,56	245	943
36	Z1180	45	10	256,6	237,4	0,308	3,34	244	949
37	Z1181	45	14	246,5	234,0	0,316	3,29	303	959
38	Z1182	45	14	248,9	232,4	0,328	3,65	323	944
39	Z1183	45	18	247,8	232,4	0,321	3,34	351	937
40	Z1204	45	18	242,3	229,6	0,341	3,69	363	933
41	Z1205	45	18	242,1	229,9	0,333	3,67	365	930
42	Z1206	45	22	241,1	229,6	0,333	3,57	396	942
43	Z1207	45	22	241,7	229,5	0,330	3,60	393	943
44	Z1208	45	24	241,1	228,9	0,322	3,47	408	947
45	Z1209	45	24	239,7	228,8	0,331	3,60	408	945
46*	Z1210*	45	24	234,3	226,7	0,323	3,49	544	996
47	Z1184	50	6	310,4	288,7	0,301	3,27	276	961
48	Z1185	50	6	320,9	295,3	0,369	4,01	264	983
49	Z1186	50	10	312,2	287,5	0,363	4,05	350	985
50	Z1187	50	10	303,0	285,8	0,362	4,04	343	986
51	Z1188	50	14	298,6	283,3	0,359	4,01	380	997
52	Z1189	50	14	298,5	283,0	0,336	3,59	378	967
53	Z1190	50	18	298,3	281,5	0,344	3,74	421	999
54	Z1191	50	18	294,9	281,3	0,346	3,75	423	1003
55	Z1192	50	22	293,1	280,6	0,350	3,85	456	1010
56	Z1193	50	22	293,0	280,5	0,349	3,81	453	1003
*Experiment conducted directly after the preceding test, without the cooling of the chamber									

In order to properly evaluate the results obtained, it was necessary to implement a consistent methodology allowing direct comparison of test trials. The parameters used for analysis were:

a) Temperatures measured at the end of the preheating phase (moment of FCV opening), denoted in the following sections as $T1_{op}$, $T2_{op}$, $T3_{op}$, and T_{wall_op}.

The abovementioned temperature measurements were used during detailed analysis, e.g., to find the relation between temperatures indicated by thermocouples and the pressure rise time. In Figure 4.1, the discussed temperature measurement was marked as T_{op}.

b) Pressure rise time, t_{rise_5s}

In the presented research, pressure rise time was measured from when the FCV was commanded to open to when chamber pressure obtained 90% of the reference value (90% $P4_{5s}$ in Figure 4.1). The rise time is often measured from the moment the pressure in the chamber reaches 5% of the reference pressure, e.g. in [115]. In the presented research, such a methodology was not implemented, as during some experiments, there was no pressure rise for a certain period of time due to low initial chamber and heater temperature and, therefore, inefficient decomposition. In order to include that period of inefficient decomposition during the comparison, it was assumed that the start point for the measurement of t_{rise_5s} would be the moment the control signal was sent to the solid state relay controlling the FCV.

In the discussed research, reference pressure was the mean pressure during the last 5 seconds before FCV closing, denoted as $P4_{5s}$ in Figure 4.1. Such an attitude was applied to minimize the influence of the time when chamber pressure was building up and the decomposition was inefficient. In the considered case, the last 5s were assumed to be a steady state period. This, of course, was not always true; as will be presented in the following sections, in some cases, the decomposition was so inefficient that undecomposed propellant accumulated in the chamber after the run.

c) Pressure fall time, t_{fall_5s}

Pressure fall time, t_{fall_5s}, was measured from when the valve was commanded to close to when the chamber pressure fell to 10% of the mean chamber pressure in the reference period - 10% $P4_{5s}$ in Figure 4.1. In some cases, as will be presented, the fall time was on the order of seconds; therefore, it was decided to relate the decay time to the mean temperatures during the fall time – T_{m_fall} in Figure 4.1. The shorter the pressure decay time, the closer the mean temperatures were to the values captured directly when the valve was closed.

d) Pressure roughness

Pressure roughness was an essential indicator of the stability of the decomposition process. It was calculated as a standard deviation of *P4* in the reference period, divided by $P4_{5s}$. The standard deviation, σ, was obtained using the formula presented in equation 4.1

$$\sigma = \sqrt{\frac{1}{n}\sum_{i=1}^{n}(x_i - \bar{x})^2} \tag{4.1}$$

In equation 4.1, n indicates the number of elements in the considered range, x_i and $\overline{x}$ are, respectively, the value of i^{th} data point and the mean value of the data set. Pressure roughness, denoted as rou, was found using equation 4.2

$$rou = \frac{\sigma}{P4_{5s}} \tag{4.2}$$

The presented attitude is general; for some specific cases, it was necessary to implement dedicated metrics; this is to be discussed in corresponding sections.

4.1.2 Preheating phase

The mean heater power measured during the preheating phase ranged from ~190 W (40 V supply) to ~320 W (50 V). The maximum preheating time for a supply voltage of 40 V, 45 V, and 50 V was 34, 24 and 22 s, respectively. The preheating time was limited for higher voltages to minimize the risk of heater damage. For the same reason, the number of tests conducted at a supply voltage of 45 and 50 V was mainly two.

Figure 4.2 from (a) to (c) presents temperatures measured after preheating sequences by three thermocouples placed in the chamber (nozzle entrance) and one attached to the external wall of the reactor. The exact location of thermocouples can be viewed in Figure 3.4; however, for convenience, simplified schematic views were provided in each figure, displaying the location of measuring junctions. Additionally, for convenience, data points corresponding to the supply voltage of 50, 45 and 40 V were denoted using red, green and magenta symbols. The black colour was used to separate runs for which propellant accumulation in the chamber might have occurred, as will be discussed later, affecting the initial temperatures in the following tests. Moreover, the symbols' shape corresponds to the specific thermocouple.

The preheating phase was thoroughly analyzed, as that part directly impacted the decomposition performance during the propellant injection sequence. As shown in Figure 4.2 (a), the highest temperature in the chamber measured at the end of the preheating phase was 717°C (50 V supply, preheating time of 22 s).

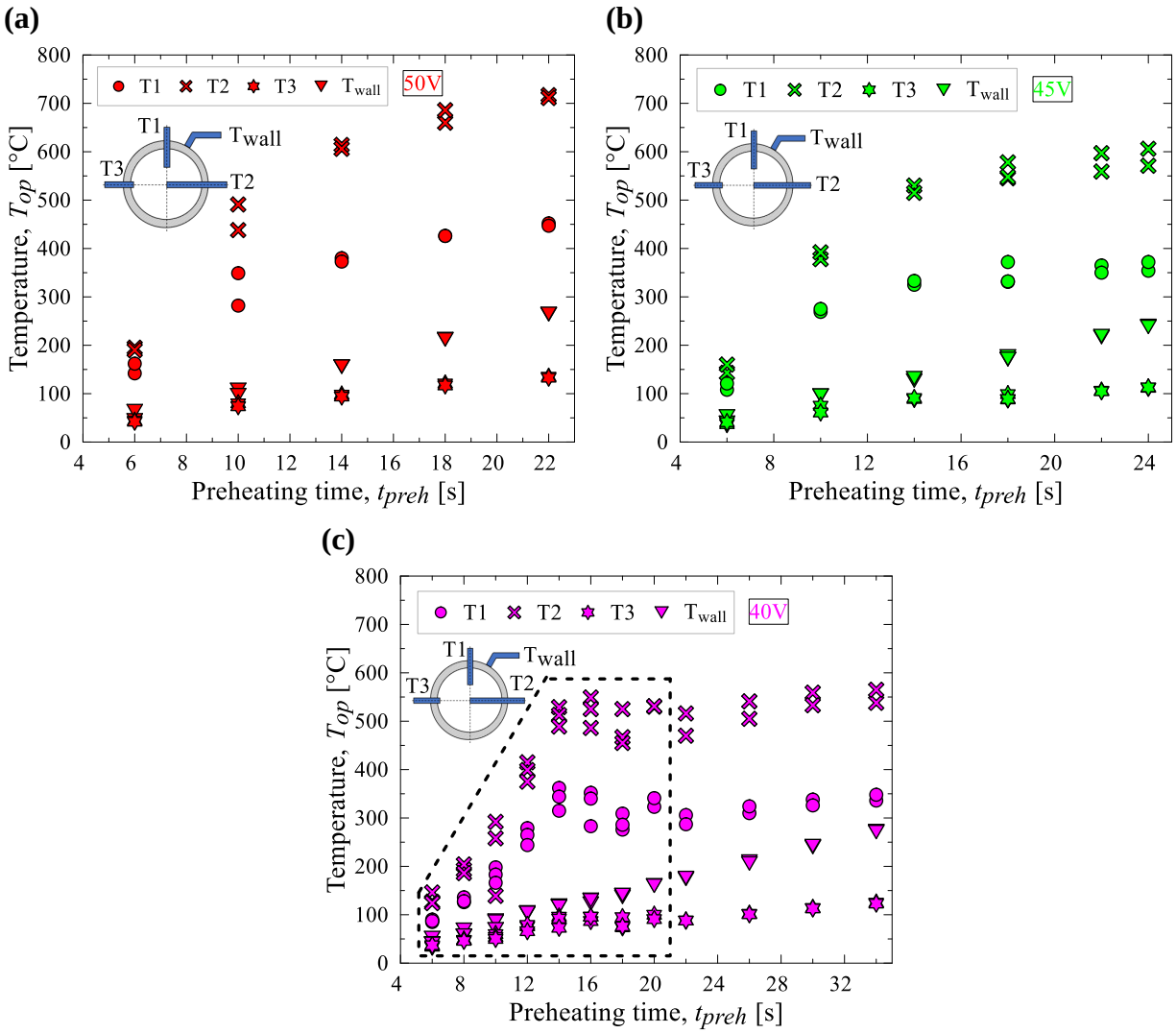

Figure 4.2 Temperatures captured directly before FCV opening, T_{op}, as a function of the preheating duration, t_{preh}. Figures **(a)**, **(b)**, and **(c)** correspond, respectively, to supply voltages of 50, 45 and 40 V.

The trends in which the temperatures captured before FCV opening changed as a function of the preheating time were as expected for supply voltages of 50 and 45 V. In the case of a 40 V supply, unexpectedly high values were registered for tests with preheating durations between six and twenty seconds. As seen in Figure 4.2 (c), of concern were tests corresponding to measurement points enclosed in the trapezoid. For the marked experiments, temperatures $T1_{op}$ and $T2_{op}$, measured in the chamber, rose sharply and nearly linearly to a value exceeding 500°C for $T2_{op}$ and 350°C for $T1_{op}$. Between the preheating time of 14 to 16s, $T1_{op}$ and $T2_{op}$ reached a maximum value in the trapezoidal area; for $T1_{op}$, the temperature after a preheating time of 14

seconds was the highest obtained among all the preheating periods for the considered supply voltage. In order to visualize this phenomenon more clearly, Figure 4.3 (a) was prepared, which shows the relationship between mean values of $T2_{op}$ and T_{wall_op} obtained after a specified preheating period for all voltages tested. It can be noted that the rise of a wall temperature as a result of different preheating times was fitted with linear functions in the considered conditions, while temperature changes for $T2_{op}$ were approximated using logarithmic fit curves. A coefficient of determination (R^2) was provided in each case.

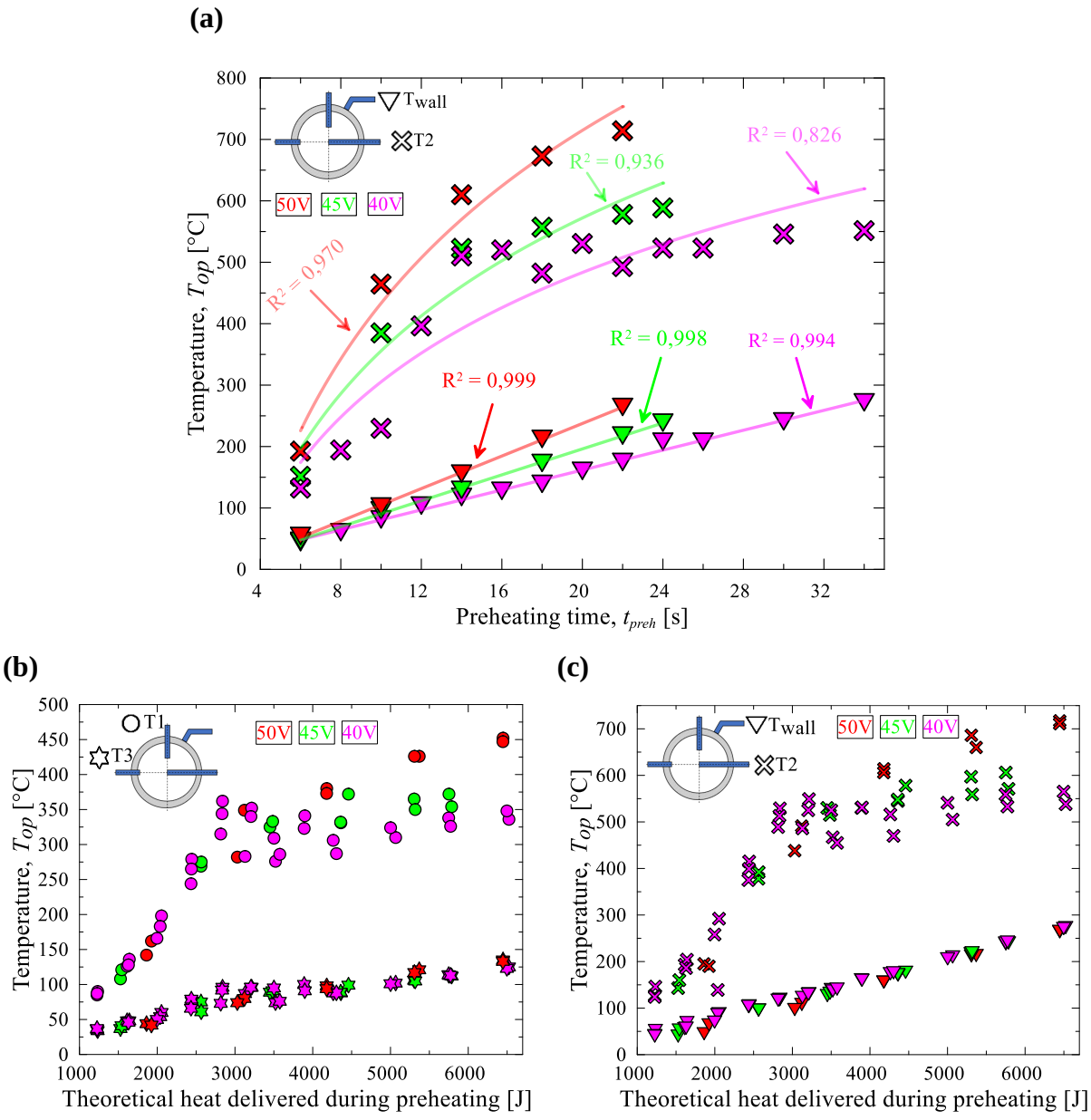

Figure 4.3 **(a)** Averaged temperatures prior to FCV opening; **(b)** theoretical heat delivered by the heater as a function of final temperatures before FCV opening, registered by *T1* and *T3;* and **(c)** *T2* and T_{wall} thermocouples.

For the 40 V case and preheating duration between 12 and 20 seconds, the mean values of temperature $T2_{op}$ significantly exceed the trendline, e.g. for t_{preh} of 14 s the difference

is ~120°C. A similar observation can be made with regard to the case of 45 V supply voltage and preheating duration of 14 s, but the magnitude of the deviation is considerably lower, and the lowest variation was observed for the highest voltage tested. The results mentioned above suggest additional heat input, apart from resistively delivered. The only possible source is hydrogen peroxide itself. The reason for the deviations is poor decomposition efficiency during marked runs. Consequently, undecomposed propellant remained in the chamber and was decomposed during the preheating sequence in the following run before opening the FCV.

The abovementioned observation is interesting, as the lowest wall temperature registered at the moment when the flow control valve was commanded to close (delivery of HTP to the chamber was stopped) was 188°C (U_{sup} = 40 V, t_{preh} = 6 s); in most cases, wall temperature significantly exceeded 200°C, and when t_{preh} was 20 seconds, and voltage was 40 V, the final wall temperature (after the complete experiment) was 300°C. Except for one experiment (the lowest voltage and the shortest preheating time), the *T2* temperature at the end of a run always exceeded 900°C.

The conditions above were insufficient to prevent the presence of residual propellant in the chamber after selected tests; consequently, the undecomposed propellant delivered to the chamber was not fully decomposed and boiled off. The amount of liquid propellant present in the chamber after closing the valve was so significant that eventually, as the temperature of the surrounding components was lowered below a level at which boiling and decomposition at a significant rate could propagate, the compound remained in liquid phase and was decomposed during the subsequent test (during the preheating phase).

Despite many tests, none of the experiments resulted in explosive decomposition that would disintegrate the chamber or damage any of the components used.

Figure 4.3 (b) and (c) was prepared to compare the temperatures obtained after different preheating times with the estimated heat delivered from the heater to the chamber. The heat input through resistance heating was directly calculated as a product of the mean heater power during the preheating phase and duration of the sequence and ranged from ~1,2 to 6,5 kJ; the latter value amounts to the heat released during the decomposition of ~2,5 g of aqueous peroxide. As seen in Figure 4.3 (b) and (c), higher heater power resulted in higher cable temperatures and, consequently, for similar heat inputs, higher temperatures measured by thermocouples with measuring junctions in the direct vicinity of the heater (*T1* and *T2*).

A decision was made to highlight experiments for which the existence of the propellant in the chamber during the preheating phase was evident from the remaining tests. Therefore,

experiments from Z1149 to Z1170 were denoted in figures using black symbols to allow the reader an easy distinction between tests where the remaining propellant was present in the chamber and those where the chamber during the preheating phase was empty, or the propellant amount was insignificant. It must be noted that the change of the initial conditions prior to propellant injection, according to the author, was not a significant issue, as the temperatures were measured at different points, and then varying initial conditions were taken into account during analysis. Of concern was the scenario when the remaining liquid was present in the chamber when the flow of fresh propellant was initiated, as that could lead to accumulation over experiments.

4.1.3 Analysis of the results

Figure 4.4 presents results obtained during the test denoted as Z1184, for which the supply voltage was 50 V, preheating time was 6 seconds, and heater power during propellant injection sequence was ~289 W.

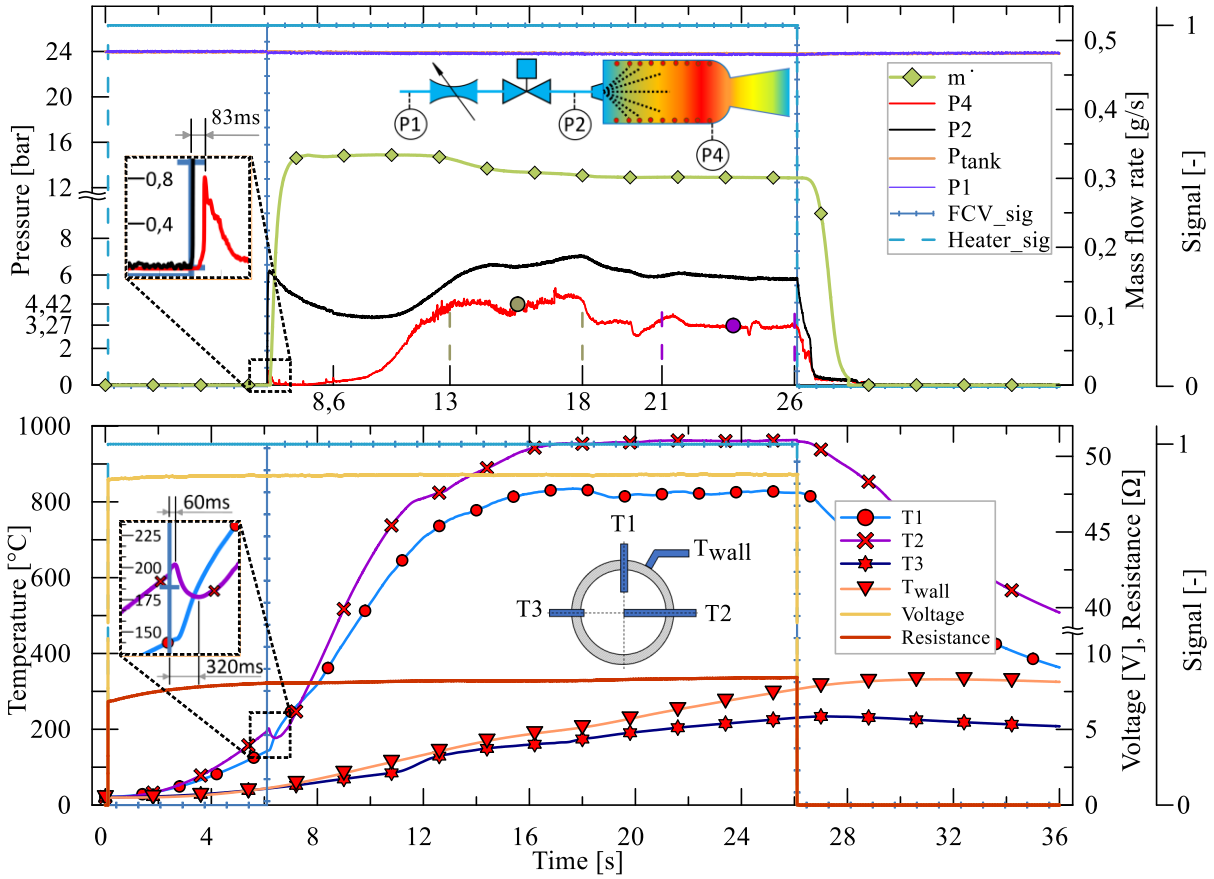

Figure 4.4 High-power experiment number Z1184; supply voltage: 50 V, preheating time: 6 s, mean heater power during the propellant injection sequence: 289 W.

As the resistance of the heating conductor is a function of temperature and rose significantly with time, for clarity, it was decided to separate the mean heater power during the

preheating phase and during the run. The variation of resistance can be easily observed in Figure 4.4, and for the presented test, varied from ~6,85 Ω directly after closing the circuit, through 8,05 Ω prior to FCV opening to 8,4 Ω at the end of the run, before FCV closing. The measured voltage was lower than the set value; the possible reasons were the accuracy of the laboratory power supply used and the voltage drop due to components such as the solid-state relay.

The traces in Figure 4.4 indicate a significant initial propellant accumulation. As can be seen, the chamber pressure (*P4*) rise was close to zero for nearly 2 seconds after the propellant flow was started; this implies that the conditions in the chamber were inadequate to initiate spontaneous decomposition, even though the temperature measured by the centrally located thermocouple ($T2_{op}$) was 195°C. The preheating time was relatively short (6 s), and given the thermal inertia of the shielded thermocouple and the fact that the measuring junction was placed ~5mm from the last heater coil, it is expected that the temperature of the heater was much greater. The temperature of the heating cable was not measured directly, but the measured current at t = 6 s was 8,05 A, which, according to Figure 3.9, yields a conductor temperature of more than 1000°C. Given the short preheating time and the fact that the heating cable comprises powdered MgO as an insulator and Inconel sheath that separates the heating conductor from the environment, it is not expected that the cable operated at such a high temperature after only 6 seconds, but it is clear that it was much higher than 195°C measured by *T2* thermocouple.

Another observation was that the measured value of temperature indicated by thermocouple *T2* fell by about 25°C after the propellant flow was initiated; this can be viewed in the corresponding zoomed area box. The local minimum temperature value was measured 320 ms after generating the valve opening signal. This implies that the undecomposed, relatively cold propellant could travel the distance to the thermocouple (38,5 mm from the injector surface). The condition at which the propellant arrived in the vicinity of the thermocouple is unknown, but direct interaction between propellant leaving the injector and thermocouple *T2* was technically possible, as only the heater was present in the chamber, occupying minimal space (~7% of the total internal volume, including the convergent section of the nozzle), and not separating the injector from the section where the temperature was measured. Chamber pressure (*P4*) and injector inlet pressure (*P2*) traces directly after opening the FCV were also studied in more detail. As seen in the magnified area, injector inlet pressure rose sharply after the command signal was delivered to the solid state relay controlling the FCV. This is in good agreement with the declared performance of the valve, as response time, according to the

manufacturer, is less than two milliseconds. Next, after 83 milliseconds, a small (~0.8 bar) spike was observed in the chamber. The spike is believed to have resulted from contact with surfaces at a temperature that was not high enough to efficiently initiate and sustain the decomposition, which allowed only a portion of the propellant to decompose locally, and next, so-called flooding took place. Flooding refers to a case when liquid propellant exists in the nozzle. In the discussed case, the liquid propellant was present not only in the nozzle but to some extent in the entire chamber. As the propellant was injected into the chamber, increasing the amount of liquid present, the heater continuously operated at a power of ~290 W. The heat delivered and the rise in temperature eventually resulted in the boiling of the liquid and, finally, decomposition, causing the accumulated propellant to decompose at an accelerated rate. In order to estimate the moment when the decomposition process accelerated significantly for the discussed experiment Z1184, a rough comparison was made between a logarithmic mean preheating temperature fit curve for *T2,* presented in Figure 4.3 (a) and *T2* trace in Figure 4.4. It was found that temperature *T2* during experiment Z1184 exceeded the preheating value at t~8,6 s. This is in good agreement with the behaviour of the chamber pressure, which started to build up at the mentioned moment, rising significantly above the steady state value, which was assumed to be the mean value during the last five seconds of operation. In Figure 4.4, two five-second periods were highlighted for comparison purposes, the first being the reference interval, as mentioned, considered a steady-state, lasting from t = 21 to 26 s and the second one, between t = 13 and 18 s. The values of mean chamber pressure in the considered intervals (illustrated in Figure 4.4 using dots) were 3,27 and 4,42 bar, indicating the decomposition of excess propellant in the initial phase. Apart from the $T2_{op}$ temperature, it must be mentioned that the wall temperature measured by the T_{wall} thermocouple during FCV opening (T_{wall_op}) was 45°C; therefore, the first observation that may be pointed out based on experiment Z1184 is that a high heater temperature (higher than the saturation temperature) is insufficient to initiate a reliable decomposition of the compound spontaneously.

Figure 4.5 illustrates experiment Z1193, for which the preheating time was extended to 22 s, and the supply voltage was the same as during test Z1184, presented in Figure 4.4, and amounted to 50 V. In the case of Z1193, the temperatures measured by thermocouples *T2* and T_{wall}, before initiating the flow, were respectively $T2_{op}$ = 711 and T_{wall_op} = 265°C – values significantly higher than for the previously analyzed result, Z1184 ($T2_{op}$ = 195°C and T_{wall_op} = 45°C). As seen in the figure, the opening of the FCV caused rapid and spontaneous decomposition initiation. The *T2* chamber temperature rose by 136°C one second after the valve was opened and reached a value of ~940°C (adiabatic decomposition temperature of 98% H_2O_2,

as depicted in Figure 1.5) five seconds after the flow of peroxide was started. The final, before closing FCV, internal chamber temperature measured in the axis of the chamber (*T2*) was 1003°C. This value, higher than the theoretical (adiabatic) one, indicates the influence of the heating cable operating at a greater temperature than measured by *T2*.

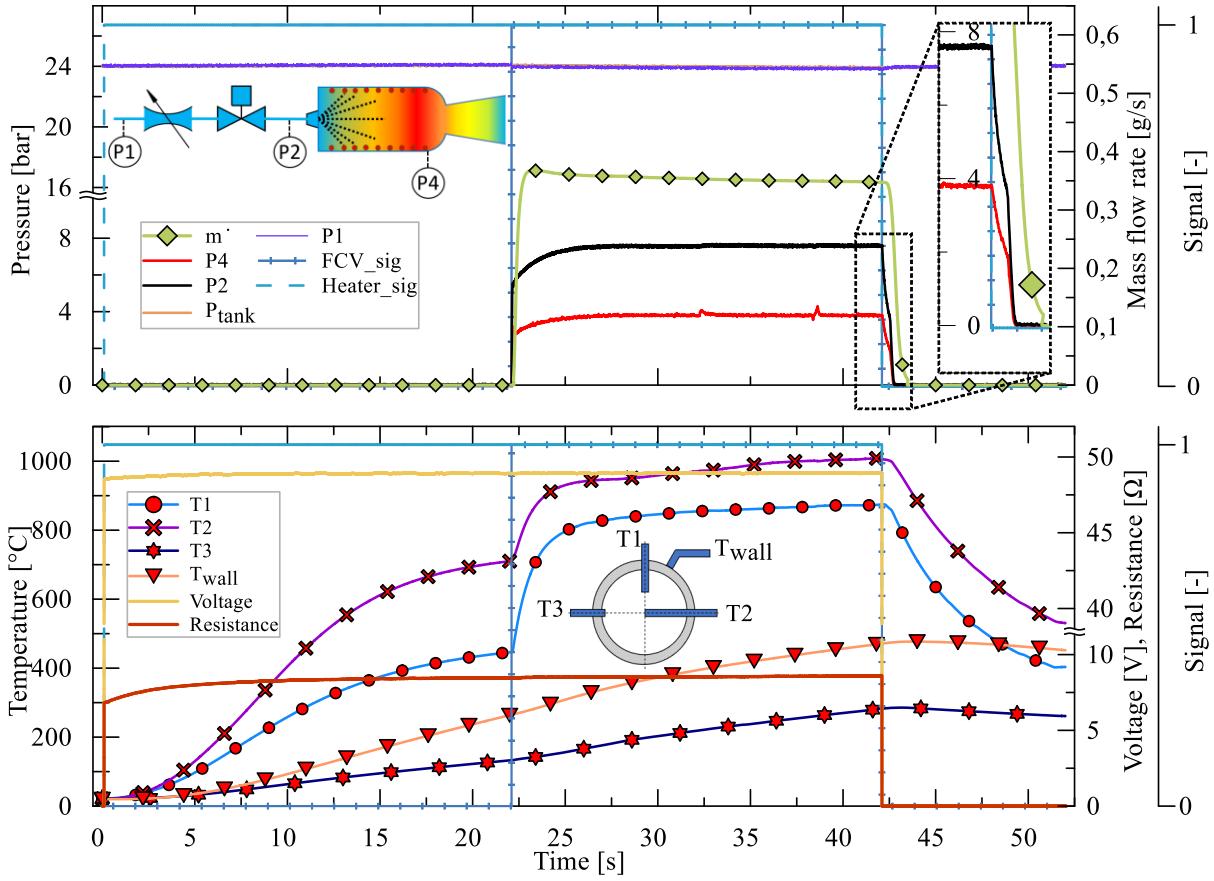

Figure 4.5 High-power experiment number Z1193; supply voltage: 50 V, preheating time: 22 s, mean heater power during the propellant injection sequence: 281 W.

The next observation was that the behaviour of chamber pressure was entirely different than for experiment Z1184. The pressure started rising promptly directly after introducing the propellant to the chamber. The pressure rise time (t_{rise_5s}), measured from when the valve was commanded to open to when it reached 90% of the mean value during the last five seconds, was 1,15 s; this is significantly less than the 5,48 s measured for experiment Z1184, presented in Figure 4.4. The chamber pressure remained steady throughout the experiment, with only two minor spikes identified at t = 32,3 and t = 38,6 s. The pressure roughness, as discussed, calculated as a ratio of standard deviation during the last 5 seconds, and the mean chamber pressure ($P4_{5s}$) during that period was 1,76%; in the case of test Z1184, the roughness was 5,83%.

The zoomed area box in Figure 4.5 shows the behaviour of the chamber and injector inlet pressure (*P4* and *P2*) directly after closing the valve. In the presented case, the fall time (t_{fall_5s}),

measured from when the valve was commanded to close to when the chamber pressure fell to 10% of reference pressure ($P4_{5s}$), was 0,58 s. For the test Z1184, the fall time was 0,68 s. Wall temperature did not stabilize during the run and was rising throughout the experiment and reached a value of 477°C, ~2 seconds after the valve was closed.

In section 4.1.2, it was mentioned that experiments were started at room temperature except for two cases. These exceptional runs were denoted as Z1170 and Z1210 and, in Table 4.1, were marked with a star. For these two cases, no cooling sequence was introduced after the preceding experiment; the aforementioned runs were initiated directly after the previous test. The results obtained for test Z1210 can be seen in Figure 4.6. The test was conducted at a supply voltage of 45 V; the preheating phase was not excluded and lasted 24 seconds.

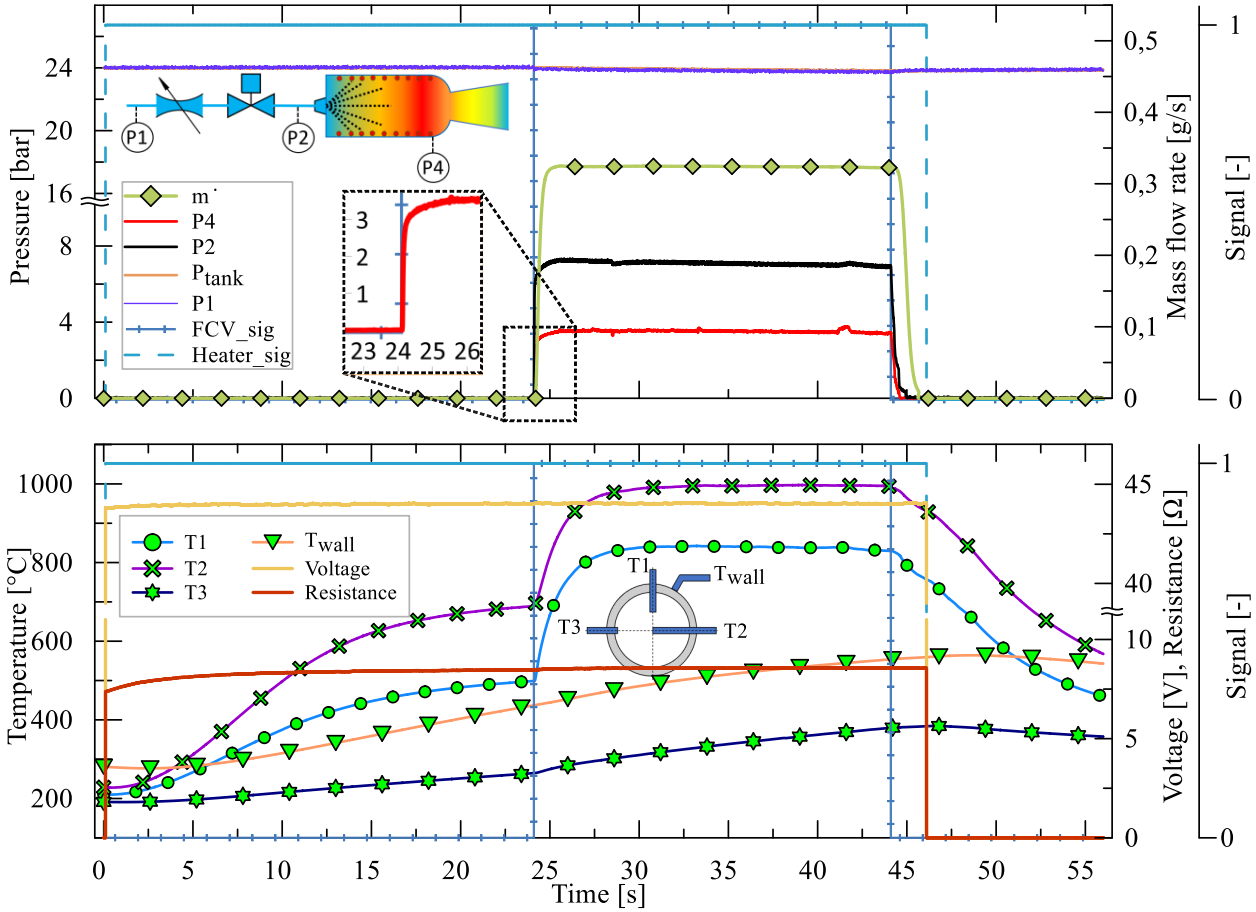

Figure 4.6 High-power experiment number Z1210; supply voltage: 45 V, preheating time: 24 s, mean heater power during the injection sequence: 227 W. The chamber cooling phase was not introduced after the preceding test.

Lack of cooling sequence before initiating test Z1210 resulted in the highest measured wall temperatures before opening and closing the FCV – respectively 436 and 554°C. This allowed the initiation of smooth decomposition, as seen in the magnified area in Figure 4.6. The pressure rise time, calculated as previously, was 0,27 s, and was the lowest value obtained

throughout the test campaign. The pressure decay time was 0,41 s, and a lower value of 0,3 s was only obtained for test Z1170, a second one, apart from Z1210, for which the cooling system was not activated after the preceding experiment. The pressure roughness for Z1210 was 2,46%, which was higher than for Z1193, but the reason was the pressure oscillation at t = 41,5 s.

The presented subsection aimed mainly to analyze in more detail test runs performed at different initial conditions; this was done using three representative examples, for which the shortest preheating time was applied, another one, where the longest preheating time for the considered supply voltage was used, resulting in much more efficient decomposition right from the start and the last one, carried out using the initially hot, uncooled chamber. It was noted that observed parameters, namely, pressure roughness and pressure rise and decay time, varied substantially and strongly depended on the initial (before delivering HTP to the chamber) conditions. The following subsections aim to determine more detailed relations and formulate concluding remarks.

4.1.3.1 Influence of temperature on pressure roughness

This subsection aims to present results concerning the influence of temperature on the stability of the decomposition process - an attempt was made to determine the relation between chamber pressure roughness and corresponding temperatures measured during experiments.

First, it was decided to compare the temperatures $T1_{5s}$, $T2_{5s}$ and $T3_{5s}$, measured by thermocouples placed directly in the chamber, and estimate each measurement's influence on the decomposition process's stability. As stated previously, pressure roughness analysis was performed using data obtained for the last five seconds before closing FCV; the standard deviation for the data was found and, next, was divided by the mean chamber pressure measured during that period. Figure 4.7 was prepared to present the discussed dependence. Apart from the direct relationship between pressure roughness and temperatures, traces of chamber pressure were presented for selected experiments to illustrate the fluctuations graphically.

As can be viewed in Figure 4.7, the range of pressure roughness obtained during this part of the test campaign was broad, with the lowest value of 0,73% (Z1200) and the highest amounting to 18,8% (Z1178). Analysis of Figure 4.7 leads to the conclusion that little to no dependence exists between pressure fluctuations and mean internal chamber temperatures measured during runs. For the centrally placed thermocouple, $T2$, the mean measured temperature ($T2_{5s}$) ranged from 864°C (Z1149, 40 V, t_{preh} = 6 s) to 1010°C (Z1192, 40V, t_{preh} = 22 s) - the heating cable's influence is evident, with the highest temperatures obtained for a supply voltage of 50 V.

The dispersion of the data presented in Figure 4.7 is significant; in some cases, even tests performed at the same conditions gave substantially different roughness values.

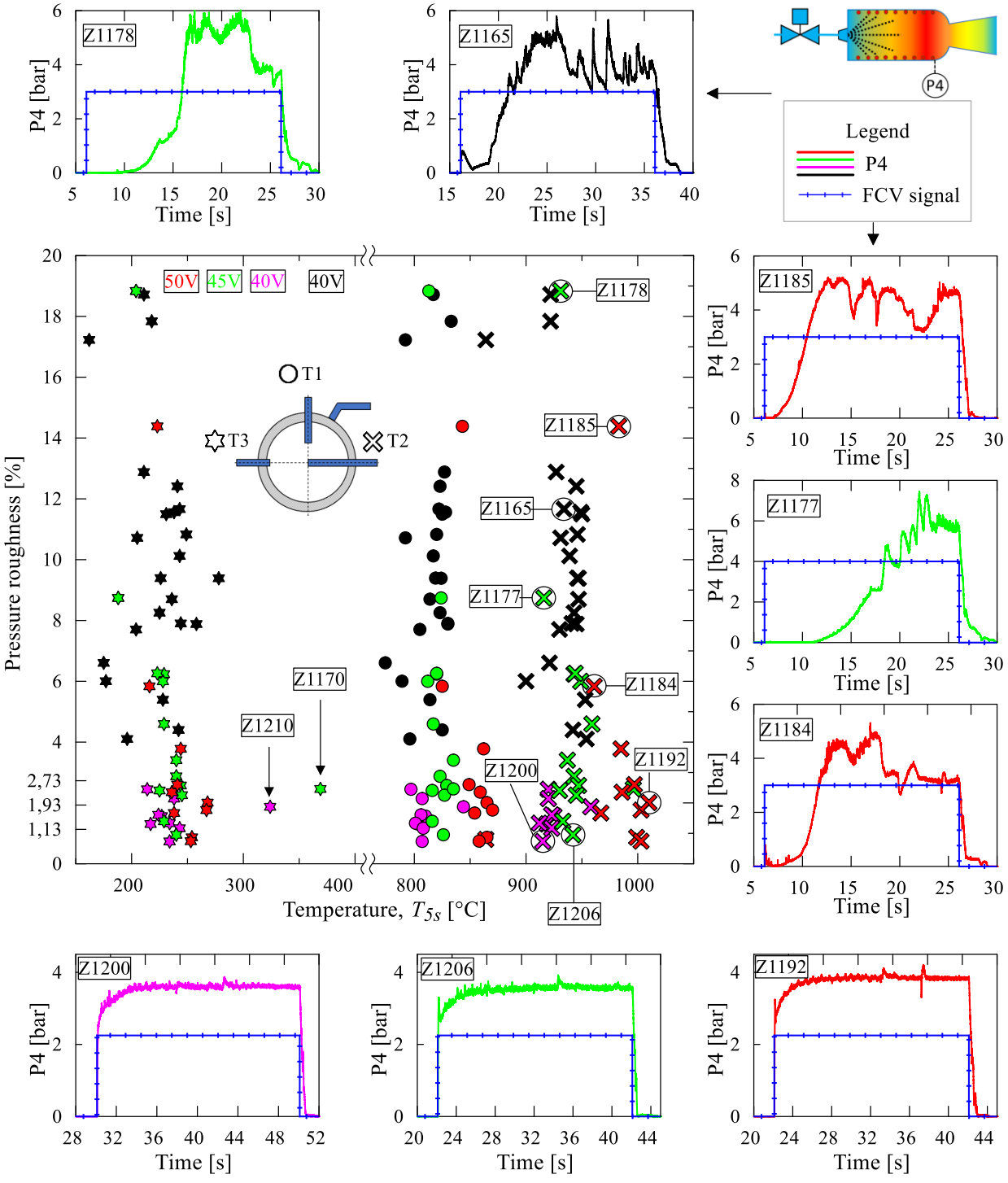

Figure 4.7 Pressure roughness, rou_{5s}, as a function of mean chamber temperatures (T_{5s}), measured in the 5 s reference period before FCV closing.

On the other hand, for each voltage tested, it was possible to achieve stable decomposition with rou_{5s} lower than 2%. It is suspected that because of the relatively short time when the valve was in an open position, in such case, the conditions in the chamber must allow spontaneous

decomposition directly after the valve opening. Otherwise, if the chamber is not preheated properly, the propellant accumulates in liquid form, and as the heat from the heater is delivered, highly unstable decomposition occurs; the excess compound is boiled off and decomposed, and as the process accelerates, significant overpressure is observed together with sharp spikes, as can be viewed, e.g. in the case of test Z1177 in Figure 4.7. The observations based on detailed analysis of tests Z1184, Z1193 and Z1210 provided in the previous subsection and data presented in Figure 4.7 lead to a conclusion that high internal chamber temperature (close to the adiabatic decomposition temperature) does not guarantee high stability of the decomposition process. The chamber structure must be adequately preheated as well.

An attempt was made to determine the relation between the external chamber wall temperature and the measured pressure oscillations. The resulting relationship can be viewed in Figure 4.8.

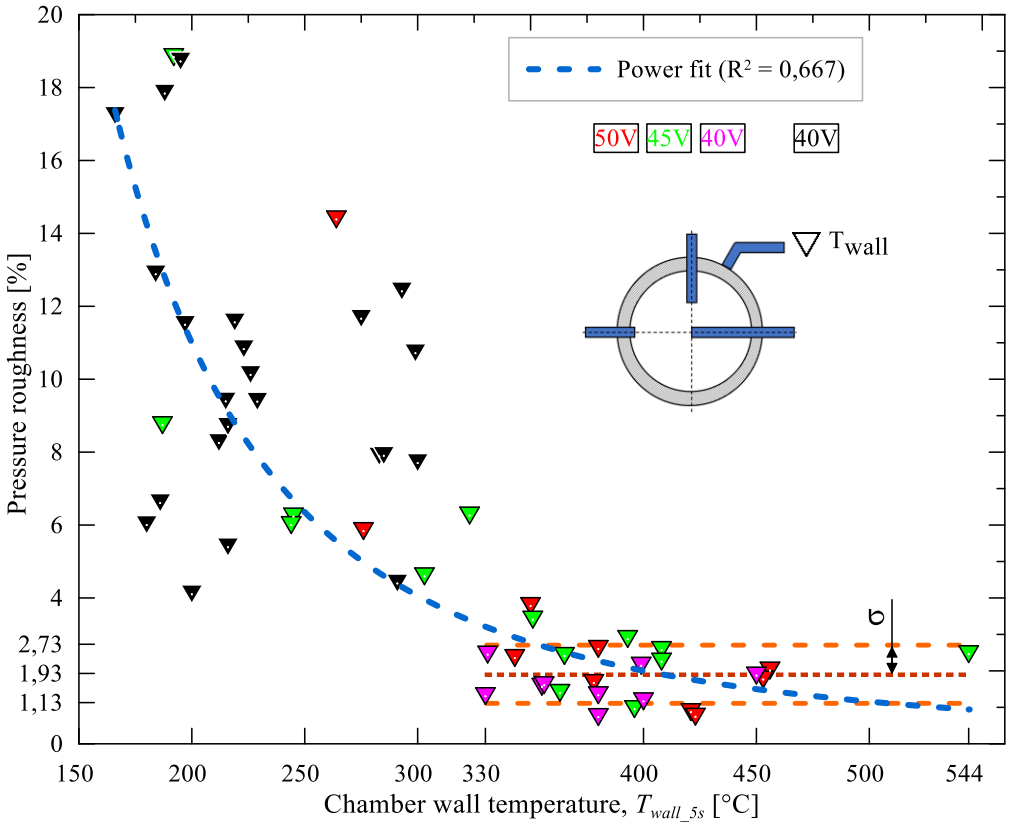

Figure 4.8 Pressure roughness, rou_{5s}, as a function of mean external chamber wall temperature (T_{wall_5s}), measured in the 5 s reference period before FCV closing.

A power function trend line best fits the data presented in Figure 4.8; however, the fit is not perfect, as the coefficient of determination obtained is 0,67. Due to a significant number of scattered measurement points in the low-temperature region and limited data for wall temperatures in the range of 450°C and more, a thorough examination of the trend was not possible. Nevertheless, it can be noted that at a wall temperature greater than 330°C, the

dispersion of data is low compared to the roughness values obtained at wall temperatures lower than ~320°C. The mean roughness value of 1,93% was found for 25 data points in the wall temperature range of 330 and 544°C, while the standard deviation, σ, in the discussed range, amounted to 0,8% - the values provided were included in Figure 4.8.

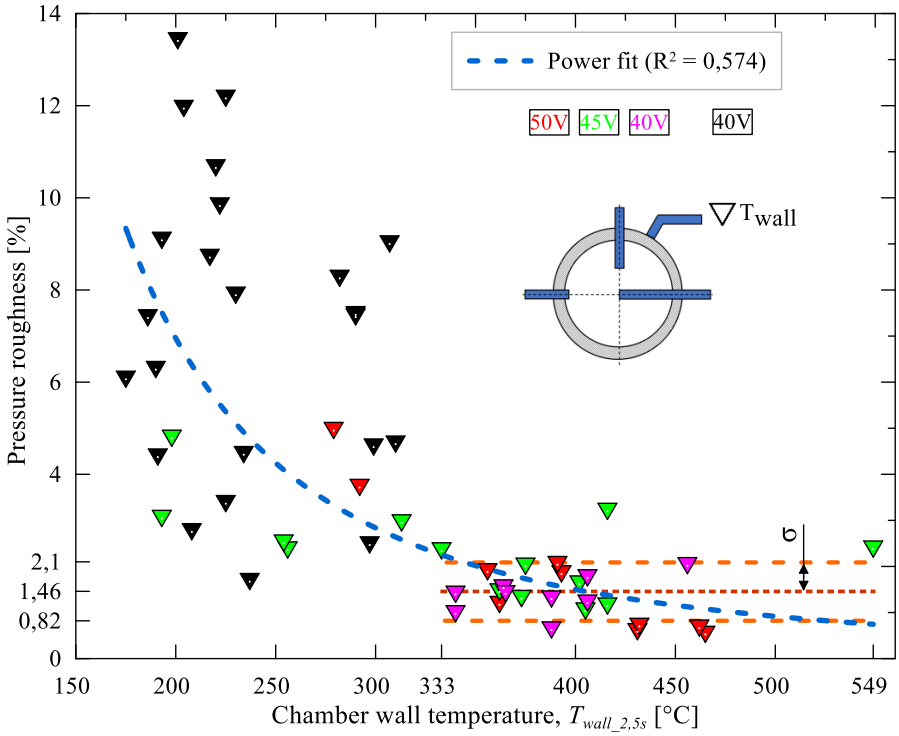

Figure 4.9 Pressure roughness as a function of mean external chamber wall temperature, measured in the 2,5 s period before FCV closing.

Figure 4.9 illustrates the behaviour of pressure roughness in the period of 2,5 s prior to the valve closing. The mean roughness measured for the wall temperature in the 333 to 549°C range was lower than for the 5 s period and amounted to 1,46% with a standard deviation, σ, of 0,64%.

4.1.3.2 Variation of pressure decay and rise time with temperature

Pressure decay (or fall – t_{fall_5s}) and rise (t_{rise_5s}) times were measured using indications of the *P4* pressure transmitter placed at the nozzle entrance. As discussed in section 4.1.1, fall time was measured from when the valve was commanded to close to when the pressure fell to 10% of the mean chamber pressure measured during the last five seconds of operation ($P4_{5s}$). As described, reference temperatures for fall times were mean values measured during the pressure decay period (t_{fall_5s}). Initially, only temperature measurements at the moment of FCV closing were considered. However, due to significant pressure decay time for some experiments, a substantial difference was observed between the two reference temperatures

considered and was up to nearly 50°C for *T2*; a similar effect was observed for the wall temperature during each test, but the magnitude was considerably lower – this was attributed to the measurement methodology and the thermal inertia of the chamber and the thermocouple. The difference was negligible for all temperatures if t_{fall_5s} was less than half a second;

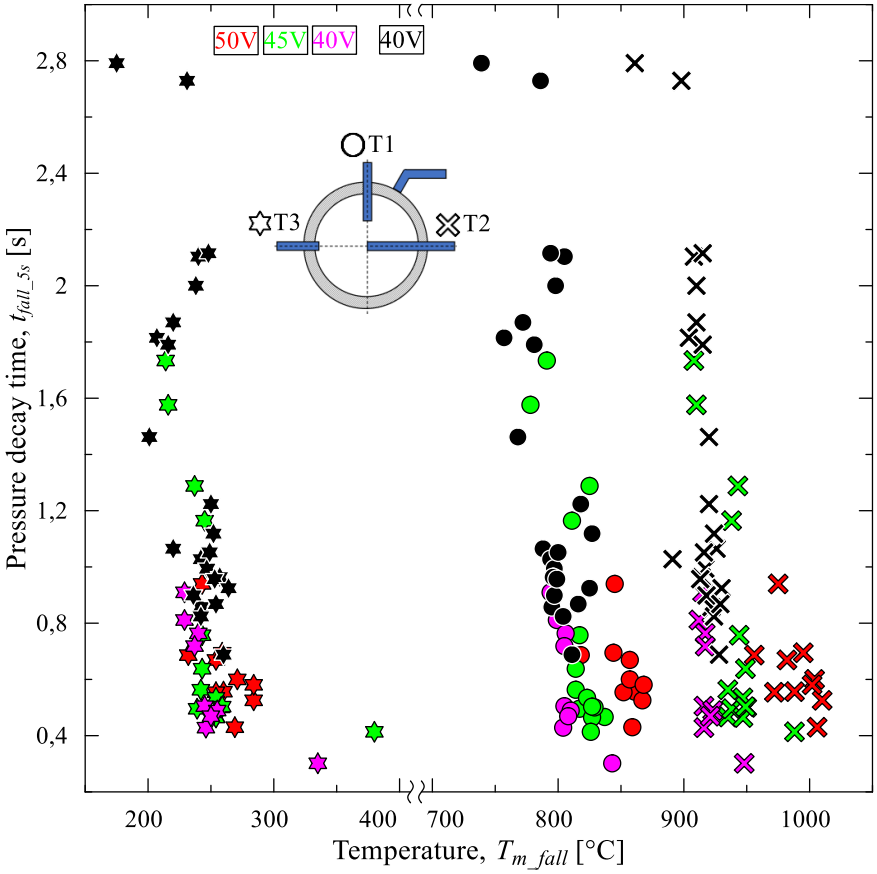

Figure 4.10 Relation between chamber pressure decay time (t_{fall_5s}) and mean internal chamber temperatures (T_{m_fall}), measured during the pressure decay period.

Figure 4.10 depicts the relation between pressure decay time, t_{fall_5s}, and the mean internal chamber temperatures, T_{m_fall}. The calculated fall times ranged from 0,3 to 2,8 s, with the lowest value obtained during test Z1210 (without chamber cooling after the preceding experiment) and the highest for test Z1149, for which the lowest supply voltage and preheating time were incorporated. A long pressure fall time, the so-called tail-of, indicates propellant accumulation - as can be viewed in Figure 4.10, the highest values of pressure decay times were measured for a heater supply voltage of 40 V and preheating time of less than 20s – this is in good agreement with the discussion provided in section 4.1.2, concerning propellant accumulation after tests, affecting the preheating phase temperatures. Figure 4.10 indicates weak, decaying characteristics of roughness with temperature. Figure 4.11 (a) to (d) were prepared separately for T_{wall}, *T1*, *T2* and *T3* to visualise trends corresponding to each temperature measured. An attempt was made to fit trend curves into the data points presented

in Figure 4.11 (a) to (d), but the dispersion of the data for the temperatures in the chamber was so significant that no trend could be fitted with reasonable accuracy. As for the wall temperature, according to Figure 4.11 (a), the power function can be used to fit the data presented, although the fit is not perfect, as the coefficient of determination is only 0,64.

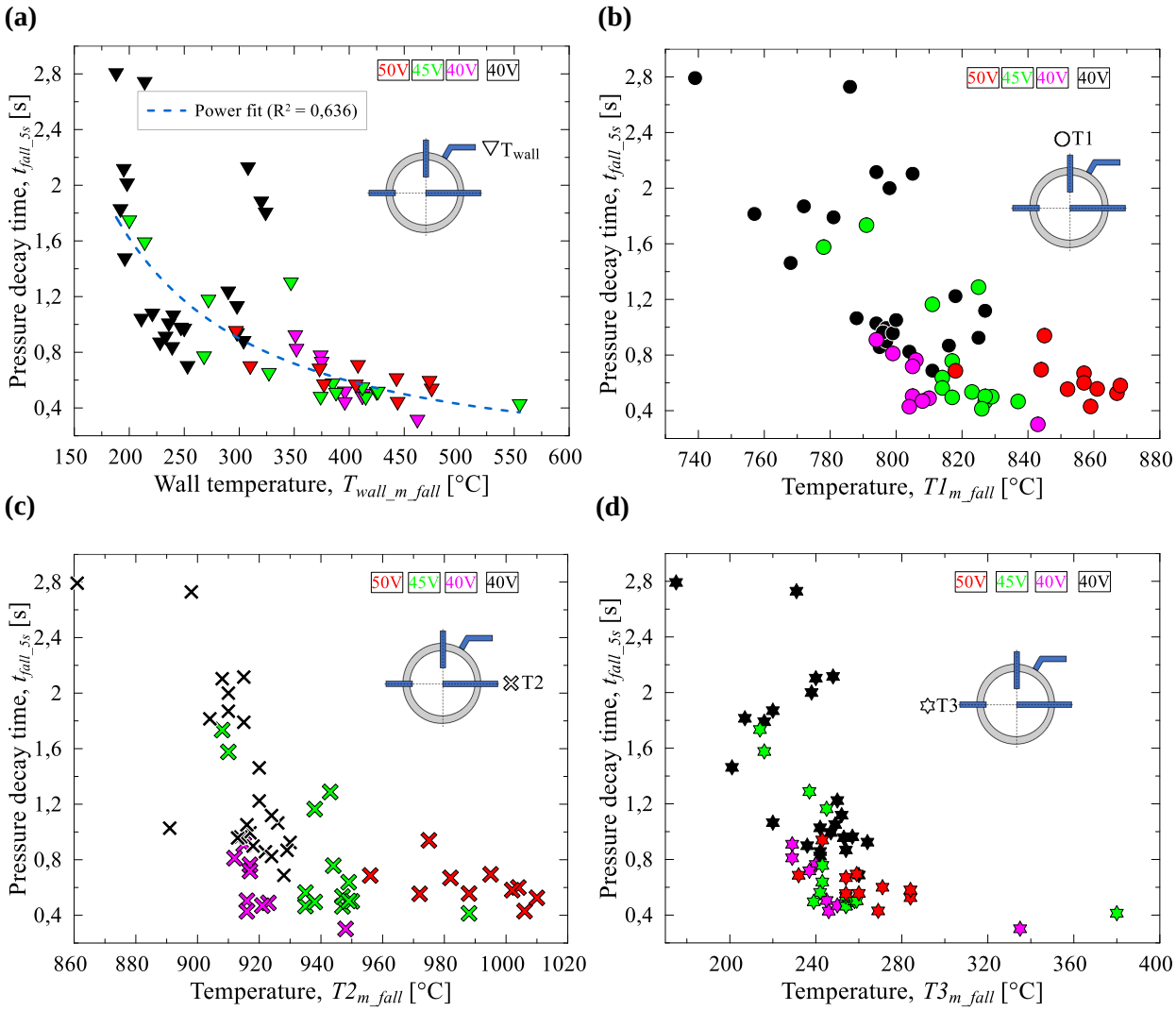

Figure 4.11 Relation between chamber pressure decay time, t_{fall_5s}, and mean temperatures measured during the pressure decay period; **(a)** $T_{wall\_m\_fall}$; **(b)** $T1_{m\_fall}$; **(c)** $T2_{m\_fall}$ and **(d)** $T3_{m\_fall}$.

The threshold wall temperature above which the decay time stabilizes is not evident, but after analysis of the data presented in Figure 4.11 (a), a temperature of 375 to 400°C may be considered a value above which the decrease, as well as dispersion, is limited when compared with the remaining data points.

Figure 4.12 illustrates the relation between chamber pressure rise times and temperatures measured directly before the opening of the FCV, T_{op}. It was arbitrarily decided that for comparison purposes, mean values of temperatures during the pressure rise time will

not be considered, as the goal was to identify the initial conditions necessary to initiate spontaneous decomposition in the chamber. Additionally, as will be shown in the following sections dedicated to tests performed at low heater power, a significant temperature rise may be registered in the chamber due to very inefficient decomposition, resulting in an insignificant pressure rise - this could negatively affect the analysis discussed.

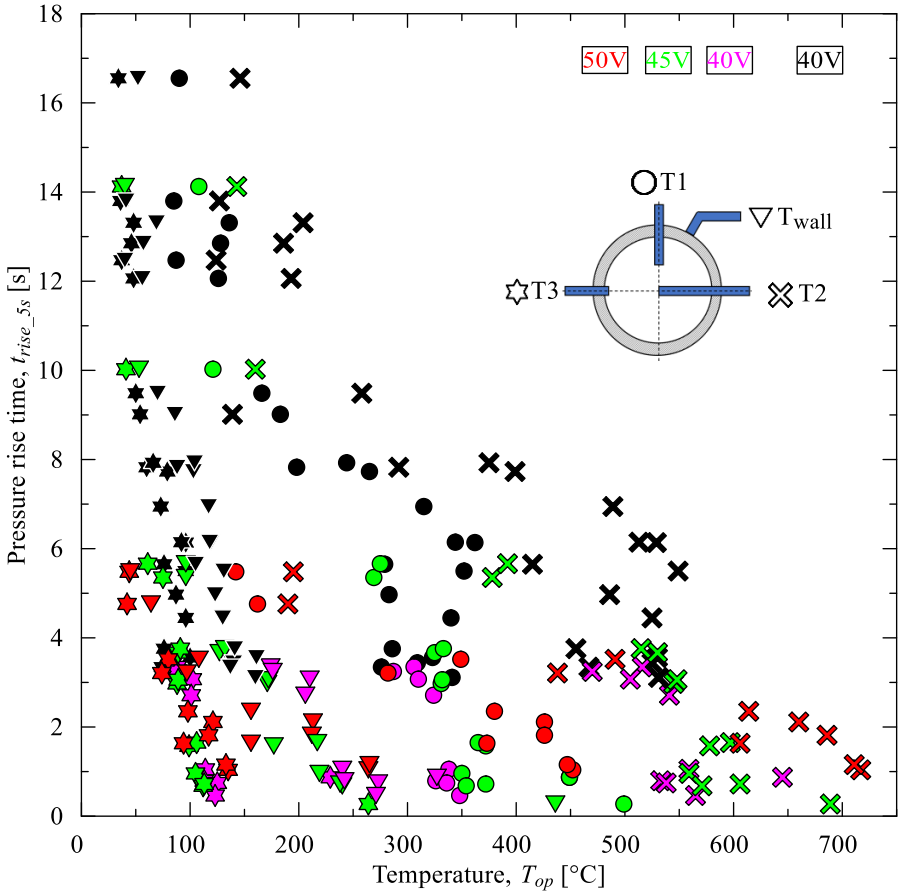

Figure 4.12 Relation between chamber pressure rise time (t_{rise_5s}) and temperatures captured when the FCV was commanded to open (T_{op}).

The rise time was measured from when the control signal was sent to the valve, until the measured chamber pressure was 90% of the mean value during the last five seconds of the run. In Figure 4.12, for comparison purposes, pressure rise time was shown as a function of all temperatures measured. The dispersion of the data is significant, as rise times ranged from 0,27 up to 16,5 s. As in previous cases, the highest value was obtained during test Z1149 and the lowest during experiment Z1210.

For clarity, Figure 4.13 (a)-(c) was prepared to present separately the influence of all three internal chamber temperatures, captured before the opening of the FCV, on the pressure rise time. Logarithmic trends fit each relation well, with R^2 of ~0,8 in each case. As for Figure 4.13 (c), concerning the influence of $T3_{op}$ on the pressure rise time, only data points

corresponding to the temperature of up to ~130°C were considered while fitting the trend line as at higher temperatures, only two data points were captured, corresponding to tests initiated without previous cooling of the chamber, and pressure rise times for the aforementioned tests Z1170 and Z1210 were on the same order as for a $T3_{op}$ temperature of ~130°C; further increase of $T3_{op}$ did not affect the pressure rise time. It must be highlighted that of all temperature measurements, *T3* was of the lowest significance, as the vicinity and influence of the flange, being a part of the nozzle, was visible and affected the measurement by a heat transfer through the shield of the *T3* thermocouple.

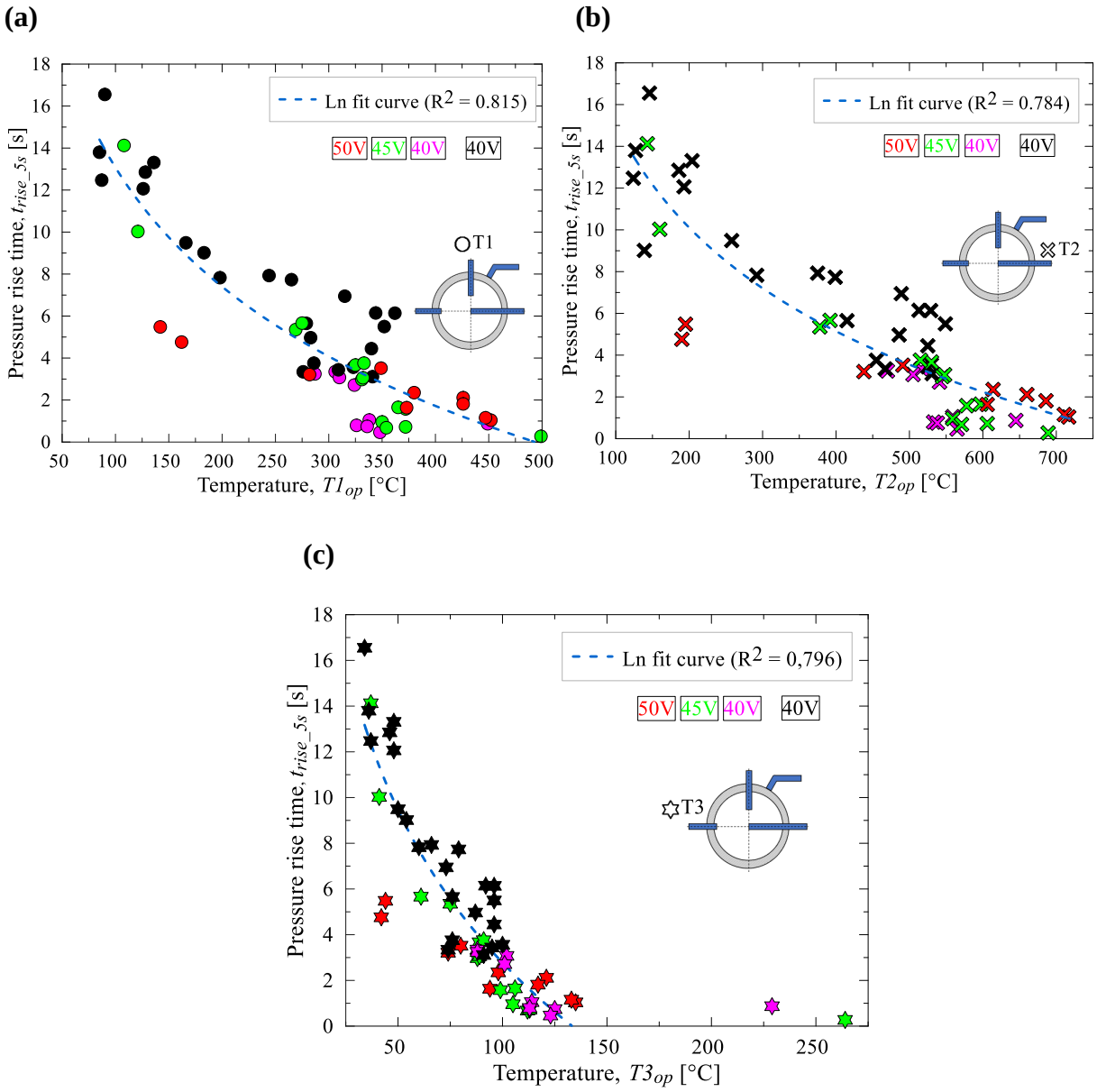

Figure 4.13 Pressure rise time, t_{rise_5s}, as a function of temperatures captured before opening of the FCV (T_{op}): **a)** $T1_{op}$, **b)** $T2_{op}$, **c)** $T3_{op}$.

Figure 4.14 shows the relation between the rise time and wall temperature. An exponential fit curve well characterizes the dependence. In order to depict the decaying dispersion in more

detail, a 95% confidence interval was added to the plot. During high-power tests, the measured wall temperatures captured before FCV opening ranged from 40 to 436°C; two highest values, 327 and 436°C were obtained during experiments Z1170 and Z1210, performed directly after the previous test (the cooling phase was omitted). The maximum wall temperature measured before opening the valve for regular tests, initiated at room temperature, was 273°C.

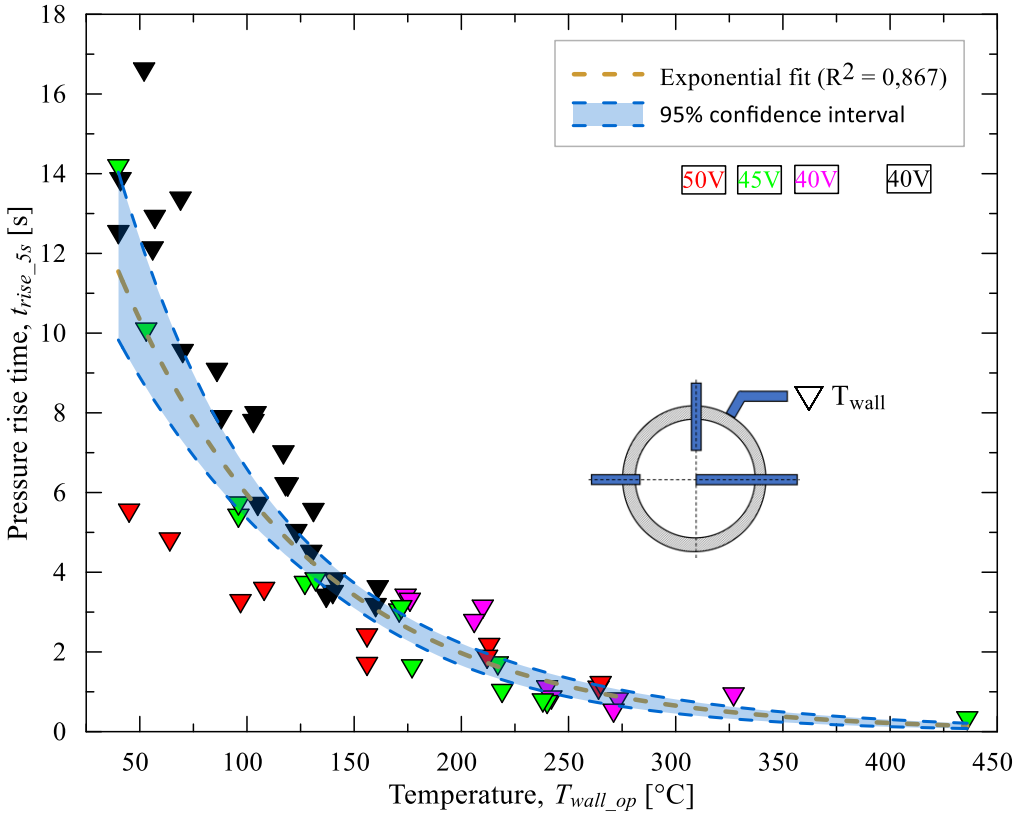

Figure 4.14 Pressure rise time, t_{rise_5s}, as a function of wall temperature, T_{wall_op}, captured before opening of the FCV.

As previously, due to a limited number of data points in the high-temperature region, it was not possible to accurately estimate the temperature above which the rise time value stabilized; it can only be stated that the mentioned limit is expected to be above 230°C. For future activities, it is planned to implement pulsed mode operation of the thruster, during which the wall temperature will be registered before each pulse, allowing achieving high wall temperatures without resistive preheating of the chamber for extended periods, therefore minimizing the risk of heater damage.

The data points corresponding to the supply voltage of 40 V and preheating time of 20 seconds and less were not excluded from the analysis presented. As shown in the provided figures, the aforementioned data points fit the trends relatively well, together with experiments performed under conditions considered representative (45 and 50 V supply).

4.1.4 Summary

The section presented discussed the results obtained during the high-power subcampaign, for which the mean heater power during the preheating phase ranged from ~190 to 320 W. The duration of the preheating phase before opening the FCV varied from 6 to 34 seconds. The valve was opened for 20 seconds during each test; 56 experiments were carried out. Except for two tests, Z1170 and Z1210, the chamber was cooled to room temperature before the following run. Below are the most significant observations:

- For tests in which the supply voltage was 40V and the preheating time ranged from 6 to 20 seconds, propellant accumulation in the chamber was observed after the test, affecting the initial temperature during the preheating sequence in the following runs. Such a phenomenon occurred despite a relatively high T_{wall} and *T2* before closing the valve – in most cases exceeding 200 and 900°C, respectively.

- Analysis of test runs where propellant accumulation was observed, affecting the preheating phase in the following tests, revealed prolonged decay times, together with the highest pressure roughness observed throughout the campaign and the most extended pressure rise times. The initial conditions, being a result of a supply voltage of 40 V and preheating times of 6 to 20 s were insufficient to guarantee initiation of spontaneous decomposition.

- The high temperature of the heater was not enough to spontaneously initiate the decomposition of the propellant used. Rapid decomposition was not initiated if the wall temperature was only slightly elevated due to short preheating time.

- It was observed that internal chamber temperatures did not affect the pressure roughness. The obtained roughness ranged from 0,73 to 18,8%, and, in many cases, the difference between measured temperatures corresponding to different roughness values was close to zero. On the other hand, roughness of less than 2% was achieved for each voltage tested – the only difference between experiments was the duration of the preheating sequence, affecting the reactor temperature.

- The plot of pressure roughness, $rou_{5s,}$ and chamber wall temperature, T_{wall_5s}, revealed that at wall temperatures of ~330°C and higher, the roughness was significantly reduced, as the mean value was 1,93% with a standard deviation of 0,8% in the temperature range of 330 to 549°C.

- Decaying characteristics were observed for the relations between pressure decay time and mean temperatures, T_{m_fall}. As for the wall temperature, an accurate threshold temperature was not found; however, in a temperature range of 375 to 400°C and higher, the dispersion of the data and decrease in the decay time stabilized.

- As for the pressure rise time presented as a function of temperatures captured before opening the valve, logarithmic curves fit the data well for $T1_{op}$, $T2_{op}$ and $T3_{op}$. The rise time decreased exponentially with the wall temperature. As previously, apparent threshold wall temperature was not observed due to limited data available, but above 230°C, the dispersion of the data was low, and the rise time did not exceed 1,5s.

4.2 Reduced heater power campaign

4.2.1 Methodology and evaluation criteria

As in the previously discussed campaign, key measures used in the current analysis were pressure roughness, pressure rise time and pressure decay time. These metrics were calculated using the same methodology as in the high-power campaign, but due to different durations of experiments concerning high and low-power tests and the fact that during low-power experiments, the heater was turned off at a defined moment while the propellant was injected into the chamber, an additional time interval was selected for analysis. To illustrate measures of particular interest and the course of a test, a graphical representation of a run was prepared and can be viewed in Figure 4.15.

The period during which the flow control valve remained open was 70 or 120 seconds long as two separate sub-campaigns were carried out, for which one of the differences was the duration of the experiment. Before each test, a preheating phase was implemented, always lasting 30 minutes. After opening the valve, the heater was supplied as in the preheating phase. After t_h = 40 or 60 s, the heater was turned off, and the propellant was delivered to the chamber for an additional time of t_{nh} = 30 or 60 s. During that period, observations were made on whether the decomposition process could be self-sustained, and the chamber pressure and temperatures were looked at thoroughly. For comparison purposes, two reference regions were selected for analysis, as previously, each 5 seconds long, one before turning the heater off and another before closing the FCV. Both regions were illustrated in Figure 4.15 as hatched areas. In the periods mentioned above, the mean chamber pressures were found ($P4_{5s\_h}$, $P4_{5s\_nh}$), as well as

mean temperatures - of particular interest were measurements carried out in the axis of the chamber ($T2_{5s\_h}$, $T2_{5s\_nh}$) and wall temperatures ($T_{wall\_5s\_h}$, $T_{wall\_5s\_nh}$).

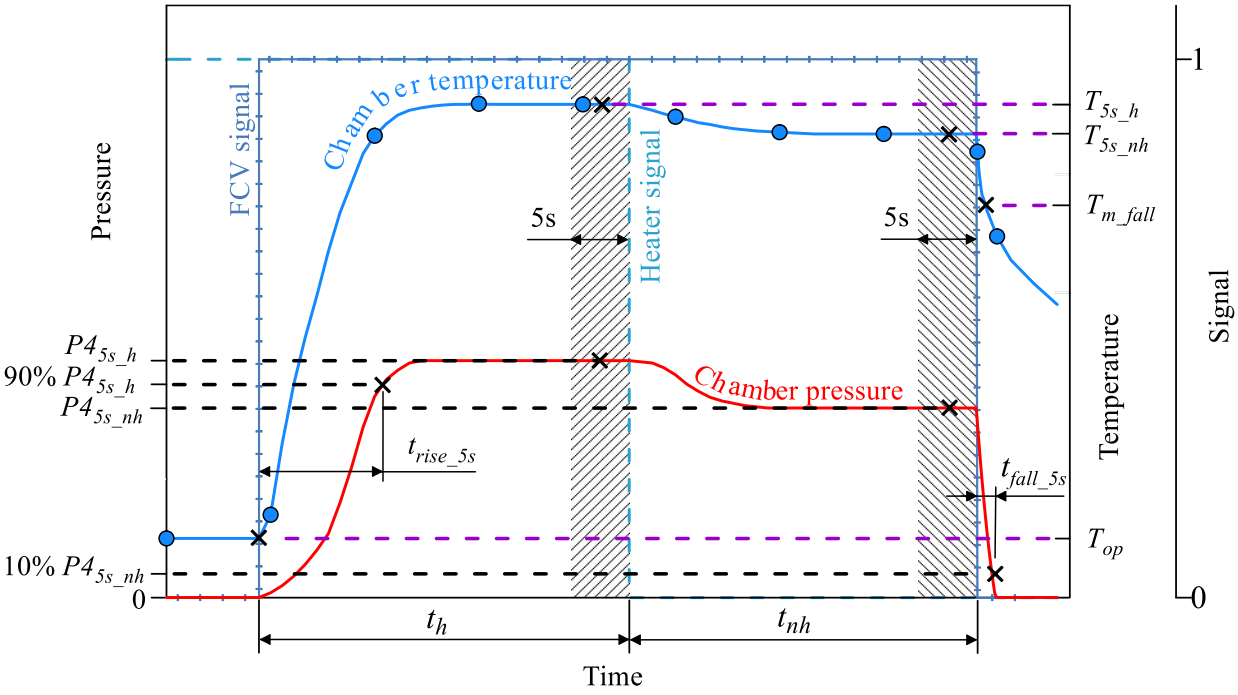

Figure 4.15 Schematic representation of a low-power, 70 or 120-second experiment. t_h – period after opening the valve during which the heater remained active; t_{nh} – duration of the phase when the heater was off, t_{rise_5s} – pressure rise time; t_{fall_5s} – pressure fall time; T_{m_fall} – mean temperature in the t_{fall_5s} period; T_{op} – temperature captured directly before opening the FCV; hatched areas – time intervals used to calculate mean reference pressures ($P4_{5s\_h}$, $P4_{5s\_nh}$), roughness and temperatures (T_{5s_h}, T_{5s_nh}). Subscripts *h* and *nh* refer to intervals when the heater was on and off, respectively. t_h was 40 and 60 s, while t_{nh} amounted to 30 or 60 s, respectively for 70 and 120 s experiments.

While calculating the pressure rise time, the mean chamber pressure obtained during the last five seconds prior to turning off the heater, $P4_{5s\_h}$, was selected as a reference value. As previously, rise time was the time necessary for the pressure to reach 90% of the reference pressure (*90% $P4_{5s\_h}$* in Figure 4.15). Regarding the decay time, the mean pressure measured in the last five seconds was taken as a reference ($P4_{5s\_nh}$). As will be shown in the following analysis, the difference between $P4_{5s\_h}$ and $P4_{5s\_nh}$ was insignificant for most cases.

As previously, different heater powers were investigated, affecting the initial temperatures, T_{op}. Apart from tests during which the propellant injection time was 70 or 120 seconds, because of safety-related issues, short, 5-second runs were executed before long experiments after the supply voltage was changed. During short tests, the chamber pressure was observed along with temperatures. Due to the test's limited duration (5 s), neither pressure rise time nor roughness were calculated.

While discussing the results, the duration of tests (70 or 120 s) will be used while referring to the specific low-power sub-campaign.

4.2.2 Reduced heater power campaign – 70-second tests

4.2.2.1 Preheating phase

In contrast to experiments carried out at high heater power, the purpose of the low power campaign was to investigate the behaviour of the test article at conditions much more resembling those obtained in catalytic, nonaugmented monopropellant thrusters. The heater power was, therefore, significantly reduced. Consequently, the preheating time had to be significantly extended and, as noted above, was 30 minutes. During the preheating phase, due to the sequence length, it was necessary to reduce the sampling rate of the data acquisition system.

Table 4.2 Set of experiments performed within the framework of a low-power sub-campaign, during which the duration of experiments was 70 seconds.

		Preheating phase				**Corresponding hot test**	
No.	**U_{sup} [V]**	ID	$T2_{max}$ [°C]	T_{wall_max} [°C]	P_{mean} [W]	ID	t_{run} [s]
1	9	Z127	175	151	10,6	Z1326	5
2	9	Z128	171	149	10,6	Z1327	70
3	8,5	Z129	156	137	9,4	Z1328	5
4	8,3	Z130	153	136	9,1	Z1330	5
5	8,3	Z131	149	131	8,9	Z1331*	70
6	8,3	Z132	147	130	8,9	Z1332	5
7	8,2	Z133	149	131	8,8	Z1333	5
8	9,5	Z134	186	163	11,6	Z1334	5
9	9,5	Z135	185	164	11,6	Z1335	70
10	10	Z136	196	176	12,8	Z1336	5
11	10	Z137	197	177	12,8	Z1337	70
12	10,5	Z138	214	191	14,1	Z1352	5
13	10,5	Z139	212	191	14,0	Z1353	5
14	10,5	Z140	211	190	13,9	Z1354	70
15	11	Z141	211	200	14,9	Z1355	5
16	11	Z142	220	200	15,0	Z1356	70
17	11,5	Z143	237	215	16,2	Z1357	5
18	11,5	Z144	235	212	16,1	Z1358	70
19	12	Z145	254	231	17,7	Z1359	5
20	12	Z146	249	226	17,5	Z1360	70
21	12,5	Z147	264	241	18,9	Z1361	5
22	12,5	Z148	266	241	18,8	Z1362	70
23	13	Z149	281	256	20,3	Z1363	5
24	13	Z150	278	253	20,2	Z1364	5
25	13	Z151	283	257	20,4	Z1365	70
*Failed experiment							

As can be viewed in Table 4.2, the mean heater power for the entire preheating sequence, denoted in Table 4.2 as P_{mean}, ranged from 8,8 to 20,4 W; this resulted in a final wall temperature, T_{wall_max}, of 130 to 257°C. As expected, the difference between the wall temperature obtained at the end of the preheating phase and the temperature measured in the axis of the chamber ($T2_{max}$) was relatively low and, depending on the test, ranged from 17 to 25°C. The lowest temperature was always registered by the thermocouple placed 1 mm inside the chamber, *T3*; this was, as discussed, because of the vicinity of the flange (nozzle section), which effectively dissipated heat, lowering the temperature locally and significantly influencing the *T3* temperature measurement.

Figure 4.16 (a) and (b) present how the temperatures changed, together with the power and resistance of the heating conductor, for preheating sequences denoted as Z145 and Z128, respectively. It can be noted in Figure 4.16 (b) that thermocouples *T1* and *T2* registered mild temperature spikes. This is believed to be caused by the remaining hydrogen peroxide and can be supported by the fact that such events occurred at a wall temperature of ~150°C, which is close to the normal boiling point of the propellant used. The boiled-off, vaporized compound possibly spontaneously decomposed while in contact with the stainless steel chamber. Considering the length of the preheating phase and the fact that the amplitude of the spikes was limited, it was assumed that all the propellant was boiled off during the preheating phase and did not affect the hot run. As seen in Figure 4.16 (a) and (b), steady-state conditions were not obtained despite a relatively long time. In order to limit the complexity of the test campaign, the duration of the preheating sequence was not extended above 30 minutes.

(a) **(b)**

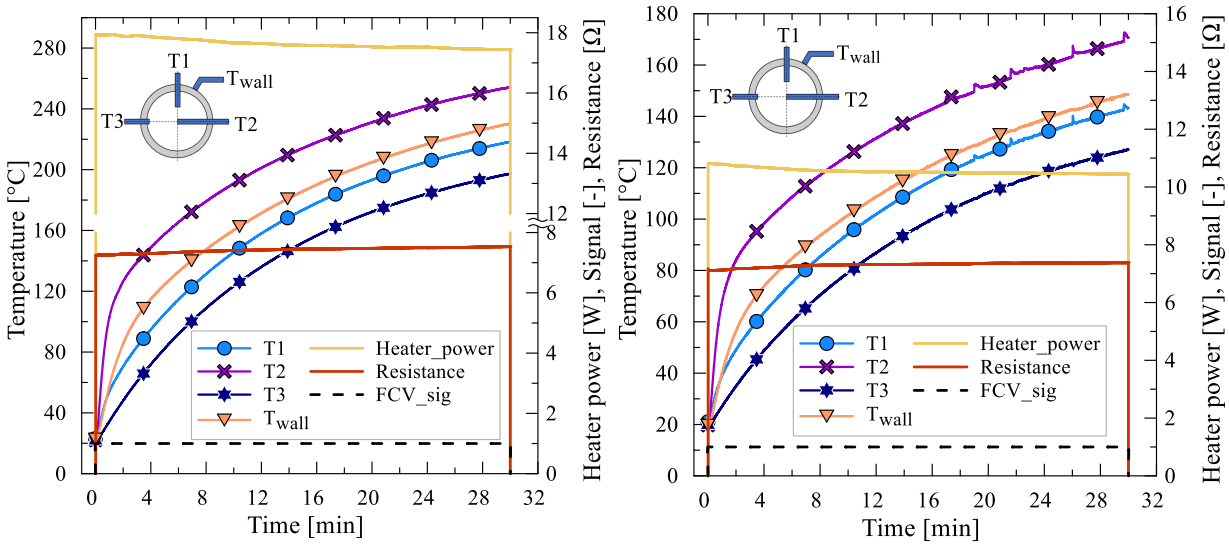

Figure 4.16 Variation of temperatures, heater power and resistance as a function of time during the 30 min preheating phase. **(a)** experiment Z145; **(b)** experiment Z128.

Figure 4.17 shows a relation between temperatures measured directly before opening the FCV (T_{op}) and the heater power. For the considered conditions, each temperature follows a linear trend.

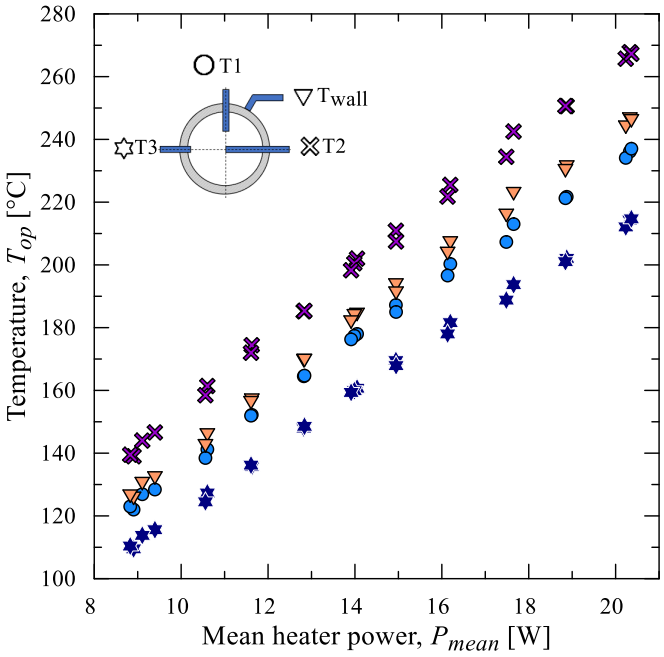

Figure 4.17 Temperatures, T_{op}, measured by thermocouples before FCV opening as a function of mean heater power during the preheating phase.

4.2.2.2 Analysis of 5-second tests

As was mentioned, for long, low-power tests lasting 70 or 120 seconds, after the supply voltage was changed, at least one run was performed, during which the propellant injection time was limited to five seconds. Such an attitude was implemented to minimize the risk of significant propellant accumulation and possible following explosive events or any unexpected response while executing the long run. After the short 5 s experiment, the results obtained were analysed, and a decision was made on whether to proceed with the long experiment.

Figure 4.18 depicts the short, 5-second test, Z1326, with a mean preheating phase heater power of only 10,6 W. The pressure rise was close to zero for the entire experiment duration – 0,1 s after the propellant was allowed to enter the chamber, a small, 1,37 bar pressure spike was registered, and after that, flooding occurred, and the chamber pressure did not exceed a value of ~0,7 bar. Apart from the pressure trace, a camera recording revealed vapour and liquid propellant issuing from the thruster's nozzle. The temperatures *T1* and *T2* rose throughout the experiment, even after closing the valve. As seen in Figure 4.18, the chamber pressure, *P4*, after the valve was closed, was still on the order of 0,5 bar. The *T2* temperature rose until a maximum of 626°C was measured approximately 12 seconds after the valve was commanded to close.

Nearly at the same time when *T2* reached its peak, the *P4* pressure fell to zero; the decomposition was highly inefficient, leading to significant propellant accumulation in the chamber. On the other hand, the temperature rise suggested a possibility of speeding up the reaction and achieving stable decomposition; therefore, a long 70 s run using the same voltage settings was carried out (test Z1327, as per Table 4.2) and will be discussed in more detail in the following subsection.

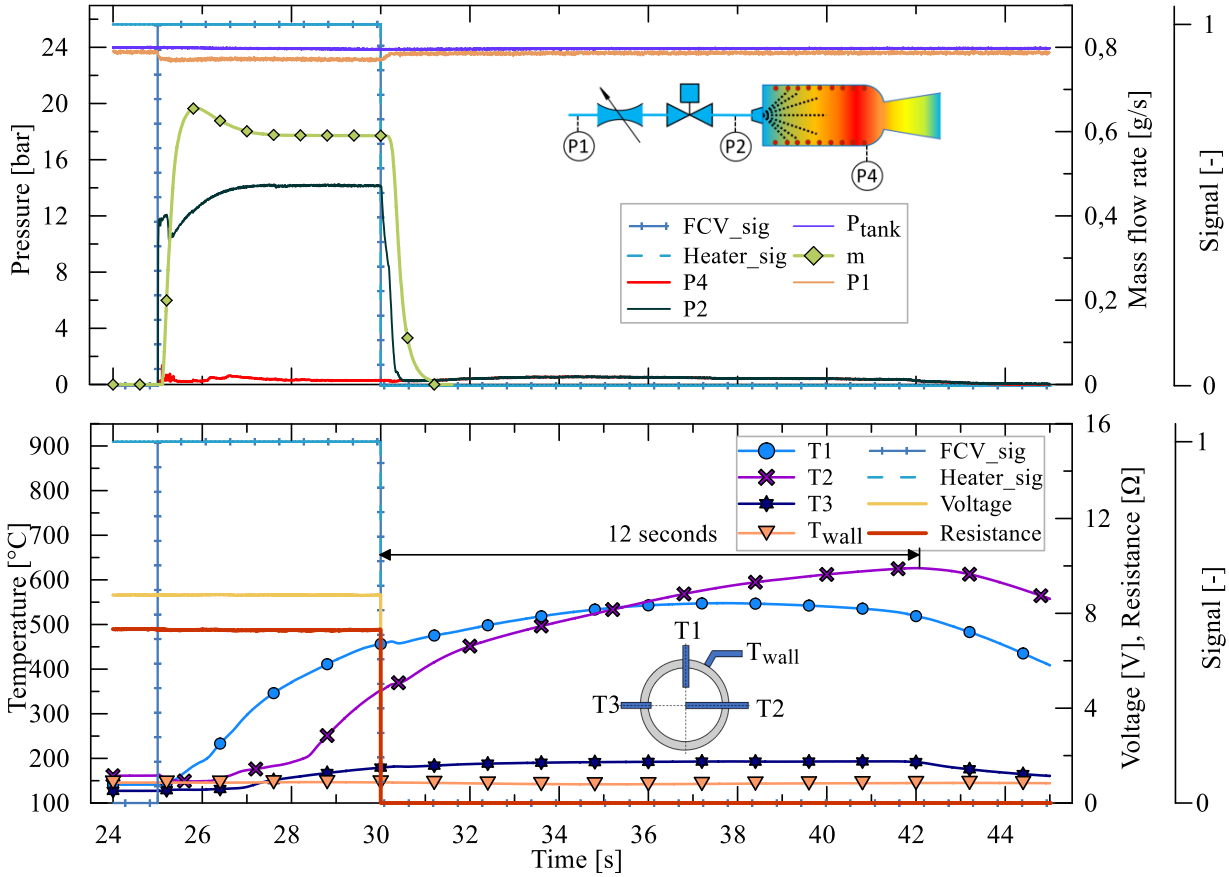

Figure 4.18 A Five-second experiment, Z1326, carried out at a supply voltage of 9 V; the mean heater power during the preheating phase was 10,6 W.

Figure 4.19 shows experiment Z1353, for which the heater power was 14W. This test was shown for comparison purposes, as the *T2* thermocouple (centrally located) measured nearly the same temperature at the moment when the propellant injection was initiated as in the previously shown experiment Z1184 (Figure 4.4), carried out with a heater power of 310 W. When the opening command signal was sent to the valve, temperatures measured by *T1*, *T2*, *T3* and T_{wall} thermocouples were, respectively, 177, 200, 160 and 184°C for test Z1353 and 142, 195, 44 and 45°C for Z1184. Apart from temperatures, the mean current measured during the preheating phase before initiating test Z1353 was 1,37 A. Using extrapolated data presented in Figure 3.9 (a), a rough estimation of the heating cable temperature gives a value of 210°C. On the other hand, in the case of test Z1184, the measured current was 8,05 A, which means that

the estimated cable temperature was more than 1000°C, as discussed in section 4.1.3. Despite nearly the same temperature measured by the thermocouple *T2*, with a much higher heating cable temperature during test Z1184, the pressure rise for test Z1353 was more prompt than during test Z1184, for which the chamber pressure was nearly zero for the first two seconds after propellant injection was started.

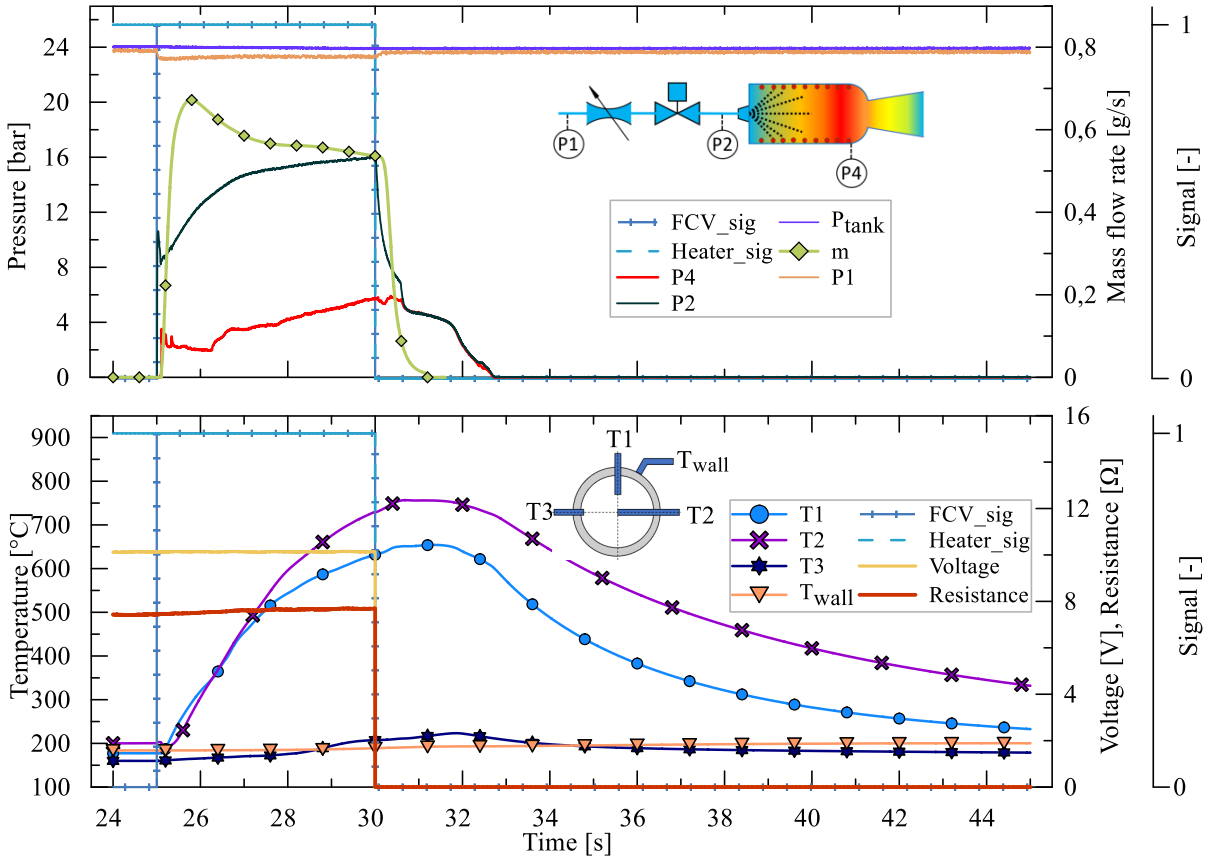

Figure 4.19 A Five-second experiment, Z1353, carried out at a supply voltage of 10,5 V; the mean heater power during the preheating phase was 14 W.

Test Z1354 was a 70-second run for which the heater power was as for Z1353; temperatures measured before opening FCV were 163, 198, 159 and 182°C, respectively, for *T1*, *T2*, *T3*, T_{wall}. The measured rise time was 4,26 s (5,48 s for Z1184), and the pressure started to build up directly after opening the valve and stabilised after ~10 seconds. The most significant difference between compared high and low-power tests (Z1184 and Z1353/Z1354) was the initial wall temperature, which in the case of the high-power experiment was only 45°C – this parameter seems to be crucial whenever a rapid and reliable response is required.

Figure 4.20 shows test Z1364, carried out at a mean heater power of 20,2 W – the highest tested in order not to damage the Viton seals. Before opening the FCV, $T2_{op}$ and T_{wall_op} were 266 and 244°C. Such conditions were sufficient to initiate relatively smooth decomposition right from the start. At the end of the test, the pressure nearly stabilized at a value of 6 bar. The

maximum *T2* temperature registered was 810°C, and the peak value occurred only about 330 ms after closing the valve.

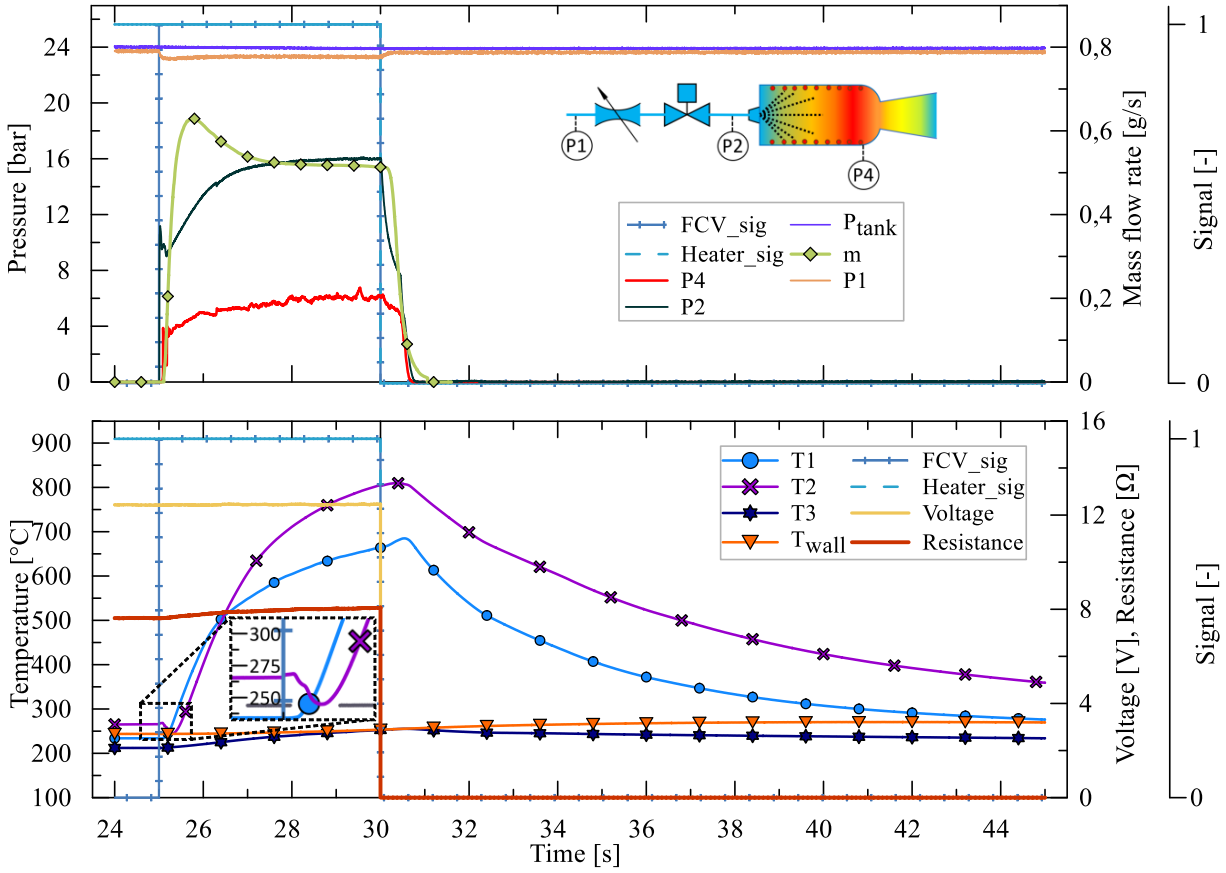

Figure 4.20 A Five-second experiment, Z1364, carried out at a supply voltage of 13 V; the mean heater power during the preheating phase was 20,2 W.

Figure 4.21 was prepared to directly compare the maximum pressures captured during short tests, the heater powers used, and the resulting wall temperatures achieved – a colour scale was added to identify the heater power for each data point included in the figure.

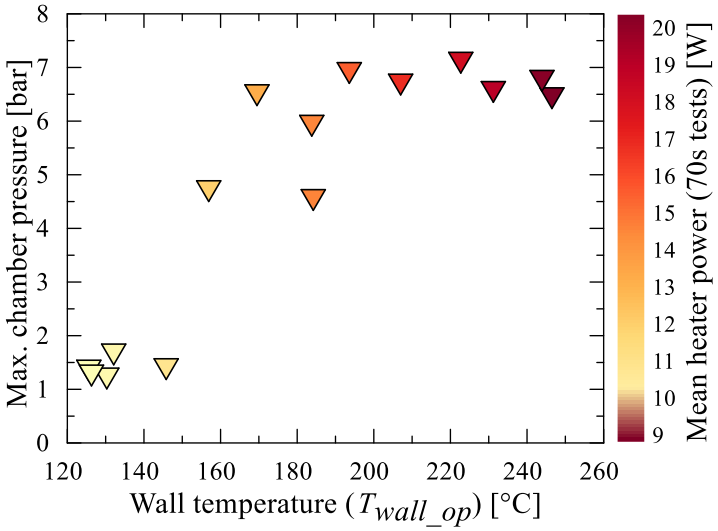

Figure 4.21 Maximum chamber pressures captured during 5-second runs as a function of wall temperatures, T_{wall_op}, captured before opening the FCV.

The steady-state pressure, determined for the long, 70-second experiments, was ~6 bar. As can be viewed in Figure 4.21, such pressure was obtained at a wall temperature as low as 170°C (mean heater power of 12,7W). Another observation is that below a temperature of 150°C, the maximum pressure was on the order of 1 up to 2 bar and was, in each case, only achieved through a rapid, short spike directly after opening the valve.

Figure 4.22 (a) and (b) show how the pressure decay time changed with *T2* and T_{wall} temperatures measured in the pressure decay period. The measured pressure decay time, for comparison purposes and because of highly inefficient decomposition in some cases, was measured from when the valve was closed to when the chamber pressure, *P4*, fell to an arbitrarily selected value of 0,05 bar. As can be seen, the decay time was from 22,2 to 0,7 s; the latter value is comparable to the lowest value obtained during the high-power campaign. As can be seen in Figure 4.22 (a) and (b), the fall time decreases linearly with $T2_{m\_fall}$ chamber temperature (R^2 = 0,94), while the relation for wall temperature is exponential with R^2 = 0,98 (logarithmic scale was used to present the data).

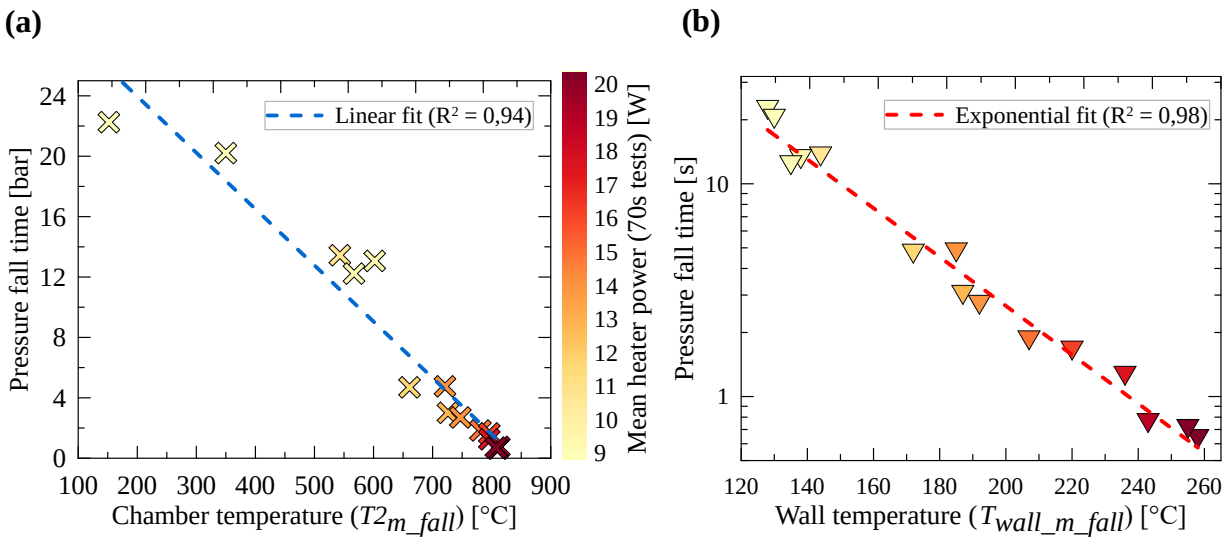

Figure 4.22 Pressure fall time during 5-second, low-power experiments. Fall time measured from when the FCV was commanded to close to when chamber pressure fell to 0,05 bar – results presented as a function of **(a)** $T2_{m\_fall}$ chamber temperature; **(b)** $T_{wall\_m\_fall}$ temperature.

4.2.2.3 Analysis of 70-second tests

Altogether, nine 70-second tests were performed at a reduced heater power. Basic information and identification numbers can be found in Table 4.3. In Table 4.3, a distinction was made between mean values of temperature and chamber pressure measured in periods when the heater was turned on – the last five seconds before turning the heater off (t = 60 to 65 s) and the last five seconds before closing FCV, when the heater was turned off (t = 90 to 95 s).

Table 4.3 Set of 70-second experiments performed within the framework of a low-power campaign.

No.	ID	t_{run} [s]	Heater on (t = 60:65 s)			Heater off (t = 90:95 s)		
			$P4_{5s\_h}$ [bar]	$T2_{5s\_h}$ [°C]	$T_{wall\_5s\_h}$ [°C]	$P4_{5s\_nh}$ [bar]	$T2_{5s\_nh}$ [°C]	$T_{wall\_5s\_nh}$ [°C]
1	Z1327	70	6,66	804	199	6,11	885	257
2	Z1335		6,10	870	236	6,00	890	286
3	Z1337		6,00	883	275	5,97	896	312
4	Z1354		6,09	874	301	6,06	851	365
5	Z1356		6,12	882	304	6,06	853	366
6	Z1358		6,11	866	321	6,05	861	403
7	Z1360		6,07	864	336	6,05	859	414
8	Z1362		6,09	877	360	6,09	882	434
9	Z1365		6,15	878	364	6,12	873	418

What can be observed is that except for the first test, denoted as Z1327, presented in Figure 4.23, the difference between chamber pressure for the heated and non-heated periods is within the measurement error of the pressure transmitter used.

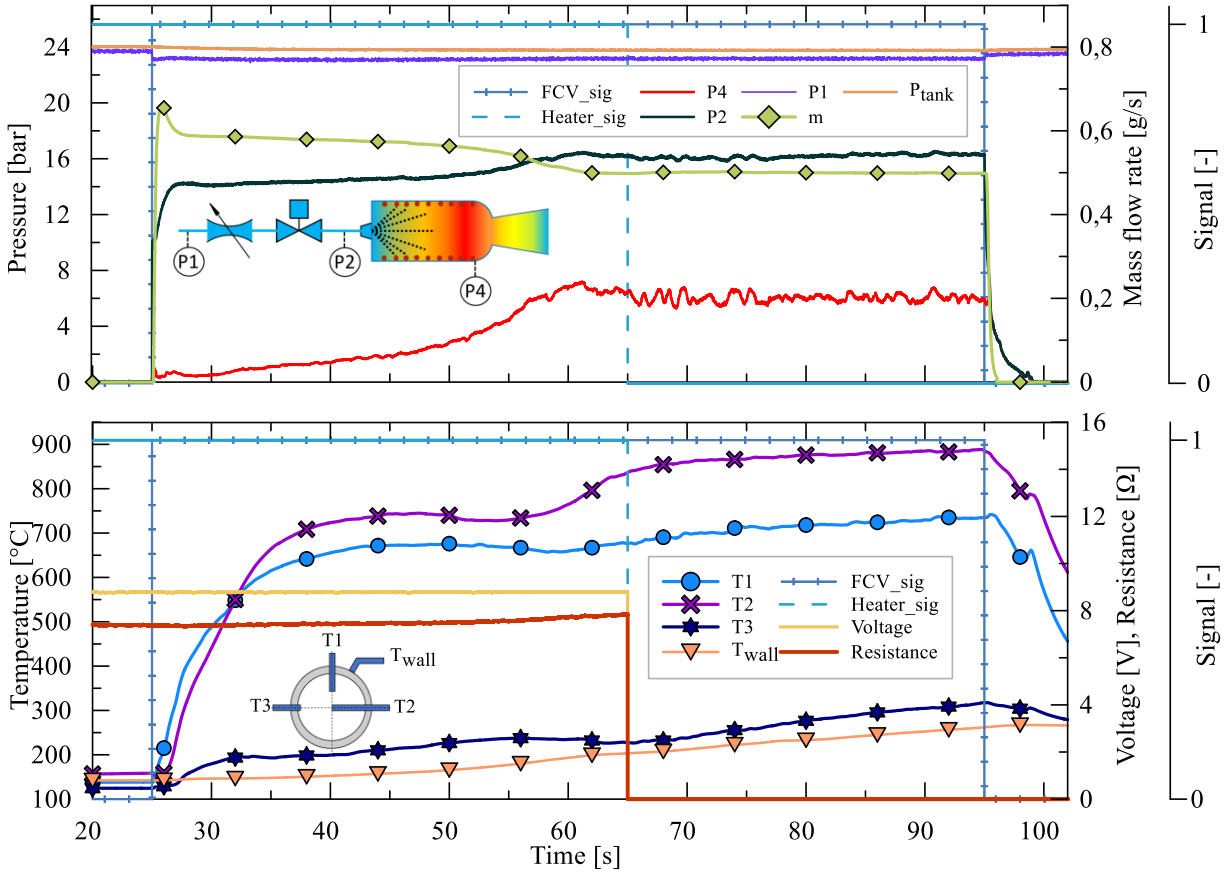

Figure 4.23 Results gathered during experiment Z1327, performed at reduced heater power; the supply voltage was 9 V, mean heater power during the 30 min preheating phase amounted to 10,6 W.

The reason for higher pressure in the heated period of the test Z1327 is propellant accumulation in the chamber and rapid decomposition of the excess compound after the conditions were favourable. As for the chamber temperature, *T2*, for the test Z1327, the difference between

the mean *T2* temperature measured in the discussed periods was 81°C – a higher temperature was achieved at the end of the run; this can be explained by the fact that the accelerating reaction at the end of the heated phase was far from optimal, as liquid propellant was, to some extent, present in the chamber and expelled through the nozzle. As can be seen in Figure 4.23, the chamber temperature, *T2*, rose significantly up to a value of ~680°C at t = 35 s (10 seconds after opening the valve) during the initial phase of the test and changed only slightly until t = ~54 s, when the accelerated rise was observed, continuing in the period when the heater was turned off, reaching a maximum value of 888°C right before closing the valve. Directly after the heater was turned off, increased chamber pressure fluctuations were observed, but the process slightly stabilized with time. Apart from the initial phase, until t = ~40 s, the wall temperature rose throughout the experiment, reaching a value of ~260°C at the end of the test.

Figure 4.24 depicts experiment Z1365, for which the highest heater power in this part of the test campaign was applied and amounted to 20,4 W. The initial wall temperature, T_{wall_op}, for the test Z1365 was 257°C. The pressure roughness measured for the heated and non-heated phases was 0,81 and 0,49%, respectively, the latter being the lowest value obtained during the entire test campaign presented in this thesis.

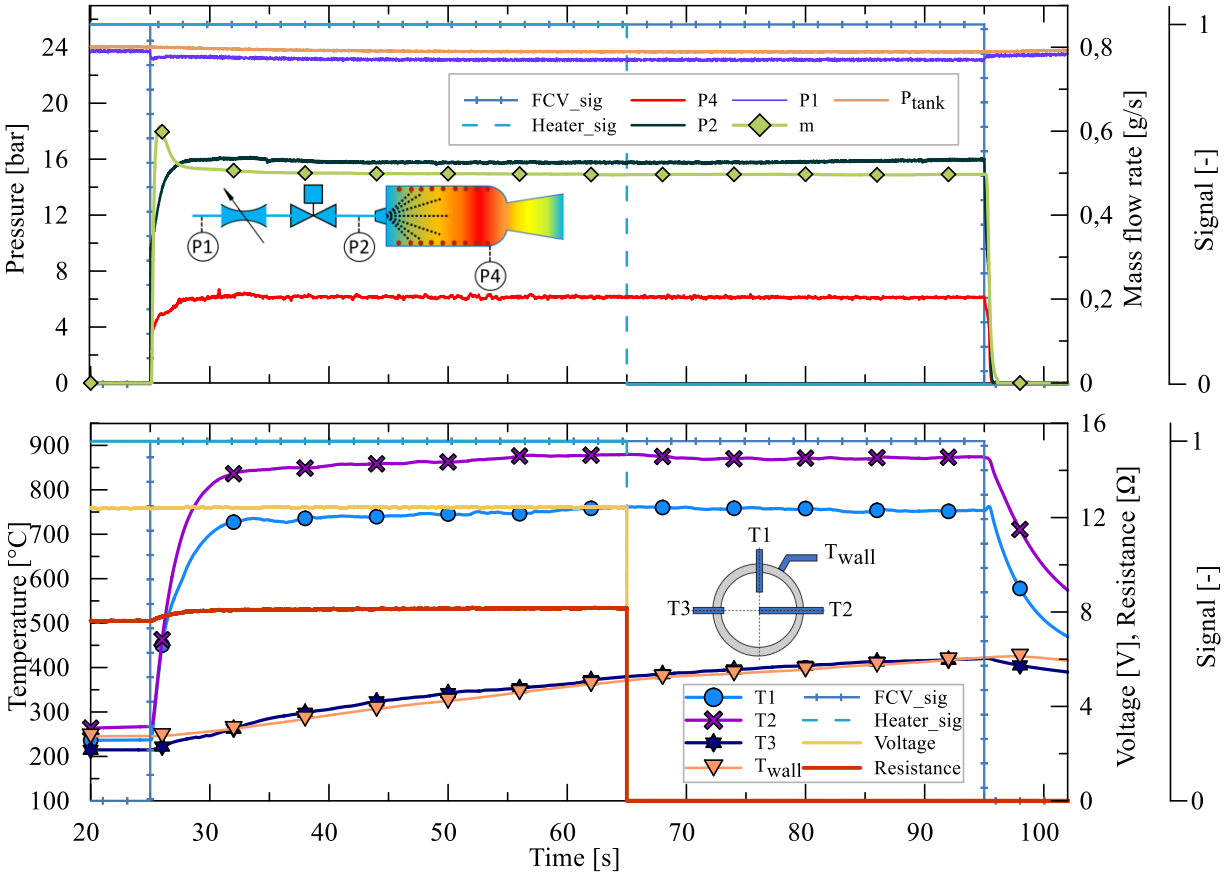

Figure 4.24 Results gathered during experiment Z1365, performed at reduced heater power; the supply voltage was 13 V, mean heater power during the 30 min preheating phase amounted to 20,4 W.

The rise time was 1,92 s, and a slight overpressure can be noted until t = 34 s; next, very smooth decomposition was achieved, and turning off the heater did not negatively affect the course of the pressure. The pressure difference for the periods when the heater was on and off was 0,025 bar, which is 20% of the total error of the transmitter. The rise in the wall temperature was undisrupted throughout the run, reaching 420°C before stopping the flow. As for the chamber temperature, *T2*, the rapid rise occurred directly after opening the valve, and at t = 32 s, 6 seconds after starting the flow, a value of 840°C was measured, and the reading insignificantly rose until the heater was turned off, reaching 880°C. In the non-heated period, a slight decrease was observed, leading to 870°C at the moment when the control signal was sent to the valve. As can be viewed in Table 7, the difference in the mean *T2* temperatures for both time periods considered was 5°C. It can be noted that the difference in *T2* is only significant for test Z1327 – the cause was discussed previously. For the remaining experiments, the difference is lower, reaching only 5°C for the last four tests.

Pressure rise and fall time

Figure 4.25 shows the relation between the pressure rise time and measured temperatures. Due to the relatively uniform temperature of the test article after the preheating phase, resulting from long preheating time and the insulation used, the difference between temperatures is not significant – as was discussed previously.

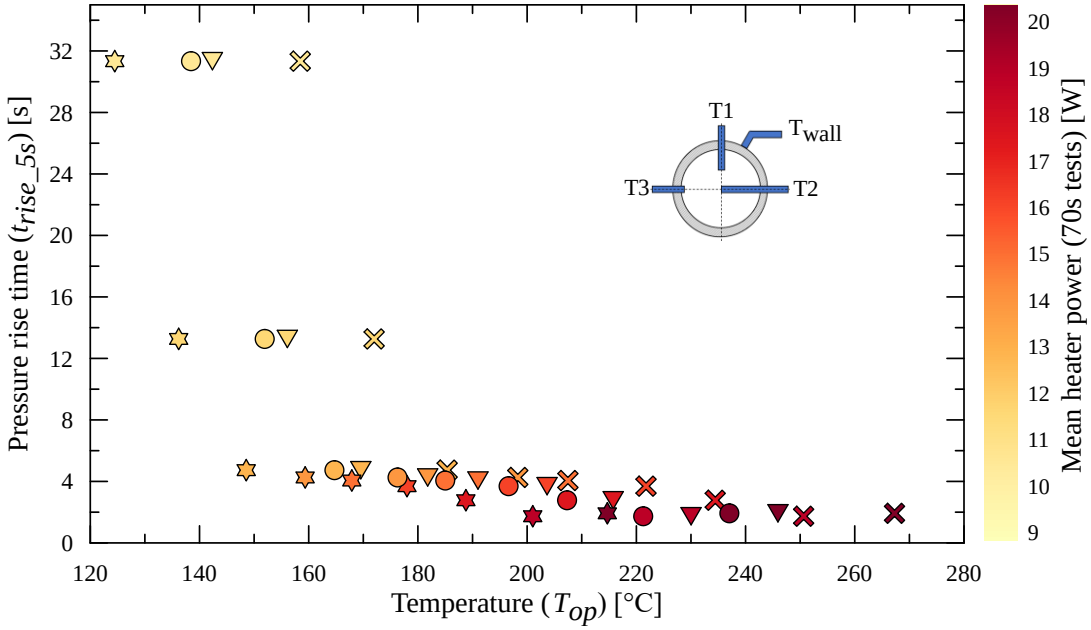

Figure 4.25 Pressure rise time, t_{rise_5s}, for 70-second experiments executed at reduced heater power, measured from when the valve was commanded to open to when chamber pressure rose to 90% of the mean value measured during the last 5 s before turning the heater off. Results presented as a function of temperatures captured before opening the FCV, T_{op}.

Figure 4.26 was prepared for clarity to show only the variation of the pressure rise time with wall temperature, T_{wall_op}. The measured rise time was from 31,3 to 1,66 s, and the observed trend can be approximated using a power function curve. It is suspected that conditions obtained after the preheating sequence, before initializing test Z1327 - the one for which the highest rise time was measured - were very close to the limiting conditions allowing initiation of the decomposition. It can also be noted that before opening the valve during the test Z1327, the temperatures $T1_{op}$, $T3_{op}$ and T_{wall_op} were lower than the normal boiling point of the propellant at a concentration used. It must be emphasised that a limited number of temperature measurements carried out does not describe the temperature distribution in the entire test article, and hot spots existed, with the heating cable, being a heat source, always having the highest temperature - which was not measured directly. Therefore, even though thermocouples measured temperatures lower than the normal boiling point, spots existed for which the temperature was higher. This issue will be continued in the following section concerning a comparison of the results obtained.

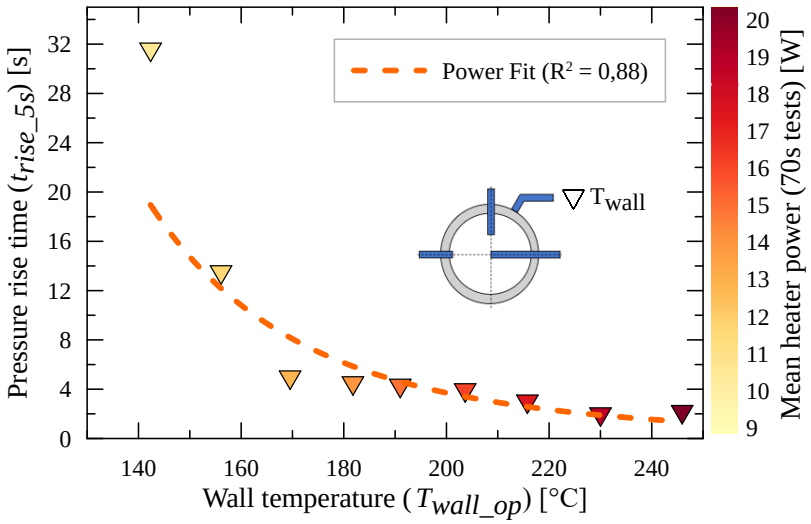

Figure 4.26 Pressure rise time, t_{rise_5s}, for 70-second experiments executed at reduced heater power, measured from when the valve was commanded to open to when the chamber pressure rose to 90% of the mean value measured during the last 5 s before turning the heater off. Results presented as a function of the wall temperature, T_{wall_op}, captured before opening the FCV.

Figure 4.27 depicts the pressure fall time as a function of temperatures measured. The longest tail-off was 3,2 s, while the shortest one amounted to 0,54 s. The latter value agrees well with the measurements carried out during high-power tests, as the mean value for the runs performed using a supply voltage of 50V was 0,62 s, with a standard deviation of 0,13 s. Regarding the supply voltage of 45V, as seen in Figure 4.11 (a), the fall time stabilised at a wall temperature of more than 350°C, and the mean value for that temperature range (350°C and more) was 0,49 s, with a standard deviation of 0,04 s. The evident difference between conditions

present during high and low-power tests that could affect the decay time was the existence of a high-temperature heater, operating until the end of the test during high-power experiments.

As shown in Figure 4.27, the influence of the $T2_{m\_fall}$ chamber temperature on the pressure decay time was limited as completely different results were obtained at similar temperatures. In Figure 4.27, tests Z1327 and Z1354 were marked, for which the pressure decay time was respectively 3,2 and 0,7 s, while the $T2_{m\_fall}$ temperature measured in the decay time was respectively 843 and 844°C. Additionally, for the discussed pair, a comparison was made between the *T2* temperatures captured when the valve was commanded to close; the temperatures registered were 886 and 849°C - a higher value measured for the test Z1327, for which longer pressure decay time was observed. One of the possible explanations for the difference in the pressure decay time is the undecomposed propellant in the chamber at the end of run Z1327, which affected the decay time. This may be supported by the fact that the mean chamber $P4_{5s\_nh}$ pressure measured for the test Z1327 was higher than for the run Z1354, while the mass flow rate in the discussed periods was the same and amounted to 0,5 g/s. On the other hand, the difference in the mean chamber pressure, $P4_{5s\_nh}$ was only 0,05 bar, which is not enough to support the explanation provided.

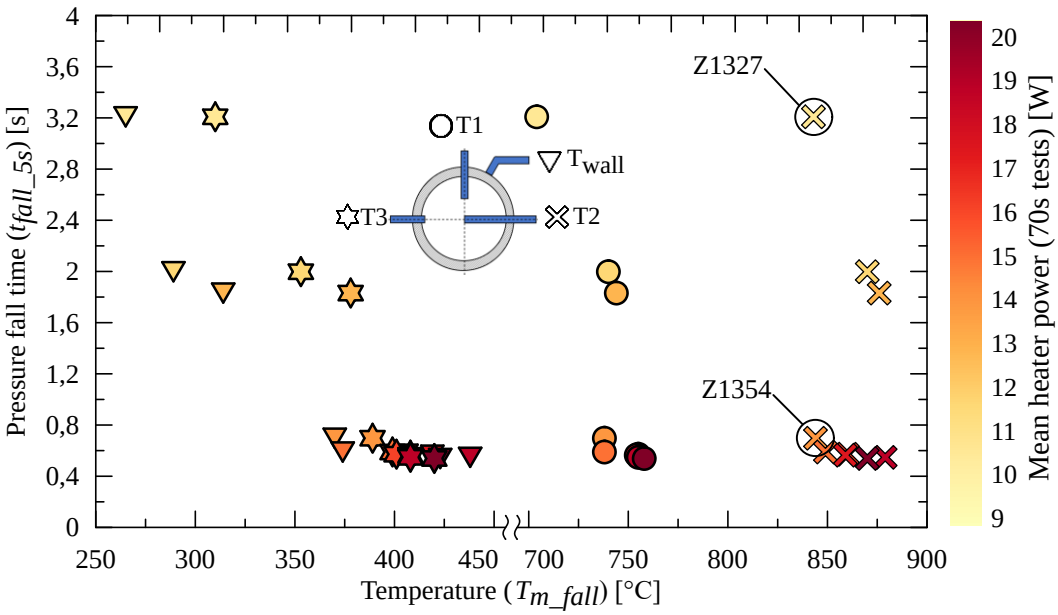

Figure 4.27 Pressure fall time, t_{fall_5s}, for 70-second experiments executed at reduced heater power, measured from when the valve was commanded to close to when chamber pressure fell to 10% of the mean *P4* during the last 5 s before closing the valve. Results presented as a function of mean temperatures in the pressure fall period, $T_{m\_fall.}$

To further explore the discussed topic and the differences encountered, the period taken for analysis was reduced to 2,5 s prior to closing FCV. For such a case, the mean mass flow rate did not change for both compared tests; the same can be stated about the chamber pressure

for the run Z1354, as the mean value was 6,05 bar, 0,01 bar less than for the 5-second interval. The newly calculated mean chamber pressure for experiment Z1327 was 5,99 bar, 0,12 bar less than previously. Relatively high-amplitude and low-frequency pressure fluctuations were observed in the test Z1327, resulting in a change of mean values of pressure depending on the time interval selected for analysis. An additional observation based on Figure 4.27 is a decaying trend for internal chamber temperatures, T1 and T3, with a higher slope for the thermocouple placed close to the wall (*T3*). This indicates the influence of the wall on the results obtained during the discussed measurements. Wall temperature was studied next.

Figure 4.28 was prepared to isolate the data concerning pressure fall time and the wall temperature. The number of data points is low, but the trend is evident, and a power function curve fits the data points very well, with R^2 of 0,94. For wall temperatures of more than 370°C, the pressure decay time remained relatively constant and varied between 0,7 and 0,54 s. This is in good agreement with the results obtained during high-power tests presented in Figure 4.11 (a), but a more detailed discussion concerning the comparison of the data obtained will be given in the following sections, where the results obtained during the 120-second campaign will be shown.

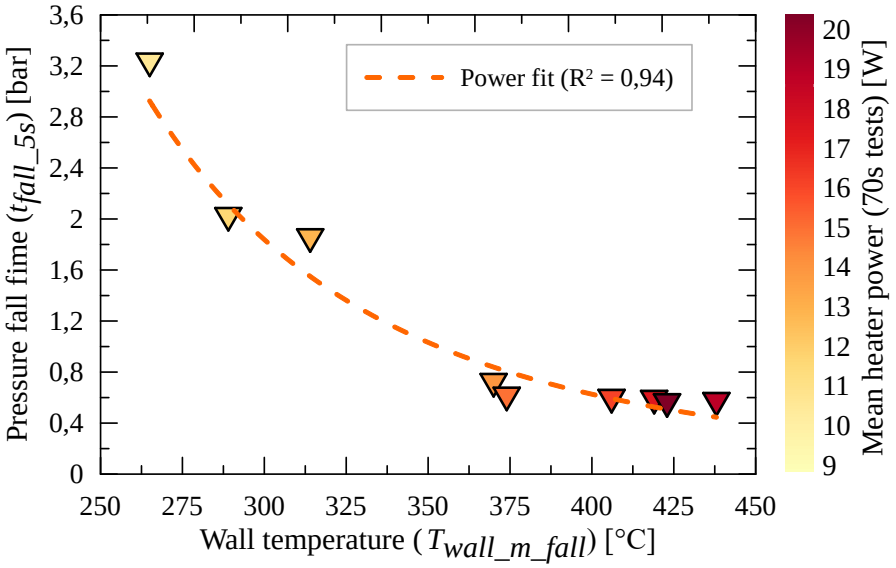

Figure 4.28 Pressure fall time, t_{fall_5s}, for 70-second experiments, executed at reduced heater power, measured from when the valve was commanded to close to when the chamber pressure fell to 10% of the mean value during the last 5 s before closing the valve, as a function of mean wall temperature in the pressure fall period.

Pressure roughness

Pressure oscillations expressed through roughness, obtained when the heater was turned off, were in the range of 0,49 to 4%. Figure 4.29 shows how the pressure roughness, measured in the last five seconds before closing the FCV, changed with temperature for the executed tests.

Trends similar to the pressure fall time were observed, with $T2_{5s\_nh}$ chamber temperature having no observable influence on the results. What is more, as in Figure 4.27, the influence of the wall is visible and alike in the case of results presented in Figure 4.29, a decaying trend was observed for the measurements of $T1_{5s\_nh}$, $T3_{5s\_nh}$ and $T_{wall\_5s\_nh}$, with the highest slope for the wall temperature. As for the roughness during the last five seconds before turning the heater off, no significant difference was observed between the two time periods considered for analysis.

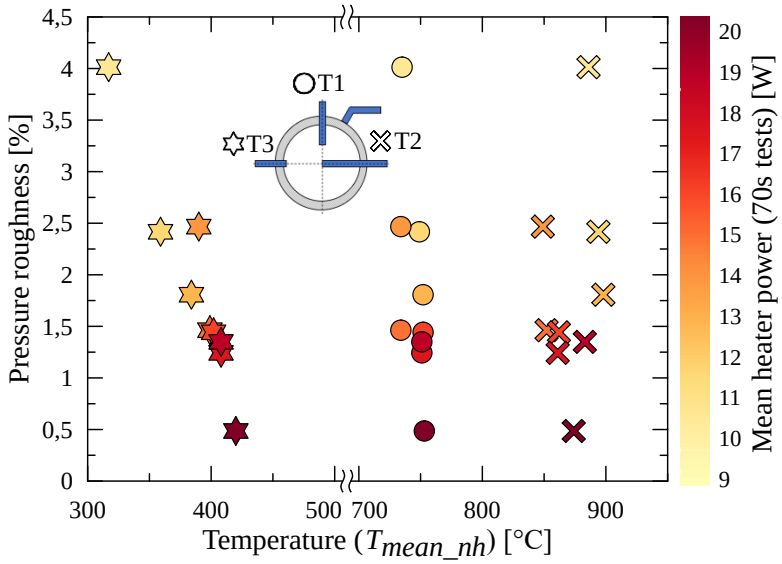

Figure 4.29 Pressure roughness measured for the 5-second period before closing the FCV as a function of $T1_{mean\_nh}$, $T2_{mean\_nh}$, and $T3_{mean\_nh}$

Figure 4.30 was prepared to visualise and compare the roughness decay as a function of the wall temperature for each experiment's heated and non-heated reference period.

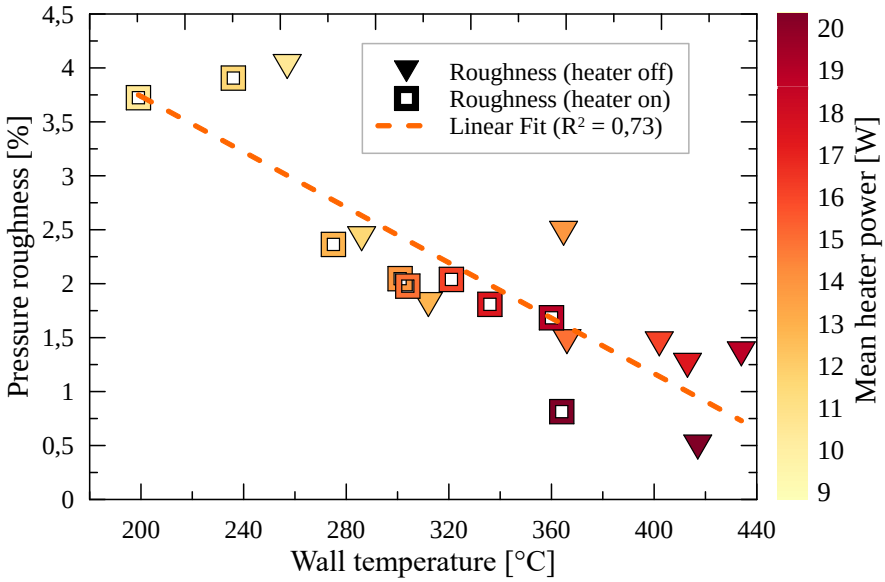

Figure 4.30 Comparison of pressure roughness measured in the 5 s reference periods when the heater was on and off. Tests performed during low-power, 70-second sub-campaign.

Except for two tests, Z1327 and Z1356, the roughness was always lower at the end of the test before closing the valve, when the heater was off. As shown in Figure 4.30, when combining all the data points available, the obtained trend can be fitted with a linear curve with a coefficient of determination of 0,73. Observing a clear threshold within the considered wall temperature range was impossible, but it is expected that a further increase in the wall temperature would not have affected the roughness significantly as for high power mode tests, at a wall temperature above 360°C, the mean roughness was 1,77%, with a standard deviation of 0,68%.

4.2.2.4 Summary

The presented section discussed tests executed at reduced heater power, ranging from 8,8 to 20,4 W. The preheating time before each experiment was extended to 30 minutes. Nine 70-second tests were performed, together with 15 experiments that lasted 5 seconds each, executed prior to long runs, to analyze the results preliminarily. The following highlights are to be pointed out:

- During short 5s runs, it was observed that the maximum pressure captured rose sharply if the external wall temperature before opening the valve exceeded 150°C.
- For 5-second tests, the pressure fall time, down to 0,05 bar, decreased linearly with $T2_{m\_fall}$ and exponentially with the wall temperature, $T_{wall\_m\_fall}$.
- While comparing high and low-power tests featuring nearly similar $T2_{op}$ temperatures, it was found that the start-up characteristics were superior for low-power experiments, for which the wall temperature was higher, and the temperature distribution before opening the valve was more uniform.
- During 70-second tests, data points illustrating the relation between pressure rise time and wall temperature were fitted with a power function. The highest wall temperature before initiating an experiment, due to technical limitations, was 246°C; this allowed to achieve a pressure rise time, t_{rise_5s}, of 1,92 s
- As for long, 70-second runs, it was found that the wall temperature controls pressure fall time and pressure roughness. Data points describing pressure fall time as a function of wall temperature were fitted with a power function curve, while roughness decreased linearly with wall temperature. For a wall temperature of 370°C and more, the pressure decay time remained relatively stable and amounted to ~0,6 s.

- Turning the heater off 40 seconds after the propellant injection was started did not negatively affect the decomposition quality. The process was self-sustaining.

- For most cases, the difference between mean chamber pressure measured in reference periods for the heated and non-heated parts of runs was within the measurement error of the sensor. The difference between $T2_{5s\_h}$ and $T2_{5s\_nh}$ was 5°C for the last four experiments, for which the mean heater power during preheating was between 16,1 and 20,4 W.

4.2.3 Reduced power campaign – 120-second tests

The part of the test campaign described in the current subsection aims to present experiments concerning the final configuration of the test article, which was investigated to extend the previously discussed research and expand the database. Some minor modifications were implemented and will be discussed hereafter.

First, compared to 70-second tests, the duration of experiments was extended to 120 seconds. The heater was active for the first 60 seconds after opening the valve and was deactivated for the remaining part of the run (60 s). As in the previous case, the preheating phase lasted 30 minutes. The software was modified and allowed to change the sampling rate during the experiment, eliminating the notch in the heater signal. As a result, a single experiment included the preheating phase, and the FCV was opened directly after the preheating sequence, which eliminated the temperature decay after preheating and before opening the valve. Next, the thruster's insulation was upgraded by adding ~5mm of the insulating material on the cylindrical part of the chamber; additionally, a cap was used to cover part of the nozzle section. Figure 4.31 compares the temperatures obtained after the preheating phase (70 s tests, before 10 s notch) and before opening the FCV (T_{op}) for each part of the low-power test campaign as a function of the mean heater power during the 30-minute preheating phase.

In Figure 4.31, for clarity, only fit curves were presented (in each case, the coefficient of determination, R^2, exceeded 90%), showing the variation of final temperatures before opening of the FCV and at the end of the preheating phase. Three cases were considered: T_{wall_op} and $T2_{op}$ temperatures for the campaign in which the final experiment duration was 120s and two cases for the part of the campaign in which the run length was 70 s; the first case is the final temperature at the end of the preheating phase, before the ten-second notch when the sampling rate was changed, and the second case are temperatures measured before opening the FCV. It

can be noted that initial temperatures for the discussed conditions (120 s tests) are nearly the same as in the preheating phase for the 70s tests; therefore, the direct influence of the additional insulation is insignificant, as measured by the thermocouples available.

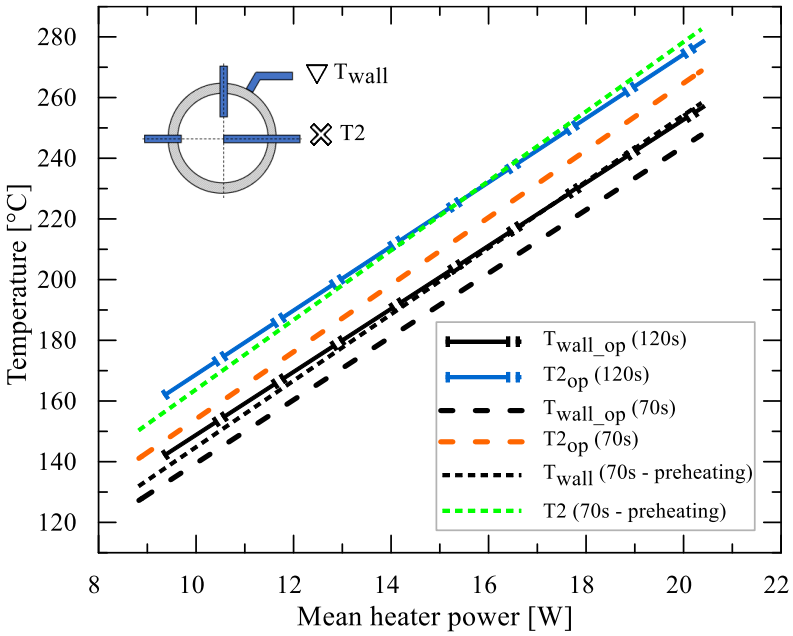

Figure 4.31 Temperatures measured directly before opening the flow control valve (T_{wall_op} and $T2_{op}$) and temperatures after the preheating phase, before the 10 s notch, for 70-second tests ($T2$ and T_{wall}).

As in the previously discussed 70-second, low-power runs, before 120 s experiments were carried out, short tests were performed, lasting five seconds. Such runs were carried out for each supply voltage investigated. Table 4.4 summarizes all eleven short tests along with some basic information concerning the voltage settings, mean heater power in the preheating phase, $T2_{op}$ and T_{wall_op} and corresponding pressure fall time, down to 0,05 bar, denoted here as $t_{fall\_0,05}$, together with maximum chamber pressures, $P4_{max}$, measured during the experiment.

Table 4.4 Primary data concerning 5s experiments conducted within the framework of a 120s low-power campaign

No.	ID	U_{sup} [V]	P_{mean} [W]	$T2_{op}$ [°C]	T_{wall_op} [°C]	$t_{fall\_0.05}$ [s]	$P4_{max}$ [bar]
1	Z1415	8,5	9,33	159	140	16,28	0,64
2	Z1417	8,5	9,32	159	140	9,88	1,89
3	Z1423	9	10,50	174	156	2,76	6,18
4	Z1424	9	10,51	205	157	3,41	6,10
5	Z1425	9	10,53	175	156	3,87	5,96
6	Z1438	9,5	11,46	185	167	1,89	6,16
7	Z1439	9,5	11,45	185	167	1,95	6,22
8	Z1454	10	12,53	194	175	1,57	6,46
9	Z1455	10	12,45	194	174	1,68	6,02
10	Z1463	10,5	13,62	209	187	1,59	5,69
11	Z1464	10,5	13,65	207	187	1,36	5,93

Figure 4.32 shows an exemplary 120 s test, Z1443, performed at a supply voltage of 9,5 V and a mean heater power of 11,4 W. Before initiating propellant flow, the wall and *T2* chamber temperatures were 166 and 184°C, respectively – such initial conditions allowed to achieve a pressure rise time, t_{rise_5s}, of 2,8 s.

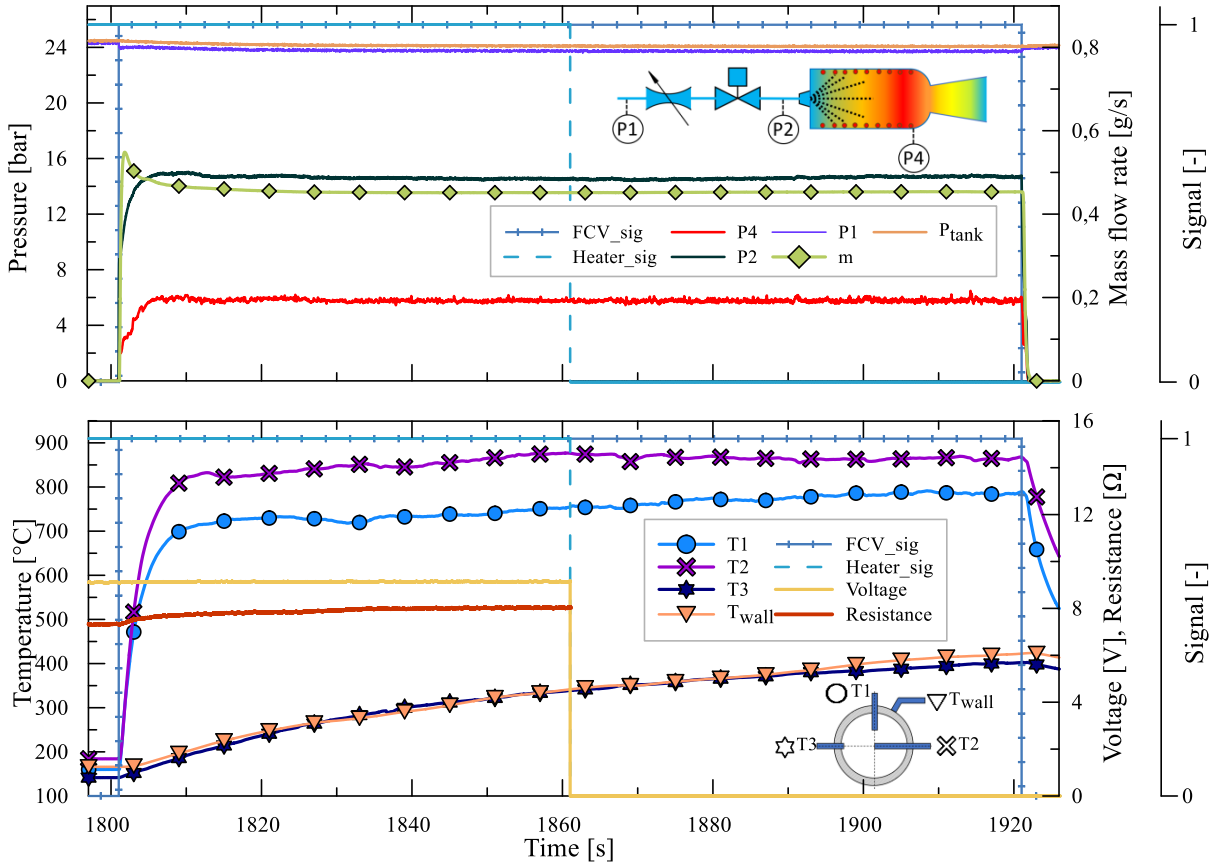

Figure 4.32 Results gathered during 120-second experiment Z1443, performed at reduced heater power; the supply voltage was 9,5 V, mean heater power during the 30 min preheating phase amounted to 11,4 W.

The chamber pressure trace during test Z1443 was smooth, but as can be viewed in Figure 4.32, the fluctuations slightly rose at the end of the run when compared to the first half of the experiment, and the roughness measured in 5 s reference periods when the heater was on and off amounted to 1,1 and 1,8% with a mean chamber wall temperature of 337 and 420°C, respectively.

Table 4.5 gathers data concerning long, 120 s tests and information such as mean heater power, P_{preh}, mass flow rate, $\dot{m}_{5s}$, chamber pressure, $P4_{5s}$, mean internal chamber temperature, $T2_{5s}$ and wall temperature, T_{wall_5s} for the 5-second periods when the heater was on and off.

Altogether, thirty 120 s runs were carried out. During tests, the heater power ranged from 9,3 to 20,4 W. Five runs were performed for each voltage, except for the last configuration tested, for which the voltage setting was raised from 10,5 to 13 V (yielding power of 20,4 W). As for

the short tests, in most cases, two experiments were carried out for each supply voltage, except for a voltage setting of 9 V; in that case, it was decided to extend the number to three.

Table 4.5 Primary data concerning low-power, 120-second experiments.

No.	ID	P_{preh} [W]	Heater on (t=55:60 s)				Heater off (t=115:120 s)			
			$P4_{5s\_h}$ [bar]	$T2_{5s\_h}$ [°C]	$T_{wall\_5s\_h}$ [°C]	$\dot{m}_{5s\_h}$ [g/s]	$P4_{5s\_nh}$ [bar]	$T2_{5s\_nh}$ [°C]	$T_{wall\_5s\_nh}$ [°C]	$\dot{m}_{5s\_nh}$ [g/s]
1	Z1418	9,3	5,90	856	289	0,468	5,93	860	368	0,465
2	Z1419	9,3	5,95	864	285	0,471	5,93	873	362	0,467
3	Z1420	9,3	5,96	863	286	0,47	5,93	870	382	0,467
4	Z1421	9,3	5,96	861	314	0,468	5,96	854	407	0,465
5	Z1422	9,3	5,96	870	313	0,475	5,92	865	427	0,471
6	Z1399	10,3	5,97	870	327	0,477	5,93	868	444	0,475
7	Z1401	10,3	5,97	870	332	0,474	5,95	865	439	0,474
8	Z1402	10,2	6,02	856	330	0,474	5,99	860	428	0,475
9	Z1403	10,2	6,03	869	341	0,48	6,05	871	448	0,479
10	Z1404	10,2	5,98	848	344	0,477	5,96	870	443	0,476
11	Z1433	10,5	5,90	852	310	0,456	5,89	861	377	0,453
12	Z1434	10,5	5,84	856	299	0,458	5,85	866	370	0,456
13	Z1435	10,5	5,84	860	304	0,456	5,81	873	378	0,454
14	Z1436	10,5	5,79	847	311	0,455	5,79	863	373	0,453
15	Z1437	10,5	5,82	849	311	0,461	5,82	872	380	0,459
16	Z1440	11,5	5,72	855	320	0,449	5,67	857	390	0,449
17	Z1441	11,5	5,81	857	354	0,454	5,83	848	442	0,453
18	Z1442	11,4	5,82	869	340	0,456	5,79	860	425	0,456
19	Z1443	11,4	5,77	875	337	0,453	5,76	864	420	0,452
20	Z1445	11,4	5,74	857	326	0,454	5,76	864	402	0,452
21	Z1456	12,4	5,64	870	317	0,444	5,58	874	399	0,442
22	Z1457	12,4	5,75	845	341	0,454	5,73	866	404	0,453
23	Z1460	12,4	5,70	861	339	0,45	5,68	880	423	0,449
24	Z1461	12,5	5,67	853	345	0,446	5,67	871	421	0,446
25	Z1462	12,4	5,71	855	348	0,451	5,73	870	418	0,451
26	Z1465	13,6	5,66	856	359	0,445	5,69	871	423	0,443
27	Z1466	13,7	5,78	846	352	0,451	5,78	871	431	0,449
28	Z1468	13,7	5,84	854	359	0,459	5,87	871	430	0,457
29	Z1470	13,7	5,84	852	367	0,459	5,86	870	427	0,458
30	Z1471	20,4	5,90	883	422	0,457	5,85	888	481	0,457

As seen in Table 4.5, turning off the heater in the middle of the run did not affect considerably either chamber pressure or temperature. The difference between $P4_{5s\_h}$ and $P4_{5s\_nh}$ was within the measurement error of the sensor and was up to 0,05 bar. The mean *T2* chamber temperature, measured in reference periods, for 23 experiments was higher when the heater was turned off.

The results presented will be analysed and discussed in more detail in the following subsections, along with the overall data comparison.

4.3 Comparison of the results

This section compares the results obtained during the entire test campaign presented in this dissertation. The data points corresponding to each part of the test campaign and specific metrics were presented in common figures, and the results were discussed and summarized. First, a comparison was made between the results gathered during 5-second tests executed before long runs in low-power sub-campaigns. The following subsection will present an analysis of 70 and 120-second experiments, and the results will be compared with data corresponding to the high-power investigation.

4.3.1 Analysis of 5-second tests

Figure 4.33 was prepared to compare the results gathered during 5-second tests performed during 70 and 120-second campaigns and shows how the maximum *P4* chamber pressure, captured during runs, changed as a function of the initial wall temperature, T_{wall_op}, measured directly before opening the FCV. It can be noted that data points corresponding to 120s trials fit well with the previously presented results concerning the 70s campaign. As previously, a sharp rise can be observed in the maximum chamber pressure when crossing the temperature threshold, amounting to the normal boiling point of the propellant used. In Figure 4.33 and the following figures, for clarity, two colour scales for mean heater power were included, separately for 70 and 120 s tests.

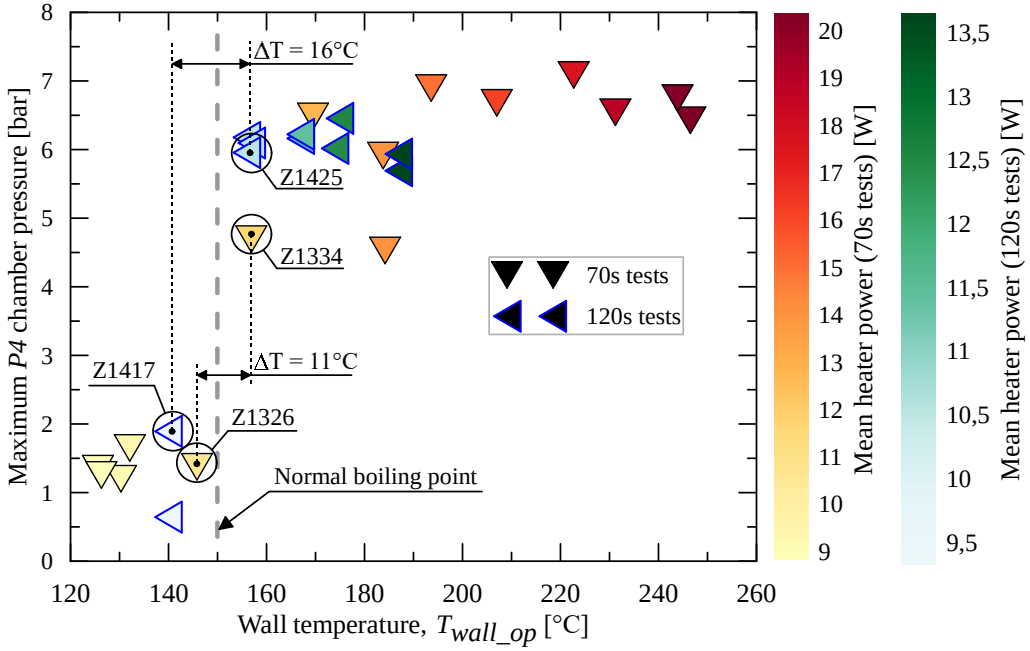

Figure 4.33 Maximum chamber pressure, *P4*, measured during low-power, 5-second tests as a function of the initial wall temperature, T_{wall_op}, captured before initiating the propellant flow.

In Figure 4.33, selected data points were encircled, corresponding experiment identifiers were marked, and the difference in wall temperature (T_{wall_op}) was highlighted. It can be noted that a difference in the wall temperature on the order of 11°C for the 70 s campaign and 16°C for the 120s campaign resulted in substantially higher chamber pressures measured. In the case of tests Z1326 and Z1334, the wall temperatures before opening the valve and maximum chamber pressures were respectively 146°C; 1,38 bar and 157°C; 4,7 bar. As for tests Z1417 and Z1425 (120 s campaign), the values were 140°C; 1,9 bar and 156°C; 5,96 bar.

Another metric used for comparison was the highest *T2* chamber temperature measured during the 5-second test in the period when the valve was in an open position. As was presented in section 4.2.2.2, during some tests, the highest *T2* temperature was obtained after closing the valve – such a temperature was not used in the presented comparison, as the goal was to study the dynamic response of the unit. Figure 4.34 shows how the *T2* temperature, measured at the moment when the FCV was commanded to close ($T2_{Cvc}$), changed as a function of the wall temperature measured when the propellant flow was initiated (T_{wall_op}). As can be viewed, the difference in $T2_{Cvc}$ for tests Z1326 and Z1334 was 299°C, and for experiments Z1417 and Z1425 was 262°C. As before, the difference in initial wall temperatures for the pairs discussed was 11 and 16°C. Results presented in Figure 4.33 and Figure 4.34 are obviously connected, as efficient decomposition results in rapid pressure build-up and high decomposition temperature is an output.

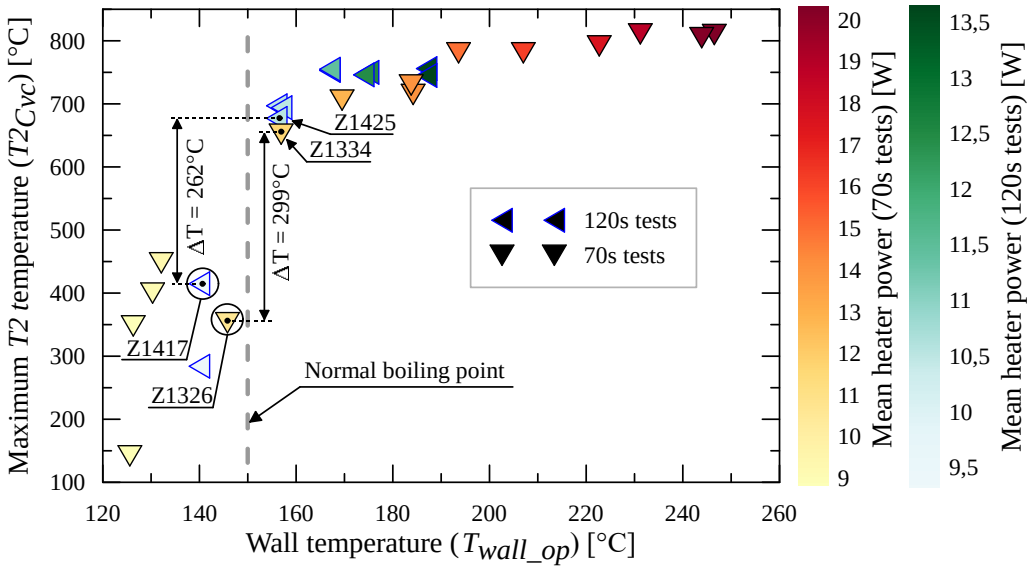

Figure 4.34 Relation between the $T2_{Cvc}$ chamber temperature captured before closing the valve at the end of 5 s tests as a function of the wall temperature (T_{wall_op}) measured before initiating the propellant flow.

Figure 4.35 presents the pressure fall time, measured from when the valve was closed to when the *P4* chamber pressure fell to 0,05 bar, as a function of the mean wall temperature in

the pressure fall period. The mean wall temperature for seven tests was below 150°C, and the lowest pressure fall time measured for that 7-point dataset was 9,9 s (test Z1417). As for experiment Z1425, the fall time was 3,9 s – the difference was 6 seconds, while the difference in the wall temperature was 36°C (143 and 179°C, respectively, for tests Z1417 and Z1425). The same was observed for runs performed during the 70 s test campaign. In the case of runs Z1326 and Z1334, the fall times were respectively 13,4 and 4,7s, while the reference wall temperatures amounted to 144 and 172°C, yielding a difference of 28°C; it is worth recalling that when the valve was opened, the initial difference in wall temperature was 11°C. In Figure 4.35, discussed tests were marked, and differences in the pressure fall time for each pair considered were provided. A magnified area was added in Figure 4.35 to highlight the difference between the results obtained for 70 and 120 s tests; it can be viewed that trends are similar, being exponential relations, fitting the data points well, as the coefficient of determination is greater than 0,95 in each case, but the trend lines are slightly shifted.

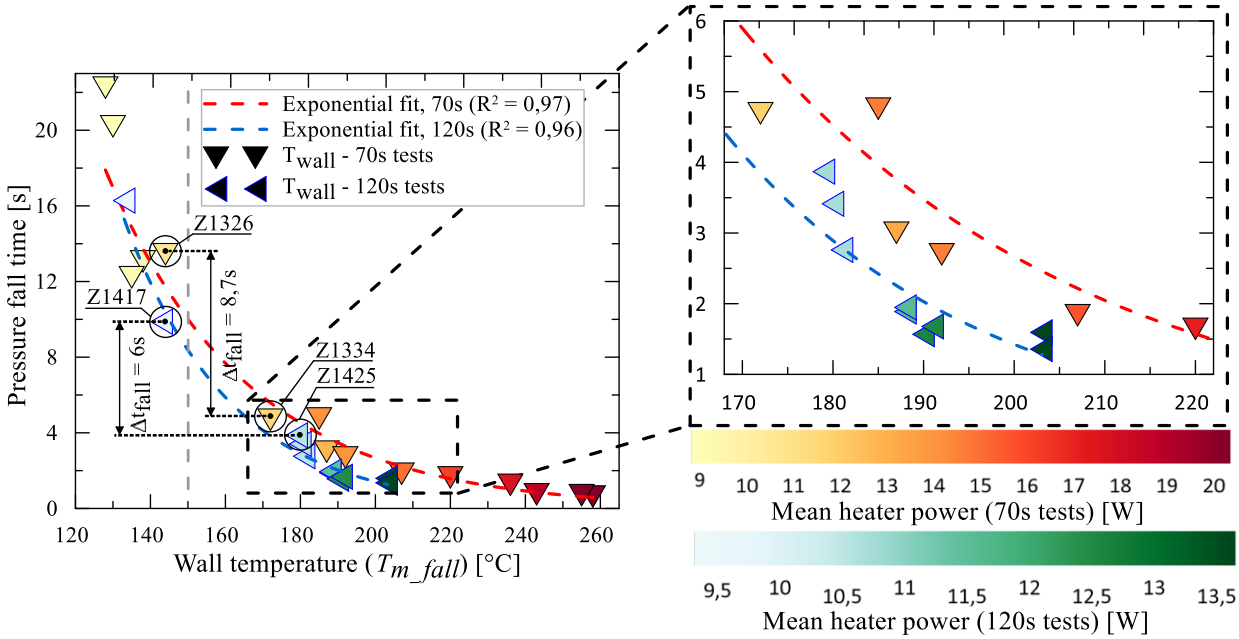

Figure 4.35 Pressure fall time, down to 0,05 bar, as a function of mean wall temperature measured in the pressure fall period during 5-second, low-power experiments.

A possible explanation for the shift is the temperature distribution that could be positively affected due to the upgraded insulation of the chamber. Consequently, more favourable conditions could be achieved, allowing the pressure to fall more rapidly while executing tests concerning 120-second campaign. As the wall temperature was measured only at a single point on the wall's outer side, it was impossible to examine the temperature distribution thoroughly.

A concluding remark concerning the presented comparison is that if the chamber's temperature is greater than the normal boiling point (experiments were conducted at

atmospheric pressure), it is possible to initiate a relatively smooth decomposition reaction. It must be highlighted again that for some tests discussed here, the wall temperature was lower than 150°C; however, minor chamber pressure and temperature rise were registered despite that. This can be explained by the fact that for the cases in which the lowest initial wall temperature of 125°C was measured, the corresponding *T2* chamber temperature was 140°C; this implies that the temperature of the heat source, the heating cable exceeded 150°C making it possible to initiate the reaction. Further research is necessary to understand the process in more detail, as the variables affecting the results are, e.g. the chamber design and geometry, chamber materials (catalytic properties), injection type and mass flow rate of the propellant.

4.3.2 Long tests; high and low heater power - comparison

This section discusses the combined results obtained for the high and low-power modes. Pressure rise times, roughness and pressure fall times were compared. Additionally, characteristic velocity was analyzed as an essential parameter concerning chemical rocket propulsion. The results were presented in common figures in dedicated subsections.

4.3.2.1 Pressure rise time

Figure 4.36 shows how the pressure rise time changed with the initial wall temperature for all long runs performed in the test campaign presented and discussed in this thesis. As can be noted, up to the initial wall temperature, T_{wall_op}, of approximately 200°C, the data points follow different trends. Above that value, the results converge and seem to follow a common trend. Few sources of initial (T_{wall_op} below 200°C) discrepancy can be identified.

As for the high-power mode, it must be emphasized that experiments were carried out at conditions far from a steady state. The heater power in each test was up to two orders of magnitude higher when compared to the low-power experiments, resulting in much higher heating cable temperature, and the preheating time was from ~50 to 300 times shorter; on that account, the external wall temperature measured before opening the valve did not reflect internal conditions accurately. That is why, e.g. for the supply voltage of 50V and measured initial wall temperature of ~50°C, it was possible to obtain pressure rise times comparable to wall temperatures of 150 and 200°C for 120 and 70-second, low-power tests.

In the case of low-power experiments, a difference in trends between 70 and 120 s tests is clearly visible; the rise time for 120-second tests is considerably shorter. A possible cause could be the upgrade of the chamber insulation.

Another possible factor was the break in the preheating process implemented during 70 s tests. Possibly, after turning off the heater (the heater was off for 10 seconds), the temperature of the heating element was lowered significantly and was not raised to the initial temperature during the 20-second sequence (which aimed to compensate for the temperature decay) before opening the FCV. Analysis was performed of the influence of the $T2_{op}$ temperature on the pressure rise time, instead of T_{wall_op}, for 70 and 120s tests, and the offset in trends was still present. The temperature of the heating cable was not measured directly; therefore, further research is necessary to confirm that suspicion.

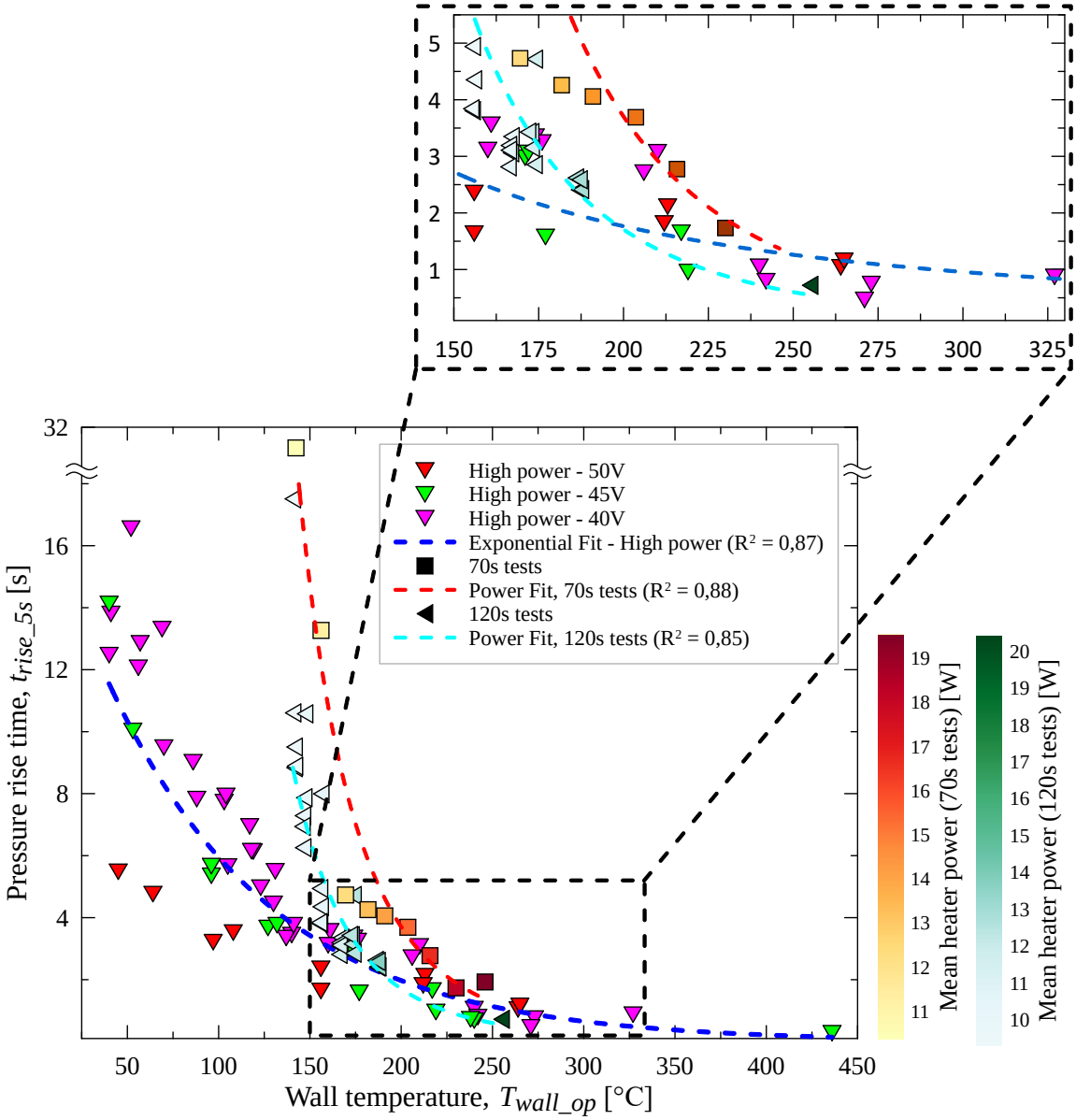

Figure 4.36 Pressure rise time, t_{rise_5s}, as a function of initial wall temperature, T_{wall_op}, captured when the valve was commanded to open.

Based on the data obtained, defining an accurate limiting wall temperature above which repeatable results can be obtained is impossible. In the case of 120 s, low-power tests, the

shortest pressure rise time was 0,72 s and was measured when the wall temperature was 255°C. During 70s runs, the lowest pressure rise time was 1,93 s, at an initial wall temperature of 246°C. As for the high-power experiments, the most rapid pressure rise was obtained for the test Z1210 (without previous thruster cooling) and amounted to 0,27s at a wall temperature of 436°C; the second and third lowest values were 0,46 and 0,68 s, respectively, for a wall temperature of 271 and 240°C. It is expected that if adequately insulated, the test article used should allow repeatable start-up at a wall temperature exceeding at least 250°C.

4.3.2.2 Pressure fall time

Figure 4.37 shows how the pressure fall time (t_{fall_5s}) changed as a function of mean wall temperature measured in the period corresponding to the pressure fall time ($T_{wall\_m\_fall}$).
The first observation is that for high-power experiments, as in the case of the pressure rise time, lower wall temperatures were required to obtain specific fall times when compared to low-power 70 s experiments. The expected cause is the same as previously. Additionally, in the high-power mode, the heater was turned off at the moment when the valve was closed; therefore, a high amount of heat was delivered to the unit until the measurement of the pressure decay time was initiated. The dispersion of the data points for the high-power mode is significant compared to the remaining results. Another observation is that the results obtained for 120-second, low-power tests remained relatively stable for all conditions tested. This is because of the duration of runs, 50 seconds longer than for the 70-second campaign, which resulted in slightly higher chamber temperature and possibly more uniform temperature distribution and, therefore, lower dispersion of the results. As for 120 s tests, the mean value of pressure decay time for all runs was 0,74 s, with a standard deviation of ~0,09 s.

Figure 4.37 shows that the wall temperature of ~367°C (the lowest wall temperature measured during the 120s test campaign) and more allowed to obtain a relatively repeatable pressure decay time. As for the data points concerning the entire test campaign and corresponding to the wall temperature greater than 367°C, the mean value of pressure decay time was 0,65 s with a standard deviation, σ, of 0,14 s. The values mentioned were marked as dashed black lines in the magnified area in Figure 4.37.

4.3.2.3 Pressure roughness

Figure 4.38 depicts the evolution of pressure roughness for all tests performed as a function of mean wall temperature in the 5-second time periods used. It can be easily noted that high-power

tests gave extensively dispersed results when compared to data points corresponding to low-power runs. In the case of low-power experiments, two data points were used for each test, calculated for the period when the heater was turned on and off; the exact methodology of calculating this parameter was discussed in section 4.2.1.

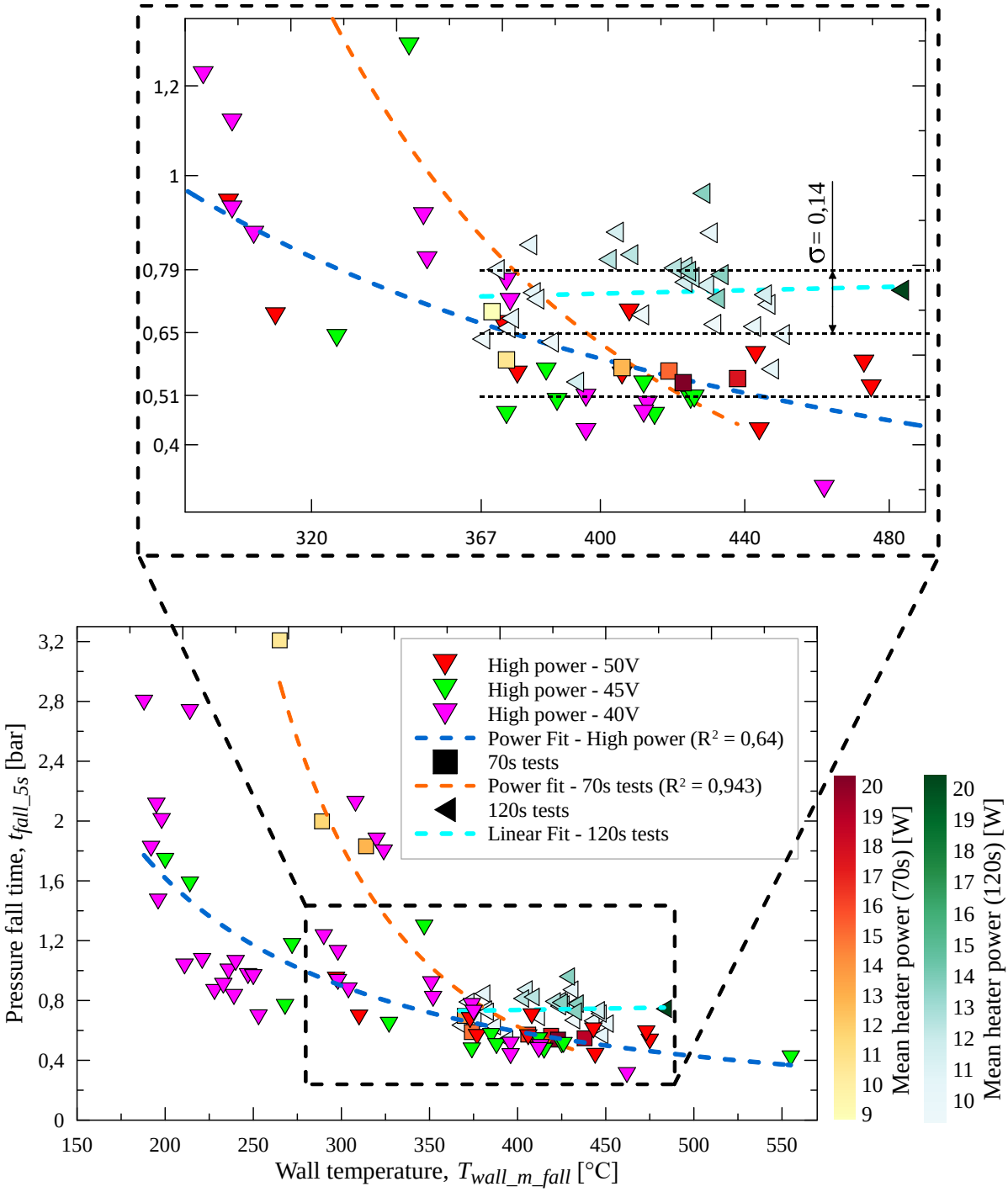

Figure 4.37 Comparison of the pressure fall time (t_{fall_5s}) as a function of mean wall temperature ($T_{wall\_m\_fall}$) measured in the pressure fall period.

It can be seen that the highest roughness values during low-power, 70-second tests were 3,7; 3,9 and 4% at corresponding mean wall temperatures of 199, 236 and 257°C, respectively.

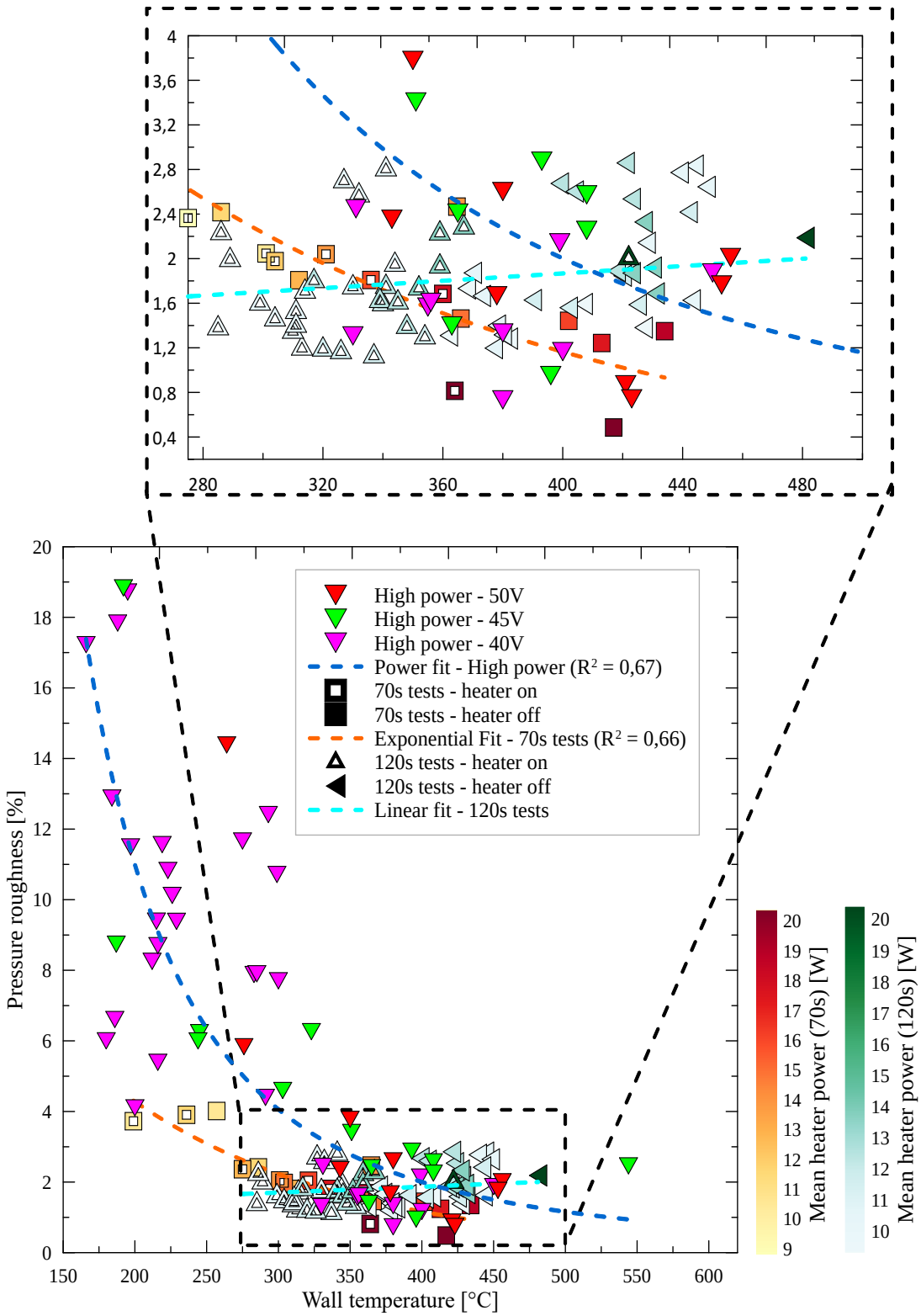

Figure 4.38 Comparison of pressure roughness as a function of mean wall temperature ($T_{wall\_5s\_h}$ and $T_{wall\_5s\_nh}$) obtained for all tests executed throughout the test campaign.

For the mentioned range of wall temperature, from 199 to 257°C, each data point corresponding to a high-power campaign represents more significant pressure fluctuations. On the other hand, high-power data points present within the discussed wall temperature range are experiments carried out with a supply voltage of 40 and 45V, with a preheating time of up to 16 and 10

seconds, respectively – tests for which propellant accumulation occurred as a consequence of inefficient initial decomposition, as discussed in section 4.1.2.

Regarding low-power experiments (70 and 120 s), as seen in the magnified area in Figure 4.38, the roughness remains relatively stable for a wall temperature of 275°C and higher; the mean value was 1,81% with a standard deviation of 0,51%. While discussing the pressure roughness concerning high-power tests, in section 4.1.3.1, it was observed that roughness stabilized at a wall temperature of 330°C and more. As can be seen, in the case of low-power runs, this parameter remains relatively stable at nearly 60°C lower wall temperatures. It is suspected that due to short duration of experiments in the case of high-power tests, the temperature distribution in the chamber was not uniform, and cold spots existed, especially in the nozzle section of the thruster, which comprised a stainless steel flange, for which the temperature could be lower than for the wall section used to measure the temperature. However, this calls for additional research incorporating more temperature sensors.

As can be viewed in the magnified area in Figure 4.38, the roughness corresponding to 120-second tests was slightly rising with wall temperature. In general, it was observed that chamber pressure traces corresponding to selected experiments revealed fluctuations rising with time (temperature). A possible cause is the influence of the temperature on the injection system; therefore, this observation may be a characteristic of the injection system used.

4.3.2.4 Decomposition temperature and characteristic velocity

Figure 4.39 was prepared to show the relationship between internal chamber temperatures, $T2_{5s}$, measured during the high-power campaign in 5 s reference periods before closing the valve and the corresponding mean heater powers in preheating sequences. A colour scale was added to highlight the preheating duration corresponding to each data point. It can be observed that most of the scattered points correspond to experiments executed with a preheating time of less than 20 s. The influence of the heater power on temperature is evident, affecting the measurements; in the case of 50V supply voltage, the measured mean internal chamber temperatures, $T2_{5s}$, exceeded 1000°C, which is more than the normal, adiabatic decomposition temperature of the propellant used, amounting to T_{ad} = 945°C (calculated using NASA CEA software, 98% HTP, the initial temperature of the propellant: 20°C, chamber pressure: 6 bar). In order to allow easy comparison between the measurements and the theoretical adiabatic value, temperature efficiency, η_{T2}, was added in figures, being the ratio of measured temperatures and the adiabatic value, T_{ad}.

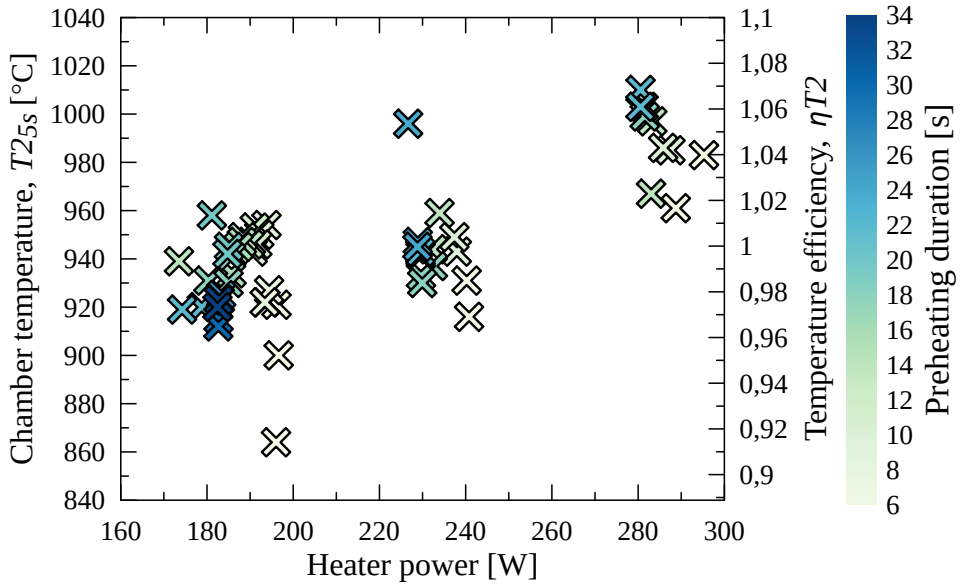

Figure 4.39 Mean internal chamber temperatures, $T2_{5s}$, measured during high-power experiments as a function of mean heater power during the preheating sequence.

Figure 4.40 (a) shows mean internal chamber temperatures, $T2_{5s}$, measured in the reference periods corresponding to the 120 s, low-power campaign. The figure includes temperatures corresponding to the periods when the heater was turned on and off. As mentioned in section 4.2.3, no direct influence of the heater on measured temperature exists. In Figure 4.40 (b), results concerning 70 s tests were presented, and for comparison purposes, averaged temperatures for each voltage tested during the 120 s campaign were presented as single points; as previously, no clear dependence was observed.

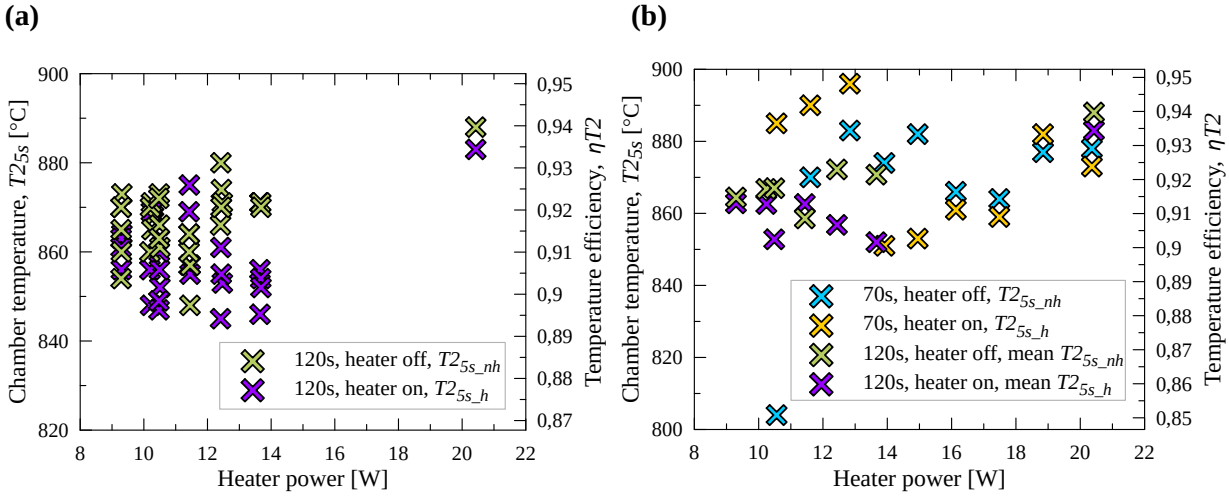

Figure 4.40 Relation between internal chamber temperatures and heater power. **(a)** 120 s campaign, data points corresponding to reference periods when the heater was on and off; **(b)** data points corresponding to 70s campaign, results concerning 120 s campaign were included as averaged values for each voltage tested.

Figure 4.41 shows how the characteristic velocity, c^*, calculated for high-power experiments using reference pressure, $P4_{5s}$ and measured mass flow rate of the propellant, as

per equation 1.8, changed as a function of measured heater power. As previously, the efficiency of characteristic velocity was included in figures; c^* efficiency, η_{c^*}, is a ratio of experimentally obtained value, c^*_{exp}, and the theoretical one, c^*_{theo}, amounting to 1016 m/s (as previously, calculated using NASA CEA software). It can be observed that c^* obtained in each case exceeds the theoretical one. One of the factors potentially affecting the results is the heat delivered to the flow through resistive heating; a detailed analysis concerning that phenomenon was not carried out. An additional observation is that for some tests, c* exceeded the theoretical value by more than 50%. This can be explained by the well-described propellant accumulation, resulting in significant overpressure at the end of the run, affecting the pressure measurement and characteristic velocity, which can be confirmed by the preheating duration, as in each case such a high c^* was obtained, the corresponding duration was within the range of 6 to 16 s.

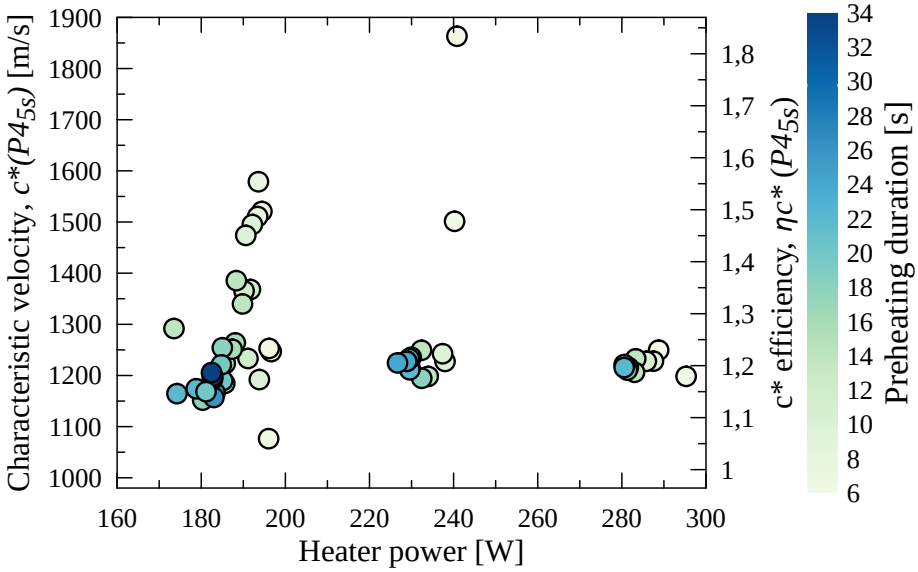

Figure 4.41 Characteristic velocity, calculated for high-power experiments using reference pressure, $P4_{5s}$, and mass flow rate of the propellant, $\dot{m}_{5s}$.

Characteristic velocity was additionally analyzed using an alternative attitude by employing directly equation 1.9. This allows to estimate c^* using measured chamber temperature. The discussed method, however, requires knowledge concerning specific heat ratio, κ, and mean molecular mass of the decomposition products, M. Both κ = 1,2516 and M = 22,56 were calculated using NASA CEA software. Figure 4.42 shows the results concerning high-power experiments, and the figure is a rescaled version of the data presented in Figure 4.39. It can be noticed that experiments for which exceedingly high $c^*(P4_{5s})$ values were found (Figure 4.42) represent tests for which the efficiency of the decomposition process was low. This is because, as discussed, the highly accelerated decomposition of accumulated propellant led to overpressure, but the decomposition itself was of low quality, resulting in a

lower temperature, which was reflected when calculating $c^*(T2_{5s})$. Based on chamber temperature, the calculated c^* efficiency was between ~97 and ~103%.

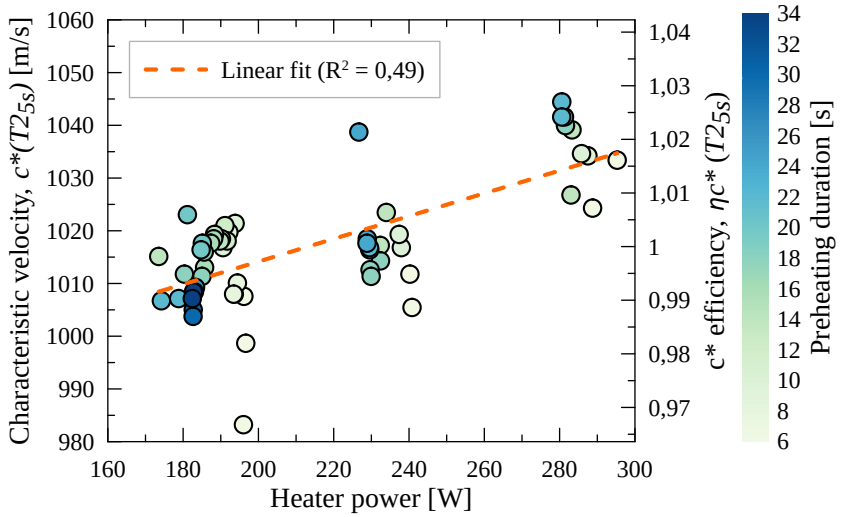

Figure 4.42 Characteristic velocity, based on $T2_{5s}$ internal chamber temperature as a function of heater power for high-power experiments.

Figure 4.43 (a) shows the relation between c^*, estimated based on chamber temperature ($T2_{5s\_nh}$) as a function of heater power, for low-power, 120 s experiments. The values are between ~96 and ~98%. Figure 4.43 (b) shows $c^*(T2_{5s\_nh})$ for 70 s experiments together with 120s results, averaged for each voltage tested, as a function of mean heater power. The values of $c^*(T2_{5s\_nh})$ for 70 s campaign do not differ from 120 s tests, and the values are, as previously, between ~96 and ~98%.

(a) **(b)**

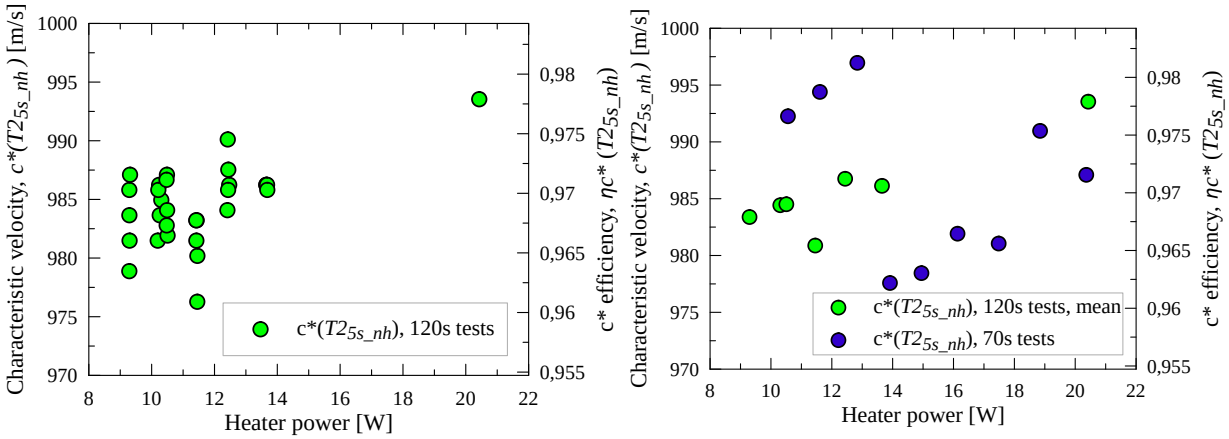

Figure 4.43 Relation between characteristic velocity, based on the measured chamber temperature, $T2_{5s\_nh}$, and mean heater power. **(a)** 120s experiments **(b)** 70s experiments and 120s tests with averaged values for each voltage tested.

It must be emphasized that single-point, $T2$ temperature measurement does not take into consideration the temperature profile in the chamber; therefore, the expected mean plenum

chamber temperature is lower than measured; as a consequence, c^* based on temperature is expected to be overestimated.

The results concerning c^* based on pressure were not provided for low-power experiments, as the values obtained greatly exceeded 100%, and the reasons were not fully understood; therefore, dedicated research is necessary to address that issue.

4.3.2.5 Summary

- A comparison of results corresponding to 5 s, low-power tests confirmed that the maximum chamber pressure measured during runs rose sharply if the wall temperature before initiating the flow, T_{wall_op}, exceeded ~150°C – a temperature corresponding to the normal boiling of the propellant used.

- It was observed that in the case of 5 s experiments for which T_{wall_op} was in the vicinity of 150°C, substantially different *T2* chamber temperatures were measured before closing the valve if T_{wall_op} was only slightly below or above the aforementioned threshold. In the case of 70 s campaign, ΔT_{wall_op} of 11°C between experiments (146 and 157°C) resulted in the difference of *T2* before closing the valve on the order of 300°C. As for 120 s campaign, ΔT_{wall_op} of 16°C (140 and 156°C) gave 262°C of difference in $T2_{Cvc}$. This is connected with the observation provided in the first point, as efficient decomposition results in rapid pressure rise and high temperature.

- Observation similar to provided in the previous points was registered for pressure fall time, down to 0,05 bar, for 5 s experiments concerning 70 and 120 s campaigns. Pressure fall time decreased exponentially with mean wall temperature measured in the pressure fall period. The difference in the decay time for neighbouring tests, where the value of ~150°C separated the discussed wall temperatures during the pressure decay period, was 8,7 and 6s (70 and 120 s campaign).

- While comparing pressure rise times for low-power, 70 s, 120 s and high-power experiments, it was observed that datasets corresponding to each sub-campaign followed different trends up to the initial wall temperature, T_{wall_op}, of ~200°C; above that value, results converged. The possible sources of discrepancy of the data at temperatures of less than 200°C are: (I) short duration of high power experiments, together with high heater temperature; as a consequence, the measured wall temperature

did not reflect the internal conditions properly. (II) Modified insulation of the test article during 120 s low-power sub-campaign. (III) break in the preheating phase during low-power, 70 s tests, necessary to switch the sampling rate of the data acquisition system.

- The dispersion of the data corresponding to pressure fall times for high-power experiments was significant when compared to the remaining tests. The results concerning low-power, 120 s runs remained relatively stable – due to duration of tests, resulting in $T_{wall\_m\_fall}$ of at least 367°C and, possibly, more uniform temperature distribution due to the insulation used.

- The highest pressure roughness measured during the low-power campaign amounted to 4% and was captured during the 70s test at a wall temperature, $T_{wall\_5s\_nh}$, of 257°C. It was observed that during low-power tests, the roughness value stabilized at a wall temperature ~60°C lower than in the case of high-power sub-campaign. The roughness during 120 s experiments rose slightly with wall temperature.

- Analysis of characteristic velocity, based on internal chamber temperature, showed that for low-power experiments, the values obtained were between ~96 and ~98% and for high-power tests ranged between ~97 and ~103%.

Summary and conclusions

The work presented in this dissertation aimed to characterize experimentally a sub-Newton electrothermal thruster using 98% hydrogen peroxide as a propellant.

In the current environment, space activities are no longer a domain of large national and international space agencies, and many relatively small, privately owned companies operate in parallel. The evolution presented is termed ‘New Space’, and one of the primary objectives is to make space activities more affordable. A trend that aims to reduce the application of toxic propellants used in satellite propulsion systems can be observed. Hydrogen peroxide is one of the promising candidates to be used in low-cost units; therefore, research concerning the compound mentioned above is necessary to better understand its properties and build an experimental database to be used by engineers and analysts.

In the first part of this dissertation, the author performed an extensive literature review and provided information concerning the physical properties of hydrogen peroxide and the fundamentals of space propulsion, including the classification of propulsion systems used and the fundamentals of rocket propulsion. Next, a discussion concerning the decomposition of hydrogen peroxide was provided. Different modes of decomposition were included, and data concerning thermal decomposition and explosive characteristics of hydrogen peroxide were presented. In the following sections, information concerning electrically heated hydrazine thrusters was included, which, owing to limited data available concerning hydrogen peroxide, aimed to introduce the technology of noncatalytic, nonaugmented thrusters in which no dedicated catalytic bed was implemented.

In order to perform the required research, a dedicated test rig was developed, and a thorough description of the facility was given. The thruster used during the research employed a cylindrical decomposition chamber with an internal diameter of 15 mm and a length of 40 mm and was equipped with a resistively heated cable. The chamber was preheated for a defined time, and after the preheating sequence, the propellant injection was initiated. The decomposition process was characterized by means of pressure rise time, pressure fall time, pressure roughness and characteristic velocity. During the research, supply voltage and preheating duration were varied by changing the settings of the laboratory power supply.

Altogether, 122 experiments were conducted. The entire test campaign was divided into three parts. First, a so-called high-power campaign was carried out, during which the valve was opened for 20 s, and the duration of the preheating sequence ranged from 6 to 34 s. The mean heater power was from ~190 to ~320 W.

Next, a low-power campaign was executed. The heater power ranged from 8,8 to 20,4 W, and the preheating sequence was extended to 30 minutes in each test. This part of the campaign was divided into two sub-campaigns; during the first one, the valve was opened for 70 s, the heater remained active for 40 s, and was turned off afterwards. In the second part of the low-power campaign, the experiment duration was extended to 120 s, and the heater was active for 60 s after opening the valve.
After changing the voltage settings of the laboratory power supply, short, 5-second tests were executed to investigate the decomposition quality before initiating long runs.

A detailed summary of the most significant observations was provided at the end of sections concerning high and low-power campaigns and comparison of the results. Due to substantial amount of data gathered, all of the observations were not be provided here again; instead, below are the most valuable findings.

1) During the high-power campaign, propellant accumulation in the chamber was observed after tests employing the lowest voltage and preheating time of up to 20 s. It was also noticed that high heater temperature was insufficient to initiate spontaneous decomposition; rapid initiation of the reaction was not possible if the temperature of the wall was only slightly elevated due to short preheating time.

2) Internal *T2* chamber temperature during high-power runs did not considerably affect the pressure roughness. It was observed that above a wall temperature of ~330°C, the roughness was significantly reduced.

3) Further analysis of high-power tests showed that the decay time stabilised above 375 to 400°C. The pressure rise time decreased exponentially with initial wall temperature, and above ~230°C, the dispersion of the data was significantly reduced, and the rise time did not exceed 1,5 s.

4) As for the low-power campaign, it was observed that for 5-second tests, the maximum chamber pressure and temperature in the chamber, measured in the axis,

rose sharply if the initial wall temperature was higher than ~150°C, corresponding to the propellant's normal boiling point. Similar observations were made for the pressure fall time; if the mean wall temperature in the pressure fall period was higher than ~150°C, the decay time was significantly reduced.

5) Long, low-power experiments confirmed the thesis provided in section 2.1, that the decomposition process can be self-sustained after the heater is turned off, and no significant decay of chamber pressure and temperature was registered in the period when the heater was not active.

6) Despite many tests performed, none of the experiments resulted in an explosive event.

It is recommended to continue the research presented in this dissertation. As for future work, it would be beneficial to investigate the influence of propellant concentration on the operating characteristics of the test article. As was stated, it is advantageous to use as high a concentration of H_2O_2 as possible, but, e.g. due to the limited availability of 98% HTP or lack of experience with the highly concentrated compound, activities are often performed using H_2O_2 at a concentration sometimes as low as 87,5%.

Additionally, the research presented employed a reactor of a relatively large size. Investigation should be carried out to define the limiting reactor loading for which effective decomposition can be maintained. On that account, testing higher propellant mass flow rates is recommended. What is more, alternative chamber geometries should be investigated as well, including the implementation of chamber packing.

Bibliography

[1] A.T. Sheik, U.I. Atmaca, C. Maple, G. Epiphaniou, Challenges in threat modelling of new space systems: A teleoperation use-case, Adv. Sp. Res. 70 (2022) 2208–2226. https://doi.org/10.1016/j.asr.2022.07.013.

[2] D.L. Hitt, C.M. Zakrzwski, M.A. Thomas, MEMS-based satellite micropropulsion via catalyzed hydrogen peroxide decomposition, Smart Mater. Struct. 10 (2001) 1163–1175. https://doi.org/10.1088/0964-1726/10/6/305.

[3] P. Wexler, ed., Information Resources in Toxicology, Fifth Edit, Elsevier, 2020. https://doi.org/10.1016/C2016-0-04946-X.

[4] C.N. Ryan, E. Fonda-Marsland, G.T. Roberts, A. Lear, E. Fletcher, L. Giles, M.J. Palmer, D. Gibbon, Experimental Validation of a 1-Newton Hydrogen Peroxide Thruster, J. Propuls. Power. 36 (2020) 158–166. https://doi.org/10.2514/1.B37418.

[5] M. Ventura, E. Wernimont, J. Dillard, Hydrogen Peroxide - Optimal For Turbomachinery and Power Applications, in: 43rd AIAA/ASME/SAE/ASEE Jt. Propuls. Conf. Exhib., American Institute of Aeronautics and Astronautics, 2007. https://doi.org/10.2514/6.2007-5537.

[6] E. Wernimont, M. Ventura, G. Garboden, P. Mullens, Past and present uses of rocket grade hydrogen peroxide, Gen. Kinet. LLC. (2005).

[7] M. Ventura, P. Mullens, The use of hydrogen peroxide for propulsion and power, in: 35th Jt. Propuls. Conf. Exhib., American Institute of Aeronautics and Astronautics, 1999. https://doi.org/10.2514/6.1999-2880.

[8] L. Broughton, W. Kretschmer, Development of the Beta 1 Rocket Motor, Royal Aircraft Establishment, Farnborough, Report No. R.P.D.10, 1951.

[9] D. Millard, The Black Arrow Rocket: A History of a Satellite Launch Vehicle and its Engines, Science Museum (Great Britain), London, 2001.

[10] J. Owens, Intelsat Satellite Onboard Propulsion Systems, Past and Future, in: Satell. Commun. Adv. Technol., American Institute of Aeronautics and Astronautics, 1977: pp. 187–198. https://doi.org/10.2514/5.9781600865299.0187.0198.

[11] L.S. Swenson, J.M. Grimwood, C.C. Alexander, This New Ocean. A History of Project Mercury, NASA SP-42, National Aeronautics and Space Administration, NASA History Office, 1998.

[12] B.C. Hacker, J.M. Grimwood, On The Shoulders of Titans. A History of Project Gemini, Scientific and Technical Information Office, National Aeronautics and Space Administration (NASA), Washington D.C., 1977.

[13] Experience with the X-15 Adaptive Flight Control System, by Staff of the Flight Research Center, Edwards, California. NASA TN D-6208, 1971.

[14] J. Baumeister, RL10 Engine Ability to Transition from Atlas to Shuttle Centaur Program, in: 50th AIAA/ASME/SAE/ASEE Jt. Propuls. Conf., American Institute of Aeronautics and Astronautics, 2014. https://doi.org/10.2514/6.2014-3669.

[15] E.J. Wucherer, T. Cook, M. Stiefel, R. Humphries, J. Parker, Hydrazine Catalyst Production - Sustaining S-405 Technology, in: 39th AIAA/ASME/SAE/ASEE Jt. Propuls. Conf. Exhib., American Institute of Aeronautics and Astronautics, 2003. https://doi.org/10.2514/6.2003-5079.

[16] R.R. Schreib, T.K. Pugmire, S. Chapin, The hybrid (hydrazine) resistojet, in: 5th Propuls. Jt. Spec., American Institute of Aeronautics and Astronautics, 1969. https://doi.org/10.2514/6.1969-496.

[17] W. Ley, K. Wittmann, W. Hallmann, eds., Handbook of Space Technology, John Willey & Sons Ltd, 2009. https://doi.org/10.1002/9780470742433.

[18] M. Ventura, E. Wernimont, S. Heister, S. Yuan, Rocket Grade Hydrogen Peroxide (RGHP) for use in Propulsion and Power Devices - Historical Discussion of Hazards, in: 43rd AIAA/ASME/SAE/ASEE Jt. Propuls. Conf. & Exhib., American Institute of Aeronautics and Astronautics, 2007. https://doi.org/10.2514/6.2007-5468.

[19] J. Foust, Sherpa tug starts raising orbit more than a month after launch, SpaceNews.

(2022). https://spacenews.com/sherpa-tug-yet-to-start-raising-orbit-a-month-after-launch/.

[20] A.J. Musker, J.J. Rusek, C. Kappenstein, G.T. Roberts, Hydrogen Peroxide - From Bridesmaid to Bride, in: 3rd ESA Int. Conf. Green Propellants Sp. Propuls., Poitres, France, 2006. http://10048.indexcopernicus.com/abstracted.php?level=5&ICID=1213534.

[21] W. Schumb, C. Satterfield, R. Wentworth, Hydrogen Peroxide Part 2, 1953.

[22] Hydrogen Peroxide Handbook, Canoga Park, CA, 1967.

[23] M.J. Sidi, Spacecraft Dynamics and Control, Cambridge University Press, 1997. https://doi.org/10.1017/CBO9780511815652.

[24] A.K. Maini, V. Agrawal, Satellite Technology, John Wiley & Sons, Ltd, Chichester, UK, 2010. https://doi.org/10.1002/9780470711736.

[25] D. Krejci, P. Lozano, Space Propulsion Technology for Small Spacecraft, Proc. IEEE. 106 (2018) 362–378. https://doi.org/10.1109/JPROC.2017.2778747.

[26] M. Zaberchik, D.R. Lev, E. Edlerman, A. Kaidar, Fabrication and Testing of the Cold Gas Propulsion System Flight Unit for the Adelis-SAMSON Nano-Satellites, Aerospace. 6 (2019) 91. https://doi.org/10.3390/aerospace6080091.

[27] J. Kindracki, K. Tur, P. Paszkiewicz, Ł. Mężyk, Ł. Boruc, P. Wolański, Experimental research on low-cost cold gas propulsion for a space robot platform, Aerosp. Sci. Technol. 62 (2017) 148–157. https://doi.org/10.1016/j.ast.2016.12.001.

[28] G. Rarata, K. Rokicka, P. Surmacz, Hydrogen Peroxide as a High Energy Compound Optimal for Propulsive Applications, Cent. Eur. J. Energ. Mater. 13 (2016) 778–790. https://doi.org/10.22211/cejem/65005.

[29] A.S. Gohardani, J. Stanojev, A. Demairé, K. Anflo, M. Persson, N. Wingborg, C. Nilsson, Green space propulsion: Opportunities and prospects, Prog. Aerosp. Sci. 71 (2014) 128–149. https://doi.org/10.1016/j.paerosci.2014.08.001.

[30] M. Wilhelm, M. Negri, H. Ciezki, S. Schlechtriem, Preliminary tests on thermal ignition

of ADN-based liquid monopropellants, Acta Astronaut. 158 (2019) 388–396. https://doi.org/10.1016/j.actaastro.2018.05.057.

[31] W. Kopacz, A. Okninski, A. Kasztankiewicz, G. Rarata, P. Maksimowski, FirePhysChem Hydrogen peroxide – A promising oxidizer for rocket propulsion and its application in solid rocket propellants, 2 (2022) 56–66. https://doi.org/10.1016/j.fpc.2022.03.009.

[32] U. Gotzig, G. Schulte, A. Sowa, New generation 10N bipropellant MMH/NTO thruster with double seat valve, in: 35th Jt. Propuls. Conf. Exhib., American Institute of Aeronautics and Astronautics, Reston, Virigina, 1999. https://doi.org/10.2514/6.1999-2594.

[33] H. Kang, S. Kwon, Green hypergolic combination: Diethylenetriamine-based fuel and hydrogen peroxide, Acta Astronaut. 137 (2017) 25–30. https://doi.org/10.1016/j.actaastro.2017.04.009.

[34] H. Kang, D. Jang, S. Kwon, Demonstration of 500 N scale bipropellant thruster using non-toxic hypergolic fuel and hydrogen peroxide, Aerosp. Sci. Technol. 49 (2016) 209–214. https://doi.org/10.1016/j.flowmeasinst.2011.05.001.

[35] J. Kindracki, P. Paszkiewicz, Ł. Mężyk, Resistojet thruster with supercapacitor power source – design and experimental research, Aerosp. Sci. Technol. 92 (2019) 847–857. https://doi.org/10.1016/j.ast.2019.07.010.

[36] M. Tajmar, Advanced Space Propulsion Systems, Springer Vienna, Vienna, 2003. https://doi.org/10.1007/978-3-7091-0547-4.

[37] H. Tang, X. Zhang, Y. Liu, H. Wang, Y. Shen, Performance and preliminary life test of a low power hydrazine engineering design model arcjet, Aerosp. Sci. Technol. 15 (2011) 577–588. https://doi.org/10.1016/j.ast.2010.12.001.

[38] P. Fortescue, G. Swinerd, J. Stark, eds., Spacecraft Systems Engineering, 4th Editio, Wiley, 2011.

[39] M. Barrere, Rocket Propulsion, Elsevier Publishing Company, 1960.

[40] C.D. Brown, Spacecraft Propulsion, American Institute of Aeronautics and Astronautics,

Inc., Reston, VA, 1996. https://doi.org/10.2514/4.862441.

[41] D.H. Huang, D.K. Huzel, Modern Engineering for Design of Liquid-Propellant Rocket Engines, American Institute of Aeronautics and Astronautics, Washington DC, 1992. https://doi.org/10.2514/4.866197.

[42] A.E.S. Nosseir, A. Cervone, A. Pasini, Review of State-of-the-Art Green Monopropellants: For Propulsion Systems Analysts and Designers, Aerospace. 8 (2021) 20. https://doi.org/10.3390/aerospace8010020.

[43] C.D. Brown, Elements of Spacecraft Design, American Institute of Aeronautics and Astronautics, Inc., Reston, VA, 2002. https://doi.org/10.2514/4.861796.

[44] ECSS-E-ST-35C Rev. 1, Propulsion general requirements, ECSS Secretariat, ESA-ESTEC, Requirements and Standards Division, Noordwijk, The Netherlands, 2009.

[45] D.P. Mishra, Fundamentals of Rocket Propulsion, CRC Press, 2017.

[46] P. Surmacz, Green Rocket Propulsion Research and Development At the Institute of Aviation: Problems and Perspectives, J. KONES. Powertrain Transp. 23 (2016) 337–344. https://doi.org/10.5604/12314005.1213534.

[47] R. Miletiev, I. Simeonov, V. Stefanova, M. Georgiev, Thermodynamic analysis of the hydrogen peroxide decomposition parameters, J. Therm. Anal. Calorim. 113 (2013) 985–989. https://doi.org/10.1007/s10973-012-2769-5.

[48] M. Ventura, Long Term Storability of Hydrogen Peroxide, in: 41st AIAA/ASME/SAE/ASEE Jt. Propuls. Conf. Exhib., American Institute of Aeronautics and Astronautics, Tuscon, Arizona, 2005: pp. 1–14. https://doi.org/10.2514/6.2005-4551.

[49] J.A. McMillan, Possible Implications of the Damage by Radiation in the Storage of Propellants in Outer Space and Tentative Methods for Its Measurement, IEEE Trans. Nucl. Sci. 10 (1963) 24–30. https://doi.org/10.1109/TNS.1963.4323239.

[50] W. Głuszewski, N. Okroj, Radiation stability of high test peroxide (HTP), Radiat. Phys. Chem. 183 (2021) 109399. https://doi.org/10.1016/j.radphyschem.2021.109399.

[51] R.E. Anderson, Advanced Propellant Staged Combustion Feasibility Program, Aerojet-General Corporation, Technical Report AFRPL-TR-66-6, Part II, Phase I Final Report, 1966.

[52] N. Okroj, K. Michalska, B. Jakusz, Effect of vibration and stirring on 90% and 98% hydrogen peroxide, Mater. Wysokoenergetyczne / High Energy Mater. (2018) 88–96. https://doi.org/10.22211/matwys/0160.

[53] M. Soustelle, An Introduction to Chemical Kinetics, John Wiley & Sons, Inc, Hoboken, NJ, USA, 2011. https://doi.org/10.1002/9781118604243.

[54] A. Cornish-Bowden, Fundamental of Enzyme Kinetics, Fourth Edi, Wiley, 2012. https://doi.org/10.1016/b978-0-408-70721-3.50005-9.

[55] Chemistry Part I, NCERT Textbook for Class XI, n.d.

[56] K. Laidler, Chemical Kinetics, Third Edit, Pearson Education Inc., 1987.

[57] J.H. Espenson, Chemical Kinetics and Reaction Mechanisms, McGraw-Hill, Inc., 1981.

[58] I. Chorkendorff, J.W. Niemantsverdriet, Concepts of Modern Catalysis and Kinetics, Wiley, 2003. https://doi.org/10.1002/3527602658.

[59] J.K. Nørskov, F. Studt, F. Abild-Pedersen, T. Bligaard, Fundamental Concepts in Heterogeneous Catalysis, John Wiley & Sons, Inc, Hoboken, NJ, USA, 2014. https://doi.org/10.1002/9781118892114.

[60] G.A. Samorjai, Introduction to Surface Chemistry and Catalysis, Wiley, 1994.

[61] J. Takagi, K. Ishigure, Thermal Decomposition of Hydrogen Peroxide and Its Effect on Reactor Water Monitoring of Boiling Water Reactors, Nucl. Sci. Eng. 89 (1985) 177–186. https://doi.org/10.13182/NSE85-A18191.

[62] J.S. Mok, W.J. Helms, J.C. Sisco, W.E. Anderson, Thermal Decomposition of Hydrogen Peroxide, Part I: Experimental Results, J. Propuls. Power. 21 (2005) 942–953. https://doi.org/10.2514/1.13284.

[63] M. Burnier, An Experimental Investigation of Heat Transfer to Hydrogen Peroxide in Microtubes, Massachusetts Institute of Technology, 2004.

http://hdl.handle.net/1721.1/27068.

[64] C.N. Satterfield, G.M. Kavanagh, H. Resnick, Explosive Characteristics of Hydrogen Peroxide Vapor, Ind. Eng. Chem. 43 (1951) 2507–2514. https://doi.org/10.1021/ie50503a034.

[65] C.K. McLane, Hydrogen Peroxide in the Thermal Hydrogen Oxygen Reaction I. Thermal Decomposition of Hydrogen Peroxide, J. Chem. Phys. 17 (1949) 379–385. https://doi.org/10.1063/1.1747263.

[66] P.A. Giguère, I.D. Liu, Kinetics of the Thermal Decomposition of Hydrogen Peroxide Vapor, Can. J. Chem. 35 (1957) 283–293. https://doi.org/10.1139/v57-042.

[67] C.N. Satterfield, T.W. Stein, Homogeneous Decomposition of Hydrogen Peroxide Vapor, J. Phys. Chem. 61 (1957) 537–540. https://doi.org/10.1021/j150551a006.

[68] D.C. Conway, Mechanism of the Homogeneous Decomposition of Hydrogen Peroxide, J. Phys. Chem. 61 (1957) 1579–1580. https://doi.org/10.1021/j150557a034.

[69] D.E. Hoare, J.B. Protheroe, a D. Walsh, The thermal decomposition of hydrogen peroxide vapour, Trans. Faraday Soc. 55 (1959) 548. https://doi.org/10.1039/tf9595500548.

[70] W. Forst, Second-Order Unimolecular Kinetics in the Thermal Decomposition of Hydrogen Peroxide Vapor, Can. J. Chem. 36 (1958) 1308–1319. https://doi.org/10.1139/v58-192.

[71] A.B. Hart, Thermal Decomposition of Hydrogen Peroxide in the Vapour Phase, Nature. 163 (1949) 876–877. https://doi.org/10.1038/163876b0.

[72] C.N. Satterfield, G.M. Kavanagh, R.N. Kingsbury, H. Resnick, Hydrogen Peroxide Vapor Explosions—Determination of Explosive Composition 1, J. Am. Chem. Soc. 72 (1950) 4308–4309. https://doi.org/10.1021/ja01165a540.

[73] C.N. Satterfield, P.J. Ceccotti, A.H.R. Feldbrugge, Ignition Limits of Hydrogen Peroxide Vapor, Ind. Eng. Chem. 47 (1955) 1040–1043. https://doi.org/10.1021/ie50545a046.

[74] C.N. Satterfield, F. Feakes, N. Sekler, Ignition Limits of Hydrogen Peroxide Vapor at

Pressures above Atmospheric., J. Chem. Eng. Data. 4 (1959) 131–133. https://doi.org/10.1021/je60002a007.

[75] J.M. Monger, H.J. Baumgartner, G.C. Hood, C.E. Sanborn, Explosive Limits of Hydrogen Peroxide Vapor., J. Chem. Eng. Data. 9 (1964) 119–124. https://doi.org/10.1021/je60020a040.

[76] J.G. Marshall, The quenching distances and minimum ignition energies of H2O2+ H2O vapour mixtures, Trans. Faraday Soc. 55 (1959) 288. https://doi.org/10.1039/tf9595500288.

[77] C.N. Satterfield, E. Kehat, Burning Velocities of the Hydrogen Peroxide Decomposition Flame, Massechusetts Institute of Technology, Department of Chem. Eng., 1960. Report.

[78] C.N. Satterfield, E. Kehat, Burning velocities of the hydrogen peroxide decomposition flame, Combust. Flame. 5 (1961) 273–282. https://doi.org/10.1016/0010-2180(61)90106-7.

[79] C.N. Satterfield, E. Kehat, M.A.T. Mendes, Burning rates and ignition temperatures of hydrogenperoxide solutions, Combust. Flame. 4 (1960) 99–105. https://doi.org/10.1016/S0010-2180(60)80014-4.

[80] J.M. Monger, H.J. Baumgartner, G.C. Hood, C.E. Sanborn, Detonations in Hydrogen Peroxide Vapor., J. Chem. Eng. Data. 9 (1964) 124–127. https://doi.org/10.1021/je60020a041.

[81] G.A. Campbell, P.V. Rutledge, Detonation of Hydrogen Peroxide Vapour, Inst. Chem. Eng. Symp. Ser. 33 (1972) 37. https://www.icheme.org/media/10612/iv-paper-07.pdf.

[82] Anonymous, Research and technologic work on explosives, explosions, and flames, US Bureau of Mines, Info. Circular 8387, 1967.

[83] J. McCormic, Hydrogen Peroxide Rocket Manual, Buffalo, NY, 1965.

[84] S.A. Sheffield, D.M. Dattelbaum, D.B. Stahl, L.L. Gibson, B.D. Bartman, Shock Initiation Studies on High Concentration Hydrogen Peroxide, in: 2009 Jt. Army-Navy-NASA-Air Force Meet., Los Alamos National Laboratory, La Jolla, CA, 2009.

[85] C. Bombardieri, T. Traudt, C. Manfletti, Experimental study of water hammer pressure surge, Prog. Propuls. Phys. 11 (2019) 555–570. https://doi.org/10.1051/eucass/201911555.

[86] M. Lema, F.L. Peña, P. Rambaud, J.-M. Buchlin, J. Steelant, Fluid hammer with gas desorption in a liquid-filling tube: experiments with three different liquids, Exp. Fluids. 56 (2015) 180. https://doi.org/10.1007/s00348-015-2043-2.

[87] F. Hutchinson, H. Schmitz, Adiabatic compression phenomena in hydrazine propulsion systems, in: 20th Jt. Propuls. Conf., American Institute of Aeronautics and Astronautics, 1984. https://doi.org/10.2514/6.1984-1345.

[88] F. Valencia-Bel, F. Di Matteo, W. van Meerbeeck, Assessment for Hydrazine detonability during priming system activities, in: Sp. Propuls. Conf. Col. Ger., 2014.

[89] A. Devereaux, F. Cheuret, Development Testing of a New Bipropellant Propulsion System for the GMP-T Spacecraft, in: 46th AIAA/ASME/SAE/ASEE Jt. Propuls. Conf. & Exhib., American Institute of Aeronautics and Astronautics, 2010: pp. 1–13. https://doi.org/10.2514/6.2010-6649.

[90] J. Gramatyka, P. Paszkiewicz, D. Grabowski, A. Parzybut, D. Bodych, Development of POLON — A Green Microsatellite Propulsion Module Utilizing 98 % Hydrogen Peroxide, Aerospace. (2022). https://doi.org/doi.org/10.3390/ aerospace9060297.

[91] E.W. Schmidt, ed., Hydrazine and Its Derivatives. Preparation, Properties, Applications, Second Edi, Wiley Interscience, 2001.

[92] L. Holcomb, D. Lee, Survey of auxiliary-propulsion systems for communications satellites, in: 4th Commun. Satell. Syst. Conf., American Institute of Aeronautics and Astronautics, 1972. https://doi.org/10.2514/6.1972-515.

[93] C.G. Kuan, G.B. Chen, Y.C. Chao, Development and ground tests of a 100-millinewton hydrogen peroxide monopropellant microthruster, J. Propuls. Power. 23 (2007) 1313–1320. https://doi.org/10.2514/1.30440.

[94] H. Twardy, Investigation on an electrothermal hydrazine thruster, Acta Astronaut. 4 (1977) 875–893. https://doi.org/10.1016/0094-5765(77)90019-4.

[95] R. Callens, C. Murch, Electrothermal hydrazine thruster analyses and performance evaluation, in: 8th Jt. Propuls. Spec. Conf., American Institute of Aeronautics and Astronautics, 1972. https://doi.org/10.2514/6.1972-1152.

[96] Anonymous, Hybrid Resistojet Development, Contract NAS5-21080, Final report, Lowell, Massachusetts, 1971.

[97] T.K. Pugmire, T. O'Connor, R. Shaw, W. Davis, Electrothermal hydrazine engine performance, in: 7th Propuls. Jt. Spec. Conf., American Institute of Aeronautics and Astronautics, 1971. https://doi.org/10.2514/6.1971-760.

[98] T. Pugmire, Electrothermal hydrazine reactors, in: AIAA/SAE 11th Propuls. Conf., American Institute of Aeroanutics and Astronautics, 1975. https://doi.org/10.2514/6.1975-1244.

[99] T. Pugmire, T. Oconnor, Five-pound thrust non-catalytic hydrazine engine, in: 12th Propuls. Conf., American Institute of Aeronautics and Astronautics, 1976. https://doi.org/10.2514/6.1976-660.

[100] C. Murch, C. Hunter, Electrothermal hydrazine thruster development, in: 9th Electr. Propuls. Conf., American Institute of Aeronautics and Astronautics, Reston, Virigina, 1972. https://doi.org/10.2514/6.1972-451.

[101] Monopropellant Hydrazine Resistojet, Preliminary Design Task Summary Report, NASA CR-122376, Redondo Beach, CA, 1972.

[102] C.K. Murch, Monopropellant Hydrazine Resistojet, Engineering Model Fabrication and Test Task Summary, NASA CR-132784, Redondo Beach, CA, 1973.

[103] C. Murch, R. Sackheim, J. Kuenzly, R. Callens, Noncatalytic hydrazine thruster development - 0.050 to 5.0 pounds thrust, in: 12th Propuls. Conf., American Institute of Aeronautics and Astronautics, 1976. https://doi.org/10.2514/6.1976-658.

[104] D. Zube, D. Fye, I. Masuda, Y. Gotoh, Low bus voltage hydrazine arcjet system for geostationary satellites, in: 34th AIAA/ASME/SAE/ASEE Jt. Propuls. Conf. Exhib., American Institute of Aeronautics and Astronautics, 1998. https://doi.org/10.2514/6.1998-3631.

[105] I. Hadar, A. Gany, Augmentation of low power hydrazine thrusters, Acta Astronaut. 32 (1994) 275–281. https://doi.org/10.1016/0094-5765(94)90080-9.

[106] F.X. McKevitt, F.R. Schwam, Design, performance, and operational scaling criteria for electrically augmented hydrazine thrusters, in: AIAA/SAE/ASME 20th Jt. Propuls. Conf., Cincinnati, OH, 1984. https://doi.org/10.2514/6.1984-1234.

[107] G.A. Dressler, R.E. Morningstar, R.L. Sackheim, D.E. Fritz, R. Beach, R. Kelso, Flight qualification of the augmented electrothermal hydrazine thruster, in: AIAA/SAE/ASME 17th Jt. Propuls. Conf., Palo Alto, CA, 1981. https://doi.org/10.2514/6.1981-1410.

[108] R.T. Feconda, J.I. Weizman, Satellite Reaction Control Subsystems with augmented catalytic thrusters, in: AIAA/SAE/ASME 20th Jt. Propuls. Conf., Cincinnati, OH, 1984. https://doi.org/10.2514/6.1984-1235.

[109] Aerojet Rocketdyne, Electric Propulsion Data Sheet, (n.d.).

[110] W.B. Watkins, Gas Generator for Producing Adjustable Flow, US 6,532,741 B2, 2003.

[111] J.H. Corpening, S.D. Heister, W.E. Anderson, B.J. Austin, Thermal Decomposition of Hydrogen Peroxide, Part 2: Modeling Studies, J. Propuls. Power. 22 (2006) 996–1005. https://doi.org/10.2514/1.13285.

[112] S. Lee, W. Yoon, S. Kwon, Preliminary Test of Hydrogen Peroxide Thermal Decomposition Monopropellant Thruster, in: 72nd Int. Congr. (IAC), Dubai, United Arab Emirates, 25-29 Oct. 2021, n.d.

[113] L. Mezyk, Z. Gut, K. Mohan, J. Kindracki, G. Rarata, Initial research on thermal decomposition of 98% concentrated hydrogen peroxide in thruster-like conditions, Eng. Sci. Technol. an Int. J. 31 (2022) 101054. https://doi.org/10.1016/j.jestch.2021.08.011.

[114] L. Mezyk, Z. Gut, P. Paszkiewicz, P. Wolanski, G. Rarata, Possibility of Using Thermal Decomposition of Hydrogen Peroxide for Low Thrust Propulsion System Application, in: European Conference for Aeronautics and Space Sciences (EUCASS), Milan, Italy, 2017. https://doi.org/10.13009/EUCASS2017-626.

[115] D. Jang, S. Kang, S. Kwon, Preheating characteristics of H2O2 monopropellant thruster using manganese oxide catalyst, Aerosp. Sci. Technol. 41 (2015) 24–27.